UNIVERSITY OF ALBERTA

Modelling and Design of Advanced High-Power CO_2 Laser Systems

by

James Donald Strohschein ©

A thesis
submitted to the Faculty of Graduate Studies and Research
in partial fulfillment of the requirements for the degree of
Doctor of Philosophy

DEPARTMENT OF ELECTRICAL ENGINEERING

Edmonton, Alberta
Fall, 1996

National Library
of Canada

Bibliothèque nationale
du Canada

Acquisitions and
Bibliographic Services Branch

Direction des acquisitions et
des services bibliographiques

395 Wellington Street
Ottawa, Ontario
K1A 0N4

395, rue Wellington
Ottawa (Ontario)
K1A 0N4

Your file Votre référence

Our file Notre référence

The author has granted an irrevocable non-exclusive licence allowing the National Library of Canada to reproduce, loan, distribute or sell copies of his/her thesis by any means and in any form or format, making this thesis available to interested persons.

L'auteur a accordé une licence irrévocable et non exclusive permettant à la Bibliothèque nationale du Canada de reproduire, prêter, distribuer ou vendre des copies de sa thèse de quelque manière et sous quelque forme que ce soit pour mettre des exemplaires de cette thèse à la disposition des personnes intéressées.

The author retains ownership of the copyright in his/her thesis. Neither the thesis nor substantial extracts from it may be printed or otherwise reproduced without his/her permission.

L'auteur conserve la propriété du droit d'auteur qui protège sa thèse. Ni la thèse ni des extraits substantiels de celle-ci ne doivent être imprimés ou autrement reproduits sans son autorisation.

ISBN 0-612-18113-8

Canada

UNIVERSITY OF ALBERTA

Library Release Form

Name of Author: James Donald Strohschein

Title of Thesis: Modelling and Design of Advanced High-Power CO_2 Laser Systems.

Degree: Doctor of Philosophy

Year this Degree Granted: 1996

Permission is hereby granted to the University of Alberta Library to reproduce single copies of this thesis and to lend or sell such copies for private, scholarly, or scientific research purposes only.

The author reserves all other publication and other rights in association with the copyright in the thesis, and except as hereinbefore provided, neither the thesis nor any substantial portion thereof may be printed or otherwise reproduced in any material form whatever without the author's prior written permission.

James Strohschein
RR5
Wetaskiwin, AB
T9A 1X2

OCT 4 1996
Date

Bobynin, head engineer, in response to "and you were given a time limit...":

"What do you mean given a time limit? How do you picture science to yourself? 'Oh, wonder-working steed, build me a palace by morning,' and by morning there is a palace? And what if the problem has been incorrectly stated in the first place? And what if new phenomena turn up? A time limit!"

Aleksandr Solzhenitsyn: *The First Circle*,
translated from Russian by T. P. Whitney.

UNIVERSITY OF ALBERTA

FACULTY OF GRADUATE STUDIES AND RESEARCH

The undersigned certify that they have read, and recommended to the Faculty of Graduate Studies and Research for acceptance, a thesis entitled MODELLING AND DESIGN OF ADVANCED HIGH-POWER CO_2 LASER SYSTEMS submitted by JAMES DONALD STROHSCHEIN in partial fulfillment of the requirements for the degree of Doctor of Philosophy.

Dr. C. E. Capjack
(Co-Supervisor)

Dr. H. J. J. Seguin
(Co-Supervisor)

Robert Zedosejevs for R.S. Marjoribanks

Dr. R. S. Marjoribanks
(External Examiner)

MJBrett

Dr. M. J. Brett

W Finlay

Dr. W. H. Finlay

Ronald PW Lawson

Dr. R.P.W. Lawson

A. M. Robinson

Dr. A. M. Robinson

Robert Zedosejevs for P. R. Smy

Dr. P. R. Smy

Sept 25/96

Date

For Aubry & Marion, and those who came before:
Ruth & Cody; Helen & Paul.

"It has been an abundantly good life..."

Abstract

There exists a continuing demand for new high-power CO_2 laser systems which are more compact, more versatile, and more cost effective than those currently available. This thesis advances two ongoing development efforts which address these challenges.

Diffusion-cooled RF-excited slab systems are being advanced through their incorporation into laser arrays. With such arrays, the advantages of slab devices (ultra-compactness, efficiency, and reliability) may be leveraged to multi-kW devices. This thesis considers several problems facing the advance of slab arrays. A discharge-loaded electrode model is developed to address the problem of producing a uniform discharge over large-area electrodes. This model is tested experimentally with a novel fiber-optic diagnostic, and also successfully applied to designing electrodes for a multi-kW radial array. In this design, a new approach to attaining discharge homogeneity is employed. This electrode model appears sufficiently general to facilitate design optimization protocols. The other problem addressed is that of combining the beam-elements of the array into one useful beam. A model is developed to estimate the propagation and focusing properties for the special case of radial arrays. Best-possible beam quality, quantified in terms of the M^2 constant, is estimated for both phase-locked and non-phase-locked cases. Directions for future resonator developments are also suggested.

Convectively cooled impulse-sustained systems are being advanced through "burst-mode" excitation. This thesis studies two promising implications of burst-mode excitation: enhanced discharge stability, which allows higher system powers; and optical waveform control, which imparts additional control of laser-material interactions. First, to analyze discharge instability, a 1D simulation is developed of the discharge positive column. Both through experiments and this first simulation, several physical mechanisms are identified which may enhance discharge stability under burst-mode excitation. Second, the possibilities of optical waveform control are explored experimentally. Variation of the optical envelope over a broad range of profiles is demonstrated at multi-kW average powers. Optical pulse duration and shape are readily controlled through manipulation of the discharge excitation parameters. This dependence is characterized empirically. Finally, to facilitate further simulations of both discharge stability and optical waveform control, electron transport and rate coefficients are computed.

Acknowledgment

I would like to thank my supervisors, Drs. C. E. Capjack and H. J. J. Seguin, who were present through every twist and turn of this research. They were inspiring, critical, patient (impatient!); whatever was required at the time. Having worked with them through these years, I feel equipped to face the challenges ahead.

It is also my pleasure to acknowledge the various contributions and helpful influences of many student colleagues: D. Akitt, W. D. Bilida, A. H. Labun, S. W. C Scott, C. V. Sellathamby, B. E. Swekla, and E. F. Yelden. The expert staff of the high power laser laboratory are also thanked for their help: S. Nikumb, V. Pohnert, D. Presakarchuk, and H. Reshef. I have also appreciated the comfortable yet stimulating environment created by the faculty and staff of the Department of Electrical Engineering. I would especially like to thank H. Reshef and Dr. R. P. W. Lawson, in addition to my supervisors, for helpful counsel in a variety of matters. I would also like to thank Dr. P. R. Smy, whose fine teaching example contributed to lecturing being a rewarding experience.

For their generous financial support over the years, I thank the Natural Sciences and Engineering Research Council, the Alberta Heritage Fund, the University of Alberta, the Department of Electrical Engineering, and my supervisors.

Thanks also goes to NeXT Software Inc. and Wolfram Research, whose fabulous software has aided nearly every aspect of this research, and has made pleasurable tasks which would otherwise have been arduous.

Finally, and most emphatically, I thank my family and friends for contributions innumerable!

"D.G."

Table of Contents

1 Introduction 1

1.1 High-Power Electric-Discharge Carbon Dioxide Lasers 2

1.1.1 The CO_2 Molecule 2

1.1.2 The CO_2: N_2: He Electric Laser 3

1.1.3 Glow Discharge Excitation 4

1.1.4 CO_2: N_2: He Discharge Chemistry 5

1.2 PIE Laser Systems 6

1.2.1 PIE Mechanical Apparatus 6

1.2.2 PIE Excitation 7

1.2.3 Burst-Mode Operation 8

1.2.4 Implications of Burst-Mode Operation 9

Gain Medium Uniformity 10

Optical Envelope Control 10

1.3 ZODIAC Laser Systems 11

1.3.1 RF-Excited Slab Lasers 11

1.3.2 Arrays 12

1.3.3 ZODIAC Apparatus 13

1.3.4 Design Problems 14

Gain Media Uniformity 14

Composite Beam Propagation 15

1.4 Thesis Prologue 16

Bibliography 17

2 ZODIAC: Discharge Uniformity 20

2.1 Introduction 20

2.2 Laser Apparatus 22

2.3 Slab Electrode Model (SLM) 23

2.3.1 Electrode Assembly Model 24

2.3.2 Alpha-mode RF Discharge Model 26
Conditions of Negligible Sheath Power Loss 26
Conditions of Significant Sheath Power Loss 28
2.3.3 Model Summary 29
2.4 Model Testing and Application 31
2.4.1 Optical Detector Apparatus 31
2.4.2 Detector Calibration 31
2.4.3 Results of Experiment and Computation 33
Configurations with Two Inductors 33
Configurations with Four Inductors 35
2.5 Discussion 38
2.6 Summary 39
Bibliography 40
3 ZODIAC: Beam Propagation **42**
3.1 Introduction 42
3.2 Theory 43
3.2.1 Mode Propagation 43
3.2.2 Mode Superposition 45
3.2.3 The M^2 Beam Quality Measure 45
In Two Dimensions 47
Multiple Modes 48
3.3 Non-Phase-Locked ZODIAC 48
3.3.1 Model 50
3.3.2 Estimates of M^2 Lower Bound 50
3.3.3 Experimental Verification 53
3.3.4 Far-Field Properties 54
Intensity Contour Smoothness 54
Focal Spot Size, Power Density, and Power Fraction 55
3.3.5 Non-Phase-Locked ZODIAC Conclusion 59
3.4 Phase-Locked ZODIAC 60
3.4.1 Model 60

3.4.2 Numerical Analysis 61
M^2 Calculation 61
Far-Field Central Lobe Properties 62
3.4.3 Estimates of M^2 Lower Bound 63
3.4.4 Far-Field Properties 65
Effect of Channel Number and Phase-Locking 66
Effects of Combination Radius 67
Central Lobe Characteristics 67
Angular Fill-Factor 72
3.4.5 Phase-Locked ZODIAC Conclusion 73
3.5 Summary 75
Bibliography 77

4 PIE Burst-Mode: Enhanced Discharge Stability 79

4.1 Introduction 79
4.2 Preliminary Experiments 80
4.2.1 PIE-III Apparatus 80
4.2.2 Enhanced Discharge Stability 82
4.3 Definition of Problem 83
4.3.1 CO_2 Laser Glow Discharges 83
Plasma Properties 83
Discharge Equilibrium State 84
4.3.2 Discharge Instability 86
Thermal Instabilities 87
Self-Sustained Continuous Discharges 89
Externally Sustained Continuous Discharges 91
Impulse-Sustained Continuous Discharges 91
Summary 92
4.3.3 Methods of Discharge Stability Analysis 92
4.4 CODE1: 1D Positive Column Filament Model 93

4.4.1 Simplifying Assumptions 94
Model Geometry 94
Discharge Circuit 95
Discharge Kinetics 95
4.4.2 Governing Equations 96
Maxwell's Equations 97
Electron Energy Balance 97
Neutral Particles 98
Charged Particles 99
Pulser Events 100
Discharge Chemistry 101
Ambipolar Diffusion 103
Summary of Model Coefficients 104
4.4.3 Numerical Method 105
Conservation Problem 106
Diffusion and Source Term Problem 106
Boundary Conditions 107
4.4.4 Model Results and Discussion 107
Destabilizing Mechanisms 112
Stabilizing Mechanisms 113
4.4.5 Model Evaluation 115
Chemistry 115
Vibrational Kinetics 115
Numerical Model 116
Boundary Conditions 116
4.4.6 Conclusion 116
4.5 Further PIE-III Experiments 117
4.5.1 V-I Characteristics 117
4.5.2 Instability Threshold 119
4.5.3 Pulser Power 119
4.5.4 Conclusion 120
4.6 Summary 120
Bibliography 122

5 PIE Burst-Mode: Optical Waveform Control 126

5.1 Introduction 126

5.2 Experimental Apparatus 128

5.2.1 PIE-IV 128

5.2.2 Current Waveform Measurement 129

5.2.3 Optical Detector Measurement 130

5.2.4 Data Processing 131

5.3 Experimental Results 131

5.3.1 Overview of Burst-Mode Operation 131

5.3.2 Empirical Equation Development 134

Optical Duty Cycle 136

Peak Optical Power 138

5.3.3 Summary 140

5.4 Summary 141

Bibliography 142

Appendix 5.A: Ultra-Fast High-Resolution Optical Isolator 144

Appendix 5.B: Optical Detector 148

6 PIE Burst-Mode: Electron Transport and Rate Coefficients 151

6.1 Introduction 151

6.2 Boltzmann Equation Solver 152

ELENDIF 152

GAMUT 153

Cross-Section Data 154

6.3 Tests of ELENDIF, GAMUT and Cross-Sections 154

Pure Gases 154

CO_2 Laser Gas Mixtures 156

6.4 Solutions for a PIE Gas Mixture 156

6.5 Summary 160

Bibliography 161

7 **Conclusions and Recommendations** **163**

7.1 Conclusions 163

7.1.1 ZODIAC Multi-kW Slab Array 163

Discharge Uniformity 163

Beam Propagation Characteristics 164

7.1.2 PIE Burst-Mode Operation 165

Enhanced Discharge Stability 165

Optical Waveform Control 166

Electron Transport and Rate Coefficients 166

7.2 Recommendations for Further Work 167

7.2.1 ZODIAC 167

Discharge Uniformity 167

Beam Propagation Characteristics 167

7.2.2 PIE Burst-Mode 168

Discharge Stability 168

Optical Waveform Control 169

Electron Transport and Rate Coefficients 170

Bibliography 171

List of Tables

Table 3.4-1 Summary of array configurations in Figures 3.4-4 and 3.4-5. 67

Table 4.3-1 Characteristic times of discharge processes 84

Table 4.3-2 Best-fit parameters for Figure 4.3-3 of form (4.3-4). 91

Table 4.4-1 Simplified gas chemistry model for a CO_2:N_2:He mixture. 102

Table 4.4-2 Neutral gas properties for He:N_2:CO_2:CO = 16:10:1:1Torr. 104

Table 4.4-3 Electron and ion related coefficients. 105

Table 5.3-1 Best fit parameters for equation (5.3-3) 137

Table 5.A-1 Optical isolator transmitter circuit elements. 146

Table 5.A-2 Optical isolator receiver circuit elements 147

Table 5.B-1 PEM amplifier circuit components 150

Table 6.2-1 Electron collision cross-sections used with ELENDIF. 154

List of Figures

Figure 1.1-1 Energy level diagram of the CO_2: N_2: He laser. 3

Figure 1.2-1 End-view of PIE vacuum vessel 7

Figure 1.2-2 PIE excitation and discharge circuit diagram. 8

Figure 1.2-3 Illustration of the PIE pulser sequence 9

Figure 1.2-4 Effects of PIE burst-mode operation. 10

Figure 1.3-1 Cross-sectional view of ZODIAC radial array apparatus. 13

Figure 2.2-1 Cut-away view of a ZODIAC radial array slab laser 23

Figure 2.3-1 Segmented transmission line model of an electrode assembly. 24

Figure 2.3-2 Circuit element model of an alpha-mode RF discharge 27

Figure 2.3-3 Local discharge properties as a function of local current density. 30

Figure 2.4-1 Optical detector apparatus. 32

Figure 2.4-2 Local discharge luminosity as a function of current density 32

Figure 2.4-3 Experimental results and model predictions compared for a two-inductor configuration at an average power loading of 3.4 W/cm^2. 34

Figure 2.4-4 Predicted dependence of discharge uniformity on total power dissipation and frequency, for a two-inductor configuration optimized for 40 Torr and 8.0 W/cm^2. 34

Figure 2.4-5 Experimental results and model predictions compared for a four-inductor configuration at an average power loading of (a) 4.2 W/cm^2 and (b) 5.4 W/cm^2. 36

Figure 2.4-6 Predicted dependence of discharge uniformity on total power dissipation and frequency, for a four-inductor configuration optimized for 40 Torr and 8.0 W/cm^2. 37

Figure 3.3-1 ZODIAC intensity profile at the resonator output plane: (a) typical perspex burn produced with a toric confocal resonator, [3] reproduced here to scale; (b) the basic ZODIAC array configuration parameters. 49

Figure 3.3-2 Dependence of non-PL ZODIAC dimensionless full-width divergence on beamlet aspect ratio *a*/*b*. 52

Figure 3.3-3 Dependence of non-PL ZODIAC propagation constant (M_r^2) on configuration parameters (a) r/a and a/b, and (b) r/b and a/b. 53

Figure 3.3-4 Effect of beamlet aspect ratio on far-field spot "smoothness" (the relative variation in radius around an intensity contour). 55

Figure 3.3-5 Effect in the far-field of increasing the number of channels in a non-PL ZODIAC. Beamlet aspect ratio is constant (a/b=3), and peak intensity is normalized. Plotted far-field extent is $-1.4 < sa < 1.4$. 56

Figure 3.3-6 Effect in the far-field of enlarging the greater near-field dimension while holding the lesser constant (in this case, a and b, respectively). Plotted far-field extent is $-0.75 < sa < 0.75$ 57

Figure 3.3-7 ZODIAC focal spot properties for large n and constant a. Effect of a/b on: (a) contour radii; (b) power fraction contained within the contours; and (c) the average intensity within the contours.. 58

Figure 3.4-1 ZODIAC propagation constant (M_r^2) and far-field divergence for a/b = 1.67 and various n, for (a) gaussian beamlet profiles, and (b) supergaussian profiles. 64

Figure 3.4-2 ZODIAC propagation constant (M_r^2) and far-field divergence for a/b = 4.00 and various n, for (a) gaussian beamlet profiles, and (b) supergaussian profiles. 65

Figure 3.4-3 Effect of phase-locking and n on far-field profile for a/b=1.67, a/r=2.0. 66

Figure 3.4-4 Effect of r/a on far-field properties, for a/b=1.67. 68

Figure 3.4-5 Effect of r/a on far-field properties, for a/b=4.00. 69

Figure 3.4-6 Dependance on a/b and n of focal spot power fraction and size. 70

Figure 3.4-7 ZODIAC-II (n=24 and a/b=4) central lobe characteristics, normalized with respect to the corresponding quantities for a gaussian annulus. 71

Figure 3.4-8 M_r^2 and far-field spot size as a function of angular fill-factor 73

Figure 4.2-1 Typical PIE-III discharge waveforms: (a) voltage; and (b) current, for a burst frequency of 330 Hz.. 81

Figure 4.2-2 Laser output power at the onset of instability, as a function of burst rate. 83

Figure 4.3-1 Illustrative comparison of electron rate coefficients. 85

Figure 4.3-2 Simplified illustration of discharge response to a local disturbance in neutral density and temperature. 88

Figure 4.3-3 Characteristic times for discharge constriction in a steady self-sustained discharge. Parameters for best-fit functions of form (4.3-4) are summarized in Table 4.3-2. 90

Figure 4.4-1 Geometry of a transverse flow device. 94

Figure 4.4-2 Simulated discharge (a) current and (b) voltage for a sustainer voltage of 1500V. 108

Figure 4.4-3 Evolution of the uniform positive column state with an on-axis gaussian perturbation for a representative burst-mode configuration. 110

Figure 4.4-4 Current perturbation growth as a function of average power density, for an initial 0.5% isobaric depression in gas density: (a) the maximum perturbation amplitude during the gas residence time $t < \tau_g$; (b) the perturbation amplitude at $t = \tau_g$. 111

Figure 4.4-5 Discharge properties as a function of average power density: (a) final gas temperature, and (b) average reduced field. 111

Figure 4.5-1 Final PIE-III experimental results: (a) dependence of instability threshold on burst rate and pulser power, where pulser powers are specified for CW condition; (b) dependence of average impulse energy on burst rate, while sustainer current is held constant at 15 A; (c) laser V-I characteristics. 118

Figure 5.2-1 PIE-IV circuit diagram.. 128

Figure 5.2-2 Discharge excitation voltage and current as a function of burst frequency, for P_{av}= 4 kW and n=7. 129

Figure 5.3-1 Laser output and discharge current waveforms at an average laser power of 4kW; illustrating effect of altering the number of pulses (N) while holding burst frequency (f_b) constant at 75 Hz: (a) $N = 7$; (b) $N = 27$ 132

Figure 5.3-2 Laser output and discharge current waveforms at an average laser power of 4kW; illustrating effect of altering f_b while holding N constant at 3: (a) $f_b = 357$ Hz ; (b) $f_b = 200$Hz. 133

Figure 5.3-3 Laser output and discharge current waveforms for CW operation at an average laser power of 4 kW. 134

Figure 5.3-4 Dependence of laser peak and offset power on burst frequency and average laser power for $N = 7$. 135

Figure 5.3-5 Peak laser power with respect to optical duty cycle, for $N = 7$. The solid lines represent empirical characteristics (5.3-5) and (5.3-6). 136

Figure 5.3-6 Dependence of optical duty cycle on burst frequency and average laser power for N=7.. 137

Figure 5.3-7 Optical duty cycle as a function of pulse number and burst frequency. Experimental points are for average laser powers of 2 kW, 4 kW, and 6 kW. Solid lines represent empirical equation (5.3-5). 137

Figure 5.3-8 Optical duty cycle with respect to energy per pulse and average laser power for a constant burst duty cycle (a) 10%, (b) 20%, and (c) 40%. Experimental data is represented by points, and empirical equation (5.3-5) by solid lines. 138

Figure 5.3-9 Peak laser power as a function of energy per pulse with (a) P_p averaged over $N< 15$, and (b) all data points. 139

Figure 5.3-10 Average shape factor, as a function of energy per pulse, averaged over $N < 15$. The solid curve corresponds to the distinct-pulse regime, while the dashed lines corresponds to the onset of continuous-offset. 139

Figure 5.3-11 Peak laser power with respect to burst frequency, for N=7 pulses. Points are experimental data and the solid line represents empirical equation (5.3-6), which are here extrapolated into the continuous-offset regime. 140

Figure 5.A-1 Optical isolator transfer function (a) amplitude response (b) phase response 145

Figure 5.A-2 Normalized spectral power density of typical current waveform. 145

Figure 5.A-3 Optical isolator: circuit diagrams for (a) the transmitter, and (b) the transmitter power supply. 146

Figure 5.A-4 Optical isolator: receiver circuit diagram. 147

Figure 5.B-1 PEM amplifier gain characteristics (a) amplitude response (b) phase response 149

Figure 5.B-2 Normalized spectral power density of typical optical waveform. 149

Figure 5.B-3 PEM amplifier circuit diagram. 150

Figure 6.3-1 Electron drift velocity in pure mixes of the primary CO_2 laser gases. 155

Figure 6.3-2 Comparison of ELENDIF calculations with experimental data for two CO_2 laser gas mixes at 300 K: (a) $He:N_2:CO_2 = 12:1:4$, and (b) $He:N_2:CO_2 = 30:7:1$. 157

Figure 6.4-1 Electron-collision power transfer fractions in $He:N_2:CO_2:CO = 16:10:1:1$. at 300 K to (A) elastic collisions and rotational excitation; (B) excitation of upper laser ASM of CO_2 and the first eight vibrational modes of N_2 (together these effectively constitute the upper laser level); (C) excitation of BM and SSM of CO_2; (D) excitation of CO vibrational modes; (E) electronic excitation; and (F) ionization. 158

Figure 6.4-2 Transport coefficients for electrons in $He:N_2:CO_2:CO = 16:10:1:1$ at 300 K: (a) drift velocity; and (b) reduced mean energy and characteristic energy. 159

Figure 6.4-3 Reaction rate coefficients for electrons in $He:N_2:CO_2:CO = 16:10:1:1$ at 300 K: (a) mixture weighted ionization and attachment rates for the primary gas constituents; and (b) the EEDF, from which other reaction rates for minority species can be derived using (6.4-1). 159

List of Symbols

Abbreviations / Acronyms

AC	Alternating Current
ASM	Asymmetric Stretch Mode of CO_2
BE	Boltzmann's Equation
BM	Bending Mode of CO_2
CODE1	1D model of glow discharge positive column (Chapter 4)
CW	Continuous Wave
DC	Direct Current
EDL	Electric Discharge Laser
EEDF	Electron Energy Distribution Function
ELENDIF	ELectron ENergy finite DIFference, a public domain BE solver (Chapter 6)
FFT	Fast Fourier Transform
GAMUT	Code which controls convergence of ELENDIF runs (Chapter 6)
GAT	Glow-to-Arc Transition
M2	Code which computes M^2 and far-field properties of a paraxial beam (Chapter 3)
NM	N_2 vibrational mode
PEM	Photo-electromagnetic
PIE-III	10 kW impulse-sustained fast transverse flow laser system
PIE-IV	30 kW impulse-sustained fast transverse flow laser system
PL	Phase-locked
non-PL	Non-phase-locked
RF	Radio Frequency
SLIM	SLab 1-dimensional electrode Model (Chapter 2)
SSM	Symmetric Stretch Mode of CO_2
TDL	Times diffraction limited
TEA	Transversely Excited Atmospheric
TEM	Transverse Electric and Magnetic
TL	Transmission Line

V-V	Vibrational-to-Vibrational energy transfer
V-T	Vibrational-to-Translational energy transfer
ZODIAC-I	8-channel radial slab laser array
ZODIAC-II	24-channel radial slab laser array

Roman Symbols

a	Beamlet half-width in the radial dimension
$\boldsymbol{A}_k$	Forward travelling wave phasor amplitude
b	Beamlet half-width in the transverse dimension
$\boldsymbol{B}_k$	Reverse travelling wave phasor amplitude
C	TL local lumped parallel capacitance (or) Total beam power
C_p	RF-discharge plasma column capacitance
C_s	RF-discharge sheath capacitance
d_s	RF-discharge time-averaged total sheath width
D	Inter-electrode gap
D^a	Ambipolar diffusion coefficient
D_b	Burst duty cycle
D_T	Transverse diffusion coefficient
e	Elementary charge (1.6022 10^{-19} C)
$\boldsymbol{E}(x,y,z)$	Phasor amplitude profile
E/n	Reduced electric field, in unit of Townsend: $1\mathrm{Td} \equiv 10^{-21}\,\mathrm{Vm}^2$.
E_p	RF discharge plasma column electric field (or) Energy per pulse
f	Slab excitation frequency
f_b	Burst frequency
f_p	Pulser frequency
$f(\varepsilon)$	Electron energy distribution function
G	TL local lumped parallel conductance
i	The imaginary number $\sqrt{-1}$
$\boldsymbol{I}$	Identity matrix
$\boldsymbol{I}_k(x)$	Current distribution on electrode TL segment k
I, I_1, I_2, I_s	Instantaneous intensity
$\tilde{I}$	Spatial-frequency power density
$\boldsymbol{J}_e, \boldsymbol{J}_+, \boldsymbol{J}_-$	Current densities of electrons, positive ions, and negative ions

J_d		Discharge current density
JE		Power density
k		Rate coefficient
k_a, k_d, k_i, k_r^{ei}		Rate coefficients for attachment, detachment, ionization, and electron-ion recombination
k_B		Boltzmann constant (1.3807 10^{-23} J/K)
l		Electrode length
L		TL local lumped series inductance
n		Number of electrode segments
	(or)	Number of radial array channels
	(or)	Neutral particle density
n_e, n_+, n_-		Densities of electrons, positive ions, and negative ions
N		Number of impulses per burst
m_e		Electron mass (9.11 10^{-31} kg)
M^2		Space-bandwidth-product propagation constant
p		Gas pressure
	(or)	Cyclic spatial frequency corresponding to r
$\boldsymbol{P}(x,y,z)$		Spatial frequency profile phasor
P_{av}		Average laser power
P_p		Plasma column power dissipation
	(or)	Peak laser power
P_s		Sheath power dissipation
P_{therm}		PEM thermal offset
r		Radial coordinate
	(or)	Radial array combination radius
R		TL local lumped series resistance
R_b		Ballast resistance
R_d		RF discharge resistance; $Re(\mathbf{Z}_d)$
R_d'		RF discharge resistance, corrected to account for sheath losses
R_p		RF discharge plasma column resistance
R_s		RF discharge sheath resistance
	(or)	Conductor surface resistance
s		Cyclic spatial frequency corresponding to x
S		Slab discharge area
	(or)	Shape factor
t		Cyclic spatial frequency corresponding to y

T, T_e, T_v	Gas temperature, electron temperature, and vibrational temperature
$\mathbf{u}$	Gas velocity
$\mathbf{V}_k(x)$	Voltage distribution on electrode TL segment k
$\mathbf{V}_{lhs}$	LHS electrode voltage supply
V_p	RF discharge plasma column voltage.
$\mathbf{V}_{rhs}$	RHS electrode voltage supply
V_{sst}	Sustainer voltage
w	Slab electrode width
	(or) Gaussian beam half-width
W	Beam half-width
X_c	Dielectric sidewall capacitive reactance
X_d	RF discharge reactance; $Im(\mathbf{Z}_d)$
x_k	RHS boundary of electrode segment k
X_L	Terminating inductor reactance
$\mathbf{Z}_d$	RF discharge impedance ($\mathbf{Z}_d = R_d + X_d$)
$\mathbf{Z}_k$	Shunt inductor at RHS boundary of electrode segment k
z_0	Position of beam waist
$\mathbf{Z}_0$	TL characteristic impedance

Greek Symbols

α	Townsend's first ionization coefficient
β	TL wave number
ε	Electron energy
	(or) Vibrational quanta
ε_k	Characteristic energy; $\varepsilon_k = D_T/\mu$
ε_0	Permittivity of free space (8.8542 pF/m)
γ	TL propagation constant
	(or) Townsend's third ionization coefficient
	(or) Adiabatic index
η	Kinematic viscosity
η_θ	Angular fill-factor
θ	Angular coordinate
κ	Thermal conductivity
λ	Wavelength
μ_e, μ_+, μ_-	Mobilities of electrons, positive ions, and negative ions
μ_0	Permeability of free space (0.4π μH/m)

$\nu_m, \nu_u, \nu_T, \nu_v$	Collision frequencies for electron momentum transfer, energy exchange, gas T-R heating, and vibrational excitation
ξ_T, ξ_V	Average T-R energy per particle, and average vibrational energy per molecule
Φ	Full-width beam divergence (or) Viscous dissipation function
ρ	Gas mass density
$\sigma_x, \sigma_y, \sigma_r$	Second moments of the intensity distribution, in the x, y, and r dimensions
$\sigma_s, \sigma_t, \sigma_p$	Second moments of the spatial-frequency intensity distribution, in the s, t, and p dimensions
$\sigma(\varepsilon)$	Electron collision cross-section
τ	Characteristic instability growth time
τ_g	Gas residence time
τ_{VT}	Characteristic time for V-T relaxation
$\hat{\tau}$	Sensitivity of τ to changes in power density; $\hat{\tau} \equiv (\frac{JE}{\tau})\frac{\partial\tau}{\partial JE}$
ω	Radian frequency = $2\pi f$

Other Mathematical Symbols

$\boldsymbol{A}$	Complex number
A	Scalar quantity
$Im()$	Imaginary part of ()
$Re()$	Real part of ()
$\sim$	Proportional to
$\approx$	Approximately equal to
$\equiv$	Identically equal to
$\lvert(\ )\rvert$	Absolute value of ()
$\langle(\ )\rangle$	Average value of ()
∇	Gradient
$\nabla\bullet$	Divergence
$\nabla\times$	Curl
∇^2	Laplacian
∂	Partial derivative

1

Introduction

The CO_2 laser was invented by Patel [1] in 1964 at the AT&T Bell Laboratories in Murray Hill. It is an elegant four level laser based on the low-lying vibrational-rotational transitions of CO_2. From its beginning, it has been associated with high power. Prior to Patel's innovation, it was widely believed that low pressure gas discharge lasers were inherently low power devices, and that gas laser efficiencies were limited to a few percent. [2] Patel's laser shattered these misconceptions, being the first of any type to produce CW output in excess of 100W, and by easily operating at efficiencies in excess of 10%. A rapid proliferation of CO_2 laser technology followed. The CO_2 laser has since become a workhorse in a wide variety of industrial, medical, meteorological, and military applications.

The evolution of high-power CO_2 electric discharge lasers (EDL) has proceeded through several distinct phases.[†] The first CO_2 lasers were tubular devices, DC excited and cooled by molecular diffusion to the tube walls. Limited gas cooling in these devices constrained tube diameter, so that laser output power scaled with discharge tube *length*. Kilowatt-scale systems were not practically achievable, as they required discharge tube lengths approaching 100m. [3] The introduction in 1969 of rapid convective cooling permitted *volume* scaling of laser output power. [4] Systems producing several tens of kW, based on either rapid axial or transverse gas flow, soon followed. More recent developments have CO_2 laser evolution again favoring diffusion cooling. RF-excited planar electrodes ("*slabs*") permit power scaling with discharge *area*. [5] With this technology, very compact high-power devices are possible. [6] While device powers are presently limited to 1-2 kW, with the recent advent of slab *arrays*, the scaling of slab technology to kilowatt device sizes is imminent.[7]

Over the last three decades, high power CO_2 lasers have become established in a broad variety of applications. Yet there is considerable potential for new applications. For many such applications to be viable, however, new laser devices are required which are more versatile, more compact, and more cost effective than those presently available. In this thesis, several studies are presented which will contribute to making existing convectively cooled devices more amenable to custom processing applications, and possibly more compact. In addition, studies are presented which address several development problems facing multi-kW slab arrays. It is anticipated that slab arrays will be revolutionary in industrial application, as they promise to be more efficient, simpler, and at least an order of magnitude smaller than the convectively cooled systems of comparable power. The primary mode of this investigation is numerical analysis.

[†] There are important methods of CO_2 laser excitation other than by electric discharge (*e.g.*, chemically pumped, optically pumped and gas dynamic lasers), however such devices are not in common use.

Specifically, in this thesis two numerical models are developed to facilitate the advance of multi-kW slab technology: one to aid design of slab electrodes which provide optimally uniform discharge excitation (Chapter 2), and one to estimate the beam propagation characteristics of a radial ("ZODIAC") array of slabs, in aid of selecting the array configurations most suitable for materials processing applications (Chapter 3). Regarding the advance of well-established technologies, in this thesis two promising implications of "burst-mode" discharge excitation are also investigated: enhanced discharge stability (which allows higher operational powers) is studied with a numerical model (Chapter 4); and optical waveform control (which imparts an additional degree of control to materials processing) is characterized experimentally (Chapter 5). Finally, additional simulation tools are assembled to facilitate further investigations of both discharge instability and waveform control (Chapter 6).

In the remainder of this chapter, a brief introduction to CO_2 laser discharge physics is given (Section 1.1), followed by an overview of the specific laser systems to which the thesis analysis has been applied: burst-mode PIE fast-transverse flow systems (Section 1.2), and multi-kW ZODIAC radial slab array systems (Section 1.3). The chapter concludes with a thesis prologue (Section 1.4).

1.1 High-Power Electric-Discharge Carbon Dioxide Lasers

A brief overview of the CO_2 laser is given here, focusing primarily on the discharge aspects of electric discharge lasers (EDL), which are of interest in this thesis.

1.1.1 The CO_2 Molecule [8-10]

The CO_2 molecule quantum state includes a dependence on rotational and vibrational states, as well as on electronic states. In first approximation, these aspects of molecular state are decoupled and may be considered separately. The individual vibrational modes are similarly independent. As illustrated in Figure 1.1-1, the normal vibrational modes are: the symmetric stretch mode (SSM), the asymmetric stretch mode (ASM), and the bending mode (BM). Each of these modes is well approximated by a simple harmonic oscillator because the spacing of the low-lying energy levels is nearly equal. Under conditions of interest to CO_2 lasers, each mode may be characterized by a unique Boltzmann temperature because thermalization within the modes is relatively rapid, whereas thermalization between them is not.

Vibrational-rotational transitions of the CO_2 molecule are the basis of the CO_2 laser. To facilitate laser action in electric discharges, N_2 and He are usually combined with CO_2. It can be shown that the internal energy state of a CO_2: N_2: He discharge is well represented by a five temperature model having individual temperatures for SSM, ASM, BM, the nitrogen mode (NM), and the translational temperature. [11]

1.1.2 The CO_2: N_2: He Electric Laser [12-14]

Each of the primary constituents of a CO_2: N_2: He discharge has a distinct role in laser kinetics. As indicated in Figure 1.1-1, the electric CO_2 laser is a four level laser capable of lasing in two infrared bands around 10.6 and 9.4 microns. Laser action is due to vibrational-rotational transitions of the ground electronic state of CO_2: the decay from the ASM (001) to the SSM (100) yields a photon in the 10.6 micron band, while the decay from the ASM (001) to the BM (020) yields a photon in the 9.4 micron band. Photon wavelength also depends on the initial and final rotational states. Indeed, laser oscillation may be obtained on more than 200 VR transitions in the 8 - 18 micron range. [2]

Figure 1.1-1 has been removed due to copyright restrictions. The information removed was Figure 10.31 from [15].

Figure 1.1-1 Energy level diagram of the CO_2 : N_2 : He laser. (Reprinted from [15].)

Population inversion is established by collisional pumping of the upper laser level ASM (001). Two processes are important: direct electron-CO_2 impact, and resonant energy transfer from vibrationally excited N_2 molecules. The primary role of N_2 in the discharge is to pump the upper laser level; the difference between the first NM and ASM is about 0.1 k_BT at room temperature, so resonant energy transfer between the vibrational modes occurs readily. The first half dozen or so energy levels of the NM correspond closely to those of the CO_2 ASM. Additional advantages of N_2

as a pumping agent are that its vibrational modes have large collision cross-sections, and are metastable. Hence, both pumping of the NM and energy transfer to the ASM are very efficient.

Depopulation of the lower laser level, also collision-induced and required to maintain a population inversion, is a two-step process. SSM energy transfers rapidly to the BM (a vibrational to vibrational energy transfer, or "V-V" reaction), which then relaxes to the ground state as a result of collisions (a vibrational to translational energy transfer, or "V-T" reaction). The latter process is the slower of the two. Helium is added to accelerate relaxation of the BM, thereby preventing thermal "bottlenecking" which would otherwise diminish the laser inversion and degrade laser performance. While He is very effective in depopulation of the lower laser level, it does not strongly depopulate the upper laser level. In addition, the thermal conductivity of He is about an order of magnitude larger than that of CO_2 and N_2, so its presence aids gas cooling. Helium is also inert, so it doesn't affect the discharge chemically. Its presence does however increase the electron temperature for a given reduced field strength (E/n), which results in higher rates of ionization. [16]

Laser performance necessarily deteriorates with increasing gas temperature, as maintaining a population inversion becomes increasing difficult. With increasing gas temperature, depopulation of the lower laser becomes less effective. Simultaneously, the collisional relaxation rate of the upper laser level increases. Thus, the population inversion is diminished by increased gas temperature. Additionally, the cross-section for stimulated emission decreases with increasing temperature.[12] For these reasons, the laser gases must be actively cooled. This is possible either through diffusion to chilled electrodes or walls, or by convective exchange of gas within the inter-electrode volume. Whence follow the two major classes of EDL: diffusion cooled and convectively cooled.

1.1.3 Glow Discharge Excitation

The objective of electric excitation is to establish a spatially uniform population inversion of the CO_2 vibrational levels, so as to create a uniform laser gain medium. Generally desirable for this purpose is a *glow* discharge, characterized by a uniform, moderate current density. [17] Such discharges in EDLs may be established by excitation with currents ranging in frequency from DC to microwave, [18] and also with various combinations of simultaneously applied AC and DC. [19] Vibrational excitation in an electric discharge is due mainly to electron-molecule impact. When the gas mixture and electron temperature is optimized, more than 90% of discharge power may go to direct vibrational heating.†

In low-frequency discharge-excitation, most ionization occurs in the near-electrode sheaths, where electric field strengths are highest. Electrons are generated by ion bombardment of the electrodes (γ-processes), and subsequent avalanche multiplication (α-processes) in the cathode sheath. As the excitation frequency is increased, once the excitation period is less than the electron transit time from electrode to electrode, volume ionization due to α-processes dominates. Regardless of excitation frequency, most useful vibrational excitation occurs in the bulk discharge region, outside of the near-electrode space-charge sheaths (*i.e.*, in the "plasma column", or, for DC and low-frequency excitation, in the "positive column") In the sheaths, both neutral gas and electron temperatures are typically much higher than is desirable for creating laser gain.

---

† Neutral gas heating subsequently occurs gradually as vibrational energy relaxes into translational-rotational modes.

Discharge power is inevitably limited by the onset of electro-thermal instabilities, which cause the desired diffuse current of a glow discharge to collapse into filamentary arcs. These glow-to-arc transitions (GAT) may not only limit the attainable laser power, but also threaten the laser apparatus. Instability imposed limits are more restrictive in general for DC-excited discharges than they are for AC discharges. For example, narrow-gap RF-discharges can be stable well past power loadings of interest for laser excitation. [20] The enhanced discharge stability is due mainly to the distributed ballasting provided by the capacitive near-electrode sheaths.† [21,22]

Glow discharges may be classed according to whether they are *self-sustained* (*i.e.*, internal discharge processes generate sufficient electrons to sustain a steady current), or *externally sustained* (the discharge ionization fraction must be supplemented by external sources to sustain a steady current). Examples of possible external ionization sources are ultraviolet radiation, electron beams, and independent RF or impulse voltages. There are two primary advantages to external ionization. First, it allows independent control of both electric field strength and current density, thus accommodating the choice of the optimal ionization fraction and reduced field strength (E/n). Second, in the presence of external ionization, the details of electron production are less sensitive to variations in local plasma state. Consequently, externally sustained discharges tend to be more stable than self-sustained discharges. This second advantage is especially important for DC-pumped discharges, and will be discussed at greater length in Chapter 4.

1.1.4 CO_2: N_2: He Discharge Chemistry

The energetic electrons used to pump the vibrational-rotational modes of CO_2 and N_2 also react with those species to form many secondary species, both ionic and neutral. Many hundreds of derivative species accumulate over time in a sealed system. Laser performance and discharge stability are found to depend strongly on the nature of these secondary species. While they typically do not strongly influence vibrational relaxation directly, the secondary species can strongly affect electron production and loss through recombination, attachment and detachment.

Chemical additives are often used to favorably alter discharge chemistry. For example, discharges in which negative ions are more numerous than electrons tend to be less stable than those for which electrons are the dominant species. CO, which is an effective detaching agent, is often added to suppress attachment-related instabilities. Another benefit of CO is that it prevents dissociation of CO_2 by establishing a strong formation reaction. Another common additive is Xe which, being easily ionized, causes a significant increase in electron density for a given *E/n*. Xe also changes the electron energy distribution function; its presence shifts high energy portions of the distribution down to energies more amenable to efficient excitation of the upper laser level.[8,18] Water vapor also acts as a gaseous catalyst to enhance reformation of CO_2, [23] however, it also causes rapid depopulation of the upper laser level. [8]

---

† Note however that as excitation frequency and discharge pressure are increased, ultimately this sheath-stabilizing effect is lost. With metal electrodes, for discharge conditions and electrode gaps which maximize laser power, this may occur at about 300 MHz and 150 Torr. [20]

1.2 PIE Laser Systems

Developed at the University of Alberta over the last two decades, PIE laser technology represents state-of-the-art high power CO_2 industrial lasers. The acronym Photo-initiated, Impulse-enhanced, Electrically excited [24] implies that the laser gain is created by three interacting processes, as will be described in Section 1.2.2

This thesis presents studies of phenomena in two separate PIE laser systems (PIE-III, a 10 kW device [25-28]; and PIE-IV, a 30 kW device [29]). In this section, a general overview of the PIE systems is presented, with an emphasis on discharge excitation and the burst-mode concept with which PIE technology has been significantly advanced. Also presented are the implications of burst-mode operation which have motivated the studies of Chapters 4-6. Special features of the systems relevant to those studies will be discussed in their respective chapters.

1.2.1 PIE Mechanical Apparatus

PIE lasers are fast transverse flow devices; the directions of electric current flow, gas flow and the optic axis are mutually orthogonal. A cross-sectional view of the 30 kW PIE-IV system is depicted in Figure 1.2-1 This cross section is perpendicular to the optical axis.

The laser gas mix, typically at pressures around 40 Torr, is circulated through the discharge region at subsonic velocities by the flow compressors. This gas is cooled by the heat exchangers prior to re-entry into the discharge region, which is about 10 cm wide in the direction of current flow, and about 20 cm long in the direction of gas flow. Gas flow velocities of around 50 m/s through the discharge region are typical. This rate results in a gas discharge residence time of about 3.6 ms, and corresponds to a Mach number of about 0.1. Bulk convection serves, in addition to cooling the laser gas, to sweep electro-thermal instabilities from the discharge region before they have time to develop fully.

Both electrodes are arrays of stainless steel pins several mm in diameter and several cm in length. The electrode pin density is about 1/3 cm^{-2}. Each pin is individually ballasted by an aqueous electrolyte circulated through the electrode blocks in which the pins are set. Such ballasting is required for DC discharges to maintain a steady current, since the discharge itself has

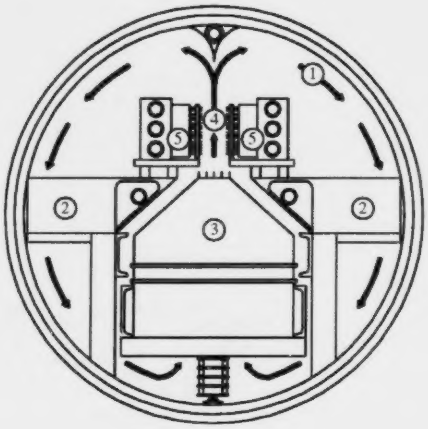

Figure 1.2-1 End-view of a PIE vacuum vessel: (1) gas flow; (2) heat exchangers; (3) axial flow compressors; (4) the discharge area; (5) fluid-ballasted multi-element electrodes. Approximate vacuum vessel dimensions are a diameter of 1.5 m and a length of 3.5m.

a negative dynamic impedance. Distributed non-linear ballast resistance and electrode segmentation also tend to enhance discharge stability. [30]

1.2.2 PIE Excitation

The PIE (Photo-initiated Impulse-enhanced Electrically excited) excitation technique produces a CW laser gain medium by the superposed application of a DC voltage (*sustainer*) and a train of high-voltage impulses (*pulser*). The sustainer voltage provides most of the pumping power (>99%), while the impulse stream is an efficient ionizer which allows a much larger DC pumping current to be maintained than would otherwise be possible.† Thus independent control of electron density and electric field strength is accommodated, allowing for separate optimization. [26]

The average electron density is controllable through adjusting the pulser frequency and/or amplitude. A pulser frequency of a few kHz is found to be sufficiently rapid to maintain a continuous discharge. The rising edge of each 50 ns impulse causes a flash of vacuum ultraviolet (VUV) radiation to be emitted from corona on the electrode pin tips. This VUV uniformly ionizes the discharge volume, and is followed by a collisional avalanche of electron multiplication driven by the remainder of the impulse ("*Photo-initiated, Impulse-enhanced*"). In this way, a uniform plasma is refreshed at the pulser frequency. The rate of plasma decay is such that quasi-CW

---

† As will be discussed in Chapter 4, it is difficult to class the PIE discharge as either self-sustained or externally sustained. It will be found that once an impulse has initiated a discharge, the DC voltage is sufficient to sustain a steady current in the absence of impulses, albeit at a reduced level relative to operation with the pulser. However, in the absence of an initial impulse, the DC voltage is unable to initiate a glow discharge.

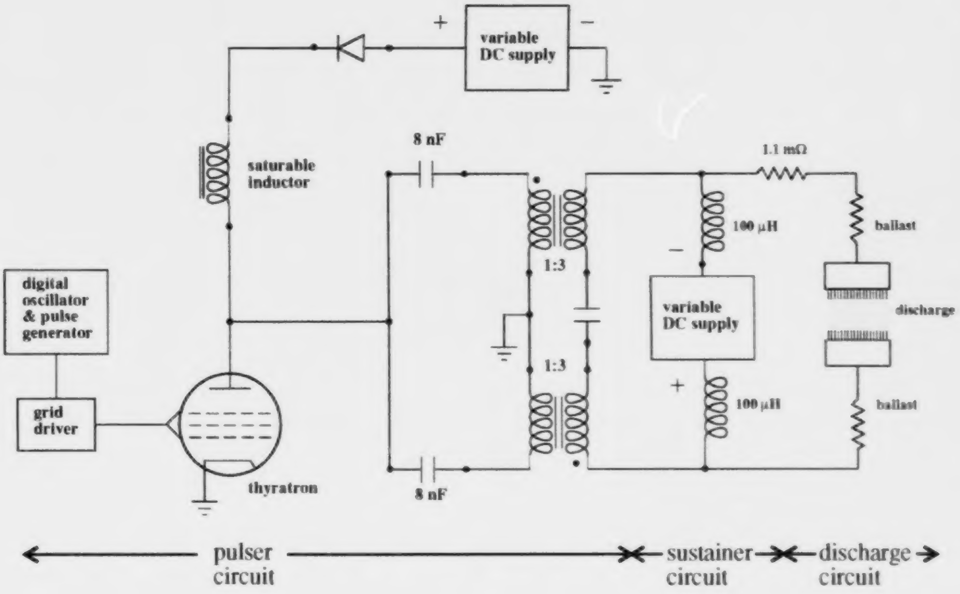
+
–
variable DC supply
saturable inductor
8 nF
1.1 mΩ
100 μH
ballast
–
1:3
digital oscillator & pulse generator
variable DC supply
discharge
1:3
+
grid driver
100 μH
ballast
thyratron
8 nF
pulser circuit
sustainer circuit
discharge circuit

Figure 1.2-2 PIE excitation and discharge circuit diagram.

operation (hereafter referred to as CW) is achieved at a pulser frequency of 5 kHz, which corresponds to a 200 μs inter-impulse period.

A diagram of the PIE excitation circuit is given in Figure 1.2-2. A hydrogen thyratron, driven by a digital pulse generator, is the primary switching element in impulse production. Dual polarity impulses are generated by cycled charging and discharging of the 8 nF capacitors. Impulse amplitudes are stepped up to around 10 kV by a pulse transformer network, [31] and are subsequently combined with the DC excitation. Isolation of the pulser and sustainer circuits is provided by 100 μH inductors. Both the DC and impulse voltages are imposed upon the discharge region through the fluid-ballasted pin electrode blocks. Total ballast resistance is 10-15 Ω. The primary difference between the PIE-III and PIE-IV circuits is that in PIE-IV, there is an additional 10mH arc-prevention inductor in series with each of the 100 μH isolation inductors.

1.2.3 Burst-Mode Operation

PIE excitation was significantly advanced through development of the burst-mode concept. [27,28] In burst-mode operation, the pulser circuit produces periodic bursts of impulses instead of a continuous stream. Pulser circuit behavior is readily modified by gating the input signal to the thyratron grid driver. In the present implementation of burst-mode, the number of pulses within

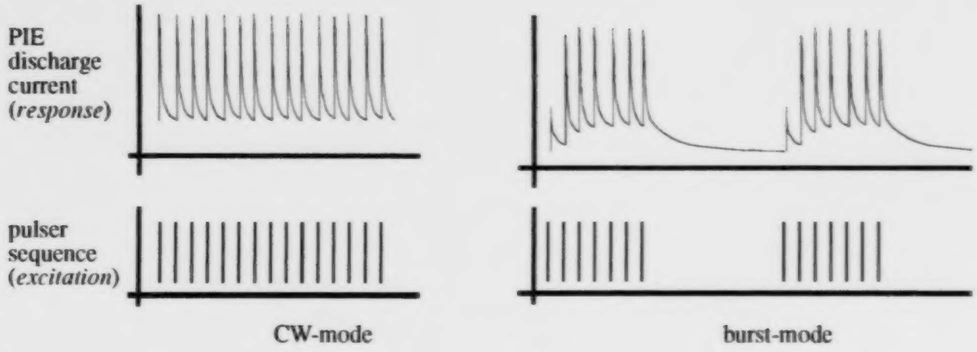
PIE discharge current (*response*)
pulser sequence (*excitation*)
CW-mode
burst-mode

Figure 1.2-3 Illustration of the PIE pulser sequence and discharge current response under conditions of CW- and burst-mode excitation These waveforms are typical of those observed in the PIE-III system for a pulser frequency of 5 kHz. [28]

each burst is constant, as is the burst repetition frequency.[†] The number of pulses within each burst, together with the pulser frequency, then determines the burst duration. If the number of bursts is held constant while the burst frequency is increased, ultimately the CW pulser mode will be achieved.

An illustrative comparison of CW and burst-mode operation is given in Figure 1.2-3. Discharge current is seen to decay substantially during the inter-burst interval, in the absence of impulse ionization. Thus, discharge pumping is much stronger during bursts than it is in the interval between them. In the illustrated example, there are 7 impulses per burst and the burst repetition rate is 330 Hz. Hence, for a pulser frequency of 5 kHz, the discharge cyclically alternates between 1.4 ms of elevated pumping level, and 1.6 ms of weaker pumping. When the inter-burst interval exceeds the gas residence time, or when the sustainer voltage is sufficiently low, the discharge may be extinguished altogether between bursts. This effect will be discussed further in Chapter 4.

1.2.4 Implications of Burst-Mode Operation

Burst-mode operation is observed to benefit laser performance in at least two aspects: enhanced discharge stability, and optical waveform control. Both have significant implications: the former to laser power scaling and device compactness, and the latter to laser material processing effectiveness and versatility. These two features of burst-mode operation will be investigated in Chapters 4-6. They will be discussed briefly here, and study objectives will be defined.

[†] That is, once the number of pulses per burst and burst frequency have been selected, they do not vary with time. More general burst-mode implementations are possible, as will be discussed in Chapter 7.

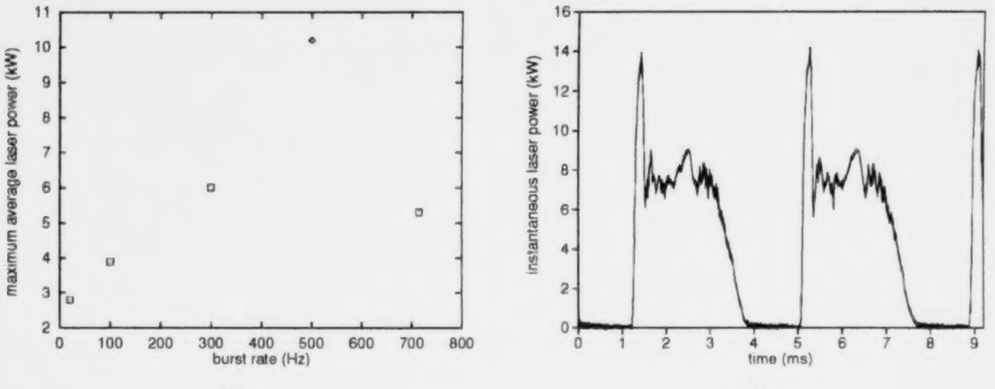

(a) **(b)**

Figure 1.2-4 Effects of PIE burst-mode operation on laser output power: (a) enhanced stability; and (b) optical waveform control.

Gain Medium Uniformity

Burst-mode operation of the PIE-III laser system has been found to considerably enhance discharge stability. In the study of Nikumb *et al.* [27,28], under burst-mode excitation the laser output power attainable prior to the onset of discharge instability was more than doubled relative to CW operation. Results of that study are given in Figure 1.2-4(a). This experimental discovery motivates a theoretical investigation of the mechanisms underlying the stabilization phenomenon, considering that discharge instability is a long-standing barrier preventing the scaling of convection-cooled CO_2 EDLs to higher powers.

The thesis study seeks to identify the mechanisms responsible for the burst-mode stabilization phenomenon, in order to facilitate future investigation and ultimately to allow its more effective employment in future PIE systems. Reasonable design goals are the operation of existing PIE lasers at higher powers, and the reduction in size of PIE systems producing a given output power.

Optical Envelope Control

Also of considerable interest are the effects of burst-mode operation on instantaneous laser power. The optical waveform may be conveniently controlled through alteration of the burst excitation frequency and duty cycle. Such control considerably improves application flexibility, moreover with little additional cost and complexity. Illustrated in Figure 1.2-4(b) is an optical waveform generated with PIE-IV – one of a wide range of possible waveforms under burst-mode conditions. This particular waveform was produced under excitation conditions of 2 pulses per burst and a burst repetition frequency of 250 Hz. Thus, burst-mode operation imparts an additional degree of control to materials processing applications.

The implications promise to be substantial. For example, the superpulsing phenomenon illustrated in Figure 1.2-4(b) is suited to deep penetration welding of carbon steels. [32] In an comparison of burst-mode and CW-mode welding, burst-mode operation was observed to give as much as a factor of 4 improvement in weld penetration for a given average laser power and weld speed. [33] Thus the potential of waveform control is demonstrated.

The objective of the thesis study will be to explore the possibilities of burst-mode optical waveform control, and in particular to quantify the connection between instantaneous laser discharge excitation and optical output. This connection is investigated experimentally, with an emphasis on waveforms relevant to pulsed applications.

1.3 ZODIAC Laser Systems

To date, multi-kW CO_2 lasers for materials processing have been mostly convectively cooled. However, with the advent and refinement of large-area slab waveguide lasers, diffusion-cooled systems appear increasingly viable. Low power (<500W) slab devices are now widely used. When scaled to multi-kW sizes, slab systems should offer considerable advantages relative to convectively cooled systems of comparable power.

Anticipating this potential is the ZODIAC slab radial-array technology being developed at the University of Alberta. The 8-channel device of Yelden [34] (ZODIAC-I) and the 24-channel device of Bilida [7] (ZODIAC-II) represent the next generation in the evolution of high-power CO_2 lasers. ZODIAC technology leverages the advantages of RF-excited slab lasers – compactness, efficiency, and reliability – to much higher device powers, while utilizing the inherent advantages of radial symmetry.

This thesis presents two studies which will aid the advance of multi-kW slab lasers. In this section, a brief overview of the ZODIAC technology is given. The section concludes with an introduction to the two problems facing slab array development which motivated the studies of Chapters 2-3.

1.3.1 RF-Excited Slab Lasers

RF-excited slab electrodes exploit the combined advantages of a narrow-gap planar electrodes and RF-excitation. Typical slab dimensions are: an inter-electrode gap of a few mm, and electrode width of 5-10 cm and lengths on the order of 1 m. One advantage of this planar geometry is a diffusion cooling capacity which depends only on the inter-electrode gap.† This allows electrode area to be increased while maintaining a constant laser gas temperature. The important advantage of RF excitation in connection with electrode area scaling is that RF excitation allows a uniform discharge to be sustained over extended electrode areas. Stable operation is possible at power densities orders-of-magnitude higher than is possible with DC-excited discharges. Laser power is then in general constrained by limited gas cooling rather than by the onset of discharge instability. An additional advantage of RF-excitation is the positive dynamic resistance of the discharge, which eliminates the need for ballast resistors and thereby allows increased electrical efficiency. [34]

---

† In contrast, the diffusion cooling capacity of an axial tube varies inversely with its diameter. In this case, the requirement of constant gas cooling limits laser power scaling to length alone. Coaxial electrodes are not limited in the same way. However, under area scaling their power/volume ratio is rapidly reduced.

Slab electrodes produce a large-area discharge which is essentially planar; typical discharge areas are many hundreds of cm^2, with an electrode gap of only a few mm. To extract optical energy from such a gain volume, typically hybrid stable-unstable resonators are used – *i.e.*, resonators which are stable in one dimension, and unstable in the other orthogonal dimension. [6,35,36] The hybrid resonator is aligned to that its stable aspect corresponds with the narrow transverse discharge dimension (*i.e.*, the electrode gap). It then supports, in that direction, linearly polarized EH waveguide modes. [37,38] The unstable resonator aspect, being orthogonal to the stable aspect, then corresponds to the larger transverse dimension. It is selected to provide discrimination against high-order modes in that dimension. [36] One-sided unstable resonators, which give a single output beam, are usually used. With such hybrid resonator configurations, single-mode laser operation is possible. [39] The laser beam produced is oblong, with its narrowest dimension being determined by the inter-electrode gap, and its greatest aspect by the unstable resonator properties. Hence, the output modes of slab lasers are typically astigmatic, having different divergences in the waveguide and unstable resonator dimensions. They are also linearly polarized. With appropriate corrective optics to compensate for the inherent astigmatism, high-quality beams are attainable which are nearly axially symmetric. [6] Slab systems based on these principles are now widely used in industry for a broad variety of applications.

One immense advantage of RF-excited diffusion-cooled slab devices relative to large-volume DC-excited convection-cooled lasers is their relative compactness. This is well illustrated by a comparison of laser output power attainable per cm^3 of discharge volume: 20 W/cm^3 for a slab laser [38] *vs.* less than 1 W/cm^3 for convection-cooled devices. Moreover, RF-excited slab devices do not require the bulky gas circulation and cooling systems essential to convectively cooled systems.

1.3.2 Arrays

Slab systems have not yet been successfully scaled to multi-kW powers. Although slab laser power scales with electrode area, this scaling is ultimately limited by standing wave and loading effects which cause non-uniform gain medium excitation and a concomitant loss of laser efficiency. Due to such considerations, and also thermal limitations, the maximum power attainable from a single slab appears to be 1-2 kW. Progressing to higher device powers apparently then requires scaling of electrode *number* as well as of electrode *area*, thereby necessitating consideration of slab *array* concepts.

This has lead to the development of a variety of linear [40-45] and radial [7,34,46-47] slab array configurations, as well as 2D arrays of square-bore waveguide lasers. [48] So far, the output powers attained with slab array have not exceeded 1kW. In this thesis, scaling ZODIAC radial arrays to multi-kW powers will be considered.

1.3.3 ZODIAC Apparatus

A ZODIAC electrode array, inspired and named after the astrological symbol, consists of many wedge-shaped metallic electrodes arranged to form a ring of large-area narrow-channel discharge gaps. This configuration is illustrated in Figure 1.3-1. Approximate scale factors for this particular device, the product of a recent dissertation by Bilida [7], are: electrode spacing, 3 mm; electrode width, 5 cm; electrode length, 1 m; and excitation frequency, 80 MHz. (A different aspect of the same electrode assembly is given in Figure 2.2-1.). Every electrode pair is independently powered at both ends by a balanced RF source. Thus, gain regions are established in the narrow inter-electrode channels. Gas cooling is by diffusion to the metal electrodes, which are in turn cooled by internal axial water flow. The entire electrode assembly, with resonator mirrors, fits tightly within a shielded vacuum vessel. The illustrated device is expected to produce output powers in excess of 10 kW.

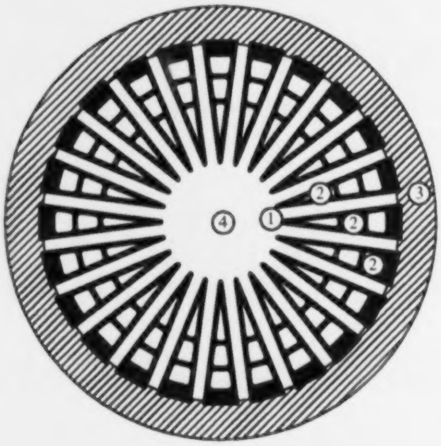

Figure 1.3-1 Cross-sectional view of ZODIAC radial array apparatus: (1) extruded aluminum electrodes, which have (2) interior water cooling channels, and are held in place by (3) ceramic spacing collars; (4) central output-coupling region. Approximate device dimensions are a diameter of 20 cm and a length of 1m.

The separate discharge channels share a common axially symmetric optical resonator. In the first ZODIAC study by Yelden [34], a range of toric and conventional unstable resonators was investigated, in both confocal and non-confocal configurations. The conventional unstable resonator produced superior beam quality in terms of focal spot size obtainable, however it requires a compacting axicon to assemble a useful beam, whereas a toric resonator does not.†

ZODIAC has many potential advantages over PIE and other convection cooled systems. Because its gas cooling is by diffusion, neither blowers nor heat exchangers are required. This results in a mechanically simple system which is more reliable, cheaper, and considerably smaller than a comparable convection-cooled system. ZODIAC compactness is well illustrated in a comparison of its output power per containment vessel volume with that of the PIE-IV device described in Section 1.2.1: 10 kW from 40 L = 250 W/L *vs.* 20 kW from 20,000 L. = 1 W/L. And again, RF discharges do not suffer from the instability problems which plague DC discharges.‡

In terms of output beam quality, the radial slab array has many advantages relative to single slabs and linear slab arrays. Most of these advantages follow from the radial symmetry of the ZODIAC geometry. For example, a radial slab array can produce a radially symmetric output beam which is either unpolarized or circularly polarized. Either is required for direction-independent materials processing.

1.3.4 Design Problems

The mechanical and power-source aspects of ZODIAC technology are now well developed. [7] Two primary difficulties remain in ZODIAC development. The first problem is attaining a uniform discharge over large-area electrode surfaces. This difficultly is common to all large-area RF-excited slabs. The second problem is how to produce one "high quality" beam by combining the emissions of many array elements. These two issues, to be addressed in thesis Chapters 2-3, will be discussed briefly here, and study objectives will be defined.

Gain Media Uniformity

For sake of uniform gain media excitation, it is desirable to attain homogeneous power deposition in all discharge regions. The power scaling problem in slab arrays is therefore twofold: how to increase the *number* of independent discharge channels while retaining the ability to initiate and sustain them all at the same power level, and how to increase individual channel *areas* while retaining uniform power deposition within each.

An obvious solution to the electrode number scaling problem is multiple power supplies. However for sake of simplicity, a single power source used with a suitable splitter is more desirable. Conventional splitters tend to produce unstable power division due to the inverse relationship between discharge impedance and power deposition. Resonant cavity power splitters have recently been shown to solve not only this problem, but also the problem of matching to variable impedance loads. [7]

---

† In a *toric* unstable resonator, the direction of resonator instability is reversed relative to that of a *conventional* unstable resonator, so that mode growth is initiated at the outer resonator edge and proceeds toward its center. [47,49,50] Output coupling is then due to spill-over *within* a central aperture of the front resonator mirror, as opposed to *around* the outer mirror edge as is the case in a conventional unstable resonator. A *confocal* unstable resonator produces a collimated output, whereas a the output of a *non-confocal* resonator either converges or diverges.

‡ This is true at least for optimized slab lasers with excitation frequencies between 50 and 250 MHz. [20] A comprehensive review of RF-excited discharge instability has not yet been performed.

While an elegant solution to number scaling has been identified, the problem of discharge non-uniformity on large-area electrodes remains. When electrode dimensions become a significant fraction of the excitation wavelength, standing wave effects over the electrode surfaces become problematic. The resulting non-uniform gain-media excitation markedly reduces laser efficiency, and in the extreme may cause a plasma instability which terminates laser operation completely. Standing wave effects may be compensated for, and area-scaling limits thereby extended, with reflection-causing circuit elements connected along the electrode. Choice of the optimal smoothing elements (type, position, and magnitude) has been addressed satisfactorily for narrow-channel waveguide devices, however, adapting this approach to large-area slabs is not straight-forward.

The objective of the thesis study will be to develop a numerical model which can be used to predict discharge uniformity on extended-area slab electrodes. Such a model, if sufficiently general, would facilitate development of optimization protocols for electrode design.

Composite Beam Propagation

The major remaining challenge of laser array design is how best to combine the emissions of many laser channels, so that the composite beam is most suitable for materials-processing applications. Since composite beam propagation and focusing properties are determined by the near-field emission patterns, both will be affected not only by the modal properties of the individual laser channels, but also by the array configuration itself. Composite beam properties are also affected by the degree of phase coherence ("phase-locking") between the array elements. For an array of identical non-phase-locked channels, on-axis far-field intensity scales as the number of channels (n), whereas with phase-locking, on-axis intensity scales by as much as n^2. Each of these factors (channel mode content, array configuration, and inter-channel phase-locking) has significant implication for laser applications, in as much as they affect beam focusing properties.

The actual modes produced by the individual waveguide channels and the supermodes produced by the entire resonator and electrode structure are not yet known. The objective of the thesis study will be to develop a model with which to estimate ZODIAC array beam propagation properties. In particular, for this first study it will be of interest to estimate best-possible system performance, and to characterize generally the effects of array configuration and phase-locking on beam propagation and focusing. These results will be useful for informing the design of subsequent ZODIAC devices.

1.4 Thesis Prologue

The objectives of this thesis are twofold: to facilitate development of multi-kW slab technology, and to explore several promising implications of "burst-mode" discharge excitation.

Regarding the first objective, Chapters 2-3 address two problems facing the advance of ZODIAC array technology: attaining optimally uniform discharge excitation, and attaining one high quality beam from the combined emissions of many array elements. In both cases, numerical models are developed with which to perform the analysis.

Regarding the second objective, in Chapters 4-5 "burst-mode" enhanced discharge stability and optical waveform control are investigated. The former analysis is again via computer simulation, while the later effect is characterized experimentally to facilitate future numerical analysis. Chapter 6 summarizes computations of electron transport and rate coefficients, required for further simulation of PIE and ZODIAC discharges

Finally, Chapter 7 summarizes all results and presents the thesis conclusions, as well as recommendations for further work.

Bibliography

[1] Patel, C. K. N. (1964): Interpretation of CO_2 Optical Maser Experiments. *Phys. Rev. Lett.* **12**, 617-619.

[2] Patel, C. K. N. (1989): Carbon Dioxide Laser A Journey from Milliwatts to Megawatts *in CO_2 Lasers and Applications*, Proc. SPIE **1042**, 112-137.

[3] Miles, P. A., and Lotus, J. W. (1968): A high-power CO_2 laser radar transmitter. *IEEE J. Quantum Electron.* **4**, 811.

[4] Tiffany, W. B., Tang, R., and Foster, J. D. (1969): Kilowatt CO_2 gas transport laser. *Appl. Phys. Lett.* **15**, 683.

[5] Abramski, K. M., Colley, A. D., Baker, H. J., and Hall, D. R. (1989): Power scaling of large-area transverse radio frequency discharge CO_2 lasers. *Appl. Phys. Lett.* **54**, 1833-1835.

[6] Nowack, R., Opower, H., Schaefer, U., Wessel, K., Hall, Th., Kruger, H., and Weber, H. (1990): High power CO_2 waveguide laser of the 1 kW category *in CO_2 lasers and Applications II* (H. Opower, ed.), Proc. SPIE **1276**, 18-28.

[7] Bilida, W. D. (1996): *Radial Array Slab Laser Excitation with a Resonant Cavity.* (Ph.D. Dissertation, University of Alberta).

[8] Witteman, W. J. (1987): *The CO_2 Laser.* (Springer-Verlag).

[9] Smith, K., Thompson, R. M. (1978): *Computer Modelling of Gas Lasers.* (Plenum Press, New York)

[10] Leland, W. T. (1982): High energy CO_2 laser amplifiers in *Applied Atomic Collision Physics v. 3 Gas Lasers* (E. W. McDaniel, and W. L. Nighan, eds.), pp. 225-250. (Academic Press, New York).

[11] Manes, K. R., and Seguin, H. J. J. (1972): Analysis of the CO_2 TEA laser. *J. Appl. Phys.* **43**, 5073.

[12] Bullis, R. H., Nighan, W. L., Fowler, M. C., and Wiegand, W. J. (1972): Physics of CO_2 electric discharge lasers. *AIAA J.* **10**, 407-414.

[13] Demaria, A. J. (1973): Review of CW high-power CO_2 lasers. *Proc. IEEE* **61**, 731-748.

[14] Nighan, W. L. (1973): Progress in high pressure electric lasers *in XI'th International Conference on Phenomena in Ionized Gases.* (Prague, 10-14 Sept. 1973).

[15] Verdeyen, J. T. (1995): *Laser Electronics*, 3rd ed. (Prentice Hall, Englewood Cliffs).

[16] Nighan, W. L. (1970): Electron energy distributions and collision rates in electrically excited N_2, CO, and CO_2. *Phys. Rev. A.* **2**, 1989-2000.

[17] Raizer, Yu. P. (1991): *Gas Discharge Physics.* (Springer-Verlag, Berlin).

[18] Schroder, K. (1988): Theoretical modelling of RF-excited laser plasmas *in GSL*, Proc. SPIE **1031**, 90-95.

[19] Hoffmann, P. (1986): Discharge behavior of a RF excited high power CO_2 laser at different excitation frequencies *in High Power Lasers and Their Industrial Applications* (D. Schoucker, ed.), Proc. SPIE **650**, 23-28.

[20] Vitruk, P.P., Baker, H.J., and Hall, D.R. (1994): Similarity and scaling in diffusion-cooled RF-excited carbon dioxide lasers. *IEEE J. Quantum Electron.* **30**, 1623-1634.

[21] Vitruk, P. P., Baker, H. J., and Hall, D. R. (1992): The characteristics and stability of high power transverse radio frequency discharges for waveguide CO_2 slab laser excitation. *J. Phys. D: Appl Phys.* **25**, 1767-1776.

[22] Wester, R., Siewert, S., and Wagner, R. (1991): Theoretical and experimental investigations of the filamentation of high-frequency excited CO_2 laser discharges. *J. Phys D: Appl. Phys.* **24**, 1796-1802.

[23] Hokazono, H., Obara, M., and Midokoriwa, K. (1991): Theoretical operational life study of the closed-cycle transversely excited atmospheric CO_2 laser. *J. Appl. Phys.* **69**, 6850-6868.

[24] Seguin, H. J. J., Nam, A. K. and Tulip, J. (1978): The photoinitiated impulse-enhanced electrically excited (PIE) discharge for high-power cw laser applications. *Appl. Phys. Lett.* **32**, 418-420.

[25] Nam, K. H., H. J. J. Seguin and J. Tulip (1979): Operational Characteristics of a PIE CO_2 Laser. *IEEE J. Quantum Electron.* **15**, 50-54.

[26] Nath, A. K., H. J. J. Seguin and V. A. Seguin (1986): Optimization Studies of a Multikilowatt PIE CO_2 Laser. *IEEE J. Quantum Electron.* **22**, 268-274.

[27] Nikumb, S. K., H. J. J. Seguin, V. A. Seguin, R. J. Willis and H. W. Reshef (1989): High-Average Power-Pulsed Performance of a Multikilowatt PIE Laser. *IEEE J. Quantum Electron.* **25**, 1725-1735.

[28] Nikumb, S. K., H. J. J. Seguin, V. A. Seguin, R. J. Willis, Z. Cheng and H. W. Reshef (1989): Burst-mode gain switched technique for high peak and average optical energy extraction. *Appl. Optics* **28**, 1624-1627.

[29] Merchant, V. E., M. R. Cervenan and H. J. J. Seguin (1985): An Industrial Quality 20 kW Infrared Laser. *Proc. LASERS '85*, 642-646.

[30] Seguin, H. J. J., Nam, A. K., Tulip, J. (1978): An efficient multielement cathode for high-power electric discharge laser applications. *J. Appl. Phys.* **49**, 4566-4567.

[31] Merchant, V. E., H. J. J Seguin and J. Dow (1979): Novel transformer designs for high-power high-repetition-rate applications. *Rev. Sci. Inst.* **50**, 1151-1153.

[32] Scott, S. W. C., K. Rogozinski and H. J. J. Seguin (1994): High peak power, burst mode operation of a multikilowatt CO_2 laser for deep penetration welding. *Appl. Phys. Lett.* **65**, 286-288.

[33] Scott, S. W. C. (1996): *A CO_2 Laser Burst Excitation Technique for Deep Penetration Welding.* (Ph.D. Dissertation, University of Alberta).

[34] Yelden, E. F. (1992): *A Compact, Multichannel, Phase-Locked, Carbon Dioxide Laser System.* (Ph.D. Dissertation, University of Alberta).

[35] Jackson, P. E., Baker, H. J., Hall, D. R. (1989): CO_2 large-area discharge laser using and unstable-waveguide hybrid resonator. *Appl. Phys. Lett.* **54**, 1950.

[36] Lapucci, A., Labate, A., Rossetti, F., Mascalchi, S. (1996): Hybrid stable-unstable resonators for diffusion-cooled CO_2 slab lasers. *Appl. Opt.* **35**, 3185.

[37] Laakmann, K. D., Steier, W. M. (1976): Waveguides: characteristic modes of hollow rectangular dielectric waveguides. *Appl. Opt.* **15**, 1334-1340.

[38] Shackleton, C. J., Abramski, K. M., Baker, H. J., and Hall, D. R. (1992): Lateral and transverse mode properties of CO_2 slab waveguide lasers. *Opt. Comm.* **89**, 423.

[39] Abramski, K.M., Baker, H.J., and Colley, A.D. (1992): Single-mode selection using coherent imaging within a slab waveguide CO_2 laser. *Appl. Phys. Lett.* **60**, 2469.

[40] Newman, L. A., Hart, R. A., Kennedy, J. T., Cantor, A. J., and DeMaria, A. J. (1986): High power coupled CO_2 waveguide laser array. *Appl. Phys. Lett.* **48**, 1701-1703.

[41] Hart, R. A., Newman, L. A., Cantor, A. J., and Kennedy, J. T. (1987): Staggered hollow-bore CO_2 waveguide laser array. *Appl. Phys. Lett.* **51**, 1057-1059.

[42] Abramski, K. M., Colley, A. D., Baker, H. J., and Hall, D. R. (1992): Phase-locked CO_2 laser array using diagonal coupling of waveguide channels. *Appl. Phys. Lett.* **60**, 530.

[43] Lapucci, A., and Cangioli, G (1993): Triple slab radio-frequency discharge CO_2 laser. *Appl. Phys. Lett.* **62**, 7-9.

[44] Lapucci, A., and Cangioli, G. (1993): Phase-locked operation of a compact three-slab-sections radiofrequency discharge CO_2 laser. *IEEE J. Quantum Electron.* **29**, 2962-2971.

[45] Baker, H. J., Hall, D. R., Hornby, A. M., Morley, R. J., Taghizadeh, M. R., Yelden, E. F. (1996): Propagation characteristics of coherent array beams from carbon dioxide waveguide lasers. *IEEE J. Quantum Electron.* **32**, 400-407.

[46] Yelden, E. F., Seguin, H. J. J., Capjack, C. E., and Nikumb, S. K. (1991): Multichannel slab discharge for CO_2 laser excitation. *Appl. Phys. Lett.* **58**, 693.

[47] Yelden, E. F., Seguin, H. J. J., Capjack, C. E., and Nikumb, S. K. (1991): A multi-channel slot discharge CO2 laser employing a toric unstable resonator. *Opt. Comm.* **82**, 503.

[48] Abramski, K. M., Colley, A. D., Baker, H. J., and Hall, D. R. (1996): High-power two-dimensional waveguide CO_2 laser arrays. *IEEE J. Quantum Electron.* **32**, 340-349.

[49] Reilly, J. P. (1975): *Unstable Optical Resonators*. (United States Patent #3,873,942).

[50] Townsend, S. W., and Reilly, J. P. (1989): Unobscured unstable resonator designs for large bore lasers *in Mirrors and Windows for High Power/High Energy Laser Systems* (C. A. Klein, ed.), Proc. SPIE **1047**, 184.

2

ZODIAC: Discharge Uniformity[†]

In this chapter, the first of two problems faced in advancing slab array technology is addressed. We consider the problem of attaining a uniform discharge over large-area electrodes.

2.1 Introduction

Since Abramski *et al.* [1] first demonstrated that the output power of RF-excited slab lasers scales with electrode area, there has been an ongoing effort to increase device powers to ever higher levels. One remaining challenge is the optimization of discharge uniformity over large-area electrodes. When electrode dimensions become a significant fraction of the exciting RF wavelength, standing wave effects can become problematic. Such standing waves cause non-uniform discharge excitation, which can markedly reduce laser efficiency, and in extreme cases cause a plasma instability which terminates laser operation completely.

Standing wave effects may be compensated for, and area-scaling limits thereby extended, by attaching reactive elements in shunt along the electrode. Reflections from these elements can potentially smooth the voltage distribution. Optimal smoothing element configurations (type, position, and magnitude) have previously been identified for narrow-channel waveguide devices, [2-5] but how best to treat the same problem in wide-channel high-power slabs has only begun to be considered. [6-8] Lapucci *et al.* [6] have advanced a numerical model which includes discharge effects, and have demonstrated that the smoothing principles established for narrow-channel devices are also applicable to slabs, but, in the case of slabs, the influence of discharge loading is significant and must be accounted for. Here, we present a similar numerical model, developed independently, which incorporates the RF discharge scaling laws of Vitruk *et al.* [9]. Our model, referred to as SLIM (SLab 1-dimensional electrode Model), is significantly more general than that of reference [6]. It accounts for the dependence of discharge properties on excitation frequency and gas pressure, as well as on power loading and electrode geometry. [7-8] Predictions of discharge uniformity by SLIM are found to agree well with experiment, so it is anticipated it will be useful for developing protocols of optimal slab electrode design.

[†] The material in this chapter has been published in references [7,8].

The problem of compensating for length effects was first considered for narrow-channel waveguide devices. It was shown by He *et al.* [2] that longitudinal voltage distributions could be analyzed in terms of simple transmission line (TL) theory. It was further noted that if the capacitive reactance of the dielectric sidewalls (X_c) dominated the discharge impedance ($\mathbf{Z}_d$), then electrode TL properties would be insensitive to the presence of the discharge. That is, if

$$|X_c| \ll |\mathbf{Z}_d|, \tag{2.1-1}$$

then TL properties are independent of discharge influence, and well-approximated as lossless. Condition (2.1-1) is easily satisfied by typical narrow-channel devices. [4]

Griffiths [3] first observed that placing shunt inductors along the electrode TL could substantially improve discharge uniformity. This technique culminated in the method of distributed parallel resonance, as summarized by Hall *et al.* [4] In this approach, a combination of continuous distributed capacitance and resonating inductors are connected in shunt along the electrode. The additional capacitance is chosen according to (2.1-1) to dominate electrode transmission line characteristics, such that they are negligibly perturbed by the discharge. The inductors are then tuned to the structure capacitance to create a uniform standing wave.

The optimal inductor configuration, which minimizes voltage non-uniformity for a given number of shunt elements, was derived by Kim *et al.* [5]. Electrodes are partitioned into n equal segments by the shunt inductors. The reactance of each terminating inductor is

$$X_L = Z_0 \operatorname{ctn}\left(\beta \frac{l}{2n}\right), \tag{2.1-2}$$

and that of each interior inductor is $X_L/2$. Here, l is the length of the electrode assembly, β is the wave number, and Z_0, the TL characteristic impedance, is purely real for a lossless TL. The smoothing-element configuration specified by (2.1-2) establishes a state of parallel resonance at the TL ends, and at the mid-points between inductors – a situation amenable to efficient matching for a variety of power coupling configurations. In the limit of $n \to \infty$, (2.1-2) reduces to a condition of homogeneous parallel resonance.

Equation (2.1-2) is valid provided that $n > \frac{l\beta}{\pi}$ and the electrode TL is well approximated as lossless. For the discharge-loaded TL to be effectively lossless, either condition (2.1-1) must be satisfied, or the discharge itself must be nearly lossless. The latter condition is satisfied if

$$R_d \ll |X_d|, \tag{2.1-3}$$

where the discharge impedance is understood to have both resistive and reactive components; that is, $\mathbf{Z}_d = R_d + iX_d$. This assumption is most reasonable at low pressures and high power loadings (*cf.* [9] and Section 2.3.3). So for the distributed parallel resonance configuration of (2.1-2) to be truly optimal, the discharge-loaded TL must satisfy at least one of (2.1-1) and (2.1-3).

Extending application of (2.1-2) to slab electrodes is problematic. Condition (2.1-1) is much more easily satisfied for narrow-channel waveguides than it is for slabs because $\boldsymbol{Z}_d$ varies inversely with channel width. Condition (2.1-3) is reasonably satisfied only for power loadings which exceed those of interest for optimal gain media excitation. For (2.1-2) to applicable to a slab electrode, the electrode structure capacitance must be increased until condition (2.1-1) is satisfied.

Augmenting structure capacitance to this degree is, however, not necessarily desirable for slab electrodes. The large shunt capacitances required tend to exacerbate discharge non-uniformity considerably by shortening the transmission line wavelength. Many smoothing inductors are then required, and discharge uniformity thereby becomes unduly sensitive to variations in excitation frequency. This may prove to be problematic for systems not using frequency-stabilized power sources. [7,10-12]

Since neither condition (2.1-1) nor (2.1-3) can be reasonably satisfied by slab electrodes, (2.1-2) is not useful for determining optimal smoothing element configurations. Moreover, because the discharge-loaded slab TL cannot be taken as lossless, the simple closed-form analysis useful for narrow-channel devices is not applicable either. Conveniently though, even in the absence of dominant structure capacitance, shunt inductors remain the smoothing elements of choice [6,7] because the discharge reactance is capacitive under conditions of interest for laser operation. [9,13] Although some of the smoothing principles applicable to narrow-channel devices are transferable to slabs, a new analytic technique is required which accommodates the effects of discharge losses and non-uniformity.

In this chapter, we present a numerical model (SLIM) able to accurately predict power deposition uniformity on slab electrodes for a wide variety of discharge conditions and smoothing element configurations: Section 2.2 describes the ZODIAC radial slab array design to which SLIM will be applied; Section 2.3 develops SLIM; Section 2.4 presents a comparison of computational predictions and experimental results, along with the fiber-optic-based detector which was developed to directly measure the discharge power distribution; and Section 2.5 is a discussion of results.

2.2 Laser Apparatus

The electrode model SLIM, described in Section 2.3, has been successfully applied in designing electrodes for the 24-channel ZODIAC slab array illustrated in Figure 2.2-1. [12] (An end view of this system was previously shown in Figure 1.3-1.) This system has 24 extruded aluminum electrodes configured in a radial array, in the manner first demonstrated by Yelden. [14] The electrodes are each 5 cm wide by 1 m long, this area defining the active region of the individual discharge channels. Periodic ceramic spacers establish a 3 mm transverse waveguide gap between the electrodes, while affecting transmission line characteristics negligibly. Avoiding external structure capacitance minimized the number of shunt inductors required to achieve a given degree

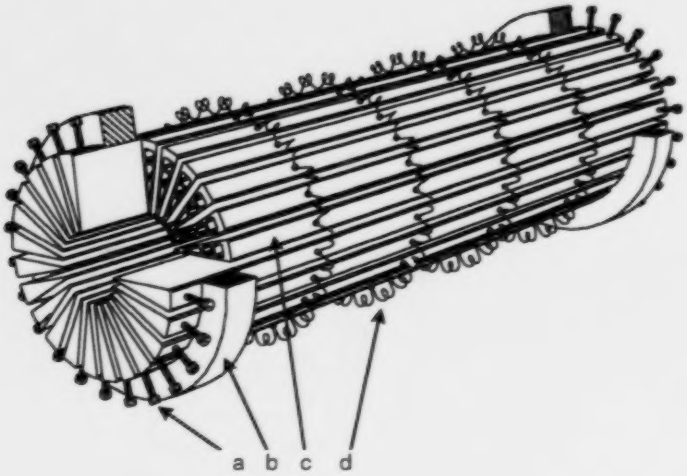

Figure 2.2-1 Cut-away view of a ZODIAC radial array slab laser (a) power feed points (b) ceramic support rings (c) extruded aluminum electrodes with interior coolant channels (d) shunt inductors

of discharge uniformity. Inductors were attached along one side of the electrodes, their position and magnitude having been selected with aid of the computational model SLIM. Four inductors, spaced evenly along the length of each electrode, ensure longitudinal discharge uniformity at power loadings around 5.5 W/cm^2.

A new resonant cavity technique is used to excite the electrodes. [12] Each electrode is powered at both ends with balanced sources, of common phase. Each source consists of a loop coupling magnetic energy from a common resonant cavity, driven by a vacuum tube oscillator. The resonant cavity is external to the electrode containment vessel, so feed-throughs are required to connect the coupling loops to the electrodes. This resonant cavity and magnetic-coupling loop technique eliminates any need for matching networks, and also provides excellent inter-channel isolation with uniform power splitting at high power transfer efficiencies. [10,11]

For all experiments reported here, the excitation frequency was 82 MHz and a laser gas mix of $He:N_2:CO_2 = 3:1:1 + 5\%$ Xe was used. Although a gas pressure of 40 Torr would have been near optimal for the gap and frequency used, [9] present study pressures were limited to 20 Torr by power supply constraints.

2.3 Slab Electrode Model (SLIM)

The slab electrode model SLIM is based on standard transmission line theory [2,4,15] supplemented by an alpha-mode RF discharge model. [9-13] Electrodes are modelled as non-uniformly loaded 1D transmission lines, while vacuum feed-throughs and interconnecting lines are modelled as lossless 1D transmission lines. Ideal voltage sources are used to represent the resonant cavity loops supplying power to the electrode ends.

SLIM computes voltage and current distributions along the length of the electrode assembly, taking due account of non-uniform discharge loading. Arbitrary configurations of smoothing elements in shunt with the discharge are fully accommodated. Although only shunt inductors are relevant to the test electrode, SLIM is easily extended to include the effects of distributed structure capacitance.

2.3.1 Electrode Assembly Model

At frequencies typical of RF-excited lasers, slab electrodes behave as a transmission line. Since wavelength effects are negligible for circuit dimensions much smaller than a wavelength, a one-dimensional longitudinal representation is sufficient for present purposes. It can be further assumed that the local discharge state depends only on the local TL state; wave propagation is TEM, and the effects of longitudinal discharge gradients are negligible. The discharge-loaded electrode may therefore be modelled as a series of contiguous TL segments, each having locally determined properties. Transmission line properties of each segment are determined by the segment geometry and the local discharge impedance.

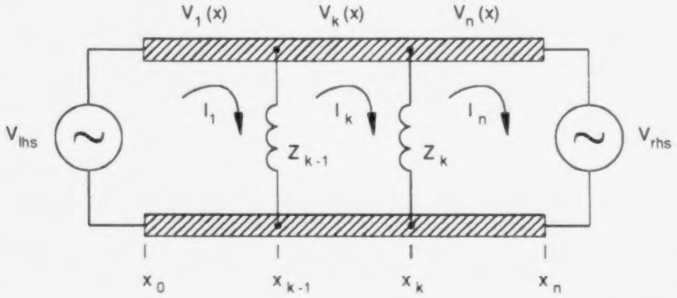

Figure 2.3-1 Segmented transmission line model of an end-driven electrode assembly with shunt smoothing inductors.

Let the electrode be divided into *n* segments, such that every shunt inductor falls on one of the segment boundaries. Figure 2.3-1 illustrates the two end segments and a typical interior segment. Consider segment *k*, of area S_k. Let x_k and $\boldsymbol{Z}_k$ denote respectively the RHS segment boundary position and the externally connected discrete impedance which defines it. Let $\boldsymbol{V}_k(x)$ and $\boldsymbol{I}_k(x)$

denote respectively voltage and current phasor distributions over the segment. Segment boundary conditions are then:

$$\begin{gathered} \boldsymbol{V}_0(x_0) = \boldsymbol{V}_{lhs} \\ \left.\begin{aligned} \boldsymbol{V}_k(x_k) &= \boldsymbol{V}_{k+1}(x_k) \\ \boldsymbol{I}_k(x_k) &= \boldsymbol{I}_{k+1}(x_k) + \frac{1}{\boldsymbol{Z}_k}\boldsymbol{V}_k(x_k) \end{aligned}\right\} \quad k = 1, \ldots, n-1 \\ \boldsymbol{V}_n(x_n) = \boldsymbol{V}_{rhs} \end{gathered} \tag{2.3-1}$$

where $\boldsymbol{V}_{lhs}$ and $\boldsymbol{V}_{rhs}$ are respectively the left and right voltage source phasors. With this segmentation approach, effects of discharge non-uniformity may be accommodated and resolved by segment subdivision. On segments with boundaries not corresponding to externally connected discrete impedances, $\boldsymbol{Z}_k \rightarrow \infty$. Externally connected distributed elements may also be treated similarly, with the corresponding TL segments having appropriately modified transmission characteristics.

If the model segments are chosen to be sufficiently small, such that on each segment TL properties may be considered homogeneous, then closed-form solutions for $\boldsymbol{V}_k(z)$ and $\boldsymbol{I}_k(z)$ are easily obtained. Segment length can be refined until this approximation is sufficiently accurate. Using lumped-element TL theory, [15] wave propagation on each TL segment may be characterized in terms of the local propagation constant γ and the local characteristic impedance $\boldsymbol{Z}_o$:

$$\gamma = \sqrt{(R + i\omega L)\,(G + i\omega C)} \qquad \boldsymbol{Z}_o = \sqrt{\frac{R + i\omega L}{G + i\omega C}} \tag{2.3-2}$$

Here ω is the angular frequency; L and R are the local series inductance and resistance, respectively; while G and C are the local shunt conductance and capacitance. TL parameters (L,R,G,C) are defined per-unit-length. In the absence of a discharge, the TL parameters are:

$$R = \frac{2R_s}{\mathrm{w}} \qquad L = \frac{\mu_o D}{\mathrm{w}} \qquad G = 0 \qquad C = \frac{\varepsilon_0 \mathrm{w}}{D}\,, \tag{2.3-3}$$

where D is the electrode gap, w is their width, and R_s is the surface resistance of the conductors, which under present conditions is negligible. In the presence of a discharge, only the parallel parameters (G and C) are altered, as summarized in Section 2.3.3. Effects of additional structure capacitance, if relevant, can be accommodated by appropriate modification of the segment L and C.

Given γ and $\boldsymbol{Z}_o$ on an homogeneous segment k, the voltage and current phasors on $x_{k-1} \leq x \leq x_k$ are:

$$\begin{aligned} \boldsymbol{V}_k(x) &= \boldsymbol{A}_k e^{-\gamma_k x} + \boldsymbol{B}_k e^{\gamma_k x} \\ \boldsymbol{I}_k(x) &= \frac{\boldsymbol{A}_k}{\boldsymbol{Z}_{o_k}} e^{-\gamma_k x} + \frac{\boldsymbol{B}_k}{\boldsymbol{Z}_{o_k}} e^{\gamma_k x}\,, \end{aligned} \tag{2.3-4}$$

where $\boldsymbol{A}_k$ and $\boldsymbol{B}_k$ are respectively the phasor amplitudes of the forward – and reverse-travelling wave modes.

Together (2.3-1) and (2.3-4) constitute a pentadiagonal system of 2 n equations for the 2 n unknown $\boldsymbol{A}_k$ and $\boldsymbol{B}_k$. This system was solved using direct matrix inversion and functional iteration, implemented jointly with Mathematica [16] and in C-Language using the Meschach library. [17] An iterative method is required due to the dependence of γ and $\boldsymbol{Z}_o$ on the local discharge state, which in turn depends upon $\boldsymbol{V}$ and $\boldsymbol{I}$. The C-Language component of numerics consists of about 1300 lines of code, not including the library structures and subroutines used. Approximately 1 sec of CPU time per iteration is required on an IBM RS/6000 560 for n=100. Typically 50 iterations are required for convergence.[†] An auxiliary visualization package was assembled in Mathematica, as well as a preliminary homogeneous-discharge model. Together, these consist of about 500 lines of code.

2.3.2 Alpha-mode RF Discharge Model

The discharge model advanced by Vitruk *et al.* [9,13] allows the local slab discharge impedance to be expressed simply in terms of several independent variables: excitation frequency f, gas pressure p, inter-electrode gap D, and local RMS current density J_d. A brief summary of this model is presented here to emphasize its relevant aspects. Model extensions required to treat operation conditions below 100 MHz, when sheath power losses are significant, are also discussed.

In the following description, the precision of all empirical parameters is better than 10% and the effect of approximations and simplifications made in model development is less than a few percent over the range of discharge conditions of interest.

Conditions of Negligible Sheath Power Loss [9,13]

An alpha-mode discharge,[‡] desired for the excitation of CO_2 waveguide lasers, consists of two transverse regions: ion sheaths adjacent to the electrode surfaces, and an intermediate weakly ionized plasma column which constitutes the active gain region. Under optimal laser excitation conditions, the plasma column occupies most of the gap. The remainder of the gap is sheath, serving among other roles as capacitive ballast to stabilize the discharge. At excitation frequencies above 100 MHz, sheath regions account for less than 10% of total power dissipation and are consequently well approximated as lossless.

[†] Computation could be considerably accelerated with a banded-matrix inversion algorithm and a more efficient iterative method. [18]

[‡] As distinct from a gamma-mode discharge. In an alpha-mode discharge, electron production is primarily by volumetric electron-impact ionization in the plasma column, whereas in an gamma-mode discharge, electron production occurs primarily in the near-electrode sheaths. Hence in the gamma-mode, secondary electrons generated by ion-impact on metallic electrodes are important. [9,19] The mode names are derived from the first (α) and third (γ) Townsend ionization coefficients.

In a lossless approximation, the ion sheath, being devoid of mobile charge carriers, admits only a displacement current. However, the weakly ionized plasma column draws a conduction current in addition to a displacement current. It follows that the discharge may be modelled as a sheath capacitance C_s in series with a parallel combination of the plasma resistance R_p and capacitance C_p, as depicted in Figure 2.3-2. For discharge conditions of interest, the model circuit elements are well approximated as linear. [9]

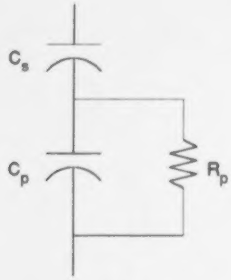

Figure 2.3-2 Circuit element model of an alpha-mode RF discharge. Valid for conditions of negligible sheath power dissipation.

The plasma column can thus be thought of as a conductance in shunt with a portion of the gap, thereby partitioning the gap capacitance into two portions. If the time-averaged total sheath width is d_s, then C_s and C_p for an electrode segment of area S are given by:

$$C_s = \varepsilon_0 \frac{S}{d_s} \qquad C_p = \varepsilon_0 \frac{S}{D - d_s}. \tag{2.3-5}$$

Sheath width is observed to vary inversely as f, to be independent of p, and to be a slightly decreasing function of J_d. As a first approximation, $d_s f$ can therefore be taken as invariant, dependant on gas composition only. For a laser mixture of He:N$_2$:CO$_2$ = 3:1:1 + 5% Xe, $d_s f \approx 42 \text{mm MHz}$. [9] In this approximation, C_s and C_p depend only on frequency, electrode dimensions, and gas mixture.

The reduced electric field (E_p/p) in the plasma column is observed to depend strongly on the parameter pD, but only weakly on J_d and f. The dependence of E_p/p on pD may be inferred from Figure 5 of [13], and is well described by

$$\frac{E_p}{p} = a + \frac{b}{pD} \tag{2.3-6}$$

with the best-fit parameters of $a \approx 156$ V$_{\text{rms}}$/(m•Torr) and $b \approx 44$ V$_{\text{rms}}$. Since E_p/p is independent of discharge loading, R_p has a negative dynamic resistance such that plasma column voltage $V_p = (\frac{E}{p})p(D-d_s)$ is independent of current density. It follows from simple phasor analysis that

$$R_p = \frac{V_p}{\sqrt{(J_dS)^2 - (\omega C_p V_p)^2}}. \qquad (2.3\text{-}7)$$

Equation (2.3-7) may be reduced to $R_p \approx V_p/(J_dS)$ because over the range of interesting discharge conditions, plasma displacement current is negligible relative to plasma conduction current. [13] Note that in the limit where $R_p \to \infty$, the discharge impedance reduces to the gap capacitance, as expected.

Conditions of Significant Sheath Power Loss

The discharge model as formulated above may be justifiably applied to both the optimal discharge conditions (*i.e.*, those maximizing laser output power) for which it was intended by Vitruk *et al.*, and non-optimal discharge conditions (*e.g.*, those considered in the present work). The model is expected to be valid for a wide range of discharge conditions of interest in CO_2 slab lasers; the model of Vitruk *et al.* encapsulates experimental results from the range f = 100-160 MHz, p = 40-100 Torr, and D = 1-3 mm. Primary model provisos are that the gas mix be $He:N_2:CO_2 = 3:1:1$ + 5% Xe and that sheath power dissipation be negligible. However, sheath power deposition scales as $1/f^2$, and below 100 MHz can no longer be neglected. [9,13] Since the model was not intended to account for sheath power loss, a modification is required to treat the 82 MHz : 20 Torr case considered here. A simple extension of the model into the sub-100 MHz regime is outlined below.

Sheath power dissipation (P_s) is related to that in the plasma column (P_p) by $(P_s/P_p)f^2$, a quantity which is invariant amongst similar discharge conditions. [13] The corresponding scaling law may be inferred from Figure 9 of [13]:

$$\left(\frac{P_s}{P_p}\right)f^2 \approx 1120\ \text{MHz}^2. \qquad (2.3\text{-}8)$$

This relation allows extension of the model to f < 100 MHz for optimal discharge conditions. Here it is assumed that (2.3-8) may also be applied to discharge conditions having non-optimal pressures. Good agreement between experiment and model predictions indicate that this assumption is sufficiently accurate for the present purposes.†

To account for power deposition in the sheath, a resistance R_s, which dissipates the power specified by (2.3-8), must be added in parallel with the C_s of Figure 2.3-2. If the discharge impedance is expressed in terms of a series resistance and reactance ($\mathbf{Z}_d = R_d + iX_d$), it can be easily shown that the presence of R_s may be treated as a correction to R_d:

---

† This agreement can in part be explained with the results of Godyak *et al.*, [20] who suggest that in low pressure argon discharges, $P_s/P_p \sim J_dS/(p(D-d_s)f^2)$. Under the discharge conditions considered here, both J_d and p were about half of optimal, leaving P_s/P_p invariant. Note however that this expression for P_s/P_p is not consistent with the similarity laws advanced by Vitruk *et al*. This conflict bears further investigation.

$$R_d' = R_d\left(1 + \frac{P_s}{P_p}\right). \tag{2.3-9}$$

This simplification follows from the conditions $\omega R_s C_s \gg 1$ (sheath capacitance dominates sheath resistance) and $\omega R_p C_p \ll 1$ (plasma resistance dominates plasma capacitance). Both are satisfied over the range of discharge conditions in this work. At 82 Mhz, (2.3-8) and (2.3-9) predict a 17% increase in R_d.

2.3.3 Model Summary

The TL model of Section 2.3.1 and the discharge model of Section 2.3.2 collectively constitute the excitation uniformity simulation SLIM. The two models are merged as follows. For each discharge loaded TL segment, the G and C of (2.3-3) are replaced with a shunt combination of conductance ($G_{\|}$) and capacitance ($C_{\|}$) equivalent to the discharge impedance. In the presence of reactive electrode structures external to the discharge area, $C_{\|}$ must be modified appropriately. Required per-unit-length quantities result from replacing the area S appearing in (2.3-5) and (2.3-7) with the electrode width.

Voltage and current distributions along the electrode length are obtained by iterating the following computational sequence until convergence is achieved

1. given f, D, p, S for each segment and the most recent value of J_d, compute for each segment C_s, C_p, and R_p using (2.3-5) and (2.3-7).
2. express the discharge impedance of each segment as $\mathbf{Z}_d = R_d + iX_d$ according to the configuration of Figure 2.3-2.
3. account for sheath power dissipation by correcting R_d according to (2.3-9).
4. express the resulting discharge impedance in terms of $G_{\|}$ and $C_{\|}$ and replace the G and C of (2.3-3).
5. solve system of (2.3-1) and (2.3-4) to obtain $\mathbf{V}_k(z)$ and $\mathbf{I}_k(z)$.
6. compute J_d for each segment using the average segment voltage and $\mathbf{Z}_d$ of the previous iteration.

Once the solution converges, the longitudinal power distribution follows from computing the average power density

$$P_d = J_d^2 R_d' S \tag{2.3-10}$$

on each segment.

Prior to proceeding to model tests, it is instructive to first consider the effect of power loading on discharge impedance in the electrodes of Section 2.2. The discharge model of Section 2.3.2 is used

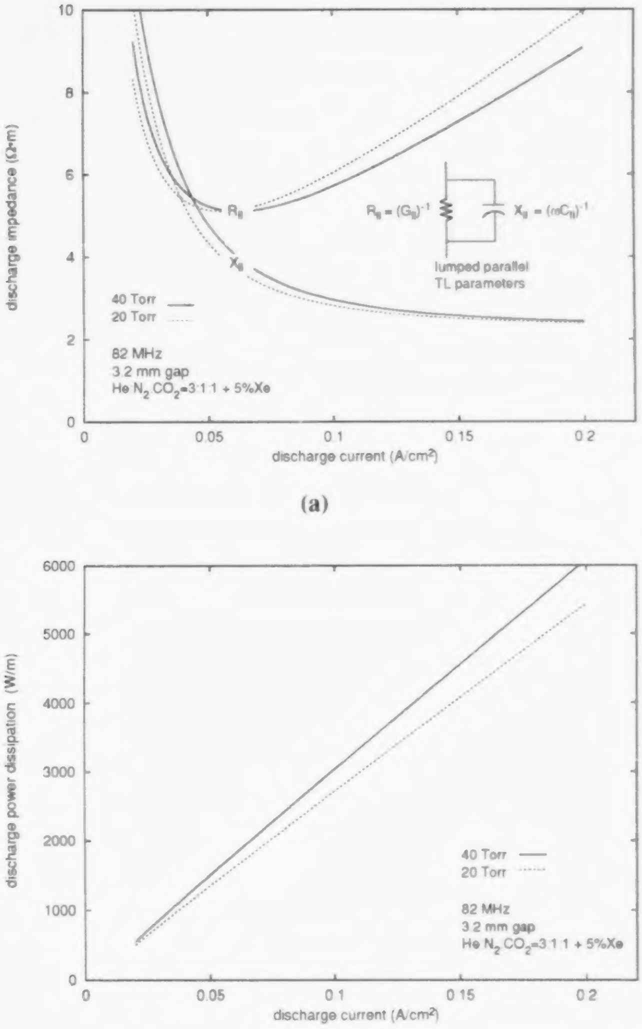

(a)

(b)

Figure 2.3-3 Local discharge properties as a function of local current density: (a) local impedance in terms of a parallel resistance and capacitance (b) local power dissipation for a slab electrode 5 cm wide.

to compute the dependence on discharge current of discharge impedance and power dissipation, and the results are shown in Figure 2.3-3. Presence of a discharge is seen to alter electrode TL properties significantly, considering that in the absence of a discharge, the total electrode capacitive reactance would be 14 ohms due to an electrode capacitance of 1.4 pF/cm. In Figure 2.3-3, $\mathbf{Z}_d$ is seen to asymptotically approach the pure reactance of C_s as power loading is increased. This behavior follows from both C_s and V_p being essentially independent of local current density, which causes V_p to be small compared to the sheath voltage drop at high current densities. [9] In Figure 2.3-3, discharge power loading is seen to be nearly proportional to discharge current. This result follows from (2.3-10) and that $R_d \approx R_p \sim 1/J_d$.

It is clear then from these results that sheath effects cannot be ignored in the design of slab electrodes. But most importantly, because the discharge reactance is capacitive, shunt inductors remain the smoothing element of choice, regardless of the magnitude of the structure capacitance. [6,7] It should also be noted that at higher power loadings, where the discharge becomes effectively less lossy, condition (2.1-3) may be nearly satisfied thereby causing the slab electrode to behave more like a lossless TL than might otherwise be expected. [6]

2.4 Model Testing and Application

SLIM predictions were tested against experimental power deposition profiles. These profiles were derived from measurements of discharge luminosity along the electrode length, making use of the fact that local discharge luminosity is a simple function of local power deposition. [21] Previous measurements of discharge uniformity have used electric probes to sample inter-electrode voltage. [6] Advantages of this luminosity method are that it is necessarily non-perturbative, it does not suffer from RFI, and its calibration is independent of discharge and excitation conditions. Also, it allows direct observation of discharge power, the quantity of interest.

Longitudinal sidelight distributions were sampled with a fiber optic sensor system described in Section 2.4.1, and transformed to power distributions as discussed in Section 2.4.2. Several comparisons between experiment and theory are presented in Section 2.4.3.

2.4.1 Optical Detector Apparatus

The distribution of discharge sidelight was sampled with optical sensors spaced evenly at 10 cm intervals along the electrode. Each sensor consisted of a plastic core optical fiber (EH4001) connected to its own phototransistor detector (Siemens SHF 350) and amplifier circuit.† As indicated in Figure 2.4-1, all optical fibers were mounted along a bar suspended beneath the electrode. Each fiber was fitted into a ceramic insulating tube which limited its field of view to the electrode gap, and to 1.6 cm at the far electrode side. Thus, each fiber sampled only a localized region of the discharge.

2.4.2 Detector Calibration

That plasma luminosity is a unique function of power deposition permits SLIM to be tested in the case of a homogeneous discharge, the scenario of greatest interest here. By sampling the luminosity distribution with optical detectors having the same relative calibration, discharge

---

† The luminosity thus sampled is mostly visible radiation due to electronic transitions.

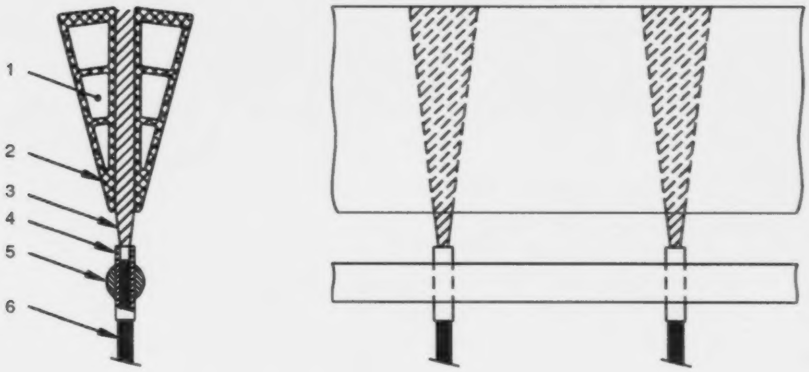

Figure 2.4-1 Optical detector apparatus (not to scale): (1) one of three interior coolant channels (2) metal electrode (3) optical sensor field of view (4) field of view limiting ceramic tube (5) optical sensor mounting bar (6) optical fiber to receiver circuit

uniformity can be confirmed independently of all other factors. For more detailed diagnostic information (*i.e.*, testing of non-uniform cases), more must be known about the relationship between discharge power deposition and luminosity.

One optical sensor, such as described in Section 2.4.1, was used to measure discharge luminosity in a test electrode segment 2 cm long, to determine the relationship between local luminosity and power dissipation. This test segment was identical to the electrodes in the 1 m laser

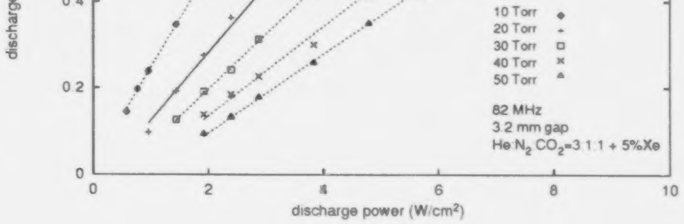

Figure 2.4-2 Local discharge luminosity as a function of discharge power loading and pressure.

assembly except for its length, which was limited to ensure discharge homogeneity.

Luminosity was observed to be a near-linear function of local power deposition over a range of pressures, as is illustrated in Figure 2.4-2. At $p \approx 20$ Torr, luminosity is nearly proportional to power deposition; in Figure 2.4-2 the linear characteristic for this pressure is seen to have negligible offset. All uniformity experiments reported here used this pressure, so in all cases the power distribution could be determined simply from a measure of relative luminosity. To derive the longitudinal power distribution, relative luminosity data was scaled to agree with the total discharge power dissipation, measured via calorimetry on electrode coolant. Calibration of the sensors was performed with a reference light source.

2.4.3 Results of Experiment and Computation

To test the accuracy of SLIM, comparisons were made between predicted and observed power deposition profiles. Several different power levels and smoothing inductor configurations were considered. Figures 2.4-3 and 2.4-5 present results for representative 2-inductor and 4-inductor configurations. Cases with odd numbers of inductors are not considered here because they were observed experimentally to be longitudinally unstable, with the discharge tending to collapse to one end of the electrode structure.

In Figures 2.4-3 and 2.4-5, errors bars on experimental points are due to the uncertainty in luminosity (5%). Uncertainty in total discharge power (5%) and inductor size (0.5 Ω) were accounted for by computing profiles for the range of possible physical conditions. Dotted lines indicate the envelope of these possible profiles. A solid line represent the computed profile which best fits experiment. Inductances values in these figures are specified in reactive Ohms at 82 MHz.

Due to power supply limitations, experiments could not be performed under optimal discharge conditions. Instead, model predictions were used to suggest how distributions would behave in such cases. Results appear in Figures 2.4-4 and 2.4-6. The scaling laws $pD = 133 \mp 8\,\mathrm{mm\,Torr}$ and $fD = 255 \mp 20$ mm MHz from [9] indicate that at 82 MHz, D=3 mm and p=40 Torr are near optimal. Optimal discharge loading was estimated using the invariant $P_p/(fS)$ [13] and the discharge conditions of Colley *et al.* [21]: 12 W/cm^2 and 125 MHz. A similar discharge state at 82 MHz : 40 Torr : 3 mm is produced by a power loading of 8 W/cm^2. This value represents a lower bound on an estimate, as corrections for sheath dissipation are neglected.

To quantify the measure of discharge uniformity, we introduce *average non-uniformity*, defined as the variance of local discharge power deposition from the mean, averaged over the full length of the electrode.

Configurations with Two Inductors

As a test of SLIM for low power loadings, the two-inductor configuration of Figure 2.4-3, was designed. Predictions indicated that an optimal non-uniformity of 5% would be achieved at an average power loading of 3.0 W/cm^2. The test presented in Figure 2.4-3 indicates that at a power

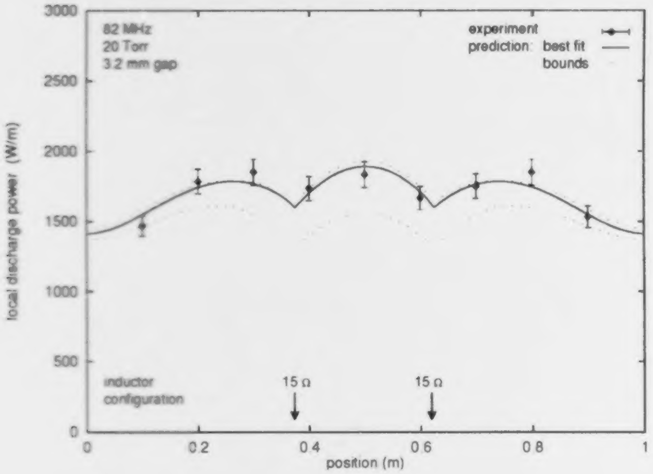

Figure 2.4-3 Experimental results and model predictions compared for a two-inductor configuration at an average power loading of 3.4 W/cm^2.

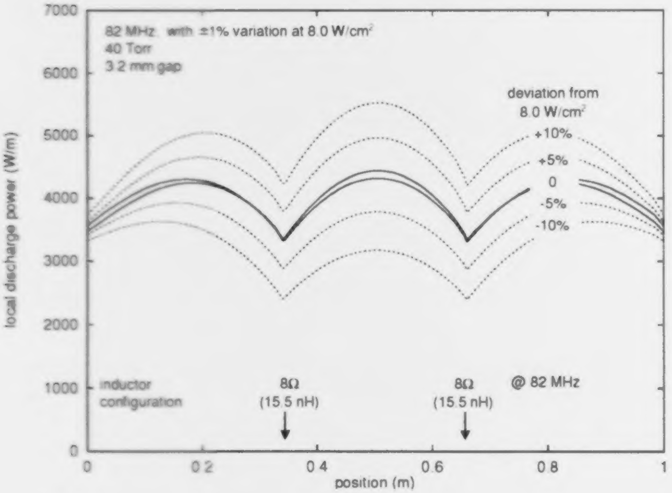

Figure 2.4-4 Predicted dependence of discharge uniformity on total power dissipation and frequency, for a two-inductor configuration optimized for 40 Torr and 8.0 W/cm^2.

loading of 3.4 W/cm^2, a 7% non-uniformity was achieved. This result is fully consistent with model predictions.

Another two-inductor configuration, shown in Figure 2.4-4, was designed for discharge conditions more nearly optimal. Optimal uniformity of 6% is predicted to occur for a power loading of 8.0 W/cm^2. The effect of total power deposition on discharge non-uniformity is also illustrated in Figure 2.4-4. Increasing total power input results in a greater fraction being deposited into the electrode center relative to its ends. Discharge uniformity is also seen to be less sensitive to variations in frequency than it is to variations in total deposited power. Uniformity is predicted to be even less sensitive to changes in pressure, with a 5% variation having a similar effect to a 1% change in frequency. Comparison of Figures 2.4-3 and 2.4-4 indicates that optimal inductor values and positions are specific to a particular power loading.

Configurations with Four Inductors

As a test SLIM for intermediate power loading conditions, a design was considered having four inductors dividing the electrode into 5 equal segments. Modelling revealed that for acceptable uniformity, inductors nearest the electrode center must be smaller than those nearest the electrode ends. This result is in contrast with those of distributed parallel resonance, and is due to discharge loading effects. Experimental results for this inductor configuration are presented in Figure 2.4-5, for average power loadings of 4.2 and 5.4 W/cm^2. Note that between the two cases in Figure 2.4-5, the inductors differ slightly. The minimal non-uniformity is predicted to be 2% and occur at 5.8 W/cm^2. As with the two-inductor case, the shunt inductors required to optimize uniformity at 8.0 W/cm^2 were also determined, with the results appearing in Figure 2.4-6. The minimal non-uniformity at 8.0 W/cm^2 is predicted to be 3%.

The quality of agreement in Figure 2.4-5(a) demonstrates SLIM's accuracy for even relatively non-uniform discharge distributions. Asymmetry in the case of Figure 2.4-5(b) bears further discussion. In principle, with an increased number of inductors, one would expect greater discharge uniformity, as is seen in the comparison of Figure 2.4-4 and Figure 2.4-6.. However, the results of Figure 2.4-5 for four inductors are considerably less uniform than those for two inductors in Figure 2.4-3. Simulations indicate that the observed asymmetry is likely due to the vacuum vessel feed-throughs used to connect the electrodes to the resonant cavity power supply.

Computations indicate that the 15% left-right asymmetry observed in Figure 2.4-5 could be caused by a 1% difference in the relative amplitudes of the two voltage sources driving each end of the electrodes. Such sensitivity is due to the mismatch between the high-impedance vacuum vessel feed-throughs and the electrode assembly. Computations further confirm that the four-inductor case of Figure 2.4-5 is much more sensitive to excitation asymmetry than is the two-inductor case of Figure 2.4-3. Indeed, a 1% source voltage asymmetry in the two-inductor case is predicted to have negligible effect on discharge uniformity.

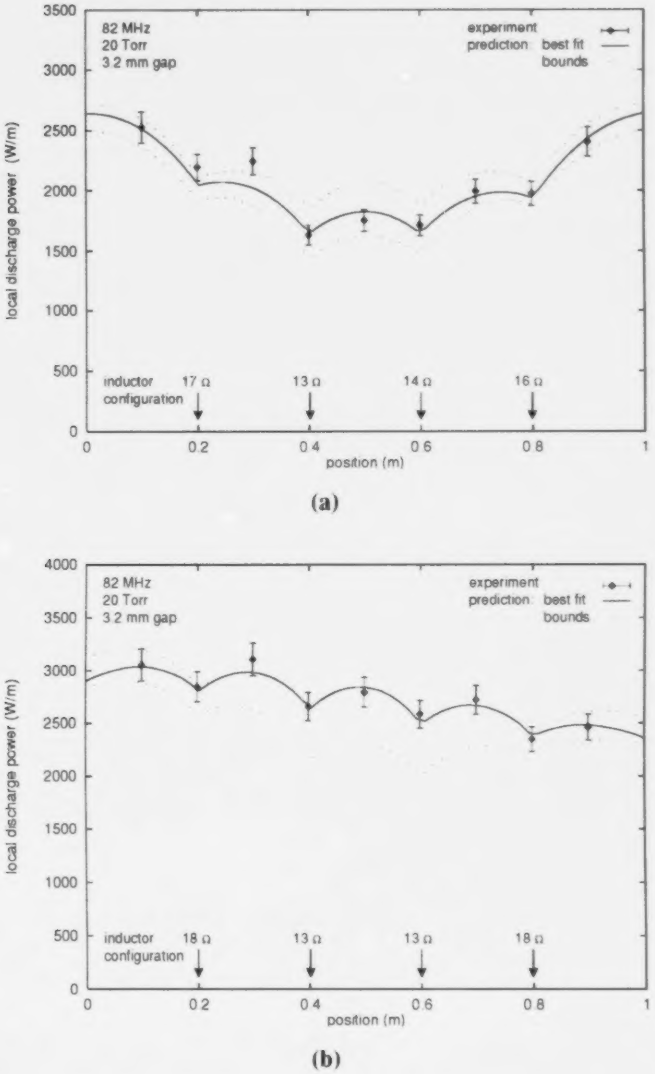

Figure 2.4-5 Experimental results and model predictions compared for four-inductor configurations at an average power loading of (a) 4.2 W/cm^2 and (b) 5.4 W/cm^2.

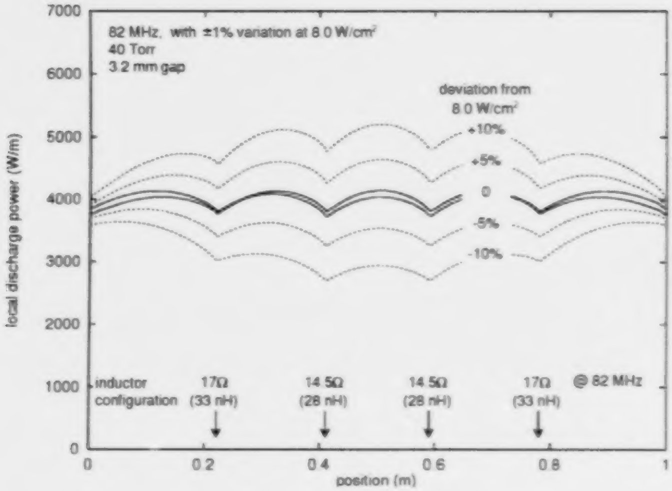

Figure 2.4-6 Predicted dependence of discharge uniformity on total power dissipation and frequency, for a four-inductor configuration optimized for 40 Torr and 8.0 W/cm^2.

A remedy to this problem is feasible through a reduction in the length and/or characteristic impedance of these feed throughs. Another approach would feature the use of termination inductors to transform the effective impedance at the electrode ends to a higher value.

It is interesting to note that the inductor configuration of Figure 2.4-6, optimized for 40 Torr and 8 W/cm^2, is very similar to that of Figure 2.4-4. Indeed, it also produces a non-uniformity of 2% under the discharge conditions of Figure 2.4-4. Similarity between the inductor configurations for the two cases is due to the discharge impedance at 40 Torr and 8 W/cm^2 differing by only a few percent from that at 20 Torr and 5.5 W/cm^2. This can be inferred from Figure 2.3-3. Such a coincidence could be a useful feature, allowing a given electrode assembly configuration to achieve good uniformity at several different CW power loadings, as an alternative to discharge pulsing. Operation in this manner would however require a deviation from optimal discharge conditions, and thereby incur some penalty in laser performance.

It is also interesting to note that the total parallel inductance in the configurations of Figures 2.4-4 and 2.4-6 is roughly equal. This result could be anticipated as follows. In a first approximation, a condition of distributed parallel resonance can be understood as existing when the total inductive reactance due to discrete shunt inductors is equal to the total capacitive reactance due to distributed capacitance. Such a condition follows from considering (2.1-2) in the $n \to \infty$ limit. Consequently, since between Figures 2.4-4 and 2.4-6 the discharge impedance distribution is invariant, then the total inductive reactance which resonates with it should also be invariant. Given this, it is not surprising that the sensitivity of uniformity to frequency variations is also very similar between the two cases.

2.5 Discussion

The good agreement between experiment and theory in Section 2.4 indicates that SLIM may be applied to non-optimal discharge conditions for $f < 100$ MHz. It can be reasonably assumed that SLIM will be similarly accurate when sheath dissipation is negligible ($f > 100$ MHz), because in that case SLIM reduces to that of Vitruk *et. al.*, which is applicable to the range $f = 100$-160 MHz, $p = 40$-100 Torr, and $D = 1$-3 mm. [13] For gas mixtures other than He:N_2:CO_2 = 3:1:1 + 5% Xe, the form of the scaling laws should remain unaltered, requiring only that new coefficients a and b for (2.3-6) be ascertained, as well as the constant $d_s f$.

Assuming discharge properties to be homogeneous was observed not to have a large effect on computational results. However, in all cases considered, accounting for the effects of discharge non-uniformity did yield predictions in better agreement with experiment. Effects of assuming globally uniform discharge properties were smallest for cases which had the most uniform discharge distribution. These effects were sufficiently small to justify using the assumption in preliminary calculations for uniformity optimization. The TL modelling approach used here, of dividing the TL into a sequence of homogeneous segments and expressing the overall solution in terms of exact solutions on individual segments, takes full advantage of this simplification.

As formulated here, SLIM requires adaptation to treat scaling of slab width, if transverse standing wave effects become significant. The TL modelling approach used here can be easily extended to treat two-dimensional problems.

In the electrode assembly designs presented in this study, the electrode structure reactance (X_c) was deliberately minimized. In doing so, the number of inductors required for a given degree of discharge uniformity was also minimized. A primary advantage is that sensitivity of discharge uniformity to variations in excitation frequency is markedly reduced. In addition to mechanical simplicity, the method also results in an open electrode design which permits unimpeded gas re-circulation.

A disadvantage of direct discharge matching is increased sensitivity of uniformity to total power loading. Indeed, good discharge uniformity over a wide range of power loadings does not appear possible, as is suggested by Figures 2.4-4 and 2.4-6. To accommodate power variability, another approach is to select inductors which optimize performance for the highest power loading of interest. Then to achieve different average discharge power loadings, the discharge can be pulsed under variable duty ratio. This approach may also be problematic from the standpoint of smoothing inductor choice, since the discharge impedance depends on pulse duration and repetition frequency. [22] This dependence for slab lasers merits further study.

2.6 Summary

A computational model (SLIM) has been presented which accurately predicts longitudinal discharge uniformity on large-area slab electrodes at the test frequency of 82 MHz. Because SLIM is expected to be valid for a wide range of discharge and excitation conditions, it should prove to be a useful tool for developing CO_2 slab laser optimization protocols. Moreover, similar models should be applicable to the optimization of other types of gas slab lasers. The novel fiber-optic detector with which the accuracy of SLIM was confirmed should also prove be useful for further slab electrode diagnostics and development. Suggestions for future extensions and investigations will be given in Chapter 7.

So far, SLIM and the detector have facilitated an alternative method of attaining discharge uniformity on large-area slab electrodes. In this method, electrode structure capacitance is minimized and shunt inductors are selected to achieve optimal discharge uniformity at a specific discharge power loading. Using this approach, electrodes were designed for the 24-channel ZODIAC described in Section 2.2. Consistent with the needs of such a system, which is powered with resonant cavity techniques, inductor number was minimized to accommodate non-frequency-stabilized power sources. Using the model on a trial-and-error basis, multiple interior shunt inductors were selected to provide good discharge uniformity at an average power loading around 5.5 W/cm^2 (*cf.* Figure 2.4-5). With this design, the slab array is expected to achieve a total laser power of 5 kW. Under optimal discharge conditions and with optimal inductor configuration (*cf.* Figure 2.4-6), the power attainable is expected to be well in excess of 10 kW. So far, 1.2 kW has been extracted from 8 discharge channels, achieving the highest powers yet reported for slab laser arrays. [12]

Bibliography

[1] Abramski, K. M., Colley, A. D., Baker, H. J., and Hall, D. R. (1989): Power scaling of large-area transverse radio frequency discharge CO_2 lasers. Appl. Phys. Lett. **54**, 1833-1835.

[2] He, D., and Hall, R. (1983): Longitudinal voltage distribution in transverse RF discharge waveguide lasers. J. Appl. Phys. **54**, 4367-4373.

[3] Griffiths, G. A. (1982): Improved discharge uniformity for transverse radio frequency waveguide CO_2 lasers in *Proc. SPIE*, vol. 335, Advanced Laser Technology and Applications (L. Esterowitz, ed.), 69-71.

[4] Hall, D.R., and Hill, C.A. (1987): Radiofrequency-discharge-excited CO_2 lasers *in Handbook of Molecular Lasers* (P.K. Cheo, ed.), pp. 165-255. (Marcel Dekker, New York).

[5] Kim, Y., Youn, C. E., Ra, J. W., and Kim, Y. S. (1990): Method for reducing the longitudinal voltage variation in transverse radio-frequency discharge waveguide lasers. J. Appl. Phys. **67**, 1127-1129.

[6] Lapucci, A., Rossetti, F., Ciofini, M., and Orlando, G. (1995): On the longitudinal voltage distribution in radio-frequency-discharged CO_2 lasers with large area electrodes. IEEE J. Quantum Electron. **31**, 1537-1541.

[7] Strohschein, J.D., Bilida, W.D., Seguin, H.J.J., and Capjack, C.E. (1996): Enhancing discharge uniformity in multichannel RF-excited CO_2 slab lasers. Appl. Phys. Lett. **68**, 1043-1045.

[8] Strohschein, J.D., Bilida, W.D., Seguin, H.J.J., and Capjack, C.E. (1996): Computational model of longitudinal discharge uniformity in RF-excited CO_2 slab lasers. IEEE J. Quantum Electron. **32**, 1289 - 1298

[9] Vitruk, P. P., Baker, H. J., and Hall, D. R. (1992): The characteristics and stability of high power transverse radio frequency discharges for waveguide CO_2 slab laser excitation. J. Phys. D: Appl Phys. **25**, 1767-1776.

[10] Bilida, W.D., Strohschein, J.D., Seguin, H.J.J., and Capjack, C.E. (1996): Multi-Channel slab CO_2 laser excitation with resonant cavities. Opt. Laser T., in press.

[11] Bilida, W.D., Seguin, H.J.J., and Capjack, C.E. (1995): Resonant cavity excitation system for radial array slab CO_2 lasers. J. Appl. Phys. **78**, 4319-4322.

[12] Bilida, W. D. (1996): *Radial Array Slab Laser Excitation With a Resonant Cavity.* (Ph.D. Dissertation, University of Alberta).

[13] Vitruk, P.P., Baker, H.J., and Hall, D.R. (1994): Similarity and scaling in diffusion-cooled RF-excited carbon dioxide lasers. IEEE J. Quantum Electron. **30**, 1623-1634.

[14] Yelden, E. F. (1992): *A Compact, Multichannel, Phase-Locked, Carbon Dioxide Laser System.* (Ph.D. Dissertation, University of Alberta).

[15] Pozar, D. M. (1990): *Microwave Engineering.* (Addison Wesley, New York).

[16] Wolfram, S. (1991):*Mathematica: A System for Doing Mathematics by Computer*, 2nd ed. (Addison-Wesley, Redwood City).

[17] Stewart, D. E., and Leyk, Z. (1994): Meschach: Matrix Computations in C *in Proceedings of the Center for Mathematics and its Applications*, vol. **32**. (Australia National University, Canberra).

[18] Boyd, J. P. (1989): *Chebychev & Fourier Spectral Methods*. (Springer-Verlag, Berlin).

[19] Raizer, Yu. P. (1991): *Gas Discharge Physics*. (Springer-Verlag, Berlin).

[20] Godyak, V. A., Peijak, R. P., and Alexandrovich, B. M. (1991): Ion flux and ion power losses at the electrode sheaths in a symmetrical rf discharge. J. Appl. Phys. **69**, 3455-3460.

[21] Colley, A. D., Baker, H. J., and Hall, D. R. (1992): Planar waveguide, 1 kW cw, carbon dioxide laser excited by a single transverse RF discharge. Appl. Phys. Lett. **61**, 136-138.

[22] Baker, H. J., and Laidler, I. (1990): Electrical characterization of pulsed and CW fast axial flow RF excited CO_2 lasers. Proc. SPIE **1225**, 349-356.

3

ZODIAC: Beam Propagation[†]

In the previous chapter, we addressed the problem of attaining uniform discharge excitation over large-area slab electrodes. With the electrode designs proposed, in conjunction with the resonant cavity power supply and matching techniques advanced by Bilida, [1] it is possible to establish uniform gain throughout all channels of a ZODIAC array. Thus, the discharge aspects of ZODIAC arrays appear to have been largely solved. It does remain, however, to consider the properties of beams produced by ZODIAC arrays; to which materials processing applications will they be well-suited? This chapter considers ZODIAC beam characteristics, particularly the effects of array configuration and phase-locking on beam propagation and focusing. Details of mode production within the individual channels are not treated in detail. Rather, in this first study, best-possible system performance is estimated through considering ideal cases.

3.1 Introduction

Slab arrays have been developed to allow the scaling of slab laser advantages such as efficiency, compactness, and reliability to much higher system powers. ZODIAC radial arrays have been developed with the intent of exploiting the advantages inherent to axial-symmetry. An application of the 8-channel ZODIAC of Yelden [2] (ZODIAC-I) to sheet metal cutting produced very good results in terms of kerf width, depth of penetration, and process speed. [3] In contrast with single slabs and linear slab arrays, the ZODIAC geometry inherently produces a focal spot which is both axially symmetric and unpolarized, and which hence dictates no preferred processing direction. These benefits, in addition to an effective reduction in focal spot size, are a result of "radial stacking" of the individual channel beamlets.

The promise of these results and a desire to further improve ZODIAC materials processing performance motivates the study of this chapter. Here, we will investigate theoretically the characteristics of beams produced by ZODIAC arrays, considering particularly the effects of array configuration and phase-locking on beam propagation and focusing. To determine these beam properties, modal properties of the individual array "beamlets" are of course critically important. In this first study, however, "ideal" beamlet properties will be assumed in order to obtain estimates of "best-possible" ZODIAC beam propagation characteristics.

[†] Portions of the material in Section 3.3 have been published in reference [3].

Beam propagation and focusing properties will be quantified in terms of the M^2 propagation constant, [4-13] a now widely recognized industry standard. M^2 is, in one interpretation, a times-diffraction-limited (TDL) number. An ideal beam has $M^2=1$, while in general, $M^2 \geq 1$. The objective of this study is to estimate a lower bound for M^2 attainable by a ZODIAC array. Also of interest are general invariants or scaling laws which may be able to relate beam propagation characteristics to the ZODIAC array configuration. The underlying motive is informing the design of subsequent generations of ZODIAC arrays, resonators, and corrective optics. Details of actual implementation will be considered only briefly here.

Chapter organization is as follows. Section 3.2 presents a brief summary of laser mode propagation and the definition of M^2. With this basis, in Section 3.3, M^2 and far-field properties are estimated for non phase-locked (non-PL) ZODIACs. In first comparisons, predictions for non-PL ZODIAC propagation agree well with experiment. The approximations are then extended in Section 3.4 to consider phase-locked (PL) ZODIACs. Observations and suggestions for future ZODIAC designs are summarized in Section 3.5.

3.2 Theory

Propagation of laser modes which are not strongly diverging is well described by paraxial theory, [14] a brief introduction of which is given in Section 3.2.1. Effects of mode superposition are likewise briefly considered in Section 3.2.2, since non-PL combination of ZODIAC beamlets necessarily results in a multi-mode composite beam; each beamlet is composed of at least one distinct mode. Only under PL conditions may the ZODIAC array possibly produce a single supermode. In Section 3.2.3, the M^2 propagation constant is defined and described.

3.2.1 Mode Propagation

Consider an arbitrary beam mode propagating within the paraxial approximation [14] along the z-axis. On any plane z, the beam's phasor amplitude profile $\boldsymbol{E}(x,z)$ can be expressed in terms of a local spatial-frequency distribution $\boldsymbol{P}(s,z)$ by a Fourier transform†

$$\boldsymbol{E}(x,z) = \int_{-\infty}^{\infty} \boldsymbol{P}(s,z)\, e^{-i2\pi sx} ds, \tag{3.2-1}$$

---

† Note that the premultipling scale factors of Fourier transforms are defined variously. They can be split between the transform and its inverse, applied to only one of them, or made to disappear altogether through choice of frequency differential. The latter approach is taken here. Note that s is a cyclic frequency, not an angular frequency.

where ***P****(s,z)* is defined by the inverse transform

$$\boldsymbol{P}(s,z) = \int_{-\infty}^{\infty} \boldsymbol{E}(x,z)\, e^{+i2\pi sx} dx. \qquad (3.2\text{-}2)$$

Expressing ***E****(x,z)* in terms of ***P****(s,z)* is equivalent to decomposing the beam into a set of infinite plane-waves. Each spatial frequency s corresponds to the angular direction of one plane-wave component, and $|\boldsymbol{P}(s,z)|^2$ is the power contained in that component. In terms of this paradigm, the paraxial approximation amounts to assuming that all significant plane-wave components propagate nearly parallel to the optic axis.

The relationship between ***P****(s,z)* and the corresponding set of plane-waves may be clarified by considering a plane-wave component propagating at angle θ with respect to the z-axis:

$$\boldsymbol{u}_\theta(x,z) = \boldsymbol{A}_\theta e^{-i\boldsymbol{k}\bullet\boldsymbol{r}} = \boldsymbol{A}_\theta e^{-i(k_x x + k_z z)}, \qquad (3.2\text{-}3)$$

where $\boldsymbol{A}_\theta$ is its phasor amplitude, and $\boldsymbol{k} \equiv (k_x, k_z) = (k\sin\theta, k\cos\theta)$ is the wave vector. All $\boldsymbol{u}_\theta(x,z)$ share a common wave vector amplitude $k = 2\pi/\lambda = \omega/c$ because mode ***E****(x,z)* is monochromatic. If we interpret integral (3.2-1) as the sum of all such plane-wave components, it follows that

$$\boldsymbol{u}_\theta(x,z) = \boldsymbol{P}(s,z)\, e^{-i2\pi sx}. \qquad (3.2\text{-}4)$$

A comparison of (3.2-3) and (3.2-4) indicates that $k_x = 2\pi s$, *i.e.*, that spatial frequency s is the cyclic frequency corresponding to the transverse wave vector k_x. The comparison further reveals that

$$\boldsymbol{P}(s,z) = \boldsymbol{A}_\theta e^{-ik_z z}, \qquad (3.2\text{-}5)$$

which allows a connection to be made between θ and s. In the paraxial approximation, k_x and k_z, become:

$$k_x \approx k\theta \qquad k_z \approx k[1 - \theta^2/2]. \qquad (3.2\text{-}6)$$

It follows then from $k_x = 2\pi s$ that $s \approx \theta/\lambda$, and

$$k_z \approx k - \pi\lambda s^2. \qquad (3.2\text{-}7)$$

The latter result indicates as expected that each plane-wave propagates with a slightly different k_z.

Using (3.2-5) and (3.2-7), paraxial mode propagation can now be expressed simply in terms of ***P****(s,z)*, which evolves along z according to

$$\boldsymbol{P}(s,z) = \boldsymbol{P}(s,z_1)\, e^{+i\pi\lambda s^2(z-z_1)} e^{-ik(z-z_1)}, \qquad (3.2\text{-}8)$$

where z_1 marks an arbitrarily positioned reference plane. Siegman [14] notes that the paraxial approximation is reasonably satisfied by all plane-wave components for which $\theta < 30^\circ$.

Several important implications follow from the preceding results.

First, diffraction does not alter the spectral content of a beam. Rather, only the relative phase of the spectral components is modified as the beam propagates. According to (3.2-8), as each spatial frequency component propagates, its phase rotates at a unique rate while its magnitude remains unaltered.

Second, each spatial frequency component can be thought of as propagating in its own unique direction. It follows from simple ray optics that an ideal focusing element will map each spatial frequency s to its own unique point on the focal plane. [15,16]

Finally, according to the previous observations, the focal profile should be independent of where the focusing element is positioned. Moving the focal plane will alter the phase profile, but not the amplitude profile. In practice however, as a beam propagates its high frequency components become increasingly difficult to capture by a lens of reasonable size. Aside from aperturing effects (which can amount to mild spatial filtering), the far-field intensity profile should be independent of focal plane position. For this reason, for the remainder of this chapter, beam focal properties and far-field divergence will be taken as equivalent.

3.2.2 Mode Superposition

Consider now two modes $\boldsymbol{E}_1$ and $\boldsymbol{E}_2 e^{i\phi(t)}$, of common polarization, superposed at one point in space, where $\phi(t)$ represents the instantaneous phase difference between the two fields. The local instantaneous intensity $I_s \equiv |\boldsymbol{E}_s|^2$ of the combined field $\boldsymbol{E}_s = \boldsymbol{E}_1 + \boldsymbol{E}_2 e^{i\phi(t)}$ is

$$I_s = I_1 + I_2 + 2\cos(\phi(t))\sqrt{I_1 I_2}. \tag{3.2-9}$$

For the laser-material interactions of interest to CO_2 lasers, only the time-averaged intensity $\langle I_s \rangle$ is relevant, since oscillations on the order of the light frequency are unimportant. For non-PL modes, the final term in (3.2-9) averages to zero, since $\phi(t)$ is either random or varies linearly with time. The net intensity is then simply the sum of the individual intensities, *i.e.*, $\langle I_s \rangle = \langle I_1 \rangle + \langle I_2 \rangle$. If the modes are phase-locked, then $\phi(t)$ is constant and interference effects result, *i.e.*, $0 \leq \langle I_s \rangle \leq (\langle I_1 \rangle^{1/2} + \langle I_2 \rangle^{1/2})^2$. These results may be generalized to n superposed modes $\boldsymbol{E}_i$. For mode contributions of equal intensity I, the net intensity is nI for non-PL modes, and for PL modes ranges between 0 and $n^2 I$.

In the far-field, effects of coherent interference may lead to increased on-axis intensity, with a concomitant reduction in central lobe size due to energy conservation. At every point on the focal plane, the contributions $\boldsymbol{P}_i$ from each mode of one spatial frequency are superposed (*cf.* Section 3.2.1). On-axis intensity can scale by as much as n^2 in the PL case, as opposed to just n in the non-PL case.

3.2.3 The M² Beam Quality Measure

It is desirable to somehow quantify laser beam "quality", so that objective standards for laser materials processing applications may be established. A beam quality measure should quantify in some way the relationship between near-field and far-field intensity patterns. A good quality beam should in some sense be nearly "diffraction limited", and a measure of beam quality should be somehow related to how much larger than diffraction limited the beam is in the far-field. The M^2 propagation constant proposed by Siegman, [10-13] which defines beam quality in terms of its space-bandwidth product, is one such measure and is now widely used in industry. According to this definition, an ideal beam minimizes the extent of the near-field width required to achieve a given far-field width. Equivalently, an optimal beam has minimal divergence for a given waist size. Beam size is characterized in terms of the second-moment ("variance") of its intensity profile.

The M^2 propagation constant is an invariant quantity, unaltered by propagation and aberration-free optics. Its definition follows from considering moment integrals of the intensity profiles $|\boldsymbol{E}(x,z)|^2$ and $|\boldsymbol{P}(s,z)|^2$. $\boldsymbol{E}(x,z)$ and $\boldsymbol{P}(s,z)$ are again understood as referring to a single mode. Generalization to multi-dimensional and multi-mode cases will follow a brief presentation of M^2 principles.

Consider the second moments of $I(x,z) \equiv |\boldsymbol{E}(x,z)|^2$ and $\tilde{I}(s,z) \equiv |\boldsymbol{P}(s,z)|^2$:

$$\sigma_x^2(z) \equiv \frac{1}{C}\int_{-\infty}^{\infty} (x-\bar{x})^2 I(x,z)\,dx, \tag{3.2-10}$$

and

$$\sigma_s^2(z) \equiv \frac{1}{C}\int_{-\infty}^{\infty} s^2 \tilde{I}(s,z)\,ds. \tag{3.2-11}$$

Here, $\bar{x}$ is the first moment of $|\boldsymbol{E}(x,z)|^2$, and C is the zeroth moment, or total power:

$$C \equiv \int_{-\infty}^{\infty} I(x,z)\,dx = \int_{-\infty}^{\infty} \tilde{I}(s,z)\,ds. \tag{3.2-12}$$

The first moment in general varies linearly with z, expressing that the beam travels along an optic axis.[†] The zeroth moment is identical for both distributions and independent of z, as is required by energy conservation.

It can be shown using Fourier theorems that σ_x evolves along z according to

$$\sigma_x^2(z) = \sigma_{x_0}^2 + \lambda^2\sigma_s^2(z - z_{0_x})^2, \tag{3.2-13}$$

where σ_{x_0} is the second moment (3.2-10) at z_0, which coincides with the beam waist. σ_{x_0} and σ_s, being reciprocal quantities, obey an uncertainty relation analogous to those between the reciprocal quantities of quantum physics. Hence, for an arbitrary paraxial beam, the product of σ_{x_0} and σ_s satisfies the inequality:

[†] Note that $\bar{s}$ may be omitted from the definition of σ_s^2 in (3.2-21) because $|\boldsymbol{P}|$, being a Fourier Transform, is an even function.

$$M_x^2 \equiv 4\pi\sigma_{x_0}\sigma_s \geq 1 \ . \tag{3.2-14}$$

This M_x^2 in (3.2-14) is then the M^2 propagation constant. The identity $M_x^2 \equiv 1$ is satisfied only when $E(x,z_0)$ describes a TEM_{00} (gaussian) profile. For all other intensity profiles, $M_x^2 > 1$.

A propagation equation of more familiar form than (3.2-13) follows from (3.2-13) and (3.2-14):

$$W_x^2(z) = W_{x_0}^2 + M_x^4 \frac{\lambda^2}{\pi^2 W_{x_0}^2}(z - z_{0_x})^2. \tag{3.2-15}$$

Here, the beam half-width is defined as $W_x(z) \equiv 2\sigma_x(z)$ so that for the special case of a gaussian intensity profile

$$I(x, z) \equiv |\boldsymbol{E}(x, z)|^2 \sim e^{-2\left(\frac{x}{w(z)}\right)^2} \ , \tag{3.2-16}$$

(3.2-15) reduces to the familiar propagation equation

$$w_x^2(z) = w_{x_0}^2 + \frac{\lambda^2}{\pi^2 w_{x_0}^2}(z - z_{0_x})^2, \tag{3.2-17}$$

where is $w_x(z)$ is the e^{-2} half-width of the beam. Eqn (3.2-15) says that the beam area, defined according to the second moment, increases quadratically with distance from the beam waist. The M^2 propagation factor is also commonly referred to as the times-diffraction-limited (TDL) number,[†] *i.e.*, the factor by which the focal spot size is larger than that produced by a TEM_{00} mode which has the same near-field width.

In Two Dimensions

In the prior discussions of mode propagation, only one transverse rectangular dimension was considered: x, and the corresponding spatial frequency s. The second orthogonal axis (y, and the corresponding spatial frequency t) may of course be treated identically, so that in rectangular coordinates beam propagation is described in terms of two quadratic laws like (3.2-15); one each for the x-axis and y-axis. On each axis then, evolution of $W(z)$ is parameterized in terms of $\{W_0, M^2, z_0\}$. In this simplified description of propagation, relevant information has been lost, [8] yet it does provide a useful first basis for analyzing the propagation of an arbitrary beam. For example, differences between $\{W_0, M^2, z_0\}$ on the principle axes gives information about the degree of mode asymmetry($W_x \neq W_y$) and astigmatism ($z_{0_x} \neq z_{0_x}$).

[†] Strictly speaking, TDL definitions should be based on the resolution imposed by diffraction through a finite diameter aperture.

For beams with multi-fold symmetry, it is useful to extend the M^2 definition from rectangular to polar coordinates. Again, the M^2 definition is based on second moments. The radial moments [10] are simply related to the rectangular ones defined previously. The second moment of $I(r, \theta, z)$ is:

$$\sigma_r^2(z) \equiv \frac{1}{C}\int_0^{2\pi}\int_0^{\infty} r^2 I(r, \theta, z)\, r\,dr\,d\theta = \sigma_x^2(z) + \sigma_y^2(z), \tag{3.2-18}$$

where $r^2 \equiv x^2 + y^2$. Similarly, the second moment of $\tilde{I}(r, \theta, z)$ is $\sigma_p^2 = \sigma_s^2 + \sigma_t^2$, where $p^2 \equiv s^2 + t^2$. From these radial moments, a radial quality factor [10] may be defined:

$$M_r^2 \equiv 2\pi\sigma_{r_0}\sigma_p. \tag{3.2-19}$$

Also, the radial spot half-width [10] is

$$W_r(z) = 2^{1/2}\sigma_r(z). \tag{3.2-20}$$

It follows from these definitions that W_r and σ_r obey propagation laws analogous to (3.2-13) and (3.2-15).

Multiple Modes

To treat beams composed of multiple non-PL modes, the moment definitions (3.2-10) and (3.2-12) must be generalized. [6,10,13] For m distinct non-PL modes, these integrals become

$$C = \iint I_s\,dx\,dy \qquad \sigma_x^2 = \frac{1}{C}\iint (x-\bar{x})^2 I_s\,dx\,dy \qquad \sigma_s^2 = \frac{1}{C}\iint s^2 \tilde{I}_s\,ds\,dt. \tag{3.2-21}$$

where, according to the results of Section 3.2.2, the time-averaged intensities are

$$I_s = \sum_{j=1}^{m} |\boldsymbol{E}_j|^2 \qquad \tilde{I}_s = \sum_{j=1}^{m} |\boldsymbol{P}_j|^2. \tag{3.2-22}$$

As before, $\bar{x} = \frac{1}{C}\iint x I_s\,dx\,dy$ is the 'center-of-gravity' of the entire intensity profile. The important distinction of the multi-mode cases is that $\boldsymbol{P}_i$ must be determined separately for each mode. This consideration is really only relevant for theoretical computations of M^2. For experimental determinations, only I_s is directly observable. Hence, M^2 must be determined from it alone. This is usually done by measuring $W(z)$ at several z, and finding the best-fit quadratic function of form (3.2-15).

In the following sections, the M_r^2 propagation will be used to quantify propagation characteristics of ZODIAC array emissions.

3.3 Non-Phase-Locked ZODIAC

A typical perspex burn pattern produced by ZODIAC at its output plane is shown in Figure 3.3-1(a). This pattern was produced with the 8-channel ZODIAC-I, using a confocal toric unstable resonator.† [2] There are seen to be eight distinct oblong beamlets; one corresponding to each discharge channel. The greater beamlet dimension corresponds to the unstable resonator direction, and the lesser dimension to the electrode-imposed waveguide direction. These beamlets are not phase-locked, and each is linearly polarized along its greater dimension, parallel to the electrode faces. [2] When focused, they combine to form a single axially uniform spot that is unpolarized and has a e^{-1} focal spot smaller than would be produced by any of the individual beamlets. [3]

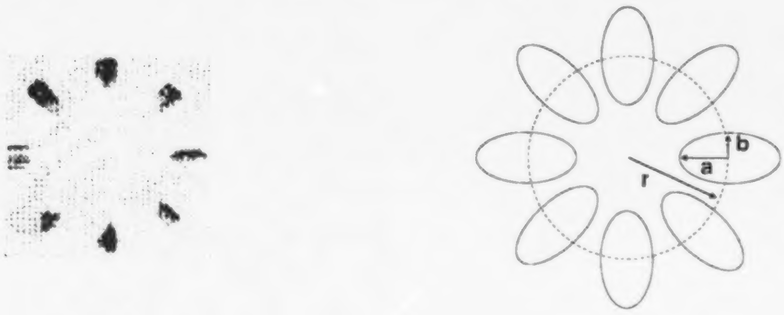

(a) **(b)**

Figure 3.3-1 ZODIAC intensity profile at the resonator output plane: (a) typical perspex burn produced with a toric confocal resonator, [3] reproduced here to scale; (b) the basic ZODIAC array configuration parameters: the beamlet characteristic dimensions *a* and *b*, and the beamlet combination radius *r*.

A heuristic explanation is possible of how eight independent beamlets focus into a single fine spot exhibiting no polarization. Each beamlet with an non-unity aspect ratio in the near-field generates in the far-field an oblong spot having its greater dimension perpendicular to that of the near-field profile. All beamlets propagate parallel to the optical axis, by virtue of the ZODIAC geometry and the common confocal unstable resonator. They are therefore focused to the same spot on the optical axis, where they superpose. Beamlet pairs with common orientation merge together, so that the composite focal spot consists of four superposed oblong spots oriented at 45 degree intervals. Although each beamlet spot is linearly polarized, the composite spot so derived exhibits no net polarization on a time averaged basis because the beamlets are not phase-locked. A circular focal spot, effectively smaller than that of a single beamlet, might be expected, considering that all beamlets intersect to contribute power in the focal region near the optic axis, whereas each beamlet contributes energy to a different part of the focal profile periphery.

---

† A *confocal* unstable resonator produces a collimated output, the wavefront of which at the resonator output coupling plane is flat, to first order.

3.3.1 Model

Further assessment of ZODIAC beam propagation requires a more detailed model. To facilitate this preliminary study, several significant approximations will be made. This first study will not consider in detail mode production in the individual ZODIAC channels. Instead, we will consider how composite beam propagation is more broadly affected by the radial array configuration as identified in Figure 3.3-1(b): the beamlet characteristic dimensions *a* and *b*, and the array combination radius *r*. With this approach, it will be possible to estimate a lower bound attainable with non-PL ZODIAC systems.

In first approximation for confocal unstable resonators, the resonator output is collimated. This implies that the beamlet phase-fronts are essentially flat at the resonator output plane, where there is effectively then a beam waist. To compute beam M^2 thus requires only knowledge of the electric field phasor distribution at the resonator output plane, $\boldsymbol{E}_0(x, y)$:

$$\begin{tikzcd} & I_o(x,y) = |\boldsymbol{E}_0(x,y)|^2 \\ \boldsymbol{E}_0(x,y) \arrow[ur] \arrow[dr] & \\ & \tilde{I}(x,y) = |F\{\boldsymbol{E}_0(x,y)\}|^2, \end{tikzcd} \tag{3.3-1}$$

where $F\{\ \}$ denotes the Fourier transform (3.2-2). All of the moments required for a calculation of M^2, as defined in (3.2-19), may be derived from $I_o(x, y)$ and $\tilde{I}(x, y)$.

In the absence of knowing the actual resonator modes, it is convenient to approximate the oblong beamlet generated within each ZODIAC channel as an asymmetric gaussian distribution. It can be easily shown that M_r^2 of an oblong beamlet is minimized when both its greater and lesser beamlet profiles are gaussian. It follows by extension, as will be discussed in the following section, that asymmetric gaussian beamlets also minimize M_r^2 of a non-PL ZODIAC.

It will also be assumed that for small *r*, it is possible for the beamlet intensity distributions to be overlapped at the output plane while still retaining a flat phase front.† It will be assumed that beamlets may combine in this way with both those across the optic axis and with neighboring beamlets. The details of achieving such "aperture filling" will not be treated here. It is expected that solutions will be possible with some combination of reflective compactors [14,17], low-pass spatial filtering, [16,20] and phase filtering with diffractive optical elements (DOEs). [26-32]

3.3.2 Estimates of M^2 Lower Bound

With this model, we are able to determine the M^2 propagation constant for an *ideal* non-PL ZODIAC. Because of the ZODIAC's multi-fold axial symmetry, of interest is the radial propagation constant M_r^2, as was defined in (3.2-19).

Since the beamlets are non-PL, each beamlet is considered to be a separate mode. Hence, computation of composite M_r^2 requires solving the moment integrals (3.2-21) and (3.2-22), with

---

† After propagating some distance, the distributions will in any case overlap due to diffraction. However, with the diffractive spreading, the phase fronts will also have become curved.

$m=n$. However, a simplification is possible. First, all radial intensity moments will be independent of the angular axis orientation because the ZODIAC beamlet configuration is rotationally symmetric. Second, since there are no interference effects between the beamlets, the (normalized) second-moments are independent of channel number n. Hence, computing ZODIAC M_r^2 reduces to computing M_r^2 for a single representative beamlet, except that the first-moments of the intensity distribution are zero (*i.e.*, the distribution center-of-mass is on the optic axis).

Simplest to consider is one representative beamlet in rectangular coordinates (x,y), centered at $(r,0)$. In this case, for a gaussian intensity profile, the electric field strength at beam waist (where the phase-profile is flat) is

$$\boldsymbol{E}_0(x,y) = \exp\left[-(y/b)^2 - \left(\frac{x-r}{a}\right)^2\right], \tag{3.3-2}$$

where a and b are the e^{-2} intensity half-widths, and r is the radius of the ring defined by the beamlet centers. The corresponding far-field distribution is proportional to the spectral content of (3.3-2), as defined by (3.2-2):

$$\boldsymbol{P}_0(s,t) = \pi a b e^{-(a\pi s)^2} e^{-(b\pi t)^2}. \tag{3.3-3}$$

With (3.3-2) and (3.3-3), the waist and spectral second moments, σ_{r_0} and σ_p respectively, are found to be:

$$\sigma_{r_0}^{\ 2} = \frac{1}{4}[a^2+b^2+4r^2], \tag{3.3-4}$$

and

$$\sigma_p^{\ 2} = \frac{1}{4\pi^2}\left[\left(\frac{1}{a}\right)^2 + \left(\frac{1}{b}\right)^2\right]. \tag{3.3-5}$$

The near-field waist moment is seen in (3.3-4) to be dominated by the largest near-field *beam* dimension $\{a,b,r\}$, whereas the smallest near-field *beamlet* dimension $\{a,b\}$ dominates the far-field divergence in (3.3-5). The dimensionless divergence $\Phi' = a\Phi$ is plotted in Figure 3.3-2, using the definition for full-width divergence (Φ) which follows from (3.2-6) and (3.2-20):

$$\Phi = 2^{3/2}\lambda\sigma_p. \tag{3.3-6}$$

The far-field is unaffected by the combination radius r because in the far-field each beamlet is mapped to the optic axis, regardless of near-field beamlet position relative to the optic axis.† Practically, this means that the ZODIAC far-field divergence and focal spot size are independent of r. This was also observed experimentally by Yelden, for both toric and conventional unstable resonators.‡ [2] Although the focal spot size is independent of r, the beam depth of field is not. It increases with r, and so therefore does M^2.

---

† All similar spectral components are mapped to their own unique position on the focal plane. Since near-field beamlet positioning does not affect the beam spectral content, the far-field intensity distribution is unaltered.

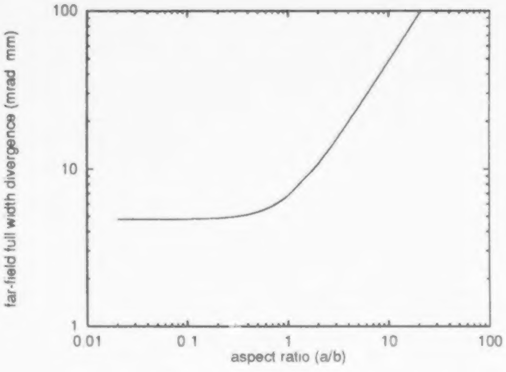

Figure 3.3-2 Dependence of non-PL ZODIAC dimensionless full-width divergence $\Phi' = 2^{3/2}\lambda a\sigma_p$ on beamlet aspect ratio *a*/*b*.

It also follows from (3.3-4) and (3.3-5) that M^2 is scale independent, since it depends only on the dimensionless configuration parameters *r*/*a* and *a*/*b*:

$$M_r^2 = \frac{a}{2b}\sqrt{\left[1+\left(\frac{b}{a}\right)^2\right]\left[1+\left(\frac{b}{a}\right)^2+4\left(\frac{r}{a}\right)^2\right]} \qquad (3.3\text{-}7)$$

That is, if these two quantities are invariant between two cases, then the propagation constant is also invariant. This scale-independence result is easily generalized, using the reciprocal relationship between near-field and far-field scaling: $E(\alpha x) \Leftrightarrow P(s/\alpha)$. In all cases, M^2 depends only on the relative proportions of the near-field profile.

Figure 3.3-3 presents the M^2 propagation factor as a function of beamlet configuration. Figure 3.3-3(a) is most easily interpreted as scaling with the greater near-field beamlet dimension (*a*) held constant. M^2 is seen in this case to be an increasing function of both *r*/*a* and *a*/*b*. The former increase is due to the near-field width increasing while the far-field divergence remains constant. The latter increase is due to the opposite effect. Figure 3.3-3(b) is most easily interpreted as scaling with the lesser near-field beamlet dimension (*b*) held constant. Physically, this could be accomplished by increasing resonator magnification while holding the waveguide dimension constant.

The results of Figure 3.3-3(b) suggest that an M_r^2 of less than 5 will be difficult to achieve with a non-PL ZODIAC. Although the model assumes that for *r*/*a* beamlets may overlap in the near-field while retaining a flat phase-front, such aperture filling cannot be achieved in practice with

---

‡ In that study of toric resonators, when the output coupling aperture became sufficiently small for the beamlets to merge together, the focal spot size was found to become inversely dependent on *r*. This increase in angular divergence was presumably due to two factors: the beam exiting the confines of the electrode waveguides, and perhaps also the cusp at the toric resonator center. As *r* was decreased, the beamlet aspect ratio reversed just prior the formation of forming a continuous annulus.

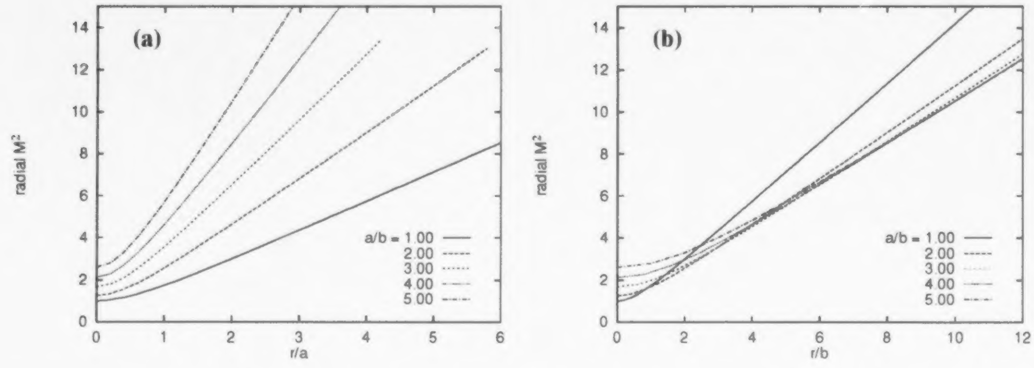

Figure 3.3-3 Dependence of non-PL ZODIAC propagation constant (M_r^2) on configuration parameters (a) *r/a* and *a/b*, and (b) *r/b* and *a/b*.

simple reflective elements alone.[†] It follows from geometric considerations that if the beamlets do not overlap in at the beam waist, then the ZODIAC configuration parameters must approximately satisfy the inequality $r/b - a/b > n/\pi$. Subject to this constraint, there exists for a given n an optimal aspect ratio and combination radius which minimizes M^2. The minimum attainable M^2 increases with n, as is seen in Figure 3.3-3(b), as does the optimal aspect ratio *a/b*. So, for example, for n=8, the minimum $M^2 \approx 5$ occurs for $a/b \approx 1.5$, while for n=24 the minimum $M^2 \approx 11$ occurs for $a/b \approx 2$.

Again, the results of Figure 3.3-3 represent the *lower bound* on M^2 and far-field divergence. In practice, many factors will combine to increase the composite M^2. Near-field beamlet profiles will actually be neither gaussian in amplitude, nor flat in phase. In particular, divergence effects due to the toric resonator cusp and waveguide dimensions have not been considered. Further, beamlets may be multi-mode, and have significant non-paraxial content due to diffraction from the resonator output coupling aperture.

3.3.3 Experimental Verification

These possible factors not withstanding, preliminary experiments suggest that the gaussian approximation is surprisingly good. With a 25 cm focal length lens, a focal spot diameter of 0.9mm was produced with the 24 channel ZODIAC structure described in Sections 1.3.3 and 2.2 ($a \approx$6mm, $b \approx$1.5mm, $r \approx$18mm). [1] It can be shown with (3.2-13) and (3.2-19) that the M_r^2 of a beam focused by a lens of focal length f is

$$M_r^2 \approx \frac{2\pi}{\lambda f} \sigma_{r_f} \sigma_{r_L}. \tag{3.3-8}$$

[†] It is however possible in principle with diffractive and refractive optics.

where σ_{r_f} and σ_{r_L} are the second moments at the lens and at the focal spot, respectively. It follows then from (3.3-4) and (3.3-8) that for the ZODIAC of [1], $M_r^2 \approx 14$. This compares quite favorably with the lower bound $M_r^2 \geq 12.6$ from (3.3-6), as it does with the M^2 of 20-30 recently obtained with a 2D incoherent array of CO_2 waveguide lasers. [19]

This experimental result may also be used to estimate of the average beamlet propagation factor $\langle M_{r_b}^2 \rangle$. Given that a single beamlet and the non-PL ZODIAC composite beam produce identical σ_p, it follows from (3.2-20) that

$$M_r^2 = (\sigma_{r_0}/\sigma_{r_{0b}})\langle M_{r_b}^2 \rangle, \tag{3.3-9}$$

where σ_{r_0} and $\sigma_{r_{0b}}$ are the near-field second moments at the waist of the composite beam and a single beamlet, respectively. Both may be estimated from (3.3-4). Equation (3.3-9) then suggests that $\langle M_{r_b}^2 \rangle \approx 2.3$, which again compares favorably with the minimum $\langle M_{r_b}^2 \rangle \geq 2.1$, obtained from (3.3-6).

It should be noted that it may be rather inaccurate to use the ZODIAC near-field and far-field beam size estimates reported in [1] as approximations to the second moments σ_{r_0} and σ_{r_f}, as was done here. These experimental measurements were derived from perspex burns, not from second moment calculation of a measured intensity profile, as would be proper. Also, it is known that M_r^2 measurements are artificially reduced if substantially oversized focusing optics are not used. [8,20] Small focusing optics are effectively low pass filters, allowing the most strongly diverging beam components to escape. These spatial frequencies would otherwise necessarily reduce the M_r^2.

3.3.4 Far-Field Properties

Although a small M^2 does not appear to be readily achievable with a non-PL ZODIAC, its output beam does have some advantages relative to those produced by incoherent linear arrays. These advantages follow primarily from the axial symmetry of ZODIAC. [3] In the following section, the effect of radial beamlet stacking on focal spot smoothness, size, and power density is discussed. Herein, the focal spot will be defined as the region bounded by an intensity contour at which the focal plane intensity has fallen to some specified fraction of the maximum, *e.g.*, e^{-1}. Also, given the correspondence between the *far-field divergence* and the *focal plane intensity profile* discussed in Section 3.2.1, the two terms will be used interchangeably.

Intensity Contour Smoothness

In contrast with linear stacking, radial stacking of oblong incoherent beamlets dramatically alters the focal intensity profile, as is illustrated in Figure 3.3-5. Beam 'symmetry' is seen to be significantly enhanced as the number of beamlets n is increased. Figure 3.3-6 further suggests that for larger aspect ratios (a/b), more discharge channels are required to achieve a given degree of focal spot symmetry, at least in the peripheral zones of the focal profile. To quantify this observation, we define smoothness as the relative variation in radius around an intensity contour.

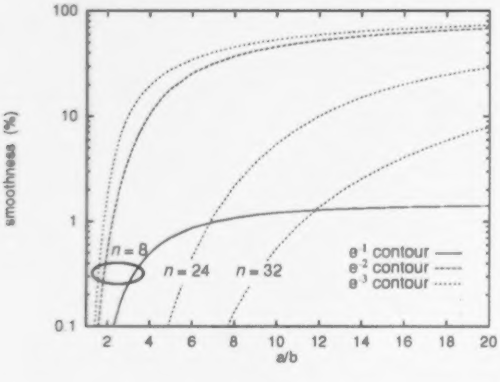

Figure 3.3-4 Effect of beamlet aspect ratio on far-field spot "smoothness" (the relative variation in radius around an intensity contour)

Figure 3.3-4 indicates that n=8 is sufficient to achieve less than 2% ripple in the e^{-1} contour over the range of *a*/*b* considered, and n=24 is sufficient to keep the ripple of both the e^{-1} and e^{-2} contours well under 1%.

In practice, an additional significant advantage derived by stacking a large number of beamlets radially is that non-uniformities in each beamlet are averaged over the central focal region. The importance of such averaging is emphasized by Figure 3.3-1(a), where large differences may be seen between the beamlets of the preliminary 8 channel system. [2] These differences and irregularities notwithstanding, in sheet metal cutting tests with this system, direction-independent processing was achieved. This was possible because of the axial ZODIAC symmetry, both in terms of beam intensity profile and polarization.† [2,3] It is expected that small changes in resonator alignment during operation can also be sufficiently averaged to have negligible effect on the composite beam focal parameters. [3]

Focal Spot Size, Power Density, and Power Fraction

For the remainder of this discussion, it will be assumed that the number of ZODIAC channels *n* is large, such that the composite focal spot is effectively circular. If this is so, then the beam far-field characteristics depend only on the beamlet aspect ratio (*a*/*b*). Again, Figure 3.3-4 indicates that *n* need not be very large for this to be a good approximation.

Figure 3.3-7 indicates the dependence of far-field properties on *a*/*b*, under conditions where *a* is held constant. With *a* constant, increasing *a*/*b* from 1 amounts to decreasing the lesser near-field dimension while holding the greater one constant, whereas decreasing *a*/*b* from 1 amounts to increasing the greater near-field dimension while holding the lesser one constant. Again, the latter

---

† When an asymmetric focal spot is used for multi-directional cutting, its largest dimension will determine the worst-case kerf width.

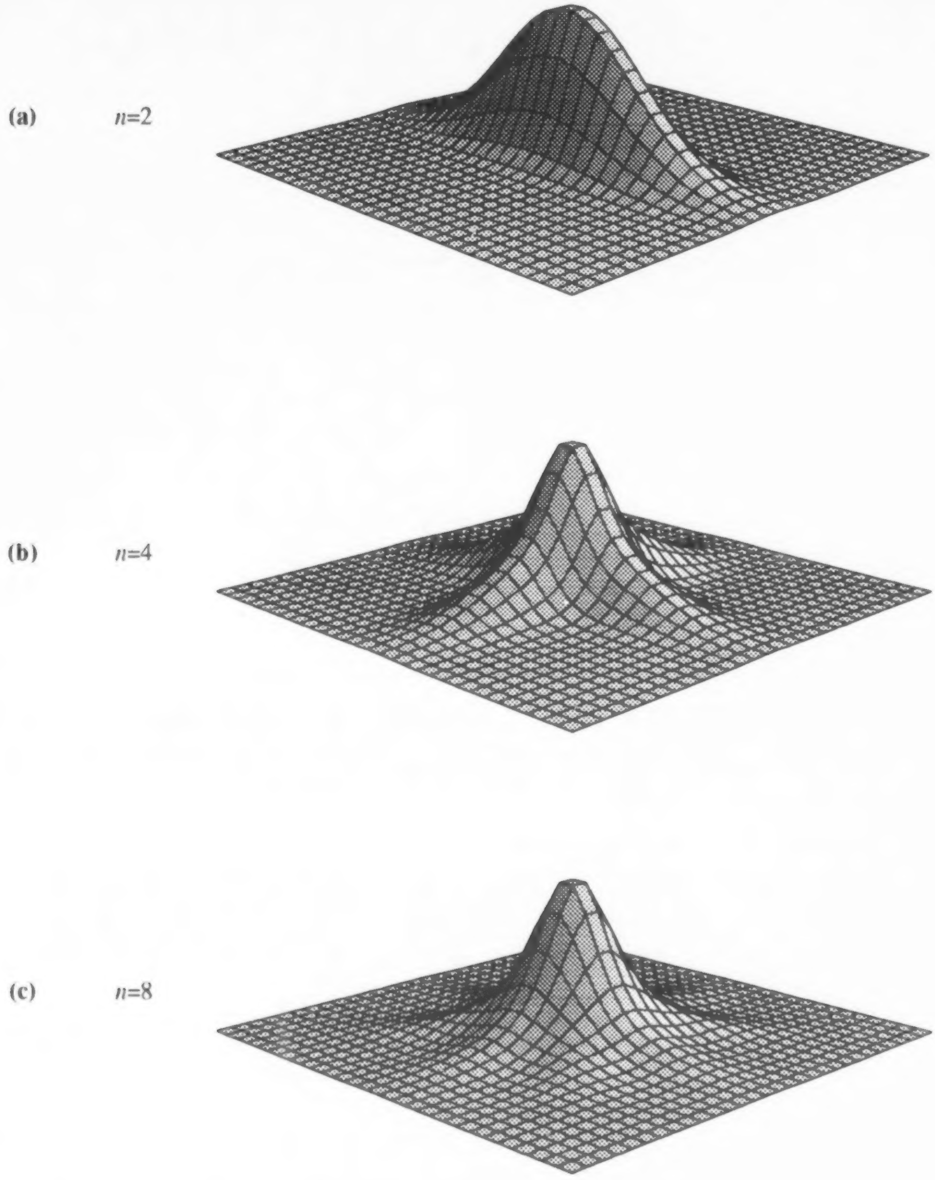

Figure 3.3-5 Effect in the far-field of increasing the number of channels in a non-PL ZODIAC. Beamlet aspect ratio is constant (a/b=3), and peak intensity is normalized. Plotted far-field extent is $-1.4 < sa < 1.4$.

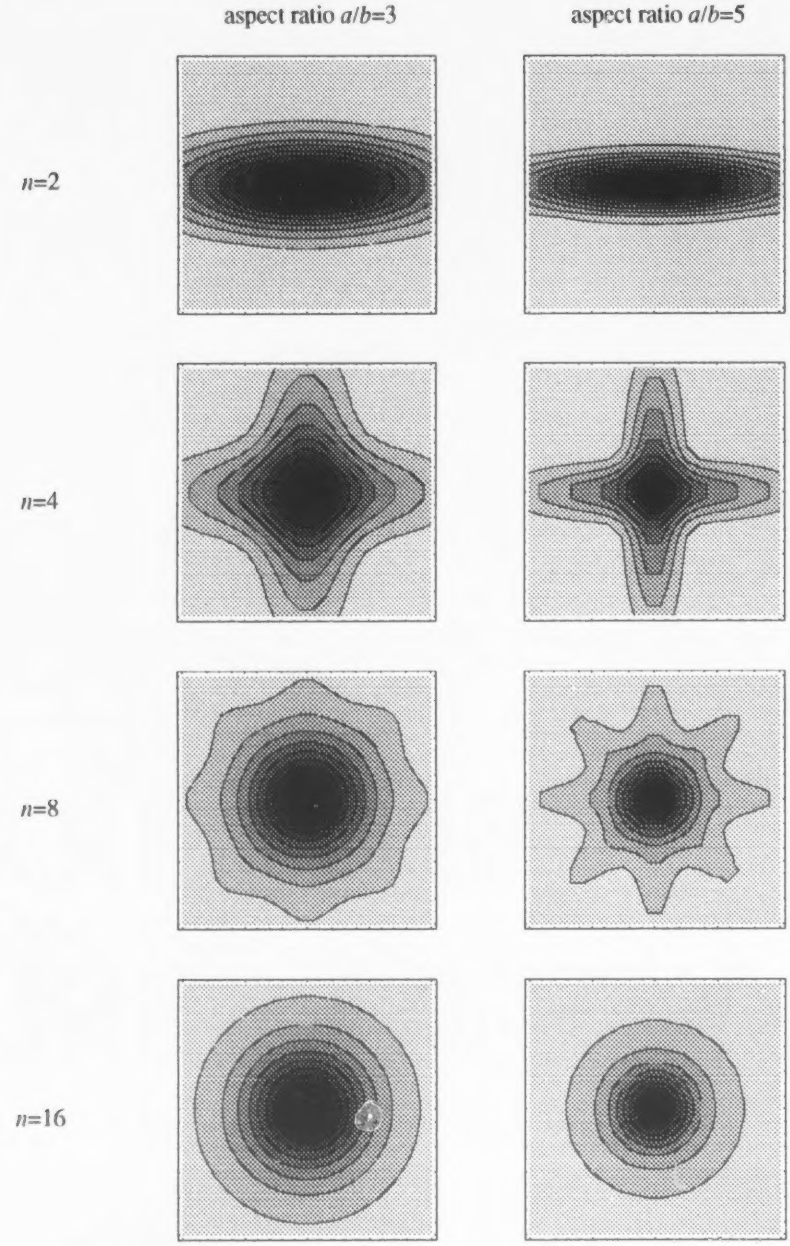

Figure 3.3-6 Effect in the far-field of enlarging the greater near-field dimension while holding the lesser constant (in this case, a and b, respectively).
Plotted far-field extent is $-0.75 < sa < 0.75$.

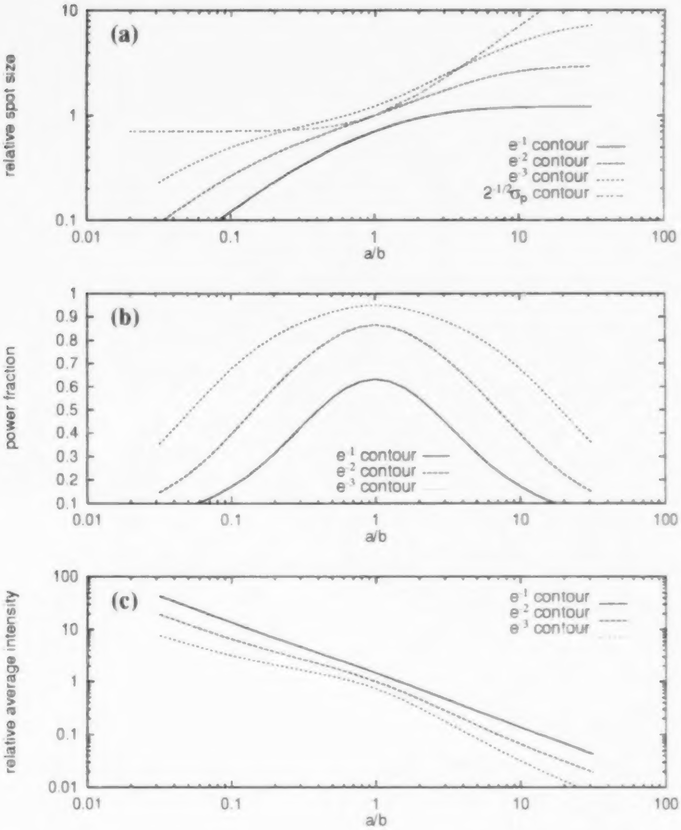

Figure 3.3-7 ZODIAC focal spot properties for large *n* and constant *a*. Effect of *a*/*b* on: (a) contour radii; (b) power fraction contained within the contours; and (c) the average intensity within the contours. Contour radii and average intensities are given relative to those of the e^{-2} contour of the *a*/*b*=1 case.

effect could be accomplished by increasing resonator magnification while holding the waveguide dimension constant. This is the change represented in Figure 3.3-6.

Figure 3.3-7(a) indicates that the focal spot size may be reduced arbitrarily *relative to that of the symmetric spot* by increasing one of the (symmetric) beamlet dimensions. Conversely, by decreasing one of the beamlet dimensions, the focal spot size increases asymptotically *relative to that of the symmetric spot*, to approach a constant. This again demonstrates that the focal spot size is determined mostly by the greater near-field dimension (*i.e.*, the lesser far-field dimension). This result, which was also observed in Figure 3.3-6, is not unexpected. According to simple geometric considerations, the central spot is by definition where all the beamlets intersect. σ_p is seen to exhibit the opposite behavior since, according to (3.3-5), it is determined mostly by the lesser near-field beamlet dimension.

Figure 3.3-7(b) indicates that as the beamlet aspect ratio moves away from 1, an increasing fraction of the total beam power falls into peripheral regions of the focus. This accounts for the behavior of σ_p observed in Figure 3.3-7(a); σ_p, being a second moment, is increased by more power falling further from the optic axis. Since it is the lesser near-field dimension which results in the majority of power in the periphery, σ_p is determined mostly by that dimension.

Figure 3.3-7(c) indicates that the average focal spot intensity may be increased arbitrarily *relative to that of the symmetric spot* by increasing one of the beamlet dimensions. Conversely, by decreasing one of the beamlet dimensions, the average focal spot intensity may be decreased arbitrarily *relative to that of the symmetric spot.* This indicates that performance of a ZODIAC beam in terms of focal spot intensity and size will be bounded by that of two symmetric gaussian cases having the same total power, and near-field radii a or b. The ZODIAC beam, unless it is composed of symmetric beamlets, will necessarily have a smaller power fraction in its focal spot.

The results of this Figure 3.3-7 suggest that if the ZODIAC resonator magnification is increased while the waveguide dimension is held constant, the system focal spot size will be decreased and the focal power density increased. This feature may be beneficial for some materials processing applications, although it is achieved at the expense of an increased power fraction in the peripheral beam regions. Indeed, through modification of the beamlet aspect ratio, the focal profile could be tailored to meet specific processing requirements.

For some applications, a focal profile with a bright central lobe yet with a considerable power fraction in the wings may be desirable. However, although in principle the spot size may be made arbitrarily small, to do so is not necessarily desirable for all applications. For example, with laser cutting, a condition would eventually reached where the average energy deposition rate within the focal zone could no longer maintain a sufficiently rapid process speed to negate thermal conduction losses into the substrate bulk. Under such conditions, process efficiency should drop to the point where kerf width and heat affected zone are increased unacceptably. Consequently, the optimum aspect ratio is dependent on the process and the properties of the workpiece.

3.3.5 Non-Phase-Locked ZODIAC Conclusion

A non-PL ZODIAC system produces an unpolarized circular focal spot, which makes it inherently well suited to many materials processing applications. Estimates of the lower bounds on M_r^2 indicate that without beamlet overlap at the beam waist, an M_r^2 of less than 5 cannot be attained. The minimum attainable M_r^2 without aperture filling increases with the beamlet aspect ratio (a/b) and number (n). For example, for modest beamlet aspect ratios (a/b=3 to 5), minimal M_r^2 is predicted to fall in the range 6-8 for n=8, and in the range 12-14 for n=24. This is consistent with experimental observations of $M_r^2 \approx 14$ in the 24-channel ZODIAC-II, for which $a/b \approx 4$.

Given ZODIAC's advantages in terms of compactness and simplicity, improved beam quality is not required for it to be attractive for some materials processing applications. This is particularly true for applications which do not simultaneously require a small focal spot and a large depth of field (*i.e.*, a small M^2), such as for example surface treating, paint stripping, and cutting thin materials. Still, it is expected that considerable improvement in ZODIAC M^2 could be achieved through some combination of phase-locking, spatial filtering, and corrective optics. In the following section, we proceed with the gaussian beamlet model to consider the potential of phase-locked radial arrays.

3.4 Phase-Locked ZODIAC

Now we will consider the effects of phase-locking on beam propagation and far-field focusing properties, endeavoring in particular to quantify the dependence of these properties on array configuration, and to estimate best-possible system performance. Gaussian beamlet profiles were assumed in the analysis of Section 3.3 in order to define the lower bound on M^2 achievable with a non-PL radial array. The analogous assumption in the PL case is complete phase-locking (*i.e.*, operation in a single supermode). In practice, one would expect multi-mode operation, which would necessarily increases the composite M^2. [13]

Phase-locking of an 8-channel ZODIAC array was investigated experimentally by Yelden. [2] In a study of injection locking,† the percentage of phase-locking between channel pairs was observed to range between 40%-90%, depending on the relative orientation of the channels. [2,21] Each discharge channel was found to have a preferred polarization orientation which the injected signal could not entirely overcome. These results were obtained with nickel-plated electrodes. The latest ZODIAC systems, in contrast, use dielectric coated electrodes, which have a very small difference between the loss constants of TE and TM modes. [18] It is therefore expected that with them a much larger degree of phase-locking should be attainable for a given magnitude of injection.

For this first estimation of PL radial array propagation characteristics, as with the non-PL consideration, we will consider only idealized cases. Complete phase-locking of all channel emissions will be assumed. Additional model assumptions are outlined in Section 3.4.1. The computer code developed to facilitate calculations are described in Section 3.4.2. Estimates of best-possible M^2 and far-field properties for PL radial arrays are summarized in Sections 3.4.3 and 3.4.4, respectively.

3.4.1 Model

For this simplified PL ZODIAC beam model, in addition to assuming that complete phase-locking between resonator channels is possible, it will be assumed that supermodes exist which are characterized by identical in-phase emissions from each channel. Moreover, it will be assumed that such supermodes produce the minimum M^2 attainable with radial arrays.‡ Assuming in-phase single-mode operation amounts to treating the ZODIAC composite beam as a single apertured plane wave which experiences amplitude modulation, but not phase modulation. For the beamlet profiles, the gaussian beamlets used for the non-PL considerations will be retained. Although the gaussian profile does not for the PL case give an estimate of minimal M^2 (as it did for the non-PL case), its use here does provide a basis for continued comparison. Moreover, the agreement between calculated and measured M^2 in the non-PL case gives some confidence that the gaussian profile is a reasonable first approximation to the actual beamlet profile.

---

† A single beam of constant polarization was injected along the optic axis of a conventional unstable resonator.

3.4.2 Numerical Analysis

The simplifications possible when computing M^2 for a non-PL ZODIAC cannot be extended to treat the PL case because of inter-beamlet interaction. Hence, a numerical code M2 was developed to facilitate a general study of ZODIAC beam properties. M2 computes the far-field intensity distribution and M^2 quality factor of an arbitrary paraxial beam, given the intensity and phase profile *at the beam waist.* M2 also computes far-field intensity contour widths and their contained power fractions. Solution convergence is monitored and controlled, so that a specified accuracy may be achieved.

Code design is modular and robust. In total, M2 consists of about 1700 lines of FORTRAN and C-Language code, not including public domain subroutines. Execution times on an IBM RS/6000 560 typically vary between 1-10 minutes per case for 0.1% tolerance calculations, depending on number of beamlets and the required mesh resolution. Code accuracy was confirmed against solutions obtained for various non-PL cases in Section 3.3.2, and for the case of 2 PL gaussian beamlets separated by 180°, for which a closed form solution is readily derived. A more detailed description of the code follows.

M^2 Calculation

The radial quality factor $M_r^2 \equiv 2\pi\sigma_{r_0}\sigma_p$ may be calculated given the electric field phasor distribution $\boldsymbol{E}_0(x,y)$ at the beam waist, as was discussed in Section 3.3.1. Again, for an unstable confocal resonator, the beam waist may in first approximation be taken to coincide with the resonator output plane. Hence, $\boldsymbol{E}_0(x,y)$ for the ZODIAC beam is the field distribution at the resonator output.

In M2, $\boldsymbol{E}_0(x,y)$ is described by two subroutines: one defining beamlet profile and one defining the array configuration. The integrals for σ_{r_0} and σ_p, defined by (3.2-10) and (3.2-12), are computed on a rectangular domain. When possible, linear symmetries with respect to the x or y axis are utilized to reduce the size computational domain. For example, for an even number of beamlets $n>2$, only the first quadrant need be considered. †

---

‡ That this is actually the case has not been demonstrated rigorously.

Near-field moment integrals are computed with the QUADPACK routine DQAGI, a 1D globally adaptive integrator for infinite intervals. [22] This routine also provides an estimate of solution error. Because no library routines were available to compute with sufficient speed the analogous far-field integrals, an FFT-based algorithm was developed for this purpose. $\boldsymbol{E}_0(x,y)$ was discretized on an *mxm* uniform rectangular mesh, and $\boldsymbol{P}(x,y)$ was approximated using an optimized 1D FFT algorithm by Mayer. [23] The moment integrals of $\boldsymbol{P}(x,y)$ were then computed on a finite domain with a 9-point 3^d-order accurate quadrature scheme for rectangular domains. [24] To control solution accuracy, an algorithm was developed to automatically adjust real-space mesh extent and resolution. This algorithm utilizes the reciprocal relationship between the real space and frequency space meshes to reduce to acceptable levels the aliasing and discretization errors in the spatial frequency integral. An estimate of final solution error was made based on convergence rate and the known order of the quadrature scheme (*cf.* Section 6.2: *GAMUT*). Estimated errors from the QUADPACK and FFT routines were used to estimate an upper bound on error in the computed M^2. Mesh resolution was adjusted to achieve a specified tolerance.

As a final test of solution accuracy and consistency, in all cases the normalization integral (3.2-12) is computed with both the QUADPACK algorithm and the FFT method, and compared.

Far-Field Central Lobe Properties

In addition to computing beam M_r^2, M2 computes far-field intensity contour widths and their contained power fractions. These calculations use the final discretization of $\boldsymbol{P}(x,y)$ computed in the M_r^2 calculations. In order to accelerate calculations, the central lobe is taken to be axially symmetric. M2 confirms the validity of this assumption for every case by rotating $\boldsymbol{E}(x,y)$ by half the angular distance between the beamlets, and re-calculating the central lobe properties. In both cases, the beamlets are configured so that a different primary axis of symmetry falls along the *s*-axis.

Contour widths ρ_i are estimated using Lagrange polynomial interpolation [24] along the *s*-axis. Second order interpolation was found to be sufficiently accurate for the present purposes. Contour power fractions are estimated by integrating the far-field intensity distribution over the contour area. Again, the assumption of symmetry requires that only a 1D integral be solved. This intensity integral is approximated using a combination of 3- and 4-point Simpson rules, depending on whether the number of mesh intervals within the contour is even or odd. [24] The last interval, which has a unique width, is approximated with the 2-point Trapezoidal rule. [24] The former rules are both 4th-order accurate, whereas the latter is only 2nd-order accurate. Hence, the convergence rate depended on the number of mesh intervals within the integration domain.

---

† Taking advantage of the *n*-fold axial symmetry inherent to the ZODIAC would also be possible. [25] However, to preserve algorithm generality, these simplifications were not made. As it is M2 allows, for example, the study of beamlet configurations with symmetries broken by linear phase anomalies, or non-identical beamlet profiles.

Integral accuracy was found to be limited by the estimates of p_i. Still, errors in test cases were observed to be on the order of the global error settings, typically 0.1%.

3.4.3 Estimates of M^2 Lower Bound

M2 was applied to estimating M_r^2 for the beamlet configurations of ZODIAC-I (n=8, a/b≈1.7) and ZODIAC-II (n=24, a/b≈4.0). Results of these computations are summarized in Figures 3.4-1 and 3.4-2. Results for both gaussian and supergaussian ($E_{sg}(x, y) \sim \mathrm{Exp}(-(x/a)^4-(y/b)^4)$) beamlet profiles are presented. In each figure, several PL cases are considered which have differing numbers of beamlets (n). Also included as a reference is the corresponding non-PL case, which is independent of n. In contrast with non-PL cases, in the PL cases channel number is observed to significantly affect the far-field profile.

M_r^2 of a phase-locked ZODIAC is seen in Figures 3.4-1 and 3.4-2 to remain roughly constant at nearly 1 as r/a increases, until $r/a \sim 1$ after which it increases and ultimately approaches asymptotically the M_r^2 of the non-PL case. This behavior is due mainly to the dependence of far-field divergence (defined here as $\sim \sigma_p$) on r/a, considering that $M_r^2 \sim \sigma_r\sigma_p$, and that σ_r differs little between the non-PL and PL cases. Two principal inflection points may be identified in the M_r^2 characteristics of Figure 3.4-1(a). The first inflection point is due to the waist profile becoming annular as r increases from 0, and the second is due to the angular separation of beamlets within the annulus. The first beamlet separation (radial) can be quantified in terms of a radial "fill-factor", whereas the second separation (angular) can be quantified in terms of a radial fill-factor.† This will be discussed further in Section 3.4.4. Greater separation between the beamlets corresponds to a smaller fill factor. It is notable that between the two inflection points in Figure 3.4-1(a), ZODIAC M_r^2 (with gaussian beamlets) is nearly equal to that of a gaussian annulus.

Far-field divergence of a phase-locked ZODIAC is seen in Figures 3.4-1 and 3.4-2 to decrease in inverse proportion to r/a until $r/a \sim 1$, after which it increases to asymptotically approach the non-PL divergence. The minimum divergence so defined appears to be only weakly dependent on a/b (compare for example Figures 3.4-1(b) and 3.4-2(b)). Increasing n is seen to delay the onset of σ_p approaching it's non-PL value, which for small r/a weakens the dependence of M_r^2 on r/a. For large r/a, when σ_p is identical for both PL and non-PL cases, σ_p varies inversely with a/b so that M_r^2 increases more strongly with r/a for large a/b.

A comparison of the gaussian and supergaussian cases considered suggest that M_r^2 is not unduly sensitive to the nature of the beamlet profile. The supergaussian profiles are seen to have an increased high spatial-frequency content, manifest in a larger σ_p, which causes a stronger dependance of M_r^2 on r/a.

---

† Note that the order in which the separations occur could be reversed if a/b was sufficiently large, or n was sufficiently small.

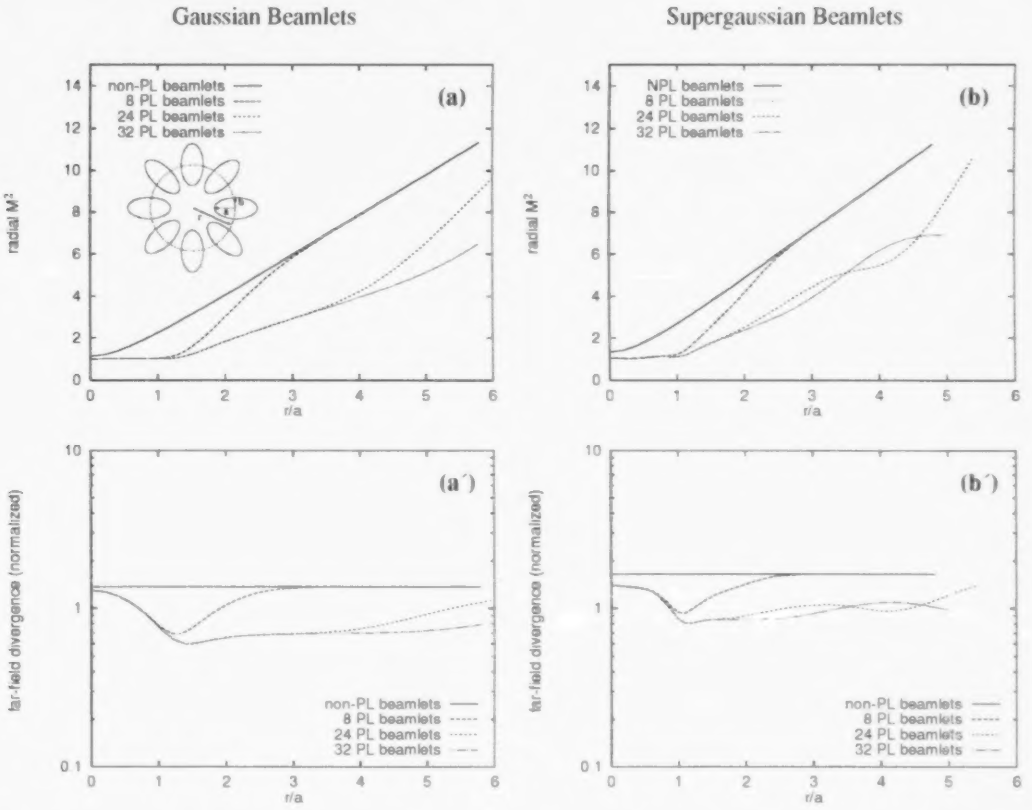

Figure 3.4-1 ZODIAC propagation constant (M_r^2) and far-field divergence for a/b = 1.67 and various n, for (a) gaussian beamlet profiles, and (b) supergaussian profiles. The far-field divergence is given relative to that of the a/b=1.0 non-PL case having the same a.

M^2 for the ZODIAC-II configuration tested in Section 3.3.3 ($a/b \approx 4$, $r/a \approx 3$) may be estimated from Figure 3.4-2(a). Ideal phase-locking would reduce system M^2 from $M_r^2 \approx 12.6$ to $M_r^2 \approx 11.1$. This is only a marginal improvement. The much larger improvements in M^2 possible with phase-locking must be achieved either through spatial filtering, [15,16] or by altering the near-field ZODIAC configuration: increasing n, decreasing r/a, or decreasing a/b. The former solution results in a loss of beam power, as will be demonstrated in the following section. The latter solution is more difficult in practice to implement, since it requires more sophisticated corrective optics. The good M^2 achieved under conditions of large n, small r/a, and small a/b is a result of aperture filling (*i.e.*, beamlet overlap). Angular beamlet overlap, which ultimately results in a continuous annulus, occurs for large n and small a/b, while overlap across optical axis, which fills in the annulus center, occurs for small r/a. These phenomena are illustrated in Figures 3.4-4 and

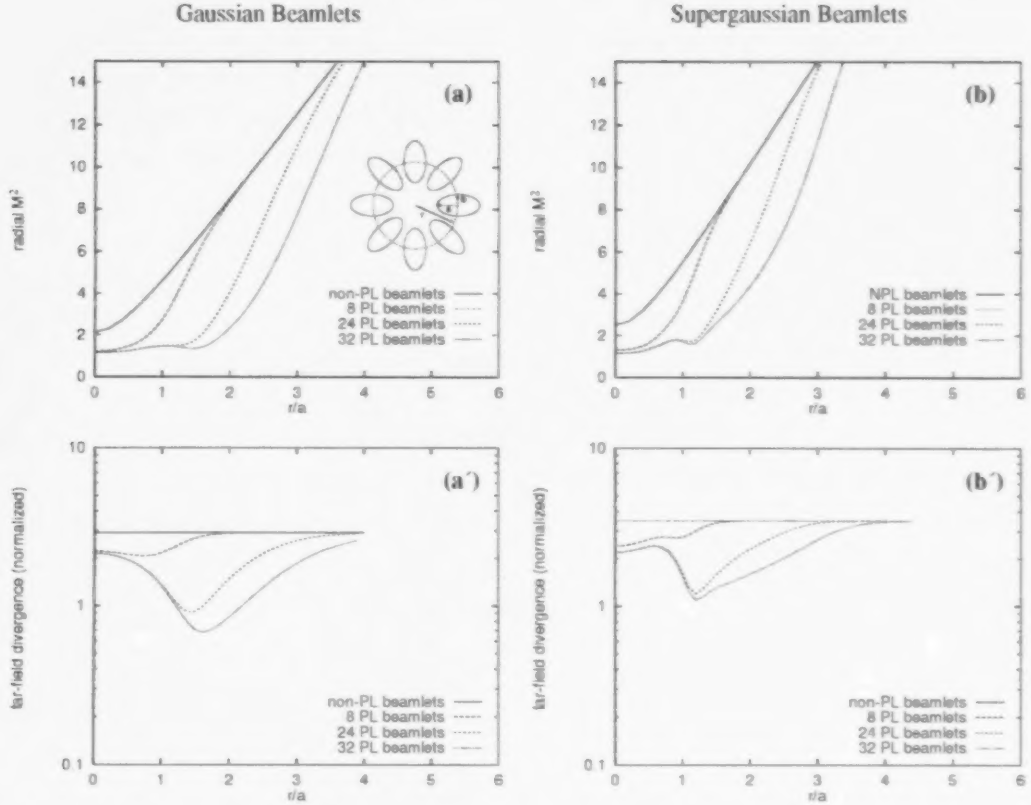

Figure 3.4-2 ZODIAC propagation constant (M_r^2) and far-field divergence for a/b = 4.00 and various n, for (a) gaussian beamlet profiles, and (b) supergaussian profiles. The far-field divergence is given relative to that of the a=b=1 non-PL case.

3.4-5, and will also be discussed in more detail the following section. Possible means of realizing aperture filling will be discussed briefly in Section 3.5.

3.4.4 Far-Field Properties

To aid interpretation of the previous results, it is instructive to consider in more detail the far-field properties of beams produced by ideal PL radial arrays. For non-PL beamlets, neither the channel number (n) nor the relative combination radius (r/a) was found to affect far-field properties, except inasmuch as n affected the "smoothness" of focal spot contours. Here, we will consider how phase-locking modifies the effects of these parameters on ZODIAC far-field properties, noting especially the effects of array fill-factor on the far-field central-lobe – its size and contained power fraction.

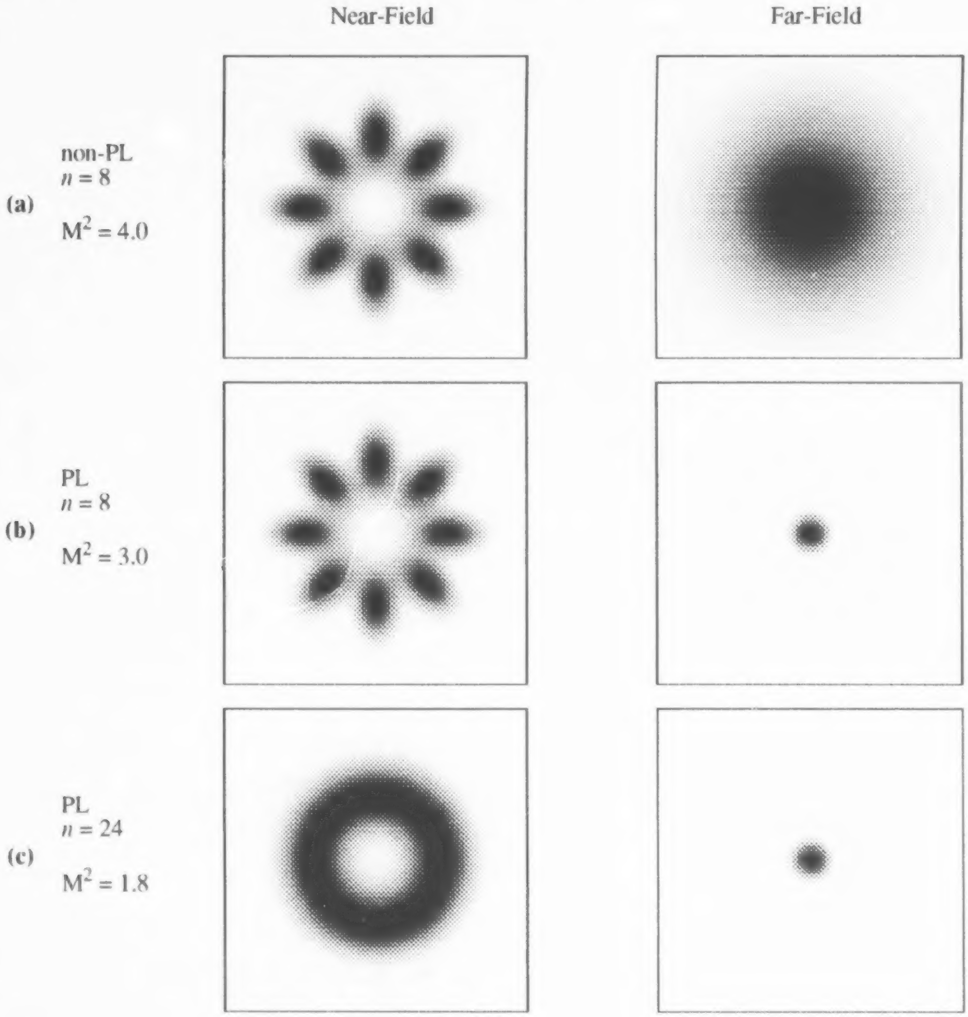

Figure 3.4-3 Effect of phase-locking and n on far-field profile for $a/b=1.67$, $a/r=2.0$. Plotted near-field extent is $-4 \le x/a \le 4$. Plotted far-Field extent is $-1 \le sa \le 1$, which corresponds to a full-width of 21.2 mm • mrad.

Effect of Channel Number and Phase-Locking

Figure 3.4-3 illustrates well the benefits of phase-locking and large angular fill-factor. Cases (a) and (b) share the same beamlet configuration. Phase-locking in case (b) is seen to dramatically reduce focal spot size relative to that of case (a). In case (c), n has been increased to 24 while all other parameters have been held constant. Thus, the angular fill-factor in case (c) is considerably higher than that of cases (a) and (b). A comparison of the far-fields in cases (b) and (c) confirms, as expected, that increasing the angular fill-factor reduces the beam's high spatial-frequency content.

Further comparison between the far-fields in (b) and (c) suggest that changing *n*, and thereby altering the angular fill-factor, leaves central lobe characteristics largely unaltered. (This is in fact the case, as will be demonstrated quantitatively in the later section *Central Lobe Characteristics*) However, the traces of high frequency detail in the peripheral lobes of case (b) cause significant deterioration of M^2 relative to case (c). This result suggests spatial-filtering as a possible means of improving PL ZODIAC M^2.

Effects of Combination Radius

Consider now the far-field effects of increasing *r*/*a* while holding all other parameters constant. Far-field central lobe size is found to depend inversely on *r*/*a*, as is illustrated in Figures 3.4-3 and 3.4-4 for the cases of *a*/*b*=1.67 and 4.00, respectively. This result is in contrast with the non-PL case, for which the far-field profile was found to depend solely on *a*/*b*. A comparison of Figure 3.4-4(b) with Figure 3.4-5 (c) further suggests that the central lobe size in the PL case is determined instead by *r*/*a*. Indeed, it can be shown that when over-the-center interactions are not important (*i.e.*, the radial fill-factor is small), the central lobe bounds are defined by Bessel function roots, the period of which varies inversely with *r*/*a*. Note that M^2 increases more strongly with *r*/*a* for higher *a*/*b*. This is because for higher *a*/*b*, the angular fill-factor decreases more strongly with

r/*a*.

Table 3.4-1 Summary of array configurations in Figures 3.4-4 and 3.4-5.

		r/a	
Case	Condition	Figure 3.4-4 ($a/b = 1.67$)	Figure 3.4-5 ($a/b = 4.0$)
(a)	minimal σ_p	1.4	1.4
(b)	$M^2 = 2$	2.1	1.6
(c)	$M^2 = 4$	3.9	2.0
(d)	$M^2 = 6$	4.8	2.3

Central Lobe Characteristics

The far-field characteristics of greatest interest in most materials processing applications are the central lobe size and its contained power fraction. Figure 3.4-6 illustrates the dependence of these quantities on *n*, *a*/*b*, and *r*/*a* for various phase-locked ZODIAC configurations. All spot sizes are give relative to that of a TEM_{00} mode (M^2=1) having the same near-field variance σ_p. (Recall that for a TEM_{00} mode, the e^{-2} width of the intensity profile is identical to $2^{1/2}\sigma_p$.)

Consider first the dependence of focal properties on *r*/*a*. For each case in Figure 3.4-6, a maximum in central lobe power fraction is seen to nearly coincide with a minimum in σ_p. This

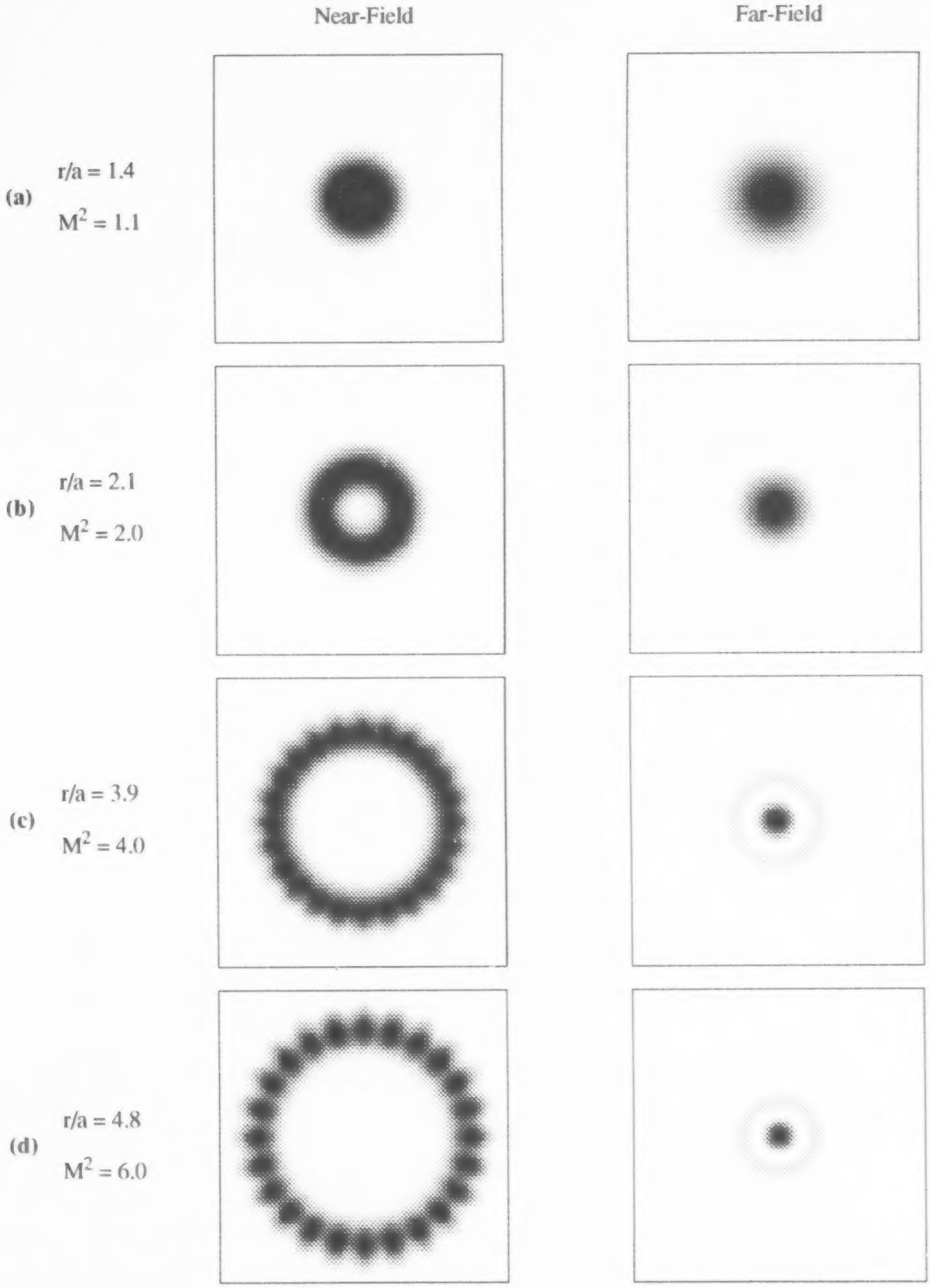

Figure 3.4-4 Effect of r/a on far-field properties, for $a/b=1.67$. Near-field extent is $-6 \le x/a \le 6$. Far-field extent is $-0.5 \le sa \le 0.5$, which corresponds to a full-width of 10.6 mm • mrad. For sake of comparison, the configurations presented in Figures 3.4-4 & 3.4-5 correspond to similar conditions, as is summarized in Table 3.4-1.

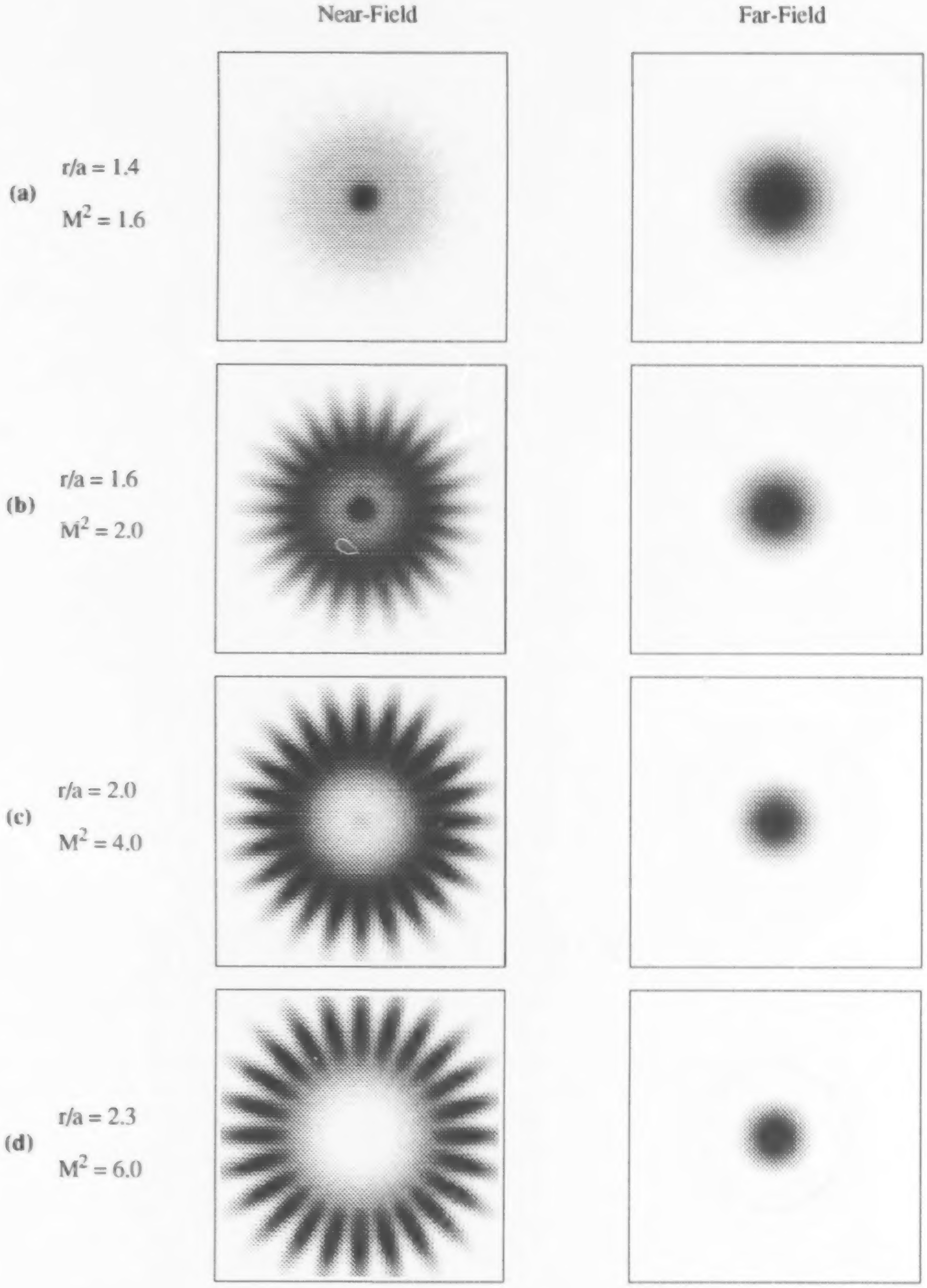

Figure 3.4-5 Effect of *r*/*a* on far-field properties, for *a*/*b*=4.00. Near-field extent is $-3 \leq x/a \leq 3$. Far-field extent is $-0.5 \leq sa \leq 0.5$, which corresponds to a full-width of 10.6 $\text{mm} \bullet \text{mrad}$. For sake of comparison, the configurations presented in Figures 3.4-4 & 3.4-5 correspond to similar conditions, as is summarized in Table 3.4-1.

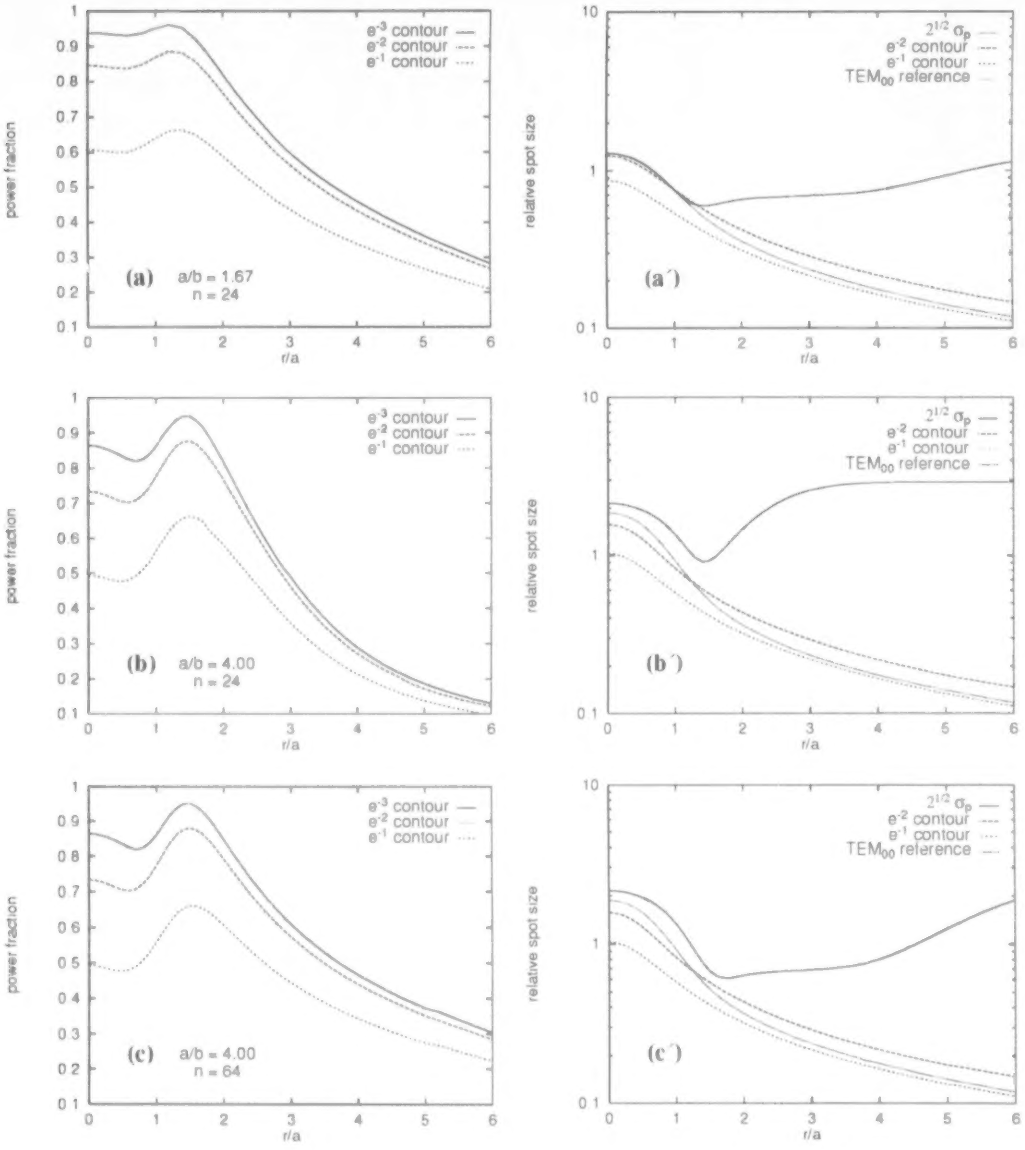

Figure 3.4-6 Dependance on *a*/*b* and *n* focal spot power fraction and size. Between (a) and (b), *n* is held constant at 24 while *a*/*b* increases from 1.67 to 4.00. Between (b) and (c), *a*/*b* is held constant at 4.00 and *n* increases from 24 to 64. The reference spot is that of the TEM_{00} mode sharing the same σ_r. All spot sizes are normalized with respect to the non-PL case having the same *a*, and *a*/*b*=1.0.

minimum σ_p occurs while there is still significant interaction between beamlets on opposite sides of the optic axis. Above $r/a \sim 2$, such across-the-center interactions become negligible and for sufficiently large n the near-field profile is essentially annular, as was seen in Figures 3.4-4 and 3.4-5. In the far-field, as r/a increases, σ_p is seen to diverge from the central lobe width. This divergence occurs because σ_p, being a second moment, is augmented by the increasing fraction of total power falling into peripheral lobes, whereas the contour radii, in terms of which the central lobe width is defined, depend only on the shape of the central lobe.† The increasing power fraction in the peripheral lobes is due to increasing high spatial-frequency content as the ZODIAC annulus becomes increasingly narrow. That the second moment estimate of spot size differs significantly from the e^{-2} spot size was also observed qualitatively in Figure 3.4-3.

Consider now the dependence of focal properties on *r/a* and *n*. Central spot size is seen in Figure 3.4-6 to be only weakly dependant on *a/b* and *n*, once over-the-center interactions are negligible. It may also be inferred from Figure 3.4-6 that the central lobe shape is only weakly dependent on *r/a*, *a/b*, and *n*. These results again confirm the heuristic observations following from Figures 3.4-4 and 3.4-5, that the central spot properties depend mostly on *r/a*. Further evidence is given in Figure 3.4-7, where central lobe power fraction and size are normalized with respect to the corresponding value for a gaussian annulus. Central lobe size and shape is seen in (b) to be nearly identical for $r/a > 2$. In contrast, the ZODIAC beam has a decreasing fraction of total power in the central lobe, as is seen in (b). It may be concluded that for a ZODIAC beam, *r/a* largely determines the central lobe intensity profile, and that the other array and beamlet characteristics determine the central lobe power fraction.

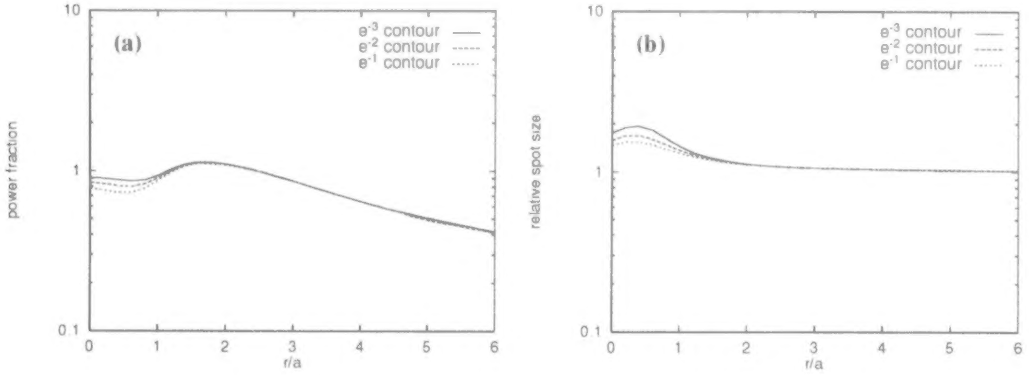

Figure 3.4-7 ZODIAC central lobe characteristics (a) power fraction and (b) relative spot size, normalized with respect to the corresponding quantities for a gaussian annulus. For the ZODIAC-II configuration; n=24 and a/b=4 (*cf.* Figure 3.4-6(b)).

---

† It is interesting to note that for every *a/b*, there seems to be an $r/a = f(a/b)$ for which in the limit $n \rightarrow \infty$, the ZODIAC near-field profile is equivalent to a gaussian of a/b=1

ZODIAC e^{-2} spot width is seen in Figure 3.4-6 to be consistently about 25% larger than the reference diffraction limited spot. M^2 degradation is due primarily to the power fraction which appears in the peripheral far-field lobes. If those peripheral lobes were truncated by spatial filtering, M^2 could be substantially improved. Indeed, Figure 3.4-6 suggests that with spatial filtering, an M^2 of around 1.3 could be obtained, albeit at the expense of large power losses. To obtain this M^2 with the ZODIAC-II configuration (Figure 3.4-6(b)), almost 50% of beam power would need to be discarded for r/a=3, which is the minimum combination radius obtainable without beamlet overlap.

While the central lobe size and shape appears to essentially independent of a/b and n, central lobe power fraction is not. Comparison of cases (a) and (b) suggests that for a given r/a, the power fraction in the central lobe decreases with a/b. Comparison of cases (b) and (c) in turn suggests that increasing n improves the central lobe power fraction. It is instructive to again consider these effects in terms of spatial frequency content. As r/a increases, the beamlets separate in the θ-direction, causing an increase in high-frequency detail. This θ-separation can be reduced by either decreasing a/b or increasing n. In (b) and (c), the onset of power loss due to angular non-uniformity is seen to be delayed by increasing n, as can be inferred from considering σ_p. It will be shown that the effects of near-field intensity variations in the θ direction may be parameterized according to an angular fill-factor. It is interesting to note that the far-field properties of cases (a) and (c) are surprisingly similar. In both cases nb/a~15. This coincidence may also be explained with a quantification of angular fill-factor.

Angular Fill-Factor

We have suggested previously that the increase in M_r^2 with r/a is due to high-frequency detail appearing in the far-field, which is caused in part by angular variations in the near-field intensity profile. In Figure 3.4-8, M_r^2 and relative spot size are plotted with respect to an angular fill-factor, defined here as

$$\eta_\theta \equiv \frac{bn}{r}. \tag{3.4-1}$$

This quantity characterizes the fraction of near-field circumference at radius r which is illuminated by beamlets. It does not account for the details of the beamlet profiles, but is a reasonable first approximation to an angular fill-factor. The far-field spot sizes in Figure 3.4-8 which correspond to similar nb/a but different a/b are seen to have similar dependences on η_θ, suggesting that η_θ is indeed a useful quantity. The significance of nb/a is that between cases with identical η_θ and nb/a, r/a is also invariant.

η_θ can be used to account for the inflection points observed in the M_r^2 characteristics, which are more clearly evident in Figures 3.4-1 and 3.4-2. The first inflection point at $r/a \approx 1$ is due to the onset of a hole appearing in the center of the near-field profile, and the concomitant increase in far-field high-frequency detail. The second, which corresponds to M_r^2 approaching that of the non-PL

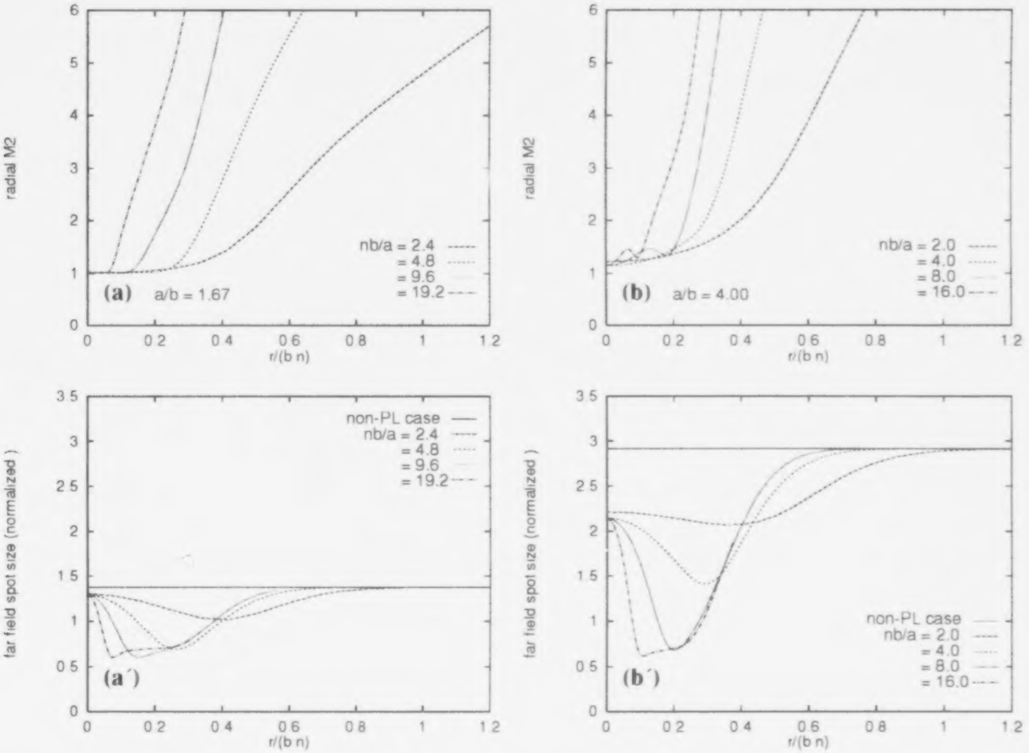

Figure 3.4-8 M_r^2 and far-field spot size as a function of angular fill-factor $\eta_\theta = r/(bn)$ for cases (a) a/b=1.67 and (b) a/b=4.00. Normalization of spot sizes is with respect to the non-PL case having the same a and a/b=1.0.

case, is due to an η_θ threshold being surpassed. This threshold coincides with the onset of beamlet separation in the angular direction, which causes an additional increase in far-field high-frequency detail. It should also be noted that $\pi\eta_\theta$ is the angular analogue of r/a: The normalized separation of beamlet centers across the origin is $2r/a$, while the normalized angular separation is $2\pi r/(nb)$. In Figure 3.4-8, the second inflection point is seen to occur at $\pi\eta_\theta \approx 1$, which is consistent with the observation of an inflection point at $r/a \approx 1$.

3.4.5 Phase-Locked ZODIAC Conclusion

In general, three conditions must be satisfied for a laser array to produce a high quality beam: the array must be phase-locked, and have properly phased emissions and a high array fill-factor. [28] In this first theoretical study of phase-locked ZODIAC performance, we have assumed that the first two conditions are satisfied and have investigated the effects of varying the array fill-factor. The ZODIAC fill-factor has two aspects: a radial fill-factor (a/r) which characterizes beamlet proximity across the optic axis, and an angular fill-factor ($\eta_\theta \equiv bn/r$) which characterizes beamlet angular proximity.

M^2 is considerably deteriorated by both the radial intensity variations which occur when $a/r < 1$, and by the angular intensity variations which occur when $\pi\eta_\theta < 1$. As r is increased from 0, satisfaction of the former inequality causes the ZODIAC M^2 to become like that of an annular beam, provided that the later limit has not already been exceeded. Satisfaction of the latter inequality corresponds to an angular separation of beamlets within the annulus, which causes the PL M^2 to approach asymptotically that of the non-PL ZODIAC. As the array fill-factors drop, M^2 increases because a larger fraction of beam power falls into the far-field high spatial-frequency lobes.

Although M^2 inevitably increases with r/a, ideal phase-locked operation does produce a central far-field lobe with nearly diffraction limited properties, albeit with a decreasing power fraction as r/a increases.[†] The central lobe profile appears to be determined mostly by r/a, while the central lobe power fraction is determined by the beamlet profile and the array fill-factors. This result suggests that low-pass spatial filtering may be a viable means to improve composite beam quality, provided that significant beam power loss is acceptable.

For a ZODIAC PL radial array to produce a composite beam with small M^2, both the radial and angular fill-factors must be high. Indeed, without aperture filling, ideal phase-locking appears to reduce M^2 relative to the non-PL case by only 20% *at most*. This corresponds to a minimum $M^2 \approx 4$ attainable with phase-locking, relative to the $M^2 \approx 5$ attainable without phase-locking (*cf.* Section 3.3.2). Without resorting aperture filling, which requires sophisticated corrective optics, there are two available strategies for reducing ZODIAC M^2.

First, M^2 may be reduced by increasing the array's radial fill-factor. This is possible either by decreasing the array channel number n, or with reflective compactors. [14,17] As an example of the former measure, for an aspect ratio of a/b=1.67 reducing n from 24 to 8 improves the minimum M^2 from 8.4 to 4.3. Of course, reducing n also reduces the maximum laser power. Reflective compactors provide an alternative means of reducing the radial fill-factor; with an axicon, the radius of the beamlet array may be reduced without altering the annulus width. However, since the beam profile is mapped in along radial lines, angular detail is also compacted. So while an axicon will improve the radial fill-factor, which is beneficial for M^2, it will simultaneously reduce the angular fill-factor by effectively increasing the beamlet aspect ratio, which is detrimental to M^2. Hence, for a given ZODIAC array configuration, there will be a compaction fraction which minimizes the final M^2.

A second strategy for reducing phase-locked ZODIAC M^2 is low-pass spatial filtering, which truncates the beam's high-frequency lobes. [16] For arrays with high fill-factors, as the filter cutoff frequency is lowered, M^2 falls much more rapidly than does the transmitted power. [20] Spatial filtering is not nearly so efficient for arrays with low fill-factors, however. For the fill-factors associated with non-overlapping ZODIAC beamlets, attaining the near diffraction limited M^2 of the central lobe ($M^2 = 1.3$) would require discarding *at least* 50% of beam power. Since ZODIAC systems are already very compact, perhaps in some circumstances such power losses would be tolerable. Of course, nearly diffraction limited performance is not required for most processing applications. The degree of power loss incurred by spatial filtering to attain more modest values of M^2 bears further investigation. For example, for a broad variety of cutting and drilling applications, $M^2 = 3$ is sufficient.

[†] Throughout these considerations, it has been assumed that M^2 is minimized by supermodes which are uni-phase and have a uniform power distribution amongst the near-field lobes, and that such "ideal" supermodes are possible. These assumptions are not necessarily valid, and require further investigation.

For more efficient conversion of low fill-factor beams into high quality beams, aperture filling techniques must be employed. A variety of aperture filling techniques using refractive and diffractive optical elements have been developed for coherent arrays of solid state and gas lasers. [26-32] In the technique most suitable to CO_2 slab arrays, the beamlets are allowed to propagate until a relatively uniform intensity distribution results from diffractive overlapping, at which point phase correction is applied to give a flat phase-front. Optimal propagation distances and types of phase correction are the subject of ongoing investigation. Several schemes have been demonstrated recently by Lescroart *et al.* for a linear array of CO_2 waveguide lasers, [32] including the optimal phase-filtering method proposed by Lapucci *et al.* [31] This diffractive-spreading technique is most easily adapted in the θ-direction of the ZODIAC array, in which the strongest divergence occurs, to obtain a high angular fill-factor. Since this technique could not be so easily employed to fill in the annulus center, it could perhaps be used in conjunction with beam compactor. A significant additional benefit of some DOE-based aperture-filling techniques is that they may also be used to phase-lock the array. [28]

3.5 Summary

This chapter has considered the effects of array configuration and channel phase-locking on ZODIAC beam propagation and focusing. Best-possible system performance in terms of the M^2 propagation factor has been estimated through considering ideal cases. Using a gaussian beamlet approximation, M^2 has been parameterized in terms of the array configuration invariants n, a/b and r/a. For a non-PL ZODIAC, it has been shown that without corrective optics which enhance the array fill-factor, $M^2 < 5$ cannot be achieved. By assuming ideal phase-locking and identical channel phasing, it also been suggested that phase-locking alone cannot considerably improve the ZODIAC M^2. Achieving $M^2 < 4$ appears to require either low-pass spatial filtering, which is relatively simple to implement but has a potentially large cost in lost beam power, or aperture-filling techniques, which are more complex to implement but which potentially have low losses and which can also be used to phase-lock the array. Solution details must be the subject of further study.

In any case, the non-PL ZODIAC is known to produce a circular unpolarized focal spot which is inherently well suited to direction-independent processing. [3] Given ZODIAC's advantages in terms of compactness and simplicity, improved beam quality should not be required for it to be an attractive choice for many materials processing applications, particularly those which do not require a small M^2.

Bibliography

[1] Bilida, W. D. (1996): *Radial Array Slab Laser Excitation With a Resonant Cavity* (Ph.D. Dissertation, University of Alberta).

[2] Yelden, E. F. (1992): *A Compact, Multichannel, Phase-Locked, Carbon Dioxide Laser System* (Ph.D. Dissertation, University of Alberta).

[3] Yelden, E. F., Scott, S. W. C., Strohschein, J. D., Seguin, H. J. J., Capjack, C. E., and Reshef, H. W. (1994): Symmetry enhancement and spot-size reduction through radial beam stacking in a multichannel CO_2 laser array. IEEE J. Quantum Electron. **30**, 1868-1875.

[4] Belanger, P. A. (1991): Beam propagation and the ABCD ray matrices. Opt. Lett. **16**, 196-198.

[5] Johnston, T.F. (1990): M^2 concept characterizes beam quality. Laser Focus World (May), 173-183.

[6] Johnston, T. F., Sasnett, M. W., Doumont, J., and Siegman, A. E. (1992): Laser beam quality versus aperture size in a cw argon-ion laser. Opt. Lett. **17**, 198-200.

[7] Jones, R. D., and Scott, T. R. (1993): Laser-beam analysis pinpoints critical parameters. Laser Focus World (January), 123-130.

[8] Lawrence, G. N. (1994): Proposed international standard for laser-beam quality falls short. Laser Focus World (July), 109-114.

[9] Ruff, J. A., and Siegman, A. E.(1992): Single-pulse laser beam quality measurements using a CCD camera. Appl. Optics **31,** 4907-4908.

[10] Siegman, A. E. (1990): New developments on laser resonators in *Optical Resonators*. Proc. SPIE **1224**, 2-14.

[11] Siegman, A. E. (1991): Defining the effective radius of curvature for a nonideal optical beam. IEEE J. Quantum Electron. **27**, 1146-1148.

[12] Siegman, A. E., Sasnett, M. W. and Johnston, T.F. (1991): Choice of Clip Levels for Beam Width Measurements Using Knife-Edge Technique. IEEE J. Quantum Electron. **27**, 1098-1104.

[13] Siegman, A. E., and Townsend S. W. (1993): Output beam propagation and beam quality from a multimode stable cavity resonator. IEEE J. Quantum Electron. **2**, 1212-1217.

[14] Siegman, A. E. (1986): *Lasers*. (University Science Books, Mill Valley).

[15] Hecht, E. (1987): *Optics*, 2nd Edition. (Addison Wesley, New York).

[16] Steward, E. G. (1983): *Fourier Optics: An Introduction*. (Ellis Horwood Limited, Chichester).

[17] Couture, M., and Piche, M. (1993): Focusing properties of an axicon pair. Can. J. Phys. **71**, 70-78.

[18] Nowack, R., Opower, H., Schaefer, U., Wessel, K., Hall, Th., Kruger, H., and Weber, H. (1990): High power CO_2 waveguide laser of the 1 kW category in *CO_2 lasers and Applications II* (H. Opower, ed.). Proc. SPIE **1276**, 18-28.

[19] Abramski, K. M., Colley, A. D., Baker, H. J., and Hall, D. R. (1996): High-power two-dimensional waveguide CO_2 laser arrays. IEEE J. Quantum Electron. **32**, 340-349.

[20] Baker, H. J., Hall, D. R., Hornby, A. M., Morley, R. J., Taghizadeh, M. R., and Yelden, E. F. (1996): Propagation characteristics of coherent array beams from carbon dioxide waveguide lasers. IEEE J. Quantum Electron. **32**, 400-407.

[21] Yelden, E. F., Seguin, H. J. J., Capjack, C. E., Reshef, H. (1993): Phase-locking phenomenon in a radial multislot CO_2 laser array. J. Opt. Soc. Am. B. **10**, 1475-1482.

[22] Piessens, R., and de Doncker, E. (1980): QUADPACK numerical integration package. (netlib.att.com)

[23] Mayer, R. (1993): FFT and FHT routines. (fft-stuff.tar.Z in pub/C-numanal on usc.edu).

[24] Zwillinger, D. (1992): *Handbook of Integration*. (Jones and Bartlett, Boston).

[25] Boyd, J. P. (1989): *Chebychev & Fourier Spectral Methods*. (Springer-Verlag, Berlin).

[26] Leger, J. R., and Swanson, G. J. (1987): Efficient array illuminator using binary-optics phase plates at fractional-Talbot planes. Opt. Lett. **12**, 245-247.

[27] Swanson, G. J., Leger, J. R. and Holz, M. (1987): Aperture filling of phase-locked laser arrays. Opt. Lett. **12**, 245-247.

[28] Leger, J. R., Holtz, M., Swanson, G. J., and Veldkamp, W. B. (1988): Coherent laser beam addition: an application of binary-optics technology. Lincoln Lab. J. **1**, 225-245.

[29] Swanson, G. J., and Veldkamp, W. B. (1989): Diffractive optical elements for use in infrared systems. Opt. Eng. **28**, 605-608.

[30] Taghizadeh, M. R., Miller, J. M., Blair, P., Bett, T. H., and Stevenson, R. M. (1993): Design and fabrication of synthetic diffractive optical elements for high power laser applications *in Fourth International Conference on Holographic Systems, Components & Applications*. (Neuchatel, Switzerland, 13-15 Sept. 1993).

[31] Lapucci, A., Quercioli, F., and Jafrancesco, D. (1993): Optimal phase filtering for high-power laser array far-field distribution. Opt. Lett. **18**, 1694-1696.

[32] Lescroart, G., Muller, R., and Bourdet, G. L. (1995): Phase filter design for efficient side lobe suppression in phase coupled CO_2 waveguide lasers array. Opt. Comm. **115**, 233-240.

4

PIE Burst-Mode: Enhanced Discharge Stability

The previous two chapters have addressed problems preventing the advance of slab array technology. For the remainder of this thesis, we will investigate several implications of burst-mode operation on PIE laser performance. As was described in Section 1.2, PIE lasers are impulse-sustained fast transverse flow systems which have been significantly advanced through pulse-periodic ("burst-mode") operation. In this chapter, we will investigate the burst-mode discharge stabilization effect observed by Nikumb *et al*, [1-4] which allows extraction of much higher laser powers. Primarily through numerical analysis, we will seek to discover the mechanisms responsible for this effect.

4.1 Introduction

Optical power extractable from a convectively-cooled electrically-excited CO_2 laser scales with discharge volume and the square of gas pressure.[†] [5] This scaling is found to be inevitably limited by the onset of plasma instabilities which, in their most damaging form, cause the desirable diffuse current of a glow discharge to constrict into an arc. [6-12] Not only does this glow-to-arc transition effectively terminate laser operation, but it may also damage the device electrodes.

Understanding of the mechanisms causing instability is less than complete, but has nevertheless been sufficient to help improve discharge performance considerably, allowing stable discharge operation at higher power densities. With DC-excited convectively cooled lasers, insights into causal mechanisms have lead to improvements in various aspects of laser design, including for example many related to gas flow, external ionization, and electrode design. Related to gas flow, rapid gas circulation is used to sweep forming instabilities out of the discharge region before they have time to fully develop. [7,9] Gas turbulence can also have a beneficial effect, because it enhances dissipative processes which then reduce the amplitude of non-uniformities which would

---

[†] Laser power also *increases* with other variations, however it doesn't *scale* as when similarity conditions are satisfied. For example, attainable laser power increases with flow velocity. However in similarity scaling, flow velocity is a dependent variable determined by the requirement that the outlet gas temperature remain constant. Also held constant in such similarity scaling are E/n and n_e/n, so that laser kinetics and chemical dynamics remain unaltered. [5] Reduced field strength (E/n) is proportional to the energy gained by electrons between collisions.

otherwise act as instability seeds. [9,13] An extreme example of problematic inhomogeneities are acoustic shock waves in pulsed laser discharges. [14] In TEA lasers, elaborate systems of damping baffles have been used to reduce their effect. [15] The detrimental effects of discharge inhomogeneities and instability dynamics may also be reduced through external ionization sources. External ionization stabilizes the discharge by reducing the dependence of local charge density on the local gas state, thus weakening an important feedback path in the instability dynamic. [11] To enhance the effect of external ionization, easily ionized additives are sometimes used. [16-21] It is also known that preionization non-uniformities can cause instabilities in large-aperture TEA lasers, [22] so pulse forming networks are designed to dynamically profile the space-charge density distribution. [23] Regarding electrode design, narrow-gap RF-excited discharges are known to be considerably more stable than DC-excited discharges because their near-electrode sheaths act as a distributed ballast. [24,25] This effect can to some extent be mimicked in DC discharges by using multi-segment electrodes. [26,27] Small area electrode may also have a stabilizing effect by shifting the cathode fall voltage into the abnormal regime, where it is in the increasing range of its V-I characteristic. [26]

Another discharge stabilization technique was discovered by Nikumb *et al.* [2] in the course of developing burst-mode excitation for PIE lasers. [1-4] (For an introduction to PIE and burst-mode, see Section 1.2.3). Nikumb *et al.* found that under burst-mode excitation, the discharge instability threshold was forestalled, allowing a non-optimized factor of 2 increase in laser output power. These experimental findings, summarized in Section 4.2, motivate this first analysis of instability growth in a PIE discharge. Section 4.3 briefly discusses relevant aspects of discharge instability, and the available methods of theoretical analysis. Section 4.4 describes a computer code developed in order to model instability growth in PIE discharges, and presents modelling results. Subsequent experiments to test model results are discussed in Section 4.5. Sections 4.6 presents final conclusions.

4.2 Preliminary Experiments

The burst-mode discharge stabilization effect was studied by Nikumb *et al.* [1-4] with the PIE-III laser system. In Section 4.2.1, a description of PIE-III is given, in supplement to the general description of PIE systems which was given in Section 1.2. This is followed in Section 4.2.2 by a summary of those experiments of Nikumb *et al.* which are relevant to our instability analysis.

4.2.1 PIE-III Apparatus

Mechanical aspects of PIE-III were similar to those of PIE-IV, the device described in Section 1.2.1. The important distinction in the case of PIE-III was its smaller discharge volume: its electrodes defined a discharge volume 9 cm wide (in the direction of current flow), 18 cm high (in

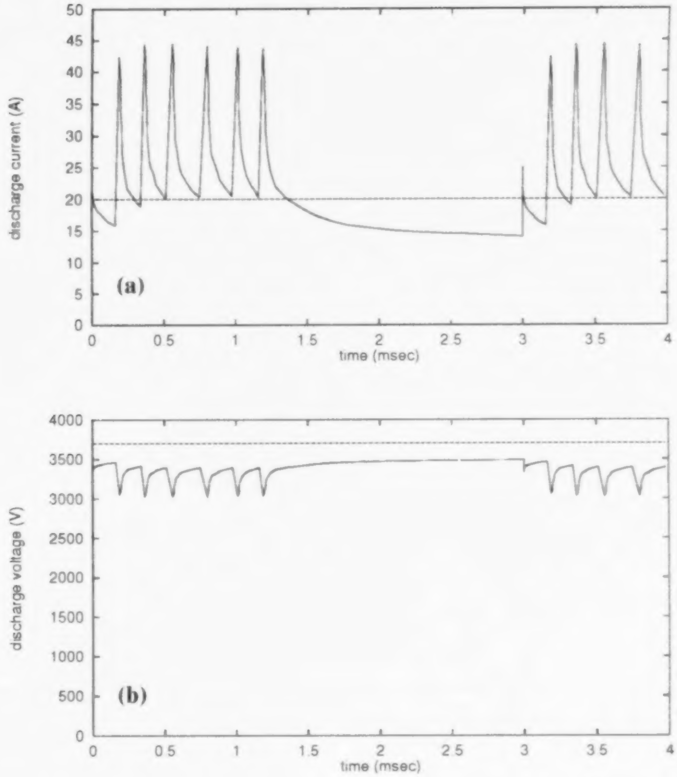

Figure 4.2-1 Typical PIE-III discharge waveforms: (a) voltage; and (b) current, for a burst frequency of 330 Hz. The average discharge current is 20 A [dashed line in (a)], and the sustainer voltage V_{sst} is estimated to be 3700 V [dashed line in (b)]. The current waveform is scaled from data in Nikumb *et al.*, [1-3] and the voltage waveform is derived from it. A ballast resistance of 15 Ω is assumed.

the direction of gas flow), and 3 m long (parallel to the optic axis), for a total discharge volume of about 50 L. [3]

The excitation circuit of PIE-III was given in Figure 1.2-2, which illustrates both the sustainer and pulser circuits fundamental to the PIE process. A typical PIE-III current response under burst-mode excitation is shown in Figure 4.2-1(a), as measured by Nikumb *et al.* In burst-mode operation, the stream of photo-ionizing and avalanching impulses which under CW-excitation occurs continuously at the pulser frequency, are instead gated so that bursts of N impulses occur at a burst repetition rate of f_b. In the case of Figure 4.2-1, there are 7 pulses per burst and the pulser frequency is 5 kHz. This same burst configuration was used for all instability experiments performed by Nikumb *et al.* (Note that for 7 pulses per burst, CW operation corresponds to f_b=715 Hz.) In Figure 4.2-1(a), the discharge current is seen to decrease strongly following each impulse event. This effect is primarily due to decay of the high plasma density which had been established by the impulse photo-ionization and avalanche.[†] The sustainer isolation inductors (*cf.* Figure 1.2-2) were sufficiently small (0.2mH) that the they did not significantly affect the rate of current decay.[‡] In between bursts, the discharge is seen to asymptotically approaches a steady self-sustained state. As will be discussed in Section 4.3.1, this steady state is determined by the sustainer voltage (V_{sst}), ballast resistance (R_b), and discharge impedance characteristic.

Not indicated in the circuit diagram (Figure 1.2-2) is that the PIE-III sustainer voltage supply was filtered with a 0.5 mF capacitor. This capacitance reduced the power supply ripple during burst-operation to negligible levels. Estimated discharge voltage is indicated in Figure 4.2-1(b).[*]

4.2.2 Enhanced Discharge Stability

In experiments with PIE-III, Nikumb *et al.* [1-4] observed that at intermediate burst rates, considerably more power could be extracted from the discharge prior to the onset of instability than was possible for either low burst rates or CW operation. It was also observed that discharge stability was worst at low burst rates. These results are illustrated in Figure 4.2-2, which shows the maximum achievable laser power as a function of f_b. Attainable laser power was doubled relative to maximum possible under CW excitation by operating at a burst repetition rate of 500 Hz. This doubling of laser power was achieved without any optimization. Moreover, the maximum power at 500 Hz was constrained by power supply limitations, not by discharge instability.

Enhanced laser performance at intermediate burst rates appears to be due to increases in both laser efficiency and discharge stability. Laser input power was not recorded in the initial experiments, however estimates suggest that decreasing the burst rate from CW to 500 Hz allowed an increase in input power of 40%. Hence, to achieve the observed 100% increase in laser output power, device efficiency must also have increased by 40% relative to CW operation. It may be hypothesized that the increase in laser efficiency at intermediate burst-rates is due to the higher reduced field strengths required to sustain a discharge. The cause of enhanced discharge stability will be the focus of the remainder of this chapter.

[†] There is now some concern that the Rogowski coils used by Nikumb *et. al.* [1-3] to measure the current did not accurately represent the current PIE-III waveform – specifically that the strong current decay observed following an impulse event was in part an artifact of the detector, and not representative of the actual current response. Unfortunately, this problem was not recognized until long after PIE-III was dismantled. The problem of more accurately determining the discharge current waveform will be addressed in Chapter 5 for the PIE-IV device.

[‡] Note that this conclusion is based on the waveform of Figure 4.2-1(a). If, for example, the variation of current amplitude over a burst period were much larger (*i.e.*, more rapid), then the inductor characteristic response time would become larger than that of the plasma decay, and would therefore be expected to significantly affect the current waveform.

[*] This voltage must be estimated, since neither the average sustainer voltage nor its waveform were recorded in the initial experiments.

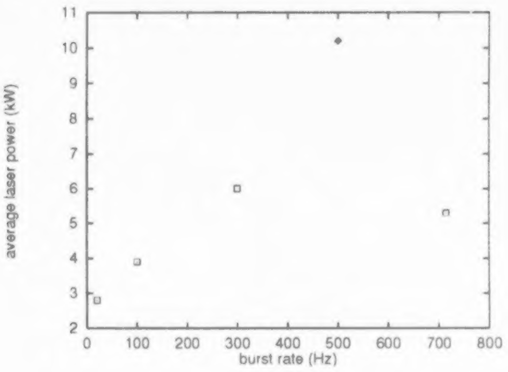

Figure 4.2-2 Laser output power at the onset of instability, as a function of burst rate. Number of pulses per burst is held constant at 7. From experiments of Nikumb *et al.* [1,3] on PIE-III. In the 500 Hz case, maximum power was constrained by power supply limitations, not the onset of instability.

4.3 Definition of Problem

The objective of this chapter will be to identify mechanisms which could produce the stability characteristic of Figure 4.2-2; *i.e.*, mechanisms which stabilize intermediate burst rates relative to CW operation, and mechanisms which destabilize low burst rates relative to intermediate burst rates. Prior to describing the numerical model developed for this purpose, in the following section some background topics will be addressed. In Sections 4.3.1 and 4.3.2, overviews of discharge processes and instability are given. In Section 4.3.3, the available options for instability analysis are briefly summarized, and a mode of analysis appropriate for the present problem is selected.

4.3.1 CO_2 Laser Glow Discharges

Here, a brief characterization is given of the glow discharges used to excite gain in typical CO_2 EDLs. Plasma properties of the discharge are reviewed, with an emphasis on characteristic process rates. Knowledge of these is required for defining a tractable discharge model. Also reviewed are the conditions for self-sustained discharge operation, which may occur during the inter-burst of burst-mode excitation. (*cf.* Figure 4.2-1(a)).

Plasma Properties

Glow discharges employed in electric CO_2 lasers are characteristically weakly ionized, with an ionization fraction below 10^{-6}. The positive column region of the discharge is quasi-neutral, and in a highly non-equilibrium state. Temperatures of electrons, vibrational modes, and the gas are typically around 10,000, 2,000, and 300 K, respectively. In large volume devices, collisional processes (ionization, attachment, recombination, *etc.*), as opposed to transport (diffusion, thermal conduction, *etc.*), dominate plasma behavior in non-sheath regions. [6,10,28] Table 4.3-1

Table 4.3-1 Characteristic times of discharge processes for conditions typical of CW CO_2 lasers ($p \approx 10$-100 Torr, $T \approx 300$-500 K, $E/n \approx 30$ Td, $T_e \approx 1.0$ eV, $T_v \approx 2000$-5000 K, $n_e/n \approx 10^{-8}$). For transport processes, the characteristic disturbance size was taken to be 1 cm. After Haas [6] and Raizer [26].

Process	Characteristic time range of values (sec)
Space-charge relaxation	10^{-10}- 10^{-9}
Collisional energy transfer	
electron temperature relaxation	10^{-9}- 10^{-8}
translation-rotation heating	10^{-3}- 10^{-2}
vibration heating	10^{-3}- 10^{-2}
vibrational relaxation	10^{-4}- 10^{-2}
Plasma kinetic processes	
direct ionization	10^{-5}- 10^{-4}
electron attachment	10^{-6}- 10^{-5}
electron detachment	10^{-6}- 10^{-5}
electron-ion dissociative recombination	10^{-4}- 10^{-3}
ion-ion recombination	10^{-4}- 10^{-3}
electronic excitation	10^{-6}- 10^{-4}
Transport and other processes	
sound propagation	10^{-5}- 10^{-4}
translation-rotation energy conduction	10^{-3}- 10^{-2}
viscous dissipation	10^{-3}- 10^{-2}
vibrational energy conduction	10^{-2}- 10^{-1}
electron thermal conduction	10^{-5}
ambipolar diffusion	10^{-2}

summarizes for a typical CO_2 laser discharge the characteristic times of important plasma processes. These are seen to be spread over a broad range (10^{-10} to 10^{-2} sec).

Discharge Equilibrium State

A host of plasma chemical interactions, in conjunction with the discharge circuit, determine the discharge transient response and equilibrium positive column ionization fraction. The reactions which directly affect electron density are: attachment and electron-ion recombination (loss processes); and ionization and detachment (gain processes). These reactions proceed at rates

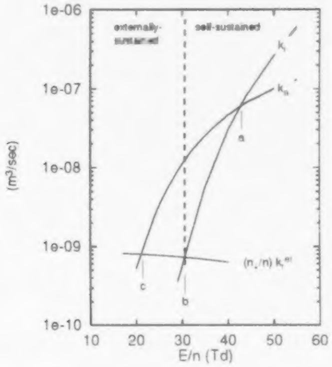

Figure 4.3-1 Illustrative comparison of electron rate coefficients for ionization (k_i), attachment (k_a) and recombination (k_r^{ei}) for representative discharge conditions. Detachment rates determine which of the electron loss processes (recombination or attachment) dominates. The weighted recombination coefficient is typical of an ionization fraction of 10^{-8}. Rate coefficients for attachment and ionization are from the ELENDIF solutions of Chapter 6, while that for electron-ion recombination is for O_2^+. (Figure after [8].)

dependent on the discharge state and chemical composition. Figure 4.3-1 presents illustrates rate coefficients for a PIE gas mixture. Self-sustained discharge operation is possible for the range of E/n between a and b. Point a corresponds to the equilibration point where attachment-dominated electron loss, whereas point b corresponds to that for recombination-dominated loss. Where in the range equilibration rests depends on the relative importance of detachment (which offsets electron attachment). An important molecule in this respect is CO, which is usually present in significant concentrations either as an additive or as a disassociation product of CO_2. CO is a very effective detaching agent, so the discharge operating point and transient responses will be greatly influenced by the amount of CO present in the discharge.

In the limit of weak detachment, electron-loss is attachment-dominated, so equilibrium occurs when attachment balances ionization;

$$k_i(E/n) = k_a(E/n). \tag{4.3-1}$$

This equilibrium occurs at 40-50 Td[†] for a typical PIE mixture. With attachment-dominated electron loss, the self-sustained ionization fraction is determined by the external circuit.

In the limit of strong detachment, in which electron-loss is recombination-dominated, the equilibrium condition is

$$\frac{n_e}{n} = \frac{k_i(E/n)}{k_r^{ei}(E/n)}, \tag{4.3-2}$$

[†] The Td (Townsend) is a commonly used measure of reduced field (E/n): $1\,\text{Td} \equiv 10^{-21}\,\text{Vm}^2$.

so that both the E/n required for self-sustained operation and the equilibrium ionization fraction are determined by the external circuit. An ionization fraction of 10^{-8} corresponds to $E/n \approx 30\text{Td}$. Current waveform measurements analogous to Figure 4.2-1(a) under conditions of lower sustainer voltage suggest that the PIE-III discharge must be recombination-dominated, since self-sustained discharge operation in the inter-burst interval is attained for discharge E/n well below 40 Td.

Equilibrium E/n below point b are accessible only when an external electron source supplements electron-impact ionization. Discharges sustained at an E/n below point c necessarily have recombination-dominated electron loss, regardless of the importance of detachment.

4.3.2 Discharge Instability

Glow discharges in CO_2 lasers must be in a highly non-equilibrium state in order to establish a population inversion amongst the vibrational modes. It isn't surprising then that at power loadings of interest in gas lasers, continuous discharges are found to be inherently unstable in the presence of small disturbances

Discharge response to a disturbance may be represented as a superposition of collective modes (sound, thermal, ionization, *etc.*). [6,28] These plasma modes are continuously excited by random disturbances typical of the discharge mechanisms. In stable discharges, these modes are damped by collisional and transport processes and do not ultimately affect the discharge state. In laser discharges however, which are highly non-equilibrium in nature, conditions are typically such that some collective modes experience sustained amplification. If growth of such collective modes is not quenched, then they will ultimately become sufficiently large to disrupt the discharge state. In this case, the discharge state will deteriorate from an initially relatively uniform state to a highly non-uniform one. In CO_2 laser discharges, these instabilities are manifest in two forms: discharge striation, and discharge constriction. [10,26,29]

Striations are plasma-density waves which propagate *parallel* to discharge current. They are an ionization instability caused by the relative magnitude and temperature dependence of the dissociative attachment and ionization rate coefficients for electrons. [8,10] They tend not to inhibit a glow discharge, but do reduce the E/n required for self-sustained operation, [30] and cause modulated laser output. Occurrence of striations does not explicitly depend on discharge power density. *Constriction*, in contrast, is caused by an instability which propagates *perpendicular* to current flow, and which causes the normally diffuse current of a glow discharge to collapse into an intense arc. [10,11] Occurrence of this glow-to-arc transition depends directly on thermal heating. Hence, it imposes an upper limit on the electrical pump power density attainable in a stable discharge. [31] Constrictions convect with gas flow, and so may be swept from the discharge area by bulk gas flow. Striations may also affect the rate of discharge constriction by affecting the discharge state. [11]

The formation of filamentary arcs in steady glow discharges is not completely understood. It is believed to originate in the boundary regions of the discharge, where heating and spatial gradients are strongest, and to then rapidly propagate across the positive column. [32-34] The instability is known to be thermal in nature, being characterized by a regenerative condition which depresses the local density and elevates the local temperature of the heavy particles. [10,12] More specifically, Haas [6] first observed that characteristic times of plasma processes are spread over a wide range (*cf.* Table 4.3-1), resulting in an effective decoupling of the many possible response modes. Through a comprehensive normal mode analysis [35,36] of infinitesimal disturbances, Haas was able to then identify with discharge contraction the sound mode, thermal mode, and the vibrational relaxation mode. The growth rate of such instabilities is a complicated function of many factors, including most critically electron production and loss mechanisms, and the vibrational energy modes. [6] Much research has subsequently been built on Haas' first analysis. Yet although instability mechanisms for infinitesimal disturbances have been identified, no comprehensive theory exists for molecular gases which connects the growth of infinitesimal disturbances to arc formation.

In the following sections, brief overviews are given of the present understanding of thermal instabilities, and their growth in self-sustained, externally sustained, and impulse-sustained CO_2 laser discharges.

Thermal Instabilities

Figure 4.3-2 provides a qualitative illustration of how a molecular discharge responds to a local disturbance in gas temperature. An increase in gas temperature (T) results in a rapid depression of gas density (n) and concomitant local elevation of E/n.[†] As indicated in the figure, an effectively instantaneous increase in electron temperature (T_e) follows. Subsequent response of the electron density (n_e) to n, T, and $T_e(E/n)$ is complicated, since it depends on a myriad of electron creation and loss reactions. In a self-sustained discharge, electron creation increases far more strongly with E/n than does electron loss (*cf.* Figure 4.3-1). Hence, an increase in E/n will necessarily result in a large increase in n_e. In general, the response of n_e to disturbance in n is strong, and stronger for attachment dominated loss than for recombination dominated loss. In externally sustained discharges, n_e response is more complex, and may be either positive or negative. [11] Changes in both T_e and n_e then affect power deposition, which is divided mainly between vibrational excitation (process 1) and direct gas heating (process 2). Vibrational temperature (T_v), which is at quasi-equilibrium between T and T_e, responds according to the relative strengths of excitation due to electron-collisions, and relaxation due to neutral-collisions (process 3). The characteristic time for V-T relaxation (τ_{VT}) is a strongly decreasing function of gas temperature.

[†] The characteristic time for acoustic relaxation is much less than the characteristic times for collisional heating and vibrational relaxation. Consequently, the initial phase of instability formation does not generate pressure disturbances. Pressure disturbances cause large disturbances to develop more slowly. [37,12]

Figure 4.3-2 has been removed due to copyright restrictions. The information removed was Figure 1 from [11]

Figure 4.3-2 Simplified illustration of discharge response to a local disturbance in neutral density and temperature. All molecular vibrational modes are lumped together. Rapid causal relationships are indicated by solid lines, while dashed lines indicate slower feedback mechanisms which may result in thermal instability.The former processes are quasisteady on the timescale of the later, at least in the initial stages of a disturbance. The heavy line of process 1 indicates that electron-impact results in much stronger vibrational heating than is does in direct gas heating. (Figure reprinted from [11].)

Thermal instability results when the collisional feedback processes reinforce at least one aspect of the disturbance, and transport processes such as thermal conduction and electron diffusion are unable to dissipate the ensuing gradients. Two modes of instability have been found to be important in convection-cooled CO_2 laser discharges: a *vibrational-relaxation*-driven *thermal mode*, and an electron-driven *vibrational* mode. [7,10,11]

A vibrational instability occurs when the increment in vibrational heating exceeds that of V-T relaxation, and results in sustained escalation of T_v. For disturbances larger than a few millimeters, this mode is unstable for all conditions of interest to high-power convectively cooled lasers, regardless of whether the discharge is self- or externally sustained.[7,11] Growth rates depend critically on how strongly n_e responds to the initial disturbance, and are limited by collisional energy transfer (processes 1-3 in Figure 4.3-2), the slowest processes in the instability sequence. Formation times range from 1-10 ms for typical discharge conditions. In this connection, one of the major functions of gas flow is to sweep locally unstable fluid elements from the discharge region in a time less than is required for an instability to develop fully. As will be discussed in the following sections, the instability growth rate is a function of input power density (JE).[†] In convectively cooled lasers then, power deposition cannot be increased beyond the point where the time for instability formation is comparable to the gas residence time (τ_g).

[†] The discussion in references [26] and [38] of a threshold n_e for instability presumably follows from a similarity scaling paradigm; when increasing pressure while holding E/p constant, a constraint on maximum JE amounts to a constraint on J and therefore also on n_e. Hence the threshold n_e is not a fundamentally significant limit. Rather, it is derivative of the fundamental JE limit.

A vibrational relaxation instability occurs when the vibrational energy reservoir collapses through V-T relaxation, and results in a sharp decline in T_v and a sustained escalation of T. This instability does not depend directly on the response of n_e to the initial disturbance. Rather, it depends fundamentally on the degree of V-T non-equilibrium, and on the temperature dependence of V-T relaxation. A high degree of non-equilibrium, when combined with a V-T rate coefficient having a strong positive dependence on T, may allow V-T gas heating to overcome the stabilizing effect of pressure equilibration. The vibrational relaxation instability typically occurs at gas temperatures exceeding those normally found in the bulk regions of laser discharges. [7] It is believed that the vibrational instability is important in the initial stages of instability development, while vibrational relaxation instability is important in subsequent stages. [11]

Self-Sustained Continuous Discharges

As was discussed in Section 1.1.3, a discharge is self-sustained when the electric field strength is sufficiently large to maintain a steady current in the absence of an external ionizing agent. [39] Under such discharge conditions, instability growth time τ is a decreasing function of input power JE, the strength of which depends on the relative rate of V-T relaxation. In limiting cases, for when V-T relaxation is either rapid relative to instability growth or very slow, τ scales as:[12]

$$\tau \sim \begin{cases} JE^{-1} & \tau \gg \tau_{VT} \\ JE^{-1/2} & \tau \ll \tau_{VT} \end{cases}, \tag{4.3-3}$$

where τ_{VT} is the characteristic time for V-T relaxation, and the constants of proportionality are a complex function of the unperturbed discharge state.† Eqn. (4.3-3) suggests that discharge instability occurs once a gas heating threshold has been exceeded; gas heating is $\sim\tau$ when energy transfer from electrons to gas temperature is effectively instantaneous, gas heating is $\sim\tau^2$ when energy transfer from electrons to gas temperature occurs slowly via V-T relaxation.

At the instability threshold, discharge conditions in fast-transverse-flow CO_2 lasers typically correspond to neither of the limiting cases in (4.3-3), since the gas residence time $\tau_g \approx \tau_{VT} \approx \tau$. Specifically, in PIE-III the gas residence time was 3.6 ms, which is comparable to the estimated τ_{VT} of 5 ms at 300 K, and 2.5 ms at 500 K. [11] Both the experimental and the theoretical results of Nighan and Wiegand [7,9] suggest that when $\tau \approx \tau_{VT}$, an intermediate scaling is satisfied, as is indicated in Figure 4.3-3. The curves in Figure 4.3-3 are well described by [†]

---

† Eqn. (4.3-3) holds for disturbances of intermediate size, for which the instability growth rate is affected neither by pressure non-equilibrium nor damping due to thermal conduction. *i.e.*, $\lambda_t \ll l \ll c_s\tau$, where λ_t is the characteristic dimension of thermal conductivity, l is the characteristic disturbance size, and c_s is the speed of sound in the gas. When l is very small, pressure equilibration within the disturbance is essentially instantaneous. When l is large, transport mechanisms are ineffective over the time of instability growth. For intermediate l, both conditions may be satisfied. In experiments, instability filaments are observed to be several cm in diameter, a size for which this approximation holds. Note again that for large l, pressure non-equilibrium within the disturbances retards disturbance growth. [37,12]

$$\tau = A\,(JE)^{\hat{\tau}}. \tag{4.3-4}$$

It is helpful to interpret the exponent $\hat{\tau}$ as a measure of how sensitive the instability formation time is to changes in power density;

$$\hat{\tau} \equiv \left(\frac{JE}{\tau}\right)\frac{\partial\tau}{\partial JE}, \tag{4.3-5}$$

so that if for instance $\tau \sim JE^{-1/2}$, then $\hat{\tau} = -1/2$. For the results of Figure 4.3-3, $-1 \le \hat{\tau} \le -1/2$, as is summarized in Table 4.3-2.

The proportionality constant A is an increasing function of gas pressure and τ_{VT}, and a decreasing function of both the sensitivity of τ_{VT} to T, and how strongly electron density increases in response to a decrease in gas density. [12] The latter sensitivity is found to be increased by the presence of negative ions. Consequently, discharges with recombination-dominated electron loss process are found to be considerably more stable than those with attachment-dominated loss. [7]

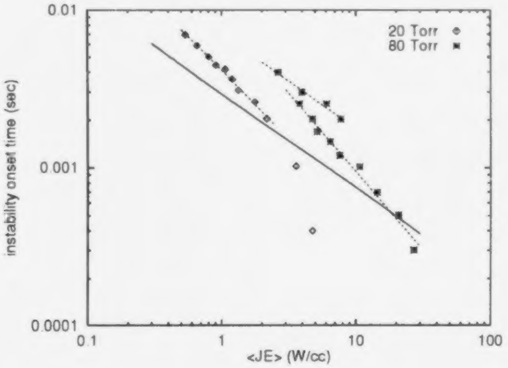

Figure 4.3-3 Characteristic times for discharge constriction in a steady self-sustained discharge. Theoretical predictions (solid line) for 20 Torr are from Nighan and Wiegand [7]. Experimental data is from Wiegand and Nighan [9] for gas mix He:N_2:CO_2 = 12:7:1. Both 80 Torr cases are with turbulent flow, induced with different generators. Parameters for best-fit functions (dashed lines) of form (4.3-4) are summarized in Table 4.3-2.

[†] Sorichetti suggests that these results should be fit by a function of form $\tau = \tau_0 \ln\,[P_0/\langle JE\rangle]$, where P_0 and τ_0 are the limiting power density and the characteristic instability growth time. [38] τ_0 is probably better identified with τ_{VT}. Moreover, the form of (4.3-4) is more consistent theoretical analysis of Nighan *et al.* Indeed, (4.3-4) produces a better fit to not only the data of Figure 4.3-3, but also to Sorichetti's results.

Table 4.3-2 Best-fit parameters for the experimental characteristics summarized in Figure 4.3-3, for fits of form (4.3-4) where JE is in W/cm^3 and τ is in msec.

pressure (Torr)	A	$\hat{\tau}$
20	4.1	- 0.9
20 (theory[7])	4.3	- 0.7
80	7.0	- 0.6
80	9.2	- 1.0

Externally Sustained Continuous Discharges

As was discussed in Section 1.1.3, a discharge is said to be externally sustained when its ionization fraction is supplemented by external sources (*e.g.*, injected high energy electrons, photoionization by UV radiation). Such discharges are found to be considerably more stable than self-sustained discharges, in addition to having another degree of freedom for optimization. The dependence of instability growth time on *JE* is the same as for self-sustained discharges (4.3-3). However, typical constants of proportionality are an order of magnitude larger. [26]

The primary reason for using external ionization is to reduce the dependence of the plasma state on low energy electron impact ionization, which is extremely sensitive to variations in electron temperature. External ionization reduces sensitivity of electron-density disturbances in T_e, by making the ionization rate sensibly independent of the local discharge state and history. However, while electron production may be less dependent on T_e, the sensitivity of electron loss may remain. This complicates instability analysis, because detailed knowledge of the important electron loss processes and their temperature dependence is required. The electron response may be either positive or negative, depending on which electron loss process is dominant. For this reason, transient response to disturbances in externally sustained discharges is expected to be highly inhomogeneous. [11]

It is desirable for sake of stability that both electron production and loss processes be relatively insensitive to disturbances in T_e, so that the feedback response to a local depression in n is weak. If detachment reactions are weak, E/n must be kept below point c in Figure 4.3-2 if the plasma is to be recombination dominated. For a discharge state between b and c, which is accessible only to externally sustained discharges, electron loss remains a strong function of E/n.

Impulse-Sustained Continuous Discharges

An intermediate category between self- and externally sustained discharges are impulse-sustained discharges. In this scenario, a rapid sequence of voltage impulses are applied to the discharge in conjunction with a DC pumping voltage. [40] During the impulses, the amplitude of which considerably exceeds that of the DC voltage, sufficient electron-impact ionization occurs to sustain an ionization fraction much higher than would be possible with the DC voltage alone. Raizer *et al.* [41] showed that this excitation configuration is potentially much more stable than a simple self-sustained discharge. This is possible because the sensitivity of the ionization rate to electron temperature $\hat{k}_i \equiv \partial \ln (k_i) / \partial T_e$ decreases with electron temperature. The response of electron-creation to a disturbance will be governed by the ionization rate averaged over the impulse repetition period.† Under conditions of similar power loading (*JE*), the time-averaged sensitivity $\langle \hat{k}_i \rangle$ in the impulse-sustained discharge will be lower than the sensitivity $\hat{k}_i$ of the self-sustained discharge. Hence, the electron response to density perturbations in an impulse-sustained discharge will be weaker than those in a self-sustained discharge. In this way, the stability of an impulse-sustained discharge can be comparable to that of an externally sustained discharge. [41]

Summary

Externally sustained discharges are potentially much more stable than self-sustained discharges, while the stability of pulser sustained discharges can approach that of an externally sustained one.

The PIE excitation system is either externally sustained or impulse-sustained, depending on the relative importance of photoionization during the impulse event. Given these observations, one may anticipate *a priori* that a PIE discharge should be less stable at low burst rates than it is at high burst rates. In Figure 4.2-1, the discharge state is seen to approach self-sustained conditions in the inter-burst interval. As the burst rate is decreased while the sustainer voltage is held constant, the discharge asymptotically approaches purely self-sustained conditions.

4.3.3 Methods of Discharge Stability Analysis

A variety of treatments exist in literature of instability growth in short-pulse or steady discharges, however there are no treatments of intermediate scenarios such as the PIE discharge, where many assumptions are not possible which would in the other cases simplify analysis. Traditional normal mode analysis, [35,36] which allows one to analyze the stability of a stationary state subject to an infinitesimal perturbation, is not applicable to burst-mode discharge conditions because they are non-steady on the time scale of instability growth. For normal mode-analysis to be applied to a non-steady discharge, either the discharge state must oscillate so rapidly that it may be considered quasi-steady on the timescale of instability growth, or it must change so slowly that it may be considered frozen while the instability grows. The analysis of impulse-sustained discharge stability by Raizer *et al.* [41] is an example of the former approximation, whereas the analysis of externally sustained discharges by Nighan [11] is an example of the later.

It is not clear *a priori* that either limit is applicable to the PIE discharge. One possible scenario is that instability grows rapidly during the burst pulsing interval, and then relaxes during the inter-burst interval. In this case, although the *net* instability growth rate would be limited by the gas residence time, the *peak* growth rate, occurring during the burst, would proceed at a rate comparable to the rate of unperturbed state change. Then the changing discharge state would interact directly with the instability growth rate. To study instability growth in a PIE discharge, a simulation approach was chosen over a perturbation method because of its inherently comprehensive nature, and because it readily allowed the non-linear growth of finite-amplitude disturbances to be modelled.

---

† This holds so long as the instability growth occurs much more slowly than the impulse-induced variations in the plasma state.

A simulation sufficiently general to allow exploration of a wide parameter-space was required because the experimental conditions could not be inferred in detail from the results of Nikumb *et al.* [1-3] Moreover, additional experiments to attain the required information were not possible because they jeopardized the laser apparatus. If, with the simulation, the burst-mode stabilization effect could be observed throughout the region of parameter space likely inhabited by PIE-III, that would be an indication of the simulation representing the actual experimental condition.

So it was necessary to create a model sufficiently general to explore a wide parameter-space, yet the computational complexities of the problem demanded numerous simplifying assumptions. A 2D+time simulation of discharge evolution was not computationally tractable, so the simulation was limited to 1D+time. In 1D, thermally instability can be treated in only one of either the sheath regions or the positive column region. A model of the positive column discharge region was chosen, assuming that the rate of arc formation (filamentation) is limited by the time required to form a channel of depressed density in the positive column.

Section 4.4 describes CODE1, the 1D positive column filament model developed to study thermal instability growth in a PIE discharge.

4.4 CODE1: 1D Positive Column Filament Model

CODE1 was developed as the first in an intended sequence of models to investigate PIE discharge stability. It models in 1D the positive column of a non-steady discharge, and may be used to study the response of the discharge to a disturbance. A cylindrical discharge volume is considered, axially symmetric and longitudinally uniform. The instability is seeded with a small on-axis density depression specified in the initial conditions. Its growth is then monitored as the discharge evolves under PIE excitation – a uniform E-field and periodic impulse events. The positive column is modelled as a weakly ionized quasi-neutral collision-dominated plasma of four fluids: neutral particles, electrons, negative ions, and positive ions. The neutral fluid is viscous, compressible, and has one vibrational energy mode.

CODE1 is described at greater length in Sections 4.4.1 through 4.4.3: Section 4.4.1 details simplifying assumptions, Section 4.4.2 gives the governing equations, and Section 4.4.3 describes their numerical implementation. Representative simulation results and a discussion of possible mechanisms responsible for the burst-mode stabilization effect are given in Section 4.4.4. Sections 4.4.5 and 4.4.6 present an evaluation of CODE1 and a summary of conclusions, respectively.

4.4.1 Simplifying Assumptions

Behavior of a PIE laser discharge is determined by a multitude of chemical and vibrational interactions, in addition to the complexities of fluid and plasma dynamics. To create CODE1, simplifying assumptions were required both to facilitate analysis and to make the model computationally tractable. Those related to geometry, the discharge circuit, and internal discharge processes are outlined in the following section. The intent of these simplifications was to considerably simplify analysis while retaining the essential problem features.

Model Geometry

The transverse-flow geometry utilized in PIE lasers is illustrated in Figure 4.4-1. Convective flow, discharge current, and the optical axis are all mutually perpendicular. Unperturbed flow and discharge properties are uniform along the optic axis, and so are essentially two dimensional. However, a 2D simulation is not yet computationally tractable. Conveniently, in a first approximation, variations in the positive column may be taken as one dimensional. Transport processes are sufficiently slow that large gradients are confined to relatively narrow regions adjacent to the electrodes. Away from the electrodes, the discharge properties vary smoothly. Within the positive column, longitudinal (*i.e.*, in the direction of current flow) variations in discharge are small, [42,43] as are those in gas flow properties. [44] In contrast, significant transverse (*i.e.*, in the direction of gas flow) gradients do arise as the flow is heated while convecting through the discharge. [44] Thermal instability growth is also strongest in the transverse dimension. [10] Thus a 1D model is justified which resolves transverse variations and which assumes uniformity in the longitudinal dimension (z) direction.

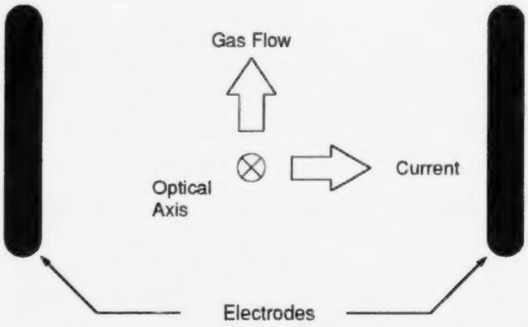

Figure 4.4-1 Geometry of a transverse flow device.

To further simplify CODE1, the effects of gas flow are neglected. Local gradients due to gas flow are assumed to be small relative to those generated by instabilities. Wassertrom and Crispin [45] suggest that the primary effect of gas flow, especially when it is turbulent, is to modify the transport coefficients such as ambipolar diffusion and thermal conductivity. Hence, CODE1 models growth of a uniform filament in a stationary cylinder of gas. The instability filament is axially symmetric and longitudinally uniform, with the imposed electric field lying along the z-axis.

It should be noted that in any 1D discharge model, the electrodes are effectively modelled as uniform potential surfaces. This means in the case of PIE discharges that the inhomogeneous excitation by the multi-pin electrode blocks (which to some extent adapt to suit local discharge conditions) cannot be accounted for. If the instability scale size were considerably smaller than the inter-pin spacing, then the electrode is would be effectively continuous. However, the instability size is expected to be comparable to the inter-pin spacing.

Discharge Circuit

Simplification of the discharge circuit is also in order. Regarding the sustainer circuit, the 500 μF filter capacitor in the voltage source allows it to be well modelled as ideal. The sustainer circuit then reduces to the supply in series with the discharge and ballast resistors. Effects of the sustainer isolation inductors on the discharge current may be neglected, given the inductor size and the current decay rate (*cf.* Section 4.2.1). The fluid ballast is modelled as a constant resistance. Although its resistance is known to depend on the average current density, [27,47] its transient response has not yet been investigated. Regarding the pulser circuit, its effect on the discharge state is modelled as an effectively instantaneous combination of photo- and avalanche-ionization coinciding with the pulser event. This pulser model will be developed in greater detail later in Section 4.4.2: *Pulser Events.*

The anode and cathode sheath voltages are known to depend on current density [26] and pulser conditions, [46] although the details of this dependence are unknown. At current levels corresponding to the instability threshold, the total sheath voltage is expected to be comparable to the ballast voltage. [46] Both voltages are expected to be increasing functions of discharge current, so in this first approximation, they are taken to be subsumed by the ballast resistance.

Discharge Kinetics

Some simplifying assumptions regarding discharge kinetics are also required to make modelling of the positive column tractable. Following the works of Haas [6] and Nighan [11], the multitude of chemical species in the discharge are modelled as a single diatomic molecular species in an atomic diluent. It is also assumed that the gas energy state may be characterized by just two Boltzmann temperatures: a translational-rotational temperature and a single vibrational temperature. These simplifications retain the essential discharge features provided that [6,11]:

- collision induced intra-mode V-V relaxation is sufficiently rapid that each vibrational and rotational mode may be characterized by a Boltzmann temperature.

- the CO_2 asymmetric stretch mode (upper laser level) and the N_2 vibrational mode are strongly coupled, and so constitute a single vibrational level at a temperature T_v.
- the symmetric stretch and bending modes of CO_2, and all rotational levels of CO_2 and N_2 are in thermodynamic equilibrium with the ambient gas temperature T.[†]

All of these conditions are known to be approximately valid for disturbances in steady discharges. [10,11] An inspection of rate coefficients [29,48-50] suggests that they should be similarly applicable to a PIE discharge. Preliminary estimates of PIE vibrational kinetics with the code TLASER [51] corroborate these assumptions. Additional assumptions made by CODE1, but which are more tenuous, are:

- reactions involving excited states are neglected (for example multistep ionization), as are the effects of excited states on discharge reaction rates.
- ionic reactions are assumed to be dominated by two species: one cation and one anion.
- vibrational modes other than those of CO_2 and N_2 do not fundamentally alter vibrational kinetics, and may be neglected. In particular, CO may violate this assumption. It is present in significant quantity in PIE discharges.
- effects of stimulated emission are neglected. Coupling between the CO_2 vibrational levels and the laser optical field is expected to exert a stabilizing influence on the discharge because it limits vibrational temperature rise. [38]

4.4.2 Governing Equations

The discharge governing equations used by CODE1 consist of the Navier-Stokes equations, [52] supplemented to describe a collision-dominated weakly ionized plasma. [6,11,53,54].

If impulses may be treated as instantaneous events, proper treatment of discharge processes relevant to instability and PIE excitation dynamics requires resolving the timescale range 10^{-7}-10^{-2} sec (*cf.* Figure 4.2-1 and Table 4.3-1). Faster processes may be taken as quasisteady, and slower process as frozen. Both space charge relaxation and electron heating are quasisteady on this timescale, and vibrational energy conduction is frozen. The behavior of all other processes must be resolved. In the remainder of Section 4.4.2, the governing equations solved by CODE1 are developed. Also discussed are the simplified pulse event and gas chemistry models used by CODE1. The section concludes with a summary model coefficients.

[†] V-T relaxation therefore effectively occurs via the V-V relaxation process $CO_2(001)+M \rightarrow CO_2(lm0)+M$, and excitation of the $CO_2(lm0)$ modes is effectively direct gas heating.

Maxwell's Equations

Space charge relaxation is rapid (requiring less than 1 ns) on the timescales of interest, so the plasma is effectively quasineutral. Magnetic effects in a PIE laser discharge are also negligible, due to the limits of discharge size, peak current and excitation frequency bandwidth. Maxwell's equations therefore reduce to

$$\nabla \bullet \boldsymbol{J} \approx 0 \qquad \nabla \times \boldsymbol{E} = 0, \tag{4.4-1}$$

where $\boldsymbol{E}$ is the electric field strength, and $\boldsymbol{J}$ is the total current density. These specify the electric field on two spatial scales. For feature sizes smaller than a Debye length (typically 10-100 μm), the radial electric field, which maintains quasineutrality, constrains the transverse electron and ion currents to balance (*i.e.*, establishes ambipolar diffusion). For larger features, the electric field is irrotational. Consequently, as is required by symmetry, the radial field vanishes since the longitudinal field is uniform. The 2D positive-column model of Galeev *et al.* suggest that this radial field accounts for only a few percent of the total reduced field. [55]

The total current density

$$\boldsymbol{J} = \boldsymbol{J}_e + \boldsymbol{J}_+ + \boldsymbol{J}_-, \tag{4.4-2}$$

where $\boldsymbol{J}_e$, $\boldsymbol{J}_e$, and $\boldsymbol{J}_e$ are the current densities due to electrons, positive ions, and negative ions, respectively. On macroscopic scales $\boldsymbol{J} \approx \boldsymbol{J}_e$, due to the much higher mobility of electrons.

Electron Energy Balance

Local electron behavior is sufficiently collision-dominated that, in the absence of strong gradients, electron temperature is determined solely by the local field strength and discharge conditions. [42] Subsequent to a disturbance, relaxation of electron temperature to equilibrium with local conditions requires 10-100 ns.† For longer times, the energy equation for electrons reduces to an effectively instantaneous balance between energy imparted to the electrons by the electric field, and energy lost through collisions:

$$\boldsymbol{J}_e \bullet \boldsymbol{E} = n_e v_u k_B T_e, \tag{4.4-3}$$

where the electron current

$$\boldsymbol{J}_e = e n_e \mu_e \boldsymbol{E} = \frac{n_e e^2}{m_e \nu_m} \boldsymbol{E}, \tag{4.4-4}$$

and where v_u and ν_m are the collision frequencies for electron energy exchange and electron momentum transfer. These collision frequencies, and all other electron related coefficients for transport and reaction rates, must be derived from the electron energy distribution function

---

† Note that the time required for the entire EEDF to reach equilibrium may considerably exceed the *average* electron relaxation time. Because of the dominant influence of low-energy inelastic collisions in molecular gases, this is less likely to occur in molecular gases than in atomic. [8]

(EEDF). [56] Due to the prominence of inelastic electron-molecule collisions, the EEDF deviates significantly from Maxwellian, [57] and so must be obtained through direct solution of Boltzmann's equation, as will be done in Chapter 6. On the timescales of interest here, the EEDF reaches equilibrium with the local *E*/*n* on a quasisteady basis, assuming that the effects of spatial gradients are small enough to be neglected. [42]

Neutral Particles

Discharge flow properties are dominated by neutral particle behavior, due to the very low discharge ionization fraction ($<10^{-6}$). Equations expressing conservation of mass, momentum, translational energy, and vibrational energy are, respectively: [6]

$$\frac{\partial}{\partial t}\rho + \nabla\bullet(\rho \boldsymbol{u}) = 0, \tag{4.4-5}$$

$$\frac{\partial}{\partial t}(\rho \boldsymbol{u}) + \nabla\bullet(\rho \boldsymbol{u}\boldsymbol{u} + p\boldsymbol{I}) = \eta\nabla^2 \boldsymbol{u} + \frac{1}{3}\eta\nabla(\nabla\bullet \boldsymbol{u}), \tag{4.4-6}$$

$$\begin{aligned}\frac{\partial}{\partial t}(n\xi_T) + \nabla\bullet(n\xi_T \boldsymbol{u}) + p\nabla\bullet \boldsymbol{u} = \\ n_e n\frac{\nu_T}{n}(T_e)k_B T_e + \frac{f_m n}{\tau_{VT}(T)}[\xi_V(T_V) - \xi_V(T)] + \kappa\nabla^2 T + \Phi(\boldsymbol{u}),\end{aligned} \tag{4.4-7}$$

$$\begin{aligned}\frac{\partial}{\partial t}(f_m n\xi_V) + \nabla\bullet(f_m n\xi_V \boldsymbol{u}) = \\ n_e n\frac{\nu_V}{n}(T_e)k_B T_e - \frac{f_m n}{\tau_{VT}(T)}[\xi_V(T_V) - \xi_V(T)],\end{aligned} \tag{4.4-8}$$

where the state variables are: the local electron density (n_e) and temperature (T_e), and the local gas density (n), mass-average velocity ($\boldsymbol{u}$), translational-rotational temperature (T), and vibrational temperature (T_V). Mass density (ρ) is $\rho = m_{av}n$, where m_{av} is the average particle mass. Thermodynamic pressure (p) and average translational-rotational energy per particle (ξ_T) for an ideal gas are

$$p = nk_B T \qquad \xi_T = m_{av}c_v T, \tag{4.4-9}$$

where c_v is the specific heat at constant volume. The molecular gas fraction f_m is also characterized by the average vibrational energy per molecule

$$\xi_V(T) = \frac{\varepsilon}{e^{\varepsilon/(k_B T)} - 1}, \tag{4.4-10}$$

where ε is the quantum of vibrational energy for the single vibrational mode.

The functional dependence of coefficients on the state variables has been indicated in (4.4-5) - (4.4-8). Kinematic viscosity (η) and thermal conductivity (κ) are approximated as uniform and independent of temperature. $\Phi(\boldsymbol{u})$ is the viscous dissipation function. [52] Conduction of vibrational energy is neglected, because it is frozen on the timescale of interest. [6,29] The characteristic time for vibrational relaxation (τ_{VT}) is T-dependent, and may be defined in terms of k_{VT}, the mixture-weighted rate coefficient for V-T energy relaxation [11,29]:

$$\tau_{VT} \equiv n k_{VT}(T) . \tag{4.4-11}$$

The quantities v_T and v_v appearing in the electron-molecule power transfer terms are the T_e-dependent collision frequencies for gas translational heating and vibrational excitation, respectively. They are related by definition to electron-molecule power transfer fractions, in analogy to (4.4-3). For example, if F_{T} is the fraction of total Joule heating (JE) resulting in direct gas thermal heating, then

$$F_T JE \equiv n_e \nu_T k_B T_e . \tag{4.4-12}$$

Note that since $\boldsymbol{J} \approx \boldsymbol{J}_e$, the contribution of ion heating to JE is negligible.

Charged Particles

Also crucially important in discharge dynamics are charged particle reactions, most notably the electron production and loss processes. On time scales of interest, conditions of quasineutrality hold, so only two conservation equations need be considered. Those for electron density (n_e) and negative-ion density (n_-) are:

$$\begin{aligned} \frac{\partial}{\partial t} n_e + \nabla \bullet (\boldsymbol{u} n_e) &= \\ & n n_e k_i (T_e) - n n_e k_a (T_e) + n n_- k_d (T_e) - n_+ n_e k_r^{ei} (T_e, T) \\ & + n S(t) + D^a{}_e \nabla^2 n_e , \end{aligned} \tag{4.4-13}$$

$$\begin{aligned} \frac{\partial}{\partial t} n_- + \nabla \bullet (\boldsymbol{u} n_-) &= \\ & n n_e k_a (T_e) - n n_- k_d (T) - n_+ n_- k_r^{ii} (T) + D^a{}_- \nabla^2 n_- , \end{aligned} \tag{4.4-14}$$

where $n_+ \approx n_- + n_e$ is the positive-ion density, and the rate coefficients are for: single-step electron impact ionization (k_r^{ei}); dissociative attachment (k_a); electron-ion recombination (k_r^{ei}); detachment (k_d); and ion-ion recombination (k_r^{ii}). All rate coefficients are understood to be mixture-weighted, so that for a particular process

$$k = \sum_j f_j k_j , \tag{4.4-15}$$

where f_{j} and k_{j} are the jth species fractional concentration and rate coefficient. $S(t)$ represents a source of external ionization, which is time dependent in the PIE excitation system. In the quasi-neutral approximation, charged-particle transport is determined by the ambipolar diffusion coefficients $D^a{}_e$ and $D^a{}_-$.[†] Because the discharge is weakly ionized and collision-dominated, neutral particles determine the convective behavior of charged particles.[‡]

[†] Note that Haas [6] uses $(D_e/n)\nabla^2\,(n n_e)$ to describe electron diffusion. How this definition would affect ambipolar diffusion is not clear.

Pulser Events

Modelling of the impulse event is problematic. First, although impulse amplitude and rise-time are known to affect UV generation, the actual relationship is unknown. Modelling of the avalanche ionization during the rapid impulse (100ns) is also difficult because the EEDF may not be in local equilibrium. For these reasons, the impulse event is not resolved by CODE1. Instead, it is treated as an instantaneous event which augments local electron density n_e by

$$\Delta n_e = \left(\frac{S}{k_i} + n_e\right)\left(e^{nk_i t_i} - 1\right), \tag{4.4-16}$$

where S and k_i are the rate coefficients for photoionization and electron-impact ionization, respectively. The photoionization is due to UV radiation generated by rapid corona on the electrode pin tips [19], and the rapid electron-impact ionization is due to the elevation of E/n during the voltage impulse. As a first approximation in (4.4-16), both forms of ionization have been taken as constant over the impulse duration t_i. Equation (4.4-16) follows from (4.4-13); at high E/n, electron loss processes may be neglected, provided that the gas remains weakly ionized.

An upper bound on the photoionization fraction created by each impulse may be estimated by assuming that all impulse energy is expended in photoionization. Little power is dissipated in the fluid ballast, because the signal is able to couple through the electrode structure capacitively. Studies of UV absorption in CO_2 laser gas mixes have found that most photoionization is due to direct ionization of an impurity with an ionization threshold in the 10-11 eV CO_2 absorption window. [16,18,21] It follows then that an ionization fraction of *at most* 10^{-6} could have been created in the experiments of Nikumb *et al.* [3] (65 mJ deposited in 50 l of discharge at 300 K and 30 Torr). For the discharge conditions of Figure 4.2-1, the peak ionization fraction is estimated to be in the range 1-5 10^{-8}.

An upper bound on $nk_i t_i$ may also be estimated from Figure 4.2-1. The discharge current is seen to vary by about a factor of 2.5 between impulses, suggesting an upper bound of about 1.5 on $nk_i t_i$. This limit should be most strongly a function of impulse power, while only weakly dependent on the sustainer voltage. To properly model the effect of electron-impact ionization during an impulse, the dependence of k_i on E/n must also be estimated. As was discussed in Section 4.3.2: *Impulse-Sustained Continuous Discharges*, that k_i is a weaker function of E/n at high E/n is a stabilizing factor in impulse-sustained discharges. [41]

As a first approximation, photoionization is taken to be the dominant source of electrons during the impulse event, so that (4.4-16) simplifies to (when $nk_i t_i \ll 1$ the avalanche multiplication factor $(e^{nk_i t_i} - 1)$ reduces to $nk_i t_i$):

$$\Delta n_e = nSt_i. \tag{4.4-17}$$

---

‡ The model assumes that the diffusive separation of neutral species is small, and that the diffusion velocities of the charged particles are dominated by the radial electric field. [6]

The rate of ionization is taken to be independent of all discharge conditions (*e.g.*, discharge current and voltage).

Discharge Chemistry

Details of plasma chemistry in a PIE discharge are unknown, yet they are expected to strongly influence both the transient and steady-state discharge characteristics, [8,58] and also the instability growth rates. [10] The balance between electron loss and production determines the electron response to a disturbance, which is, as was identified in Figure 4.3-2, a crucial link in the instability feedback loop. It is well beyond the scope this analysis to incorporate a detailed gas chemistry model which would account for the myriad chemical reactions involving the primary laser gases and their fragments. Consequently, some broad assumptions about plasma chemistry are required. Following the models of Haas [6] and Nighan, [11] considerations will be limited to identifying two dominate ion species in terms of which the essential features of discharge chemistry may be described. Electron response is known to be more sensitive to details of negative ion chemistry than it is to positive ion species, because the dominant negative ion determines the nature of the electron loss process. Strong detachment, which offsets attachment so that recombination becomes the dominant loss process, can reduce the E/n required for self-sustained operation by as much as a factor of two. [8] Discharges having attachment-dominated electron loss tend to be much less stable than those having recombination-dominated loss.[11] In choosing two dominant ions, the primary assumptions regard the relative importance of impurities and discharge by-products which may be present in closed-cycle system.

After prolonged laser gas aging, nitrogen oxides can accumulate in significant concentrations.[59] Laser performance, both in terms of efficiency and discharge stability, are observed to be seriously deteriorated once N_2O or NO_2 approach fractional concentrations of 0.1%.[30] Ion kinetics in such poisoned gas mixtures are dominated by NO^+ and NO_x^-.[59] In this case, the importance of attachment will supercede that of recombination, and attachment-detachment kinetics will influence the discharge state.

NO_x molecules are strongly electronegative, so they are good attaching agents and do not readily undergo detachment. Elimination of the NO_x^- ions is a multi-step process which first requires a charge transfer from vibrationally excited NO_x^-, and then subsequent detachment of a secondary negative ion species. [59] Consequently, when NO_x^- is the dominant negative ion, estimation of the detachment rate is not possible without a detailed chemistry model. Neither can ionization and attachment rates be estimated without knowing the relative concentrations of nitrogen oxides.

A simplified chemistry model is more tractable in the absence of nitrogen oxides. Typically other negative ions are more easily detached, so the dominant electron loss process will be more affected by the relative concentration of CO, a strong detaching agent. Consider first the case when CO is present in the discharge primarily as a by-product of CO_2 dissociation, and in small concentrations such as would be in the case of an open-flow system with a short gas residence time. The strongest dissociative attachment reactions in the discharge form the same negative ion O^- which, in the absence of a strong detaching agent, clusters with CO_2 to form CO_3^-.[8] This anion is stable and only weakly detached by CO.[8,59] In this case, O_2^+ and CO_3^- will be the dominant ions, [58,59], and a small set of reactions having known rate coefficients will reasonably approximate gas chemistry.[59] These reactions are summarized in Table 4.4-1.

Table 4.4-1 Simplified gas chemistry model for a CO_2:N_2:He mixture, assuming no poisoning and that the dominant ions are O_2^+ and CO_3^-

ionization	$e^- + CO_2 \rightarrow CO_2^+ - + 2e^-$
	$e^- + CO \rightarrow CO^+ + 2e^-$
	$e^- + N_2 \rightarrow N_2^+ + 2e^-$
dissociative attachment	$e^- + CO_2 \rightarrow CO + O^-$
	$e^- + CO \rightarrow C + O^-$
associative detachment	$CO_3^- + CO \rightarrow 2CO_2 + e^-$
	$(O^- + CO(0) \rightarrow CO_2(020) + e^-)^\dagger$
electron-ion recombination	$e^- + CO_2^+ \rightarrow CO(1) + O$
ion-ion recombination	$CO_3^- + O_2^+ \rightarrow CO_2(020) + O + O$
negative ion clustering	$O^- + CO_2 + M \rightarrow CO_3^- + M$

† when CO is abundant, this reaction supplants the CO_3^- reactions.

When CO is present in greater concentrations, as would be the case in closed-flow systems or when CO is added as a primary species, then a significant fraction of O^- ions may be detached by CO before they cluster to form CO_3^-. [8] In the limit of extremely strong detachment, detachment would offset attachment on a quasisteady basis, so that $n_-/n_e = k_a/k_d \ll 1$. Electron loss would then be recombination-dominated. If the CO fractional concentration $f \equiv [CO]/([CO]+[CO_2])$ is above 10%, then the influence of detachment will be sufficiently strong that negative-ion processes will have negligible effect, at least on steady discharge properties.[8] (It is not clear that this result is directly applicable to a gas mix with large fractions of CO in the initial mixture, since it assumes that CO is due to disassociation of CO_2.)

In a simplified chemistry model where only two ion species may be considered, one can assume either that (a) detachment is so strong that O^- ions are detached as rapidly as they are formed, with the result that O_2^+ is the dominant cation and anions may be ignored entirely; or (b) one can assume that detachment operates only on CO_3^-, so that O_2^+ and CO_3^- are the dominant ions. The actual case is likely somewhere in between, with the transient discharge response being affected by detachment of both CO_3^- and O^-.

No simulation results exist in the literature to test (these assumptions); *i.e.*, simulations of long-term gas species evolution in low pressure discharges having initially equal concentrations of CO and CO_2. That the neglect of nitrogen oxides is reasonable in closed-cycle lasers is somewhat corroborated though by the comprehensive simulation of Hokozono *et al.* [60] They predicted that for a gas mix of $He:N_2:CO_2 = 14:3:3$ in a closed cycle TEA laser, the main neutral impurity species generated by prolonged laser operation, in decreasing order of decreasing concentration, were CO, O_2, O_3, N_2O, NO_2. The nitrogen oxides were observed to have little effect on electron loss due to their low accumulated concentrations.†

Ambipolar Diffusion

Ambipolar drift rates are substantially altered by the presence of negative ions. [61] For small n_-/n_e, electrons and positive ions are constrained to diffuse at the same rate. This is required to maintain quasi-neutrality. However, when n_-/n_e becomes large, instead positive and negative ions are so constrained. Electrons are then able to diffuse freely relative to the ions without violating quasi-neutrality. Thompson [62] has shown that in the presence of negative ions, the ambipolar diffusion coefficients for electrons and the negative ion species are‡

$$\begin{aligned} D^a_{\ e} &= D_+\left[\frac{1+\gamma+2\alpha\gamma}{1+(1+\alpha(\mu_+/\mu_e))+\alpha(\mu_-/\mu_e)}\right], \\ D^a_{\ -} &= D_+\left[\frac{(\mu_-/\mu_e)(1+2\alpha+1/\gamma)}{1+(1+\alpha(\mu_+/\mu_e))+\alpha(\mu_-/\mu_e)}\right] \end{aligned} \tag{4.4-18}$$

where μ_e, μ_+, and μ_- are the electron and ionic mobilities, $\alpha = n_-/n_e$, and $\gamma = T_e/T$. Ions are assumed to be at thermal equilibrium with the ambient gas temperature. For typical discharge conditions (*cf.* Table 4.3-1) a fractional negative ion concentration $\alpha \approx 1$ increases $D^a_{\ e}$ by more than an order of magnitude.

Ionic diffusion coefficients are in principle to be derived from experimental mobility data using the Einstein relationship:

$$eD/\mu = k_BT. \tag{4.4-19}$$

---

† However, the simulations of Hokozono *et al.* assume a low initial CO_2 dissociation fraction. Subsequent disassociation into CO and by-products then accounts for much of the O_2 concentration. (O_2 is important in the formation of nitrogen oxides.) Presumably starting with a higher initial CO fraction, which would prevent the dissociation of CO_2, would alter discharge chemistry considerably, perhaps increasing the relative importance of nitrogen oxides.

‡ Although these expressions produce the expected results for the limiting cases of α, they do not appear to be strictly correct. In Thompson's derivation [62], the solution of Eq. (2) does not satisfy Eq. (1) for independent $\nabla\ n_-$ and $\nabla\ n_e$. Nevertheless, (4.4-16) and (4.4-18) continue to be cited in the literature.

However, a well-developed theory does not exist for ion transport in a molecular gas. [61] Consequently, in determining diffusion coefficients there are several uncertainties. These are: unavailability of mobility data for ion transport in molecular gases, and a mixture rule accurate for molecular ions in a molecular diluent. [63,64]. As a first approximation, ionic mobilities in helium were used to estimate ionic diffusion coefficients.

Summary of Model Coefficients

To complete the discharge model of (4.4-4)-(4.4-15) and (4.4-18)-(4.4-19), various physical parameters are required for the PIE gas mixture ($He:N_2:CO_2:CO = 16:10:1:1$). Values for electron transport and excitation rate coefficients are not available in the literature for this mixture, nor indeed are they for any gas mixture containing significant fractions of CO. Instead, coefficients for the most similar mixture available were used ($He:N_2:CO_2=12:7:1$). These could be parameterized only over the range $5\text{Td} \le E/n \le 30\text{Td}$, due to limitations in the published data. This relatively small parameterization range proved to be problematic for simulation of PIE discharge instability, as will be discussed in Section 4.4.4.

Table 4.4-2 Electron and ion related coefficients for the gas mixture $He:N_2:CO_2 = 12:7:1$, assuming that O_2^+ and CO_3^- dominate ionic reactions. Quantities in curly brackets are not needed when strong-detachment is assumed. The parameterizations are valid over the range 5 - 30 Td. Where temperature dependencies are shown, T and T_e are in units of K and eV, respectively. Note that the quantities in column one are mixture weighted. Of the quantities in column two, only k_d must be mixture weighted.

parameterized quantity†	reference	quantity‡	value	reference
$T_e\,(E/n)$	[8]*	$\{k_d\}$	$5.0\ 10^{-19}\ m^3/s$	[59]
$n\mu_e\,(T_e)$	[11]*	k_r^{ei}	$2.0\ 10^{-11}\ T^{-1}\ T_e^{-0.5}\ m^3/s$	[59]
$\nu_T/n\,(T_e)$	[11]	$\{k_r^{ii}\}$	$3.0\ 10^{-13}\ m^3/s$	[59]
$\nu_v/n\,(T_e)$	[11]	$\{\mu_0^-\}$	$1.5\ 10^{-3}\ m^2/V\text{-}s$	[63]
$k_{VT}(T)$	[11]	μ_0^+	$2.1\ 10^{-3}\ m^2/V\text{-}s$	[63]
$k_i(T_e)$	[8]			
$\{k_a(T_e)\}$	[8]			

† Rate coefficients for attachment and vibrational excitation are relatively insensitive to variations in the electron energy distribution function due to changes in gas mixture. Rate coefficient for ionization are more sensitive [8,59].

‡ Ionic reduced mobilities are related to mobility by $\mu_0 = \mu\,(p/760)\,(273/T)$, where p is in Torr, and T is in Kelvin.

* Derived from $\nu_m/n\,(T_e)$ and $\nu_u/n\,(T_e)$

Although effects of CO on electron transport and excitation rate coefficients were neglected by necessity, effects on the gas chemical, thermal, and viscous properties could be accounted for. The relevant properties are summarized in Tables 4.4-3 and 4.4-1. Properties related to electron and ion behavior are summarized in Table 4.4-2.

Table 4.4-3 Neutral gas properties for He:N_2:CO_2:CO = 16:10:1:1 at 300 K and 30 Torr.

specific heat capacity (c_p)	1650 J/kg-K	particle density (n)	$9.7\ 10^{23}$ 1/m^3
adiabatic index ($\gamma=c_p/c_v$)	1.5	average particle mass (m)	$2.47\ 10^{-26}$ kg
thermal conductivity (κ)	.0823 W/m-K	molecular fraction (f_m)	0.44
viscosity (η)	$22.5\ 10^{-6}$ kg/m-s	sound speed (c_s)	500 m/s

4.4.3 Numerical Method

In selecting numerical methods with which to solve the governing equations of Section 4.4.2, simplicity, robustness, and modularity were emphasized over computational efficiency. As is common practice in reactive-flow simulations, the time derivatives were split and the spatial- and source- terms partitioned into two sets of equations; a system of conservative equations (hyperbolic), and a system of stiff diffusion and source-term equations (parabolic).[65,66] For each numerical time step, these two sets of equations were advanced in time alternately and joined via Strang time-splitting. With this method, if Ψ^n is the state vector at time step n, the system is advanced by time Δt to time step $n+1$ with

$$\Psi^{n+1} = S_C\left[\frac{\Delta t}{2}\right] S_D[\Delta t]\, S_C\left[\frac{\Delta t}{2}\right]\Psi^n , \tag{4.4-20}$$

where $S_C[\Delta t]$ and $S_D[\Delta t]$ represent the numerical operators which advance by Δt the conservation problem and the diffusion problem, respectively. Strang splitting is second-order accurate. [67]

For both numerical operators $S_C[\Delta t]$ and $S_D[\Delta t]$, finite difference methods were used, as is discussed below. Spatial discretization was uniform, in a stationary reference frame. Size of the time step Δt was auto-adjusting according to the CFL condition and a ceiling on the fractional change in state variables per time step.

Conservation Problem

The left-hand-side terms of (4.4-5) - (4.4-8) constitute Euler's equations, which describe inviscid compressible fluid flow. In conservative form, [68] they are

$$\frac{\partial}{\partial t}U + \frac{1}{r}\frac{\partial}{\partial r}ru_r(U+A) = \frac{\partial}{\partial r}B$$

$$U = \begin{bmatrix} \rho \\ \rho u_r \\ n\tilde{\xi}_T \\ n\xi_V \\ n_e \\ n_- \end{bmatrix} \qquad A = \begin{bmatrix} 0 \\ 0 \\ p \\ 0 \\ 0 \\ 0 \end{bmatrix} \qquad B = \begin{bmatrix} 0 \\ p \\ 0 \\ 0 \\ 0 \\ 0 \end{bmatrix}, \tag{4.4-21}$$

where u_r is the radial velocity component and $\tilde{\xi}_T = \xi_T + \frac{1}{2}m_{av}u_r^2$ is the sum of non-vibrational internal energy and gas kinetic energy. This system was solved with the algorithm ETBFCT, a flux corrected transport (FCT) algorithm by Boris [69]. Method accuracy was confirmed with test convection problems.

Diffusion and Source Term Problem

The right-hand-side terms of (4.4-5) - (4.4-8), dominantly stiff source and diffusion terms, constitute the complimentary problem:

$$\begin{aligned}
\rho\frac{\partial}{\partial t}u_r &= \frac{4}{3}\eta\,\{\nabla^2 u_r - \frac{u_r}{r^2}\} \\
c_v\rho\frac{\partial}{\partial t}T &= n_e n\,(\frac{v_T}{n})\,k_B T_e + \frac{f_m n}{\tau_{VT}}(\xi_V(T_V) - \xi_V(T)) + \kappa\nabla^2 T + \Phi \\
n_m\frac{\partial}{\partial t}\xi_V &= n_e n\,(\frac{v_V}{n})\,k_B T_e - \frac{f_m n}{\tau_{VT}}[\xi_V(T_V) - \xi_V(T)] \\
\frac{\partial n_e}{\partial t} &= D^a{}_e\nabla^2 n_e + nn_e(k_i - k_a) + nn_-k_d - n_+n_ek_r^{ei} \\
\frac{\partial n_-}{\partial t} &= D^a{}_-\nabla^2 n_- + nn_ek_a - nn_-k_d - n_+n_-k_r^{ii}
\end{aligned} , \tag{4.4-22}$$

where the viscous dissipation function [52] is

$$\Phi = -\frac{2}{3}\eta\left[\frac{1}{r}\frac{\partial}{\partial r}(ru_r)\right]^2 + 2\eta\left[(\frac{\partial u_r}{\partial r})^2 + (\frac{u_r}{r})^2\right], \tag{4.4-23}$$

and the Laplacian derivative in cylindrical coordinates, assuming axial and longitudinal uniformity, is

$$\nabla^2 f = \frac{1}{r}\frac{\partial}{\partial r}(r\frac{\partial f}{\partial r}). \tag{4.4-24}$$

System (4.4-22) was solved using the Crank-Nicholson implicit scheme with central differencing [68,70] This method is second order accurate in time and space, except near the origin, where for some terms the spatial accuracy deteriorates to first order. Specifically, in the second order difference approximation to $\nabla^2 f$, the leading error term contains a term $\sim (\Delta r)^2/r$, which is effectively $\sim \Delta r$ near the origin. The same problem can be avoided with the $\frac{1}{r}\frac{\partial}{\partial r}(ru_r)$ in (4.4-23) by expanding the derivative.

Method accuracy was confirmed with test diffusion problems.

Boundary Conditions

To satisfy symmetry conditions at the origin, homogeneous Neumann boundary conditions were applied to all state variables except radial velocity, to which homogeneous Dirichlet conditions were applied. For the outer mesh boundary, where artificial boundary conditions were required, the mesh was extended to regions where the solution was relatively uniform. There, homogeneous Neumann conditions were applied. [71,72]

4.4.4 Model Results and Discussion

Of the parameter-space explored with CODE1, the most interesting results were obtained for cases with recombination-dominated electron loss and photoionization-dominated impulse ionization. For these simulations, it was assumed that electron detachment by CO was sufficiently strong to cancel attachment on a quasi-steady basis, so that negative ion concentrations were negligible (*cf.* Section 4.4.2: *Discharge Chemistry*). It was also assumed that the electron creation during each high-voltage impulse was due entirely to photoionization, with each impulse contributing an additional $\Delta n_{e_s} = nf_i$ to the local electron density, where $f_i = 10^{-7}$ is the photoionization fraction (*cf.* Section 4.4.2: *Pulser Events*).

Several compromises were required in determining the model parameters. First, $f_i = 10^{-7}$ was chosen as a compromise between reproducing both the current decay characteristic of Figure 4.2-1, and the peak electron densities, also estimated from Figure 4.2-1. Satisfying the former condition required a peak ionization fraction of 10^{-6}, whereas satisfying the later required an ionization fraction of 10^{-8}.[†] The intermediate value $f_i = 10^{-7}$ caused the discharge model conductivity to be considerably higher than the experimental estimates based on Figure 4.2-1. Second, the limited parameterization range of T_e-dependent parameters was also problematic (*cf.* Section 4.4.2: *Summary of Model Coefficients*). To keep the variation in *E*/*n* over the burst cycle within the coefficient parameterization range, while also accommodating wide variability of average power deposition and burst rate, required reducing the model ballast resistance (R_b) to 3 Ω. This smaller model resistance, 20-30% of the experimental value, partially offset the larger model currents. Ballast power dissipation in the model was typically 20% of the total input power, compared to 10% in the experimental case.

[†] This discrepancy is likely due to a large error in the measured waveform of Figure 4.2-1. There is now some concern that the current decay observed was dominated by the "droop" of the Rogowski coil, and does not represent the actual signal waveform. This problem will be discussed further in Section 4.4.6.

With these parameters, model current and voltage waveforms were found to reproduce qualitatively the experimental characteristics of Figure 4.2-1: a non-self-sustained burst interval followed by asymptotic decay during the inter-burst interval to a self-sustained state. Hence, the duration of the self-sustained state was proportional to the inter-burst interval. In Figure 4.4-2, this self-sustained state is seen under conditions of constant sustainer voltage to be independent of the burst rate. Instead, as expected, the self-sustained state was found to be determined by the external circuit (*i.e.*, V_{sst} and R_b), and the dependence of discharge conductivity on E/n.

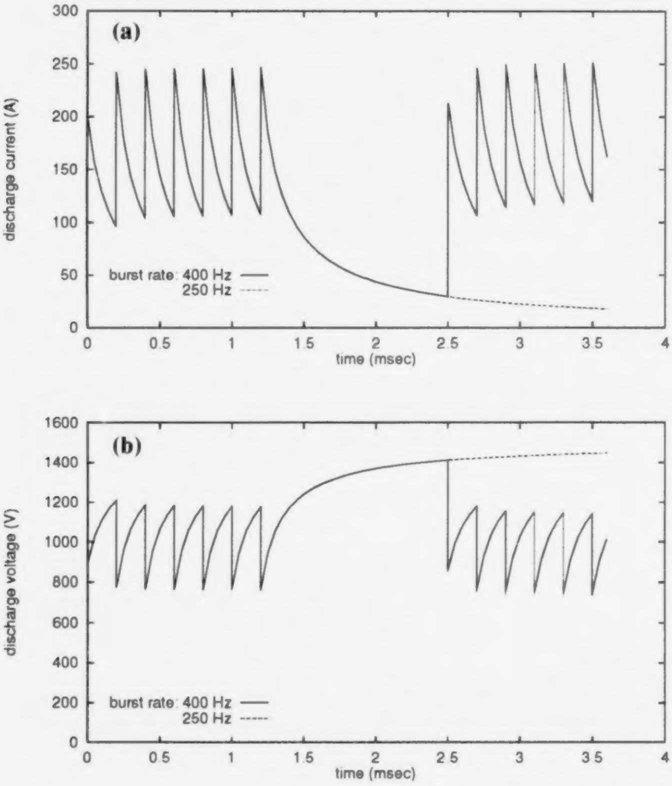

Figure 4.4-2 Simulated discharge (a) current and (b) voltage for a sustainer voltage of 1500 V. The average power loading <*JE*> is 1.8 and 2.5 W/cc for the burst rates of 250 and 400 Hz, respectively.

While CODE1 reproduced qualitatively the experimental current waveform, it predicted threshold power loadings for discharge instability well above the experimental PIE-III device limit of 1-2 W/cm^3 reported by Nath *et al.* [47] and later by Nikumb *et al.* [3] Instability growth was studied by introducing to the initial conditions an on-axis perturbation, and monitoring its evolution for the gas residence time $\tau_g = 3.6$ msec. For this perturbation, a gaussian profile with a e^{-2} half-width of 5 cm was used. Disturbances this large were observed to be affected little by thermal conduction and ambipolar diffusion, whereas smaller filaments were damped significantly by these precesses. This observation was consistent with the results of other experimental and theoretical studies. [10,12]

Simulation results for representative burst-mode conditions are summarized in Figure 4.4-3. In the left column, the unperturbed value for each of the state variables is indicated. This represents the evolution of the spatially uniform discharge state in the absence of a disturbance. This data was taken from the periphery of the 1D simulation domain. In the right column, the relative on-axis perturbation amplitude is indicated. This represents the disturbance's effect on the discharge state, and is defined for each state variable as the ratio of its on-axis value to its unperturbed (peripheral) value. (For example, the current perturbation is $\partial J/J$, where ∂J is the maximum disturbance amplitude, and J is the unperturbed current density.) For the cases considered, the maxima in the disturbance amplitude coincided with the simulation domain origin. In all simulations, an initial 0.5% isobaric depression in gas density was used as the instability seed, and the first burst sequence occurred at $t = 0$.[†]

Figure 4.4-4 illustrates the effect of average discharge power loading and burst repetition rate on current perturbation growth. The number of pulses per burst was held constant at 7, as it was for the burst-mode experiments of Nikumb *et al*. Similarly, the pulser frequency was held constant at 5kHz. Figure 4.4-4(a) indicates the maximum disturbance amplitude occurring during the gas residence time, while Figure 4.4-4(b) indicates the disturbance amplitude at $t = \tau_g$.

In CODE1 simulations, instability growth was observed to be characterized by two phases: an ionization instability followed by a more rapid and catastrophic vibrational relaxation instability.[‡] While in the first phase, instability growth was strongest during the inter-burst interval. In fact, as is seen in Figure 4.4-3(a), the photoionization pulses were observed to substantially counteract current filamentation. This effect is also manifest in Figure 4.4-4 where the *maximum* filament amplitude in (a) is seen to be greater than the *final* filament amplitude in (b). For all the burst rates indicated, the maximum filament amplitude occurred just prior to the final burst permitted by the gas residence time. The 3.6 msec gas residence time limit occurred during a burst for all cases except for 250 Hz, which had only one burst during the gas residence time.

The second, and strongest, phase of instability growth was driven by a precipitous drop in vibrational temperature, as the V-T relaxation rate soared with increasing temperature causing the

---

[†] Note that the homogeneous Neumann boundary condition applied to the outer numerical mesh boundary prevent gas convection occurs in the unperturbed solution. Hence, unlike the physical discharge, in the simulation gas pressure is proportional to gas temperature.

[‡] Contrary to expectations, strong vibrational instability was not observed preceding to vibrational relaxation instability.

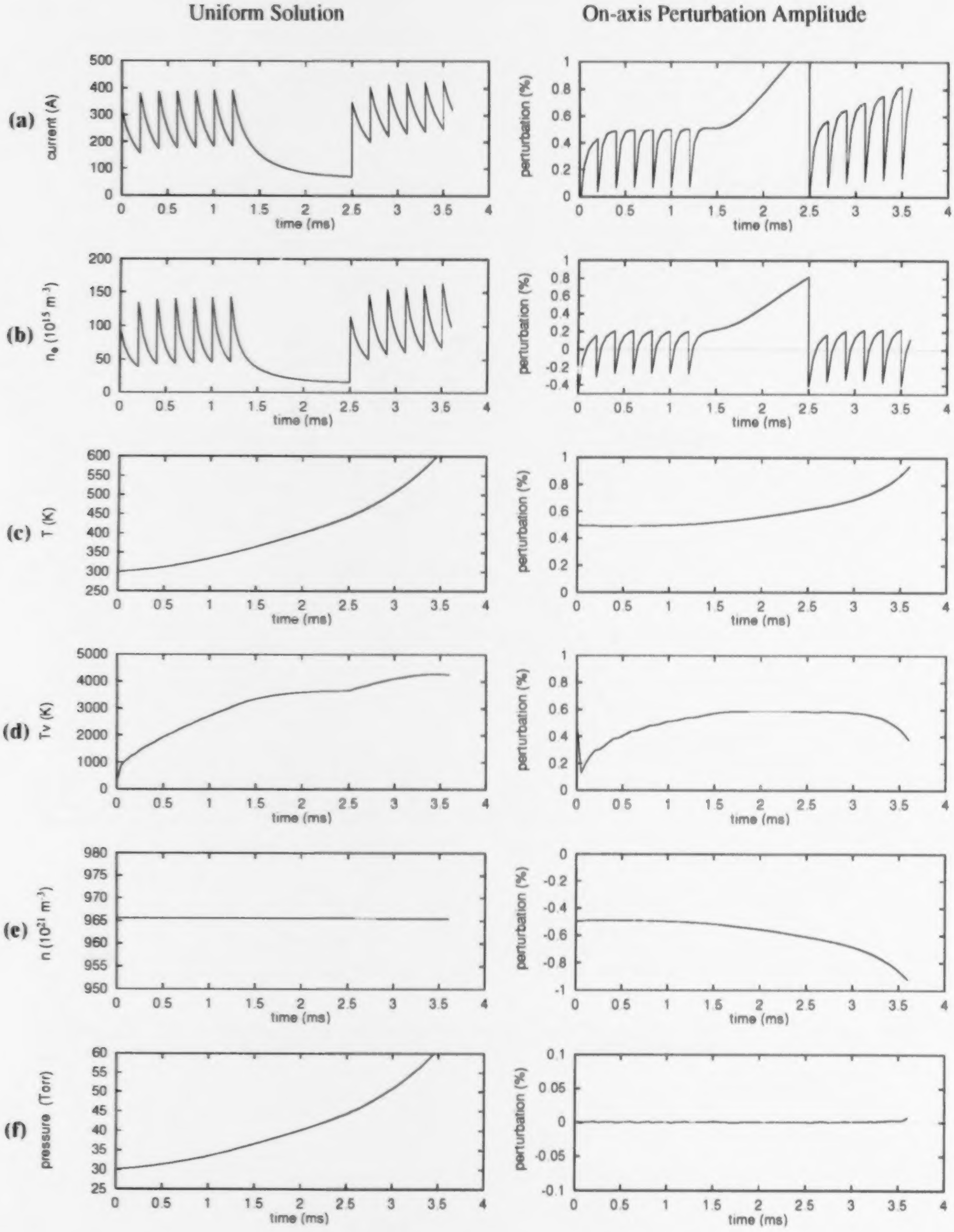

Figure 4.4-3 Evolution of the uniform positive column state with an on-axis gaussian perturbation for a representative burst-mode configuration (f_b=400Hz, V_{sst}=2700V, $<JE>$=8.2W/cc): (a) discharge current; (b) electron density; (c) gas temperature; (d) vibrational temperature; (e) gas density; and (f) gas pressure.

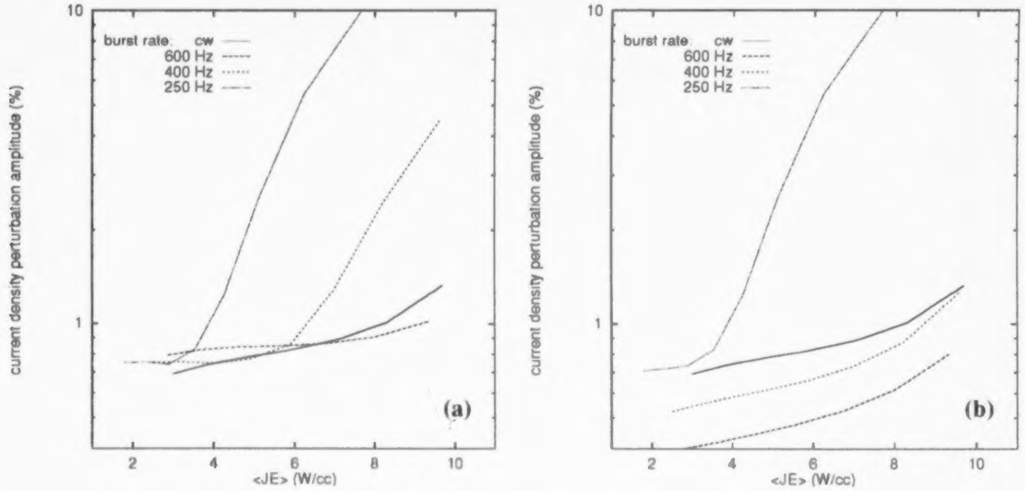

Figure 4.4-4 Current perturbation growth as a function of average power density, for an initial 0.5% isobaric depression in gas density: (a) the maximum perturbation amplitude during the gas residence time $t < \tau_g$; (b) the perturbation amplitude at $t = \tau_g$. For all cases, the pulser frequency was 5 kHz, the number of pulses per burst was 7, and the first burst sequence occurred at t = 0

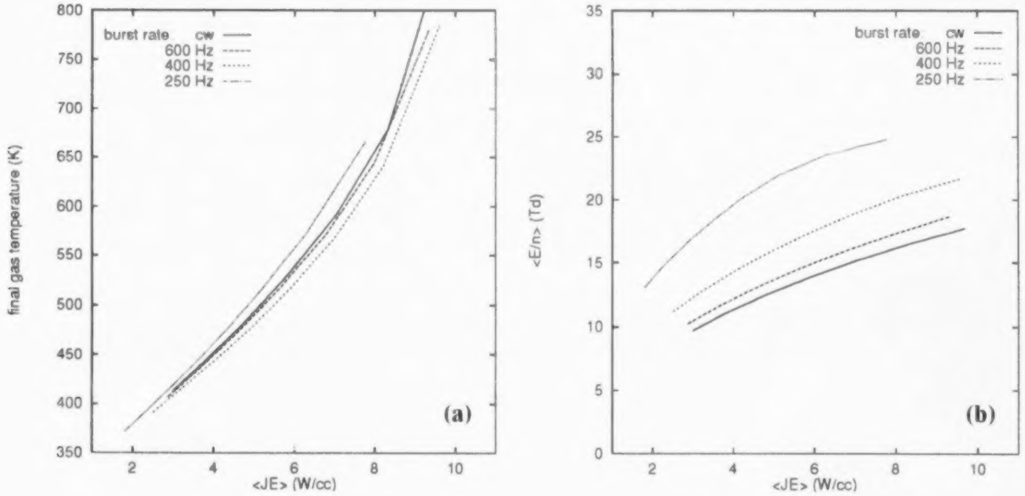

Figure 4.4-5 Discharge properties as a function of average power density: (a) final gas temperature, and (b) average reduced field. For the same simulation parameters as in Figure 4.4-4.

vibrational energy reservoir to collapse. This onset of this phase, seen in the case of Figures 4.4-3 (c) and (d) to began at approximately 3 msec, occurred when the gas temperature exceeds 450 K. (This onset temperature for vibrational reservoir collapse is characteristic of the τ_{VT} function used in the CODE1. [11]) Exit gas temperature exceeded this threshold at all burst rates for average power loadings above 4 W/cc (Figure 4.4-5(a)). However at this power loading, only in the 250 Hz case was the surge of V-T relaxation manifest as filamentation. At higher burst rates, which were characterized by slower vibrational instability growth, filamentation due to V-T relaxation was delayed by smaller gas temperature gradients.

Significantly, the stability characteristics of Figure 4.2-2 are seen to be qualitatively reproduced in Figure 4.4-4: the model discharge is most stable for intermediate burst rates, and it is least stable at low burst rates. This result is by no means conclusive, but it does help identify several relevant factors for further study. Of particular interest are mechanisms which stabilize intermediate burst rates relative to CW operation, and mechanisms which destabilize low burst rates relative to intermediate burst rates.

Destabilizing Mechanisms

Two physical mechanisms were observed in the simulation which tend to destabilize the discharge at low burst rates relative to intermediate burst rates.

First, instability growth was observed to be strongest during the self-sustained inter-burst interval, even though the average power loading was considerably less than that during the burst interval. This caused the lowest burst rates to be least stable (*cf.* Figure 4.4-4(a)). That this should be so can be seen by considering a test case where the burst rate is decreased while the sustainer voltage is held constant. Since the sustainer voltage determines the self-sustained condition achieved between bursts (*cf.* Figure 4.4-2), the instability growth rate during the inter-burst interval will be constant. However, the lower burst rates permit longer periods of self-sustained instability growth. So although the average power density has decreased, the discharge will be less stable. This observation may be quantified as follows.

The results of CODE1 suggest one may consider instability growth piece-wise, at least for low burst rates, by treating the burst and inter-burst intervals separately. State changes during the burst phase may be considered quasi-steady on the time-scale of instability growth, and therefore treated with time average quantities. [41] State changes during the inter-burst period, where the strongest instability growth occurs, proceed at a slower rate than instability growth and so may be treated as steady. [11] This approximation should be best when burst rates are sufficiently low for the discharge to become self-sustained during the inter-burst interval.

Consider then instability growth to be composed of two phases: a pulser-sustained stage of duration bf_b^{-1} experiencing an instability growth rate of $1/\tau_1$, where $0 \leq b \leq 1$ is the burst duty-cycle, f_b is the burst frequency, and τ_1 is the characteristic instability formation time during pulser-sustained operation; and a self-sustained phase of duration $(1-b)/f_b^{-1}$ with a characteristic instability formation time of τ_2. The net instability growth rate over one burst cycle is then

$$\frac{1}{\tau} = \frac{b}{\tau_1} + \frac{1-b}{\tau_2}, \tag{4.4-25}$$

where we have assumed that instability growth is exponential. Using the functional form of (4.3-3), we can reexpress this as

$$\tau = JE_1^{\hat{\tau}}\left[\left(\frac{b}{A_1}\right) + f_{JE}^{-\hat{\tau}}\left(\frac{1-b}{A_2}\right)\right]^{-1}, \tag{4.4-26}$$

where A_1 and A_2 are the constants of proportionality for pulser- and self-sustained operation, respectively, so that $\tau_1 = A_1 JE_1^{\hat{\tau}}$ and $\tau_2 = A_2 JE_2^{\hat{\tau}}$; and $f_{JE} = JE_2/JE_1$ is the fractional decrease in power density when going from pulser- to self-sustained operation. As was shown in Section 4.3.2, $-1 \le \hat{\tau} \le -1/2$ and $A_1 > A_2$, since pulser-sustained operation is more stable than self-sustained operation.

It is clear from the form of (4.4-25) that because $A_1 > A_2$, net instability growth rate over one burst cycle τ is a decreasing function of b, the burst duty-cycle. Holding JE_1 and f_{JE} constant is equivalent to holding the sustainer voltage constant, assuming that the ionization fraction created by the pulser is also invariant as b changes.

A second mechanism which would tend to further destabilize the long inter-burst interval is negative ion formation during the inter-burst interval. The results of Figures 4.4-4 and 4.4-5 were obtained for the strong-detachment limit in which all effects of negative ions were neglected. In subsequent tests, where it was assumed that detachment of O^- was weak allowing formation of the stable cluster ion CO_3^-, it was found that negative ion concentration was negligible during the burst phase, but at low burst rates exceeded the electron concentration near the end of the inter-burst interval. During the inter-burst interval, when E/n is highest, attachment increases in strength relative to both recombination and detachment because attachment gets stronger with increasing E/n, whereas detachment does not. The consequence of increased negative ion density, especially when it becomes comparable to electron density, is accelerated instability growth under self-sustained conditions. [7]

Stabilizing Mechanisms

Two physical mechanisms may also be identified which would tend to stabilize intermediate burst rates relative to CW operation.

An external ionization source is known to reduce the importance of electron-impact ionization, thereby stabilizing the discharge (*cf.* Section 4.3.2). [26] Photoionization was observed in the simulation to stabilize the discharge not only in this way, but also by selectively creating fewer electrons in regions of depressed gas density. This effect is illustrated in Figure 4.4-3(b), where the electron density disturbance is reversed by each impulse to become negative. Thus instability formation is counteracted by a reduction of local heating in the regions where thermal instabilities are forming.

In this way, photoionization strongly inhibited growth of the ionization instability mode. Slower ionization mode growth in turn delayed vibrational relaxation instability, as was described earlier. At higher burst rates, photoionization smoothing of current density resulted in smaller temperature gradients, which in turn caused relaxation instability to occur more uniformly.

This photoionization stabilization was found to be strongest at intermediate burst rates, as can be seen in Figure 4.4-4. As burst-rate is decreased from its CW-equivalent[†] while average power loading is held constant, the electron density decays further between bursts. This allows the electron density history to be more effectively erased by the photoionization of the first burst impulse. This stabilizing effect is offset, and ultimately overwhelmed at low burst rates, by the prolonged self-sustained inter-burst phase discussed previously.

It is instructive to also consider hypothetically an alternative mechanism, which would account for PIE discharges being more stable at intermediate burst-rates. If the strongest instability growth occurs during the burst interval, instead of during the inter-burst interval as was observed in the simulation, then discharge stabilization is expected when decreasing the burst rate from CW to moderate burst rates. In terms of the previous definitions, $\tau_1 \ll \tau_2$ occurs when $JE_1 \gg JE_2$, that is, $f_{JE} \ll 1$. Under these conditions, the power density averaged over a burst cycle

$$\langle JE \rangle = JE_1 (b + f_{JE}(1-b)) . \qquad (4.4\text{-}27)$$

reduces to $\langle JE \rangle \approx bJE_1$. From (4.4-25), the characteristic instability growth time is then

$$\tau \approx \frac{A_1 JE_1^{\hat{\tau}+1}}{\langle JE \rangle} . \qquad (4.4\text{-}28)$$

For discharge stability to be enhanced as the burst-repetition frequency decreases, τ must increase while $\langle JE \rangle$ is held constant and b is decreased; *i.e.*, $\partial\tau/\partial b = -\partial\tau/\partial JE_1 < 0$. From (4.4-28), this requires that

$$\hat{\tau} > -1 . \qquad (4.4\text{-}29)$$

This condition is satisfied for the discharges of interest to convectively cooled CO_2 lasers; as was shown in Section 4.3.2, $-1 \le \hat{\tau} \le -1/2$. When $\tau_1 \ll \tau_2$, reducing the burst duty cycle is equivalent to reducing the gas residence time of a continuously excited discharge. Condition (4.4-29) may hence be understood as requiring τ_1 to vary such that the energy threshold for instability increases as the excitation duration decreases.

The conditions for $\tau_1 \ll \tau_2$ appear to be satisfied by neither the simulations nor the experiments considered here. In the simulations, $\tau_1 \gg \tau_2$ was observed. In the experiments, f_{JE} was insufficiently small to allow for $\tau_1 \ll \tau_2$. For example, in Figure 4.2-1, $f_{JE} \approx 0.6$. Indeed, $\tau_1 \ll \tau_2$ is not satisfied even if $A_1 = A_2$.

[†] Again, when the pulser frequency is 5kHz and there are 7 pulses per burst and 5kHz, CW corresponds to f_b=715Hz.

This second stabilization factor does, however, merit further investigation. In the case of simulation, it may be important when the burst phase is not so strongly stabilized by photoionization. In the case of experiment, it is likely that the current waveform of Figure 4.2-1 does not accurately represent the change in power density between the burst and inter-burst intervals. This will be discussed further in Section 4.4.6.

It is also notable that in the 20 Torr case of Figure 4.3-3, $\hat{\tau} \leq -1$ at the highest power loadings considered. The transition of $\hat{\tau} > -1$ to $\hat{\tau} \leq -1$, which would occur for small burst rates under conditions of constant $\langle JE \rangle$, would destabilize low burst rates relative to intermediate burst rates.

4.4.5 Model Evaluation

Over the course of simulations with CODE1, the complexity of both the physical problem and of obtaining accurate numerical solutions became apparent. This section briefly discusses several problems experienced with the development of CODE1.

Chemistry

The results reported in Section 4.4.4 were obtained for the strong-detachment limit in which all effects of negative ions were neglected. In subsequent tests, where it was assumed that detachment of O^- was sufficiently weak to allow appreciable formation of the stable cluster ion CO_3^-, it was found that the negative ion concentration was still negligible during the burst interval, but at low burst rates had exceeded the electron concentration by the end of the inter-burst interval. (During the inter-burst interval, when E/n is highest, attachment increases in strength relative to both recombination and detachment.) In Section 4.4.4, it was remarked that this abundance of negative ions is expected to further destabilize the inter-burst interval. In these calculations however, assuming weak detachment of O^- probably resulted in an over-estimate of negative ion formation. Detachment of both O^- and CO_3^- could be treated by including a second negative ion species in the model.

The simplified gas chemistry model adopted in Section 4.4.2:*Discharge Chemistry* could in principle be tested by comparing its predictions of discharge V-I characteristic and transient current responses with experiment. [41] However, unavailability of experimental V-I characteristics and uncertainty over the actual experimental current waveform eliminated this as a possibility for CODE1.

Vibrational Kinetics

The assumption in CODE1 that the nitrogen vibrational levels and the upper laser levels remain strongly coupled, and that the V-V transfer between CO, N_2, and CO_2 may be neglected requires further investigation. Both vibrational excitation and relaxation rates are critically important to the instability growth rate.

Numerical Model

For solving governing equations which admit unstable solutions, a numerical method is required which treats both stable and unstable modes accurately. For sufficiently well resolved problems, the Crank-Nicholson algorithm, used for to solve diffusion and source term problem of CODE1, is A-stable and does not exhibit superstability. However, the stability region of the FCT algorithm used to solve the conservation problem is unknown. The stability and accuracy of the numerical scheme as whole should be characterized using test problems to confirm that the numerical method does not distort instability growth.

Boundary Conditions

The homogeneous Neumann conditions used at the outer mesh boundary conditions amount to assuming an infinite discharge extent. Preferably, a pressure boundary condition would be used to more nearly model the limited discharge extent of PIE lasers. This would effectively allow discharge pressure to equilibrate with the surrounding gas volume. In an initial effort to implement these conditions, Dirichlet BC were enforced on pressure at the simulation boundary. This approach is known to be non-physical, and to produce reflections which propagate back through the simulation domain, perturbing simulation results. [74] Indeed, edge effects were introduced which swamped the instability growing on-axis. The simulation results were then edge-dependent, with the instability growth rates depending on the radius of the simulation region. It was concluded that an edgeless simulation domain was best for preliminary studies with CODE1.[†]

4.4.6 Conclusion

The simulation effort of CODE1, though indeed a major one, must be considered as the first increment in the solution a very complex problem. Two primary difficulties were experienced in the study of discharge stability with CODE1. First, the limited parameterization range of published electron transport and reaction rate coefficients prevented exploration of a wide parameter-space. The second problem was manifest as an inconsistency between the plasma decay rate and the peak electron density implied by Figure 4.2-1(a). It is believed that this inconsistency is due the measured current decay being dominated by the Rogowski coil "droop" and therefore not representing the actual signal waveform. Thus, the experimental results upon which several key modelling assumptions and parameter choices were based are now believed to be inaccurate.

Evidence that the waveform of Figure 4.2-1(a) is inaccurate may be found in other experimental results of Nikumb *et al.* A high-speed video of the PIE-III discharge under burst-mode operation indicated that for typical excitation conditions, a glow discharge was not initiated in absence of an impulse. [3] In the video, gas elements being blown into the discharge volume are seen not to experience a glow discharge (and therefore significant current) until *after* an impulse event occurs.

[†] Subsequent generations of this simulation should incorporate a more accurate treatment of boundary conditions, such as those based on characteristic wave relations. [75]

Meanwhile, as the gas is convecting through the inter-electrode region, discharge burning persists in those gas elements which had previously experienced an impulse. This effect is probably due to an overvoltage being required to initiate an abnormal glow discharge on the electrode pins. The persistent discharge is apparently self-sustained.

The implications of this effect on burst-mode operation are significant. For burst repetition rates below $1/\tau_g$, bulk gas flow is expected to sweep the discharge from the inter-electrode gap thereby extinguishing it. For higher burst rates though, regions of self-sustained discharge will be present at all times. The videographic evidence of [3] indicates that this is indeed the case; the glow discharge is seen not to be extinguished at a burst rate of 500 Hz, for which the inter-burst interval is only 20% of the gas residence time. In the 330 Hz case of Figure 4.2-1, the inter-burst interval is about 45% of τ_g. So one would expect to see in the current waveform of Figure 4.2-1(a) a linear decrease of current during the inter-burst interval.† That this effect is not manifest in Figure 4.2-1(a) is another indication that the current waveform is spurious.

It seems then that the inter-pulse current decay should be due to two factors: plasma decay, and the convective flow effectively reducing the discharge area. In CODE1, only the former process is accounted for. This omission probably causes CODE1 to significantly overestimate the inter-burst discharge current, especially at low burst rates.

4.5 Further PIE-III Experiments

Subsequent to the simulation studies of CODE1, additional burst-mode experiments were performed with PIE-III to supplement those of Nikumb *et al.*, since several important quantities were not recorded in the original experiments. [1-4] These include laser input power, discharge V-I characteristics, and the variation in pulser power as burst conditions were altered. Knowledge of each is required for further analysis of PIE-III discharge instability. Of course, also of great interest is further experimental characterization of the burst-mode stabilization effect. Sections 4.5.1, 4.5.2, and 4.5.3 summarize respectively experimental measurements of V-I characteristics, threshold power loadings for discharge instability, and the variation of pulser power with burst conditions.

4.5.1 V-I Characteristics

Under conditions of constant current, the sustainer voltage was found to increase as the burst rate was decreased. This relationship accounts for the observation in the study of Nikumb *et al* [3] that the current threshold for lasing decreases with burst frequency. It also accounts for why in that study laser output powers obtained for a given discharge current were observed to vary inversely with burst frequency. [3]

---

† For the study of Chapter 5, an improved current detector was developed. With it, discharge current during the inter-burst interval was observed to decrease linearly, such that regardless of burst frequency, the discharge current was extinguished at a rate corresponding to the gas flow rate. These results were obtained for the PIE-IV device, so direct comparison with PIE-III of this instability study is not possible. However, this same effect was presumably observed in the PIE-III videos.

The V-I characteristics for PIE-III, illustrated in Figure 4.5-1(c), may be understood as follows. Since the majority of discharge ionization occurs during the impulse event (*cf.* Figure 4.2-1(a)), decreasing the pulser frequency reduces the average electron density and therefore also the discharge current, because $\langle I \rangle \sim \langle n_e v_e \rangle$. This trend of decreasing average current may be countered by increasing the sustainer voltage which both increases $\langle v_e \rangle$ via a larger E/n, and increases $\langle n_e \rangle$ via enhanced electron impact ionization. These experimental observations are qualitatively consistent with the CODE1 simulations.

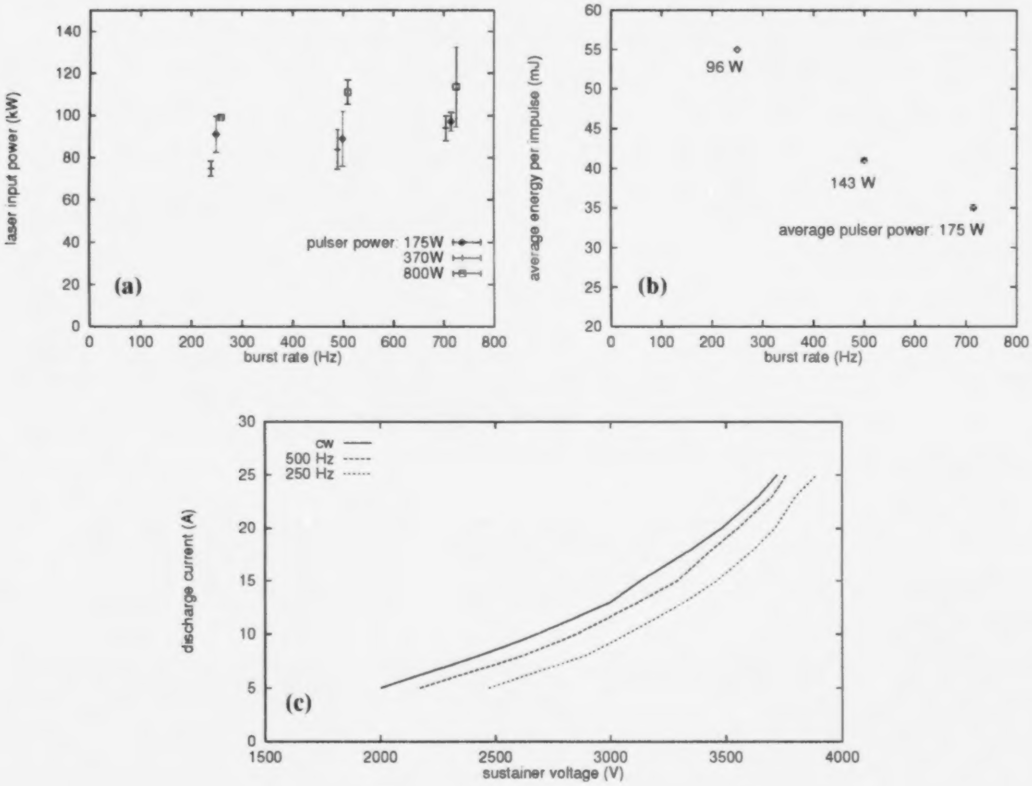

Figure 4.5-1 Final PIE-III experimental results: (a) dependence of instability threshold on burst rate and pulser power, where pulser powers are specified for CW condition; (b) dependence of average impulse energy on burst rate, while sustainer current is held constant at 15 A; (c) laser V-I characteristics. Error bars in (a) indicate standard deviations. Ballast resistance is estimated to be 10-15Ω.

4.5.2 Instability Threshold

Because further instability experiments jeopardized the laser apparatus, they were not possible until late in the device lifetime. When the experiments were finally repeated, the burst-mode stabilization effect observed previously by Nikumb *et al.* could not be reproduced. Discharge stability was found to decrease monotonically with burst rate, as is indicated in Figure 4.5-1(a). The maximum laser output power was also observed to decrease monotonically. These results are inconsistent with those of Nikumb *et al.*, where both discharge stability and laser efficiency were found to increase as the burst rate was lowered from CW.

One factor which may account for this discrepancy is that in the interval between experiments, the PIE-III containment vessel was contaminated by an oil leak. Anecdotal evidence suggests that this had an irreversible effect on laser performance. [73] Organic contaminants would be expected to alter every aspect of laser performance. An additional experimental uncertainty is due to the difficulty of determining the actual ballast resistance. It is not certain that the ballast resistance used in these later experiments is equal to that used in the initial experiments of Nikumb *et al.*

4.5.3 Pulser Power

Average pulser power was observed to depend strongly on both sustainer voltage and burst frequency. For these measurements, the sustainer voltage and burst frequency were altered while the pulser voltage supply control parameters were left unchanged, as they were for the experiments of Nikumb *et al.*[†] [4] Under conditions of constant sustainer current, the average pulser supply voltage was found to increase as the burst rate was decreased. This effect is presumably due in part to the longer charging interval allowed for the pulser circuit in the inter-burst interval. Consequently, as burst rate was decreased, the average energy per impulse was found to *increase*.[‡] These experimental results are given in Figure 4.5-1(b),[*] and have several important implications.

First, although the relative importances of photoionization and electron-impact ionization during the PIE impulses are unknown, an increase in either form of ionization during an impulse is expected to have a stabilizing effect (*cf.* Section 4.3.2). Certainly, a larger impulse amplitude will result in stronger electron-impact ionization. The current-dependence of UV creation by corona is unknown, but for sparks it scales as the cube of current. [19] In any case, the result of Figure 4.5-

---

[†] If in the original burst-mode experiments average pulser power was "held constant at 220 W" as the burst rate was varied, as is stated by Nikumb *et al.* [3], this could very well account for the increased discharge stability observed in that work at low burst rates.

[‡] Under conditions of constant discharge current, an increase in the energy per impulse is expected even if the impulse amplitude remains constant, due to increasing sustainer voltage. Similar tests under conditions of constant sustainer would also be instructive, since they would more directly indicate the effect of increasing pulser supply voltage.

[*] The characteristic of Figure 4.5-1(b) was also observed to be sensitive to changes in gas mixture. In one test case with excess N_2, the energy per impulse was observed to increase by 50% when burst rate was decreased from CW to 500 Hz.

1(b) is significant, because increased impulse energy has been observed experimentally to enhance PIE discharge stability (*cf.* Figure 4 of [47]).

Second, also relevant is that the first impulse of each burst sequence is expected to have a larger amplitude than the subsequent pulses, due to the increased charging time allowed for the pulser circuit during the inter-burst interval. The stabilizing effect of photoionization is expected to be most effective during this first impulse (see Section 4.4.4) This was observed by Hill, in an experimental study of an excitation scheme similar to PIE. [40] In that system, photoionization and electron avalanching occurred separately, in sequence. The relative ionization strengths were such that after the first impulse sequence, photoionization was ineffectual. However, the elimination altogether of photoionization was observed to reduce the *JE* instability threshold considerably.

4.5.4 Conclusion

The full implication of these experimental findings on the burst-mode experiments of Nikumb *et al.* is uncertain. Changes in discharge gas chemistry *etc.* in the interval between experiments prevent any direct connections from being made. However, one may speculate that in the original experiments, an increase in average impulse energy may in part have accounted for the increased stability observed at intermediate burst rates. In any case, these more recent experiments, in connection with the previous observation in Section 4.4.6 that the current waveform of Figure 4.2-1(a) is almost certainly spurious, should motivate further more detailed experimental investigations of the burst-mode stabilization effect.

4.6 Summary

The simulation CODE1 has been developed to study the burst-mode discharge stabilization effect observed by Nikumb *et al.* [1-3] With CODE1, one primary factor has been identified which could cause a PIE discharge to be least stable at low burst rates, as was observed by Nikumb *et al.* In CODE1 simulations, instability growth was found to be most rapid during the inter-burst interval, which is self-sustained and therefore inherently less stable than the impulse-sustained burst interval. For the simulation conditions considered, discharge power density (*JE*) during the inter-burst interval was not sufficiently low relative to that during the burst interval to offset its stronger dependence of instability growth rate on *JE*. Attachment effects were found to compound the problem of instability growth in the inter-burst interval, during which negative ions accumulated due its elevated E/n.

While destabilizing mechanisms at low burst rates were readily identified with CODE1, the identification of mechanisms which could cause more stable discharge conditions at intermediate burst-rates, as were observed by Nikumb *et al.*, was problematic. There were two primary difficulties. First, the limited parameterization range of available electron transport and reaction rate coefficients prevented exploration of a wide parameter-space with CODE1. Second, the discharge current measurement upon which several key modelling assumptions were based are now believed to be inaccurate. Thus, the actual experimental conditions to be modelled were uncertain, yet a wide parameter-space could not be explored. The former problem will be addressed in Chapter 6, where the Boltzmann transport equation is solved to obtain electron transport and reaction rate coefficients for a typical PIE mixture. The latter problem will be addressed in Chapter 5, where an ultra-fast optical isolator is developed in order to more accurately measure discharge current. (Together these provide the necessary basis for future burst-mode modelling efforts, which will be discussed briefly in Chapter 7.) These problems notwithstanding, several important factors affecting the stability of PIE discharges were identified for future considerations.

The results of CODE1 emphasized that impulse-sustained discharges can be much more stable than self-sustained discharges. In particular, photoionization was observed to strongly stabilize the discharge by selectively creating fewer electrons in the regions of depressed gas density coinciding with forming thermal instabilities. This stabilizing effect was found to be strongest at intermediate burst rates, for which the electron density history was most effectively erased by the leading burst photoionization impulse. (This effect was offset, and ultimately overwhelmed at low burst rates, by prolonged self-sustained instability growth.) A second stabilizing factor was observed experimentally. In the ionizing impulse stream, both the impulse amplitude and average energy per impulse were observed to increase as the burst rate was decreased. This behavior is expected to effect discharge stability significantly, given that the rates of both electron-impact and photo-ionization depend strongly on impulse amplitude. Increased impulse amplitude is expected to discharge stabilization, regardless of whether avalanche ionization or photo-ionization dominates during the impulse.

Finally, another possible mechanism was identified, although observed neither in the simulation nor in experiments. If instability growth during the inter-burst interval may be neglected (which is possible, for example, if the power density during the inter-burst interval is sufficiently small), then discharge stability is expected to improve with decreasing burst rate, because the instantaneous growth rate during the burst interval varies more weakly than $1/JE$. This mechanism does bear further investigation, since the discharge current waveforms of this study – both experimental and simulated – probably substantially overestimate the inter-burst current, and so do not rule out its possible relevance.

Bibliography

[1] Nikumb, S. K., Seguin, H. J. J., Seguin, V. A., and Presakarchuk, P. (1989): High repetition rate operation of a photoinitiated impulse-enhanced electrically excited CO_2 laser discharge using a burst-mode technique. Appl. Phys. Lett. **53**, 1254-1256.

[2] Nikumb, S. K., Seguin, H. J. J., Seguin, V. A., Willis R. J., Cheng, Z., and Reshef, H. W. (1989): Burst-mode gain switched technique for high peak and average optical energy extraction. Appl. Optics **28**, 1924-1627.

[3] Nikumb, S. K., Seguin, H. J. J., Seguin, V. A., Willis R. J., and Reshef, H. W. (1989): High-average power-pulsed performance of a multikilowatt PIE laser. IEEE J. Quantum Electron. **25**, 1725-1735.

[4] Nikumb, S. K (1992), personal communication.

[5] Nighan, W. L. (1973): Progress in high pressure electric lasers *in XI'th International Conference on Phenomena in Ionized Gases*. (Prague, 10-14 Sept. 1973)

[6] Haas, R. A. (1972): Plasma stability of electric discharges in molecular gases. Phys. Rev. A. **8**, 1017-1043.

[7] Nighan, W. L., and Wiegand, W. J. (1974): Causes of arcing in cw CO_2 convection laser discharges. Appl. Phys. Lett. **25**, 632-636.

[8] Nighan, W. L., and Wiegand, W. J. (1974): Influence of negative-ion processes on steady-state properties and striations in molecular gas discharges. Phys. Rev. A. **10**, 922-945.

[9] Wiegand, W. J., and Nighan, W. L. (1975): Influence of fluid-dynamic phenomenon on the occurrence of constriction in cw convection laser discharges. Appl. Phys. Lett. **26**, 554-557.

[10] Nighan, W. L. (1976): Stability of high-power molecular laser discharges *in Principles of Laser Plasmas* (G. Bekefi, ed.), pp 257 - 314. (Wiley, New York).

[11] Nighan, W. L. (1977): Causes of thermal instability in externally sustained molecular discharges. Phys. Rev. A. **15**, 1701-1720.

[12] Velikov, E. P., Pis'mennyi, V. D., and Rakhimov, A. T. (1977) The non-self-sustaining gas discharge for exciting continuous-wave gas lasers. Sov. Phys. Usp. **20,** 586-602.

[13] Bondarenko, A. V., Golubev, V. S., Dan'shchikov, E. V., Lebedev, F. V., and Ryazanov, A. V. (1979): thermal instability of a self-sustained gas discharge. Sov. J. Plasma Phys. **5**, 237-239.

[14] Baranov, V. Yu., Kazsakov, S. A., Malyuta, D. D., Mezhevov, V. S., Napartovich, A. P., Nisiev, V. G., Orlov, M. Yu., Starodubtsev, A. I., and Starostin, A. N. (1980): Average power limitations in high-repetition-rate pulsed gas lasers at 10.6 and 16 mm. Appl. Optics **19**, 930-936.

[15] Srivastava, B., Faria-e-Maia, F., Her, J., and Moran, J. (1992): High resolution computation of unsteady flows in pulsed lasers. AIAA J. **30**, 756-764.

[16] McKen, D. C., Seguin, H. J. J., and Tulip, J. (1976): Photoionization parameters in the carbon dioxide laser cases. IEEE J. Quantum Electron. **12**, 470-482.

[17] Dufour, M., Egger, H., Herziger, G., and Seelig, W. (1976): Highly uniform UV preionized CO_2 laser. Appl. Phys. **9**, 83-84.

[18] Babcock, R. V., Liberman, I., and Partlow, W. D. (1976): Volume ultraviolet photoionization from bare sparks. *IEEE J. Quantum Electron.* **12**, 29-34.

[19] Kline, L. E., and Denes, L. J. (1982): Preionized self-sustained laser discharges *in Applied Atomic Collision Physics v. 3 Gas Lasers* (E. W. McDaniel, and W. L. Nighan, eds.), pp. 387-422. (Academic Press, New York).

[20] Abrosimov, G. V., Klopovskii, K. S., Pulintes, T. S., Rakhimov, A. T., Saenko, V. B., and Suetin, N. V. (1985): Use of pulse-periodic photoionization discharges to excite quasi-cw gas lasers. Sov. J. Quantum Electron. **15,** 1487-1492.

[21] Scott, S. J., Smith, A. L. S. (1988): Ultraviolet photoionization in CO_2 TEA lasers. J. Appl. Phys. 64, 528-536.

[22] Egger, H., Dufour, M., Seelig, W. (1976): Inhomogeneities in TEA laser discharges. J. Appl. Phys. **47**, 4929-4933.

[23] Beverly III, R. E. (1988): Enhanced Transverse Discharge Stability using Preionization from an Auxiliary Barrier Discharge *in Seventh International Symposium on Gas Flow and Chemical Lasers*, Proc. SPIE **1031** pp. 458-468.

[24] Wester, R. (1991a): Frequency dependence of thermal volume instabilities in high-frequency CO_2 laser discharges. J. Appl. Phys. **70**, 3449-3454.

[25] Wester, R., Seiwert, S., Wagner, R. (1991b): Theoretical and experimental investigations of the filamentation of high frequency excited CO_2 laser discharges. J. Phys. D: Appl. Phys. **24**, 1796-1802.

[26] Raizer, Yu. P. (1991): *Gas Discharge Physics*. (Springer-Verlag, Berlin).

[27] Seguin, H. J. J., Nam, A. K., and Tulip, J. (1978): An efficient multielement cathode for high-power electric discharge laser applications. J. Appl. Phys. **49**, 4566-4567.

[28] Haas, R. A. (1982): Stability of excimer laser discharges in *Applied Atomic Collision Physics v. 3 Gas Lasers* (E. W. McDaniel, and W. L. Nighan, eds.), pp. 423-452. (Academic Press, New York)

[29] Smith, K., and Thompson, R. M. (1978): *Computer Modelling of Gas Lasers* (Plenum Press)

[30] Bletzinger, P., LaBorde, D. A., Bailey, W. F., Long (Jr.), W. H., Tannen, P. D., and Garscadden, A. (1975): Influence of contaminants on the CO2 electric-discharge laser. IEEE J. Quantum Electron. **11**, 317-323.

[31] Glagysh, G. G., and Samokhin, A. A. (1985): Limiting energy input to a glow discharge in a transverse gas flow. Teplofiz. Vys. Temp. **23**, 36-41.

[32] Glagysh, G. G., and Samokhin, A. A. (1979): Thermal discharge contraction in a fast-flow CO2 laser. Sov. J. Plasma Phys. **5**, 384-386.

[33] Kozyrev, A. V., and Korolev, Yu. D. (1981): Model of channel formation during constriction of pulsed spatial discharges. Sov. Phys. Tech. Phys. **26**, 1303-1305.

[34] Ul'yanov, K. N., and Chulkov, V. V. (1986): Instability of a glow discharge near the electrodes. Teplofiz. Vys. Temp. **25**, 1073-1079.

[35] Chandrasekhar, S. (1961): *Hydrodynamic and Hydromagnetic Stability* (Oxford University Press)

[36] Drazin, P. G., and Reid, W. H. (1981): *Hydrodynamic Stability* (Cambridge University Press)

[37] Jacob, J. H., and Mani, S. A. (1975): Thermal instability in high-power laser discharges. Appl. Phys. Lett. **26**, 53-55.

[38] Sorichetti, P. A. (1991): A Model of the Excitation Discharge of Fast Transversal Flow Lasers. IEEE J. Quantum Electron. **27**, 2340-2346.

[39] Nasser, E. (1965): *Fundamentals of Gaseous Ionization and Plasma Electronics.* (Wiley, New York).

[40] Hill, A. E. (1973): Continuous uniform excitation of medium-pressure CO_2 laser plasmas by means of controlled avalanche ionization. Appl. Phys. Lett. **22**, 670-673.

[41] Raizer, Yu. P., and Shapiro, G. I. (1978): Ionization-superheating instability of a glow discharge in time-varying fields and stabilizing effect of a train of high-voltage pulses. Sov. J. Plasma Phys. **4**, 477-481.

[42] Lowke, J. J., and Davies, D. K. (1977): Properties of electric discharge sustained by a uniform source of ionization. J. Appl. Phys. **48**, 4991-5000.

[43] von Engel, A. (1983): *Electric Plasmas: Their Nature and Uses.* (Taylor and Francis, New York).

[44] Gadiyak, G. V., Dobrivinskii, A. L., and Nasyrov, K. A. (1990): Computational modelling of a subsonic nonisentropic flow of a compressible gas in the discharge gap of a transverse flow continuous wave laser. J. Appl. Mech. Tech. Phys. **31**, 9-15.

[45] Wasserstrom, E., and Crispin, Y. (1982): Stability of glow discharge. J. Appl. Phys. **53**, 5565-5577

[46] Labun, A. H. (1991): *Reduction of Sheath Potentials in CO_2 Lasers.* (Ph.D. Dissertation, University of Alberta).

[47] Nath, A. K., Seguin, H. J. J., and Seguin, V. A. (1986): Optimization Studies of a Multikilowatt PIE CO_2 Laser. IEEE J. Quantum Electronics **22**, 268-274.

[48] Beverly III, R. E. (1982): Kinetic modelling of a fast-axial-flow CO2 laser. Opt. and Quantum Electron. **14**, 25-39.

[49] Leland, W. T. (1982): High energy CO_2 laser amplifiers *in Applied Atomic Collision Physics v. 3 Gas Lasers* (E. W. McDaniel, and W. L. Nighan, ed.), pp. 225-250. (Academic Press, New York).

[50] Witteman, W. J. (1987): *The CO_2 Laser.* (Springer-Verlag).

[51] Davis, A. R., Smith, K., and Thompson, R. M. (1975): TLASER - A CO_2 laser kinetics code. Computer Phys. Commun. **10**, 117-132.

[52] Lu, P. (1973): *Introduction to the Mechanics of Viscous Flow.* (Holt, Rinehart and Winston, Inc.)

[53] Braginskii, S. I. (1965): Transport processes in a plasma. Rev. Plasma Phys. **1**, 205-218.

[54] Mitchner, M., and Kruger, C. H. (1973): *Partially Ionized Gases.* (John Wiley & Sons)

[55] Galeev, I. G., and Timerkaev, B. A. (1987): A glow-discharge positive-column model for a flowing gas mixture. Teplofiz. Vys. Temp. **25**, 613-619.

[56] Lowke, J. J., Phelps, A. V., and Irwin, B. I. (1973): Predicted electron transport coefficients and operation characteristics of CO_2-N_2-He laser mixtures. J. Appl. Phys. **44**, 4664-4671.

[57] Nighan, W. L. (1970): Electron energy distributions and collision rates in electrically excited N_2, CO, and CO_2. Phys. Rev. A. **2**, 1989-2000.

[58] Wiegand, W. J., and Nighan, W. L. (1973): Plasma chemistry of CO_2-N_2-He discharges. Appl. Phys. Lett. **22**, 583-586.

[59] Beverly III, R. E. (1982): Ion aging effects on the dissociative-attachment instability in CO_2 lasers. Opt. and Quantum Electron. **14**, 501-513.

[60] Hokazono, H., Obara, M., and Midokoriwa, K. (1991): Theoretical operational life study of the closed-cycle transversely excited atmospheric CO_2 laser. J. Appl. Phys. **69**, 6850-6868.

[61] Mason, E. A., and McDaniel, E. W. (1988): *Transport Properties of Ions in Gases* (John Wiley & Sons)

[62] Thompson, J. B. (1961): Negative ions in the positive column of the oxygen discharge. Proc. Roy. Soc. A **250**,818-821.

[63] Ellis, H. W., Pai, R. Y., McDaniel, E. W., Mason, E. A., Viehland, L. A. (1976): Transport properties of gaseous ions over a wide energy range. At. Data Nucl. Data Tables **17**, 177-210.

[64] Ellis, H. W., McDaniel, E. W., Albritton, D. L., Viehland, L. A., Lin, S. L., Mason, E. A. (1978): Transport properties of gaseous ions over a wide energy range. Part II. At. Data Nucl. Data Tables **22**, 179-217.

[65] LeVeque, R. J., Yee, H. C. (1990): A study of numerical methods for hyperbolic conservation laws with stiff source terms. J. Comp. Phys. **86**, 187-210.

[66] Oran, E. S., Boris, J. P. (1987): *Numerical Simulation of Reactive Flow* (Elsevier Science Publishing Company)

[67] Strang, G. (1968): On the construction and comparison of difference schemes. SIAM J. Numer. Anal. **5**, 506-517.

[68] Potter, D. (1973): Computational Physics. John Wiley & Sons, Chichester.

[69] Boris, J. P. (1976): Flux-corrected transport modules for solving generalized continuity equations.

[70] Zwillinger, D. (1989): *Handbook of Differential Equations* (Academic Press, San Diego)

[71] Rogoff, G. L. (1972): Gas heating effects in the constriction of a high-pressure glow discharge column. Phys. of Fluids **15**, 1931-1940.

[72] Zauderer, E. (1983): *Partial Differential Equations of Applied Mathematics* (John Wiley & Sons)

[73] Akitt, D., and Sellathamby, C. V., personal communication.

[74] Moretti, G. (1982): "A Physical Approach to the Numerical Treatment of Boundary Conditions in Gas Dynamics" in *Numerical Boundary Conditions Proceedings*, NASA Conference Publication **2201** pp. 73-95.

[75] Poinsot, T. J., and Lele, S. K. (1992): Boundary conditions for direct simulations of compressible viscous flows. J. Comp. Phys. **101**, 104-129.

5

PIE Burst-Mode: Optical Waveform Control†

In the previous chapter, the effects of burst-mode operation on discharge stability were considered. In this chapter, we investigate the optical waveform control allowed by burst-mode operation. In particular, low duty-cycle operation produces pulsed radiation which has proven to be particularly well suited to deep penetration welding of heavy metal sections. [1] In this chapter, the connection between instantaneous laser discharge excitation and optical output is investigated experimentally, with an emphasis on waveforms relevant to pulsed applications – particularly deep penetration welding. The broader intent is to explore the possibilities of burst-mode optical waveform control, so that ultimately its advantage may be extended to other processes, and perhaps other laser systems – notably ZODIAC.

5.1 Introduction

Multikilowatt CO_2 lasers have found application in a variety of industrial material processing applications, including material cladding, cutting, surface heat treating, and welding. It is well documented that many such laser material processing interactions become increasingly effective and more economical when the optical energy is supplied to the interaction zone in a repetitively pulsed form rather than as CW radiation. For example, significant gains are found in welding high reflectivity materials such as aluminum and copper. [2]

However, CO_2 laser systems that are able to deliver pulsed multi-kilowatt average power output in a reliable and cost-effective manner are rare, due the limited flexibility of commonly used excitation systems. The PIE excitation system is not so limited; through burst-mode operation, a broad range of output waveforms may be produced. Through alteration of the impulse burst configuration (burst frequency and number of pulses per burst), laser output may be readily varied from distinct, independent pulses through to a continuous wave. Significant variation in optical pulse shape is also possible. Moreover, such pulse shaping is possible at multi-kW average power levels.

---

† Versions of the material in this chapter have been published as references [8,9].

Of particular interest is the distinct-pulse regime, which has proven to be particularly well suited to deep penetration welding of carbon steel. [3] In a comparison of burst-mode and CW mode performance, burst-mode operation was observed to achieve a factor of 2 improvement in weld penetration for a given average laser power & weld speed. [1]

Deep penetration laser welding requires establishment and maintenance of a vapor channel or keyhole throughout the material thickness. Prior to establishing a keyhole, the impinging laser radiation must first overcome the material surface reflectivity. In general, significant reflection is present until the surface temperature exceeds a thermal threshold, after which 10.6 μm energy is strongly absorbed. At this point, if sufficient energy density is present in the incident beam, a keyhole quickly forms. Thus, higher peak powers in the leading edge of incident pulses lead to more rapid keyhole formation for a given focal spot size, provided that the peak amplitude and duration are sufficient for the material thermal reflection threshold to be exceeded. While high initial peak power leads to more rapid deposition of laser energy into the material surface, appreciable average power is still necessary to maintain a keyhole, and to allow acceptable processing rates in deep penetration welds. Hence, both peak intensity and average power are important factors in deep penetration welding.

Current literature on pulsed laser welding stresses two main approaches: high repetition rate application of high peak-power, low average-power pulse trains; [2,4,5] and gated operation of CW laser systems.[6,7] Neither method is readily applicable to deep penetration welding, due to a lack of average power. In contrast, burst-mode PIE operation is able to produce pulse periodic laser output with very high peak power levels, while maintaining multi-kilowatt average powers. [8,9]

To aid application of the burst-mode process to laser material processing, it will be helpful to understand how the burst-mode control parameters affect the optical envelope of the laser waveform. Again, in burst-mode operation, the stream of photo-ionizing and avalanching impulses which under CW-excitation occur continuously at a frequency f_p, are instead gated at a burst frequency f_b and duty cycle

$$D_b \equiv N\left(\frac{f_b}{f_p}\right), \tag{5.1-1}$$

where N is the number of pulses in the resulting impulse bursts (*cf.* the burst-mode illustration, Figure 1.2-3)

In this chapter, the dependence of the laser optical envelope on the burst-mode control parameters f_b and N will be investigated, as a first study of burst-mode waveform control. Following a description of experimental apparatus in Section 5.2, in Section 5.3 experimental results are presented. Also, empirical relationships are developed which summarize the dependence of optical duty cycle and peak laser power on the discharge control parameters. Section 5.4 summarizes study findings.

5.2 Experimental Apparatus

The experiments to characterize optical envelope control were performed with PIE-IV, the fourth generation PIE system. Distinguishing features of the system are noted in Section 5.2.1, supplementing the overview of PIE systems given in Section 1.2. Optical waveforms were monitored with the optical detector described in Section 5.2.3. Discharge current waveforms, indicative of excitation conditions, were monitored with the fiber-optic optical isolator described in Section 5.2.2.

5.2.1 PIE-IV

PIE-IV is similar to PIE-III, used for the discharge instability studies of Chapter 4. Distinguishing features include a discharge volume of 80 L, [10] a 500 kVA power source, a real-time mode control system, [11,12] a digitally controlled wire feed and laser/MIG center, and a fully integrated computer controlled beam delivery and workpiece manipulation system.

The PIE-IV circuit diagram, presented in Figure 5.2-1, is identical to Figure 1.2-2 but for one important distinction: 10 mH arc prevention inductors (one for each polarity) in series with the 100 µH isolation inductors. This additional inductance prevents the rapid current decay between impulses which was possible in PIE-III, resulting in a markedly different current waveform. Implications of this feature will be further discussed in Section 5.3.1.

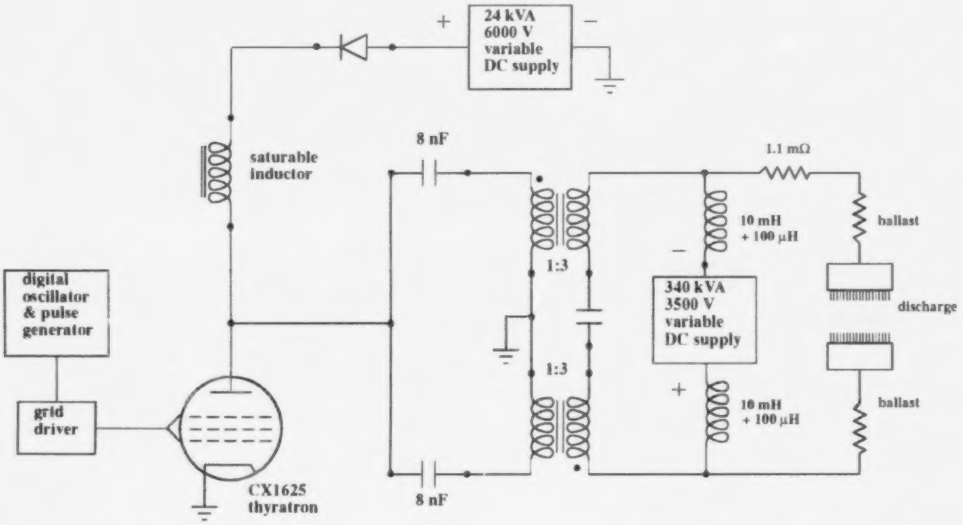
+
24 kVA
6000 V
variable
DC supply
−
saturable
inductor
8 nF
1.1 mΩ
10 mH
+ 100 µH
ballast
−
1:3
340 kVA
3500 V
variable
DC supply
discharge
digital
oscillator
& pulse
generator
1:3
+
10 mH
+ 100 µH
ballast
grid
driver
CX1625
thyratron
8 nF

Figure 5.2-1 PIE-IV circuit diagram.

Figure 5.2-2 illustrates the dependence of average discharge current and sustainer voltage on the burst frequency, under conditions of constant laser power. Figure 5.2-2 can be explained as follows. To achieve a given average current at a lower burst rate, an increase in DC sustainer voltage is required to compensate for the reduced production of electrons by the pulser. Because the curves in Figure 5.2-2 are for constant output power, the required increase in DC voltage at lower burst rates corresponds to current increasing with higher burst rates. It may also be noted in Figure 5.2-2 that the laser efficiency improved from 4 to 6% as the burst frequency is decreased from CW. Presumably this is because the higher discharge *E*/*n* required at lower burst rates is nearer that for optimal upper laser level pumping.

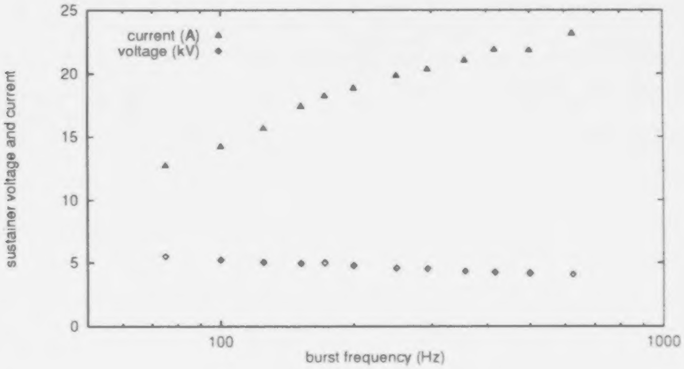

Figure 5.2-2 Discharge excitation voltage and current as a function of burst frequency, for P_{av}= 4 kW and n=7.

Burst-mode operation of PIE-IV presented a number of complications not anticipated in the initial design. The primary obstacle was insufficient sustainer voltage during pulsed operation. Indeed, in this study, 75 Hz was the minimum burst frequency for which sufficient voltage was available to attain usable output power levels. Based primarily on DC supply limitations, data was collected at 2, 4 and 6 kW, since operation over a wide range of burst frequencies was possible at these three power levels. Burst-mode operation is possible at higher average power levels, but with a corresponding decrease in f_b operating range.

5.2.2 Current Waveform Measurement

Current monitoring of high-current, high-voltage, broad-bandwidth waveforms is a non-trivial task. Attempts to measure the discharge current waveform with the available Hall effect probes and Rogowski coils proved unsuccessful;† each device gave a significantly different result, presumably due, in the case of the Rogowski coils, to signal errors introduced by saturation and droop, and in the case of the magnetic probe to limited device bandwidth.

Current waveforms were then instead obtained by sampling the voltage across a 1 mΩ precision resistor inserted in series with the discharge circuit, as is indicated in Figure 5.2-1. Optical isolators are not readily available which provide both the required degree of voltage isolation, and also μsec time resolution. Consequently, a fiber optic transmitter and receiver pair was developed and constructed, using a Motorola MFOE76 LED and a MFOD71 PIN diode. The design and performance specifications of this optical isolator are summarized in Appendix 5.A. Also, an analysis of waveform spectral content is performed to confirm that the detector bandwidth is sufficient.

5.2.3 Optical Detector Measurement

Optical waveform monitoring in the present case requires a detector which accommodates signals which have both broad bandwidth and a large dynamic range. A Vigo Sensor PEM-L-2 photo-electromagnetic (PEM) detector [15] is well suited to this application. [16,17] Implementation of the detector, as well as the low noise amplifier used in conjunction it, is discussed in Appendix 5.B. Amplifier performance specifications are included, as well an analysis of waveform spectral content to confirm that the bandwidth is sufficient.

In the PEM effect, infra-red photons are absorbed at the surface of a semiconductor producing free electron-hole pairs which diffuse from the surface into the bulk. An applied magnetic field separates the pairs as they diffuse inward. Separation results in an open circuit electrical voltage potential across the semiconductor terminals which is proportional to the intensity of the incident photons.

Our experiments indicated that this type of detector suffers from a thermally induced signal offset. Thermally generated electron-hole pairs are indistinguishable from optically generated carriers. Therefore, when the incident optical power elevates the substrate temperature, thermal electron-hole creation generates an output signal offset. This offset was observed in a number of distinct-pulse test cases, and found to depend only on the average incident laser power, to which it was proportional.

Once the source of signal offset was identified, a simple offset correction routine was incorporated in the awk processing scripts. Given n data points d_i, with known thermal offset P_{therm}, the power P_i corresponding to each d_i is computed with

$$P_i = \Lambda d_i - P_{therm} , \qquad (5.2\text{-}1)$$

where

---

† This observation raises doubts regarding the accuracy of the PIE-III current waveforms reported in Chapter 4. Those waveforms, taken from references [13,14], were obtained with one of the Rogowski coils found here to give spurious results.

$$\Lambda = \frac{(P_{av} - P_{therm})}{\frac{1}{n}\sum_{i=1}^{n} d_i} . \tag{5.2-2}$$

Here, Λ is the data scaling factor and P_{therm} is the detector thermal offset power equivalent. P_{av} is the average laser power, measured independently with a spinning-cone calorimeter.[18] This scaling method is independent of oscilloscope scale, and so allows for maximum resolution of the optical waveform.

P_{therm} was determined from a single low frequency case for which the optical output was known to decay to zero between bursts. The offset signal is taken as P_{therm} which can then be used to scale all data sets taken at the same average laser power.

5.2.4 Data Processing

A PC-based data acquisition system, in conjunction with a Phillips 3323 digital storage oscilloscope, was used to acquire, process and store signal waveforms in digital format. [3] A variety of UNIX *awk* scripts were created to process and scale the raw data files, and to subsequently automatically generate *GNUPLOT* [19] plot files with appropriate graphic scales and labelling. The scripts, in total consisting of about 400 lines, messaged one another via file records, since awk does not support subroutines. Thus, several hundred waveforms were rapidly processed and plotted. This data acquisition and processing system was used for all of the optical and current waveforms collected in this study.

5.3 Experimental Results

Experiments to characterize optical envelope control were performed with PIE-IV, using the sensor apparatus and data acquisition systems described in Section 5.2. The range possible waveforms obtainable under burst-mode operation is illustrated in Section 5.3.1. In Section 5.3.2, empirical relationships are developed to quantify the dependence of optical duty cycle and peak laser power on the burst-mode control parameters.

5.3.1 Overview of Burst-Mode Operation

Burst-mode operation of the PIE-IV laser system was observed to produce a wide variety of optical output characteristics, ranging from a purely pulsed profile to CW. Figures 5.3-1-5.3-3 present representative cases. Although these cases are for 4 kW optical output, the qualitative trend is independent of power level. A typical low burst frequency, small burst duty cycle case is shown in Figure 5.3-1(a). Such excitation induces fast rising optical pulses which have high peak power, and decay to zero in-between pulses. This characteristic profile is referred to here as *distinct-pulse*.

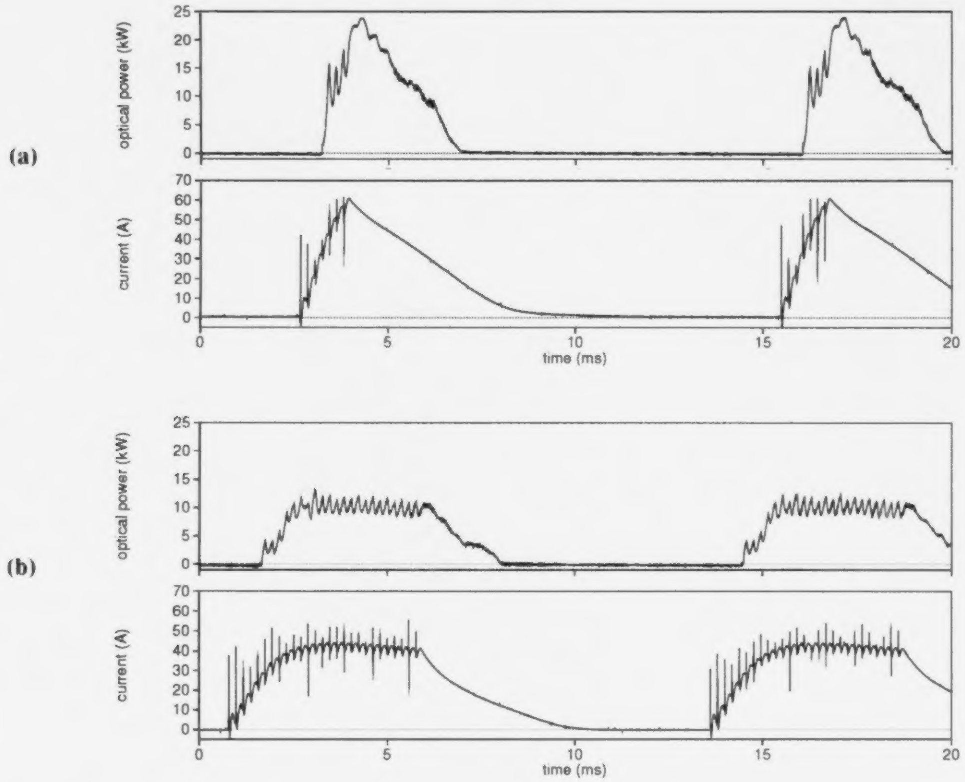

Figure 5.3-1 Laser output and discharge current waveforms at an average laser power of 4 kW; illustrating effect of altering the number of pulses (N) while holding burst frequency (f_b) constant at 75 Hz: (a) $N = 7$; (b) $N = 27$

Increasing burst frequency eventually results in continuous laser output in-between pulses, as is seen in Figure 5.3-2(a). This characteristic profile is referred to here as *continuous-offset*. Under CW excitation, both the discharge current and optical output waveforms retain an oscillatory nature, a result of the 5 kHz excitation. This is seen in Figure 5.3-3. In all current waveform plots, the vertical spikes are due to pulser circuit noise, and are coincident with pulser impulses. A more detailed discussion follows of how variation in the discharge control parameters affects burst-mode operation, in terms of both the discharge current and optical output waveforms.

In the distinct-pulse regime, as illustrated in Figure 5.3-1(a), each successive impulse on the leading edge of a burst increases the discharge conductivity. As was discussed in Chapter 4, this is due to an increase in the average electron density over the pulser cycle. Increasing electron density occurs only so long as electron gain exceeds electron loss over the pulser cycle. If N were to be increased with f_b held constant, ultimately an equilibrium state would be reached, where electron loss over the pulse period would offset electron gain over the same period. This asymptotic

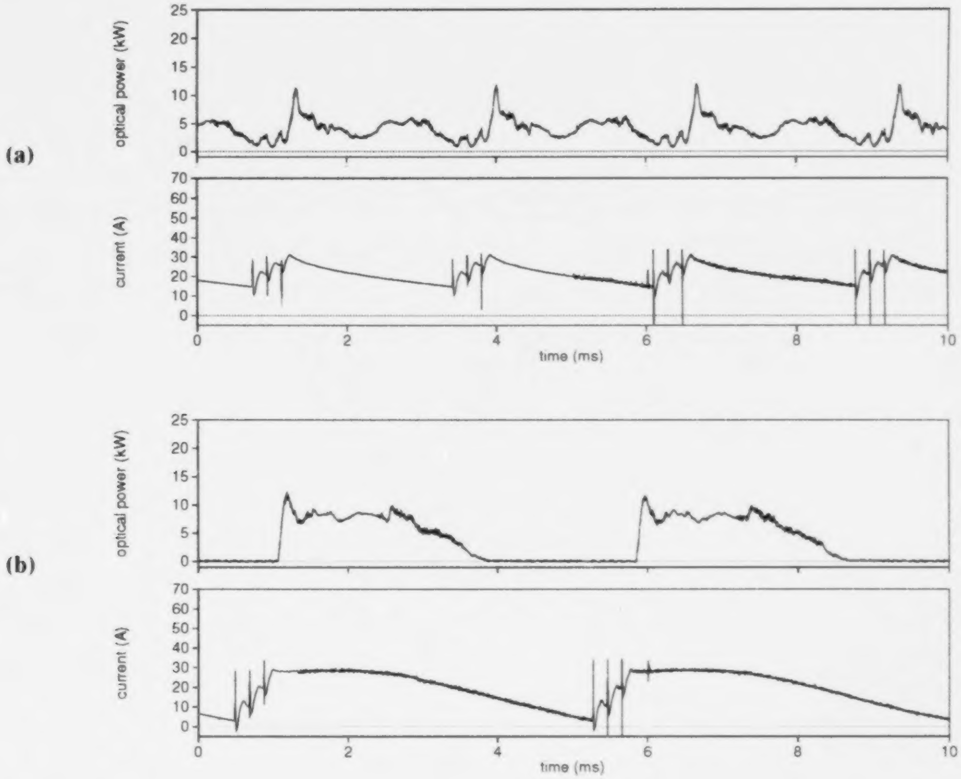

Figure 5.3-2 Laser output and discharge current waveforms at an average laser power of 4 kW; illustrating effect of altering f_b while holding N constant at 3: (a) f_b = 357 Hz; (b) f_b = 200 Hz.

approach to equilibrium is illustrated in the case of Figure 5.3-1(b), which has the same burst frequency as the case of Figure 5.3-1(a), but also a much larger burst duty cycle. As the discharge state reaches equilibrium, so too does the output laser power. Rates of current rise and decay are limited by the 20 mH arc prevention inductance to a characteristic time of approximately 1 msec.

The decay of current to zero in the inter-burst interval is indicative of the non self-sustained nature of the PIE discharge. It is notable that the final 3.5 ms of the current decay in the inter-burst interval is approximately linear. One may hypothesize that since this time corresponds to the gas residence time, the linear decay is related to an effective reduction of discharge area caused by convective flow sweeping the abnormal glow discharge from the inter-electrode area. (*cf.* Section 4.4.6).[†]

[†] This observation again raises doubts about the accuracy of the PIE-III current waveforms reported in Chapter 4, obtained from [13,14]. Those waveforms did not exhibit the linear decay seen here, although videographic evidence of PIE-III discharge operation did indicate that discharge area decreased (linearly) with time, during the inter-burst interval.

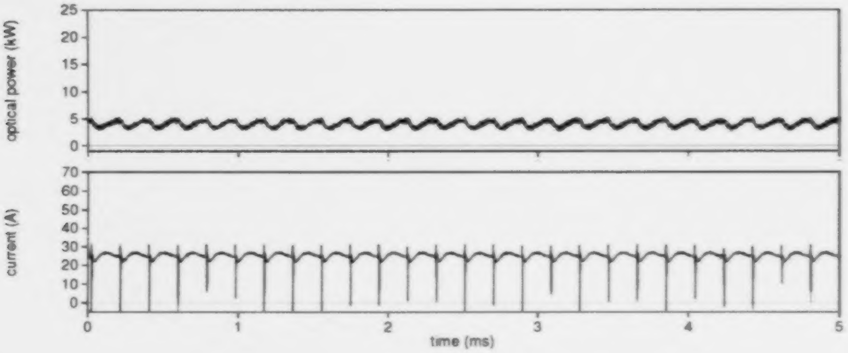

Figure 5.3-3 Laser output and discharge current waveforms for CW operation at an average laser power of 4 kW.

As either N or f_b is increased, eventually the discharge current will have insufficient time to decay to zero between bursts. This is true for both of the cases presented in Figure 5.3-2. However, since there is a threshold input power required for lasing, it is still possible for the optical waveform to decay to zero, as is true in the case of Figure 5.3-2(b). This is a consequence of laser resonator cavity losses. The gain-switched spike seen in both Figure 5.3-2 is characteristic of burst configurations which allow the discharge current to drop below the lasing threshold during the inter-burst interval.

As either N or f_b is increased further, eventually the burst sequence becomes a continuous impulse stream, and CW excitation is attained. In Figure 5.3-3, a relatively constant discharge state is seen to be maintained by a f_p=5 kHz impulse stream. Oscillation of discharge conditions over the pulse cycle result in periodic modulation of the optical waveform. While Figure 5.3-3 indicates PIE output intensity is not constant under conditions of CW excitation, welding performance is comparable to that of other industrial CW systems. [1] Under normal welding conditions, on time scales associated with acceptable processing rates, this 5 kHz modulation is quasi-steady.

5.3.2 Empirical Equation Development

As is demonstrated in Figures 5.3-1 to 5.3-3, burst excitation is capable of producing a wide variety of optical outputs, ranging from pulsed to continuous. The transition from the distinct-pulse regime, through the continuous-offset regime to CW excitation as f_b is increased is illustrated in Figure 5.3-4. As f_b increases while N is held constant at 7, the peak power decreases to approach asymptotically its CW value. At approximately 200 Hz, a continuous offset appears in-between the optical pulses.† Finally, at 715 Hz, CW operation is achieved for N=7. Figure 5.3-4 demonstrates that this characteristic is independent of average laser power. Note that average CW power is the average of the peak and offset powers, as they are defined here (*cf.* Figure 5.3-3).

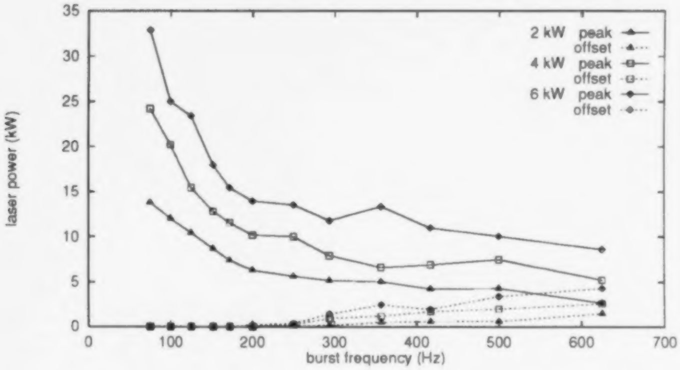

Figure 5.3-4 Dependence of laser peak and offset power on burst frequency and average laser power for N=7.

It is the distinct-pulse regime ($f_b < 200$ Hz) that is of primary interest for application to deep penetration processing. Of particular interest in this application are the waveform peak power (P_p), energy per pulse (E_p) and optical duty cycle (D_o). [3] In general, the higher the peak optical power, the deeper is the weld penetration, for a given processing rate. [17] Also, for complete penetration through the material, and for keyhole formation, a threshold E_p must be exceeded. [17] In the distinct-pulse regime, energy per pulse is simply defined as

$$E_p = \frac{P_{av}}{f_b}. \tag{5.3-1}$$

Closely linked to the P_p and E_p is D_o, which represents the on-time of the optical output in the pulse train.

Peak power is found to be inversely proportional to optical duty cycle when average power is held constant, as indicated in Figure 5.3-5. This expected result follows from conservation of energy. At small optical duty cycles, a large gain-switched population inversion results in extremely high peak power and subsequent rapid decay (*cf.* Figure 1.2-4(b)). As optical duty cycle is increased, peak power drops off due to weaker gain media pumping; for a given average power deposition, the larger the excitation duty cycle is, the smaller the initial gain switched population inversion is.

In the ensuing section, empirical relationships will be developed which express P_p and D_o in the pulse-periodic regime as simple functions of N, f_b, and P_{av}. These results will be useful for developing a pulsed laser welding specification. [17]

---

† For f_b=200 and N=7, the inter-burst interval is approximately equal to the gas residence time. The observation of distinct pulses only at lower frequencies is again is consistent with the interpretation of Chapter 4 that the final current decay in the inter-burst interval is due to an effective reduction of discharge area by convective flow (*cf.* Section 4.4.6)

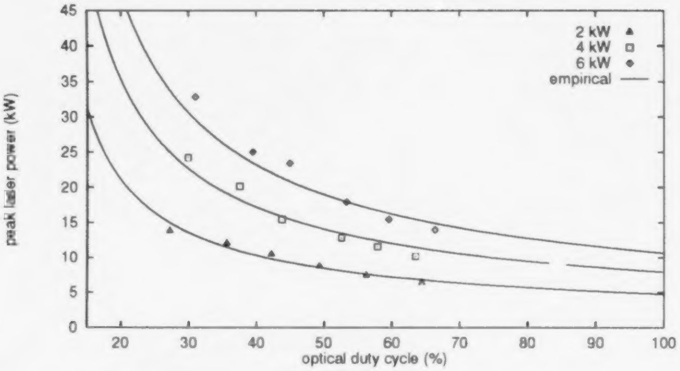

Figure 5.3-5 Peak laser power with respect to optical duty cycle, for $N = 7$. The solid lines represent empirical characteristics (5.3-5) and (5.3-6).

Optical Duty Cycle

In the distinct-pulse regime, D_o is roughly proportional to f_b, and depends only weakly on total average power. This is shown in Figure 5.3-6. As f_b increases into the continuous-offset regime, the D_o vs. f_b characteristics for different power levels become non-linear and diverge from one another. It is further observed in the distinct-pulse regime that D_o depends simply on N, allowing an empirical equation of the form $D_o(f_b,N)$ to be developed.

First, consider the dependence of D_o on f_b with N held constant at 7, as is illustrated in Figure 5.3-6. Only a weak dependence of D_o on laser power is observed. Neglecting this dependence, the best linear fit to the data of Figure 5.3-6 is

$$D_0|_{N=7} = 0.290f_b + 7.85 \tag{5.3-2}$$

Next, consider the dependence of D_o on N over the range of burst frequencies in the distinct-pulse regime. Figure 5.3-7 presents experimental results for the average power range 2-6kW. Dependence at each frequency is seen to be essentially linear, and so may be represented by

$$D_0 = \alpha N + \beta. \tag{5.3-3}$$

Table 5.3-1 contains a summary of the best fit linear relationships for the combined data of all power levels. Conveniently, α is in turn also a linear function of f_b: the best fit linear function is

$$\alpha = 0.010f_b + 0.40 . \tag{5.3-4}$$

Now the general empirical equation for D_o, having the form of (5.3-3), follows from (5.3-2) and (5.3-4):

$$D_0 = (0.010f_b + 0.40)N + 0.22f_b + 5.0 \tag{5.3-5}$$

Optical duty cycle characteristics predicted by this relation are indicated in Figure 5.3-7 as solid lines. The discrepancy between empirical prediction and experiment is seen to be typically less than 10%.

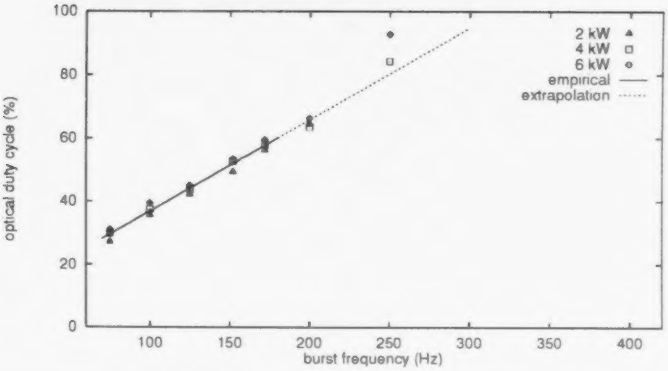

Figure 5.3-6 Dependence of optical duty cycle on burst frequency and average laser power for N=7.

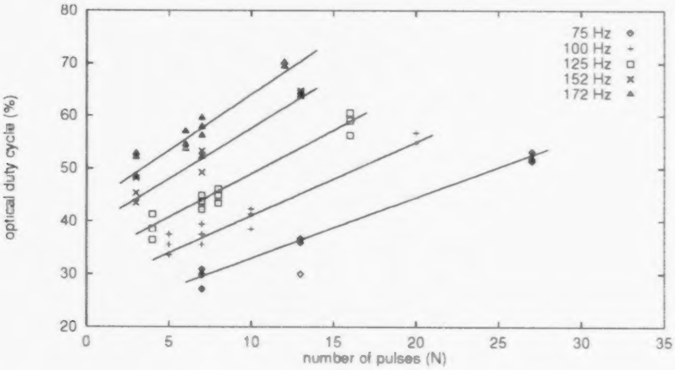

Figure 5.3-7 Optical duty cycle as a function of pulse number and burst frequency. Experimental points are for average laser powers of 2 kW, 4 kW, and 6 kW. Solid lines represent empirical equation (5.3-5).

Table 5.3-1 Best-fit parameters for equation (5.3-3)

f_b	α	β
75	1.15	21.6
100	1.39	27.1
125	1.64	32.6
152	1.91	38.5
172	2.11	42.9

As a further test of (5.3-5), and illustration of pulsed laser behavioral characteristics, the dependence of D_o on E_p is considered for cases of constant burst duty cycle. In Figure 5.3-8, cases of 10%, 20%, and 40% burst duty cycles are presented. Experimental data is again seen to be well represented by (5.3-5). Given this degree of agreement, (5.3-5) capture the essence of D_o dependence on the discharge control parameters.

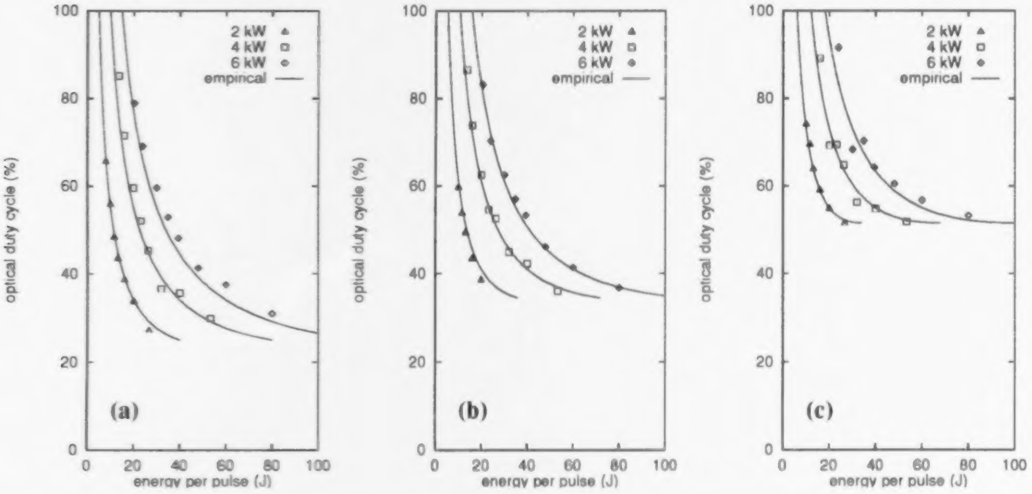

Figure 5.3-8 Optical duty cycle with respect to energy per pulse and average laser power for a constant burst duty cycle (a) 10%, (b) 20%, and (c) 40%. Points represent experimental data, and solid lines represent the empirical equation (5.3-5).

Peak Optical Power

In the distinct-pulse regime, P_p is observed to depend most strongly on E_p, and also to a lesser extent on N. An empirical equation for P_p of the form $P_p(E_p, N)$ is hypothesized.

Experiments indicate that P_p depends most weakly on N for $N < 15$. Moreover, for $N < 15$, a large fraction of the observed variation on P_p with N appears to be due to random error. If P_p is averaged over $N < 15$, a simple relationship between average P_p and E_p results, as is illustrated in Figure 5.3-9(a). The relationship is well approximated as:

$$P_p = 1.2\,(E_p)^{0.75} \quad \text{kW}, \tag{5.3-6}$$

were the units of E_p are Joules. The form of this equation is constant with the expectation that $P_p \rightarrow 0$ in the limit of small E_p. In Figure 5.3-9(b), a comparison is given between empirical equation (5.3-6) and P_p without averaging over the dependence on N. The discrepancy for $N < 15$ cases is less than 25%. All of the points scattered well below the empirical characteristic

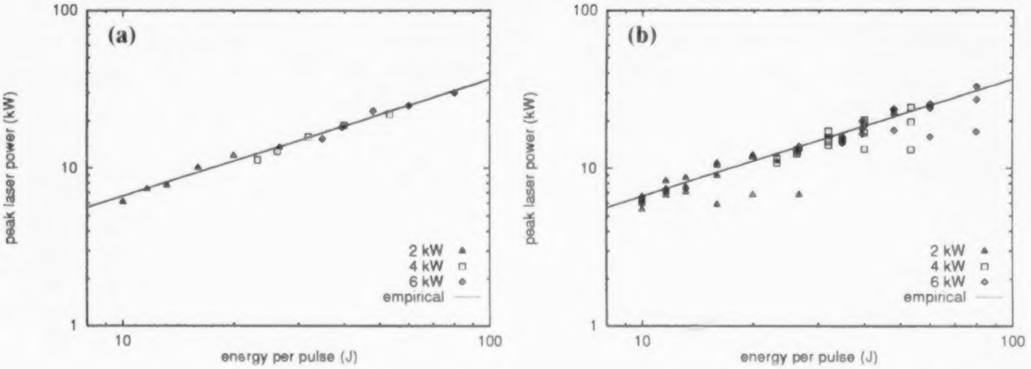

Figure 5.3-9 Peak laser power as a function of energy per pulse (a) with P_p averaged over $N < 15$, and (b) with all data points.

corresponding to $N > 15$ cases. It is apparent that (5.3-6) does not capture the entire functional dependence of P_p on burst control parameters.

In other preliminary analysis, it appears that the N dependence may be described in terms of dependence on pulse profile shape.[†] A simple numerical characterization of the pulse shape follows from a 'shape factor'

$$S \equiv \frac{f_b E_p}{D_o P_p}, \tag{5.3-7}$$

defined such that $E_p = S\,(P_p D_o / f_b)$. In this definition, S is seen to be a geometric factor, with S=0.5 corresponding to a triangle, and S=1.0 corresponds to a rectangle. In the distinct-pulse

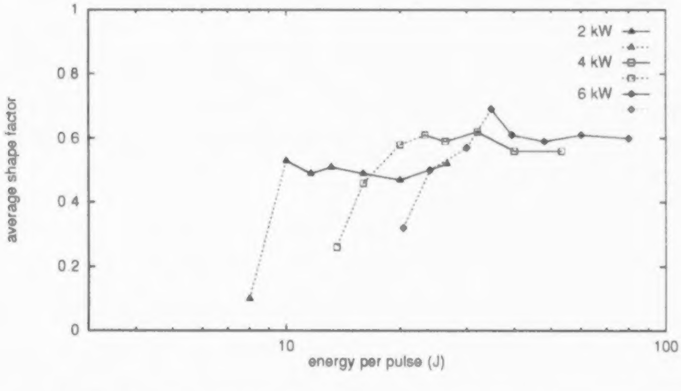

Figure 5.3-10 Average shape factor, as a function of energy per pulse, averaged over N<15. The solid curve corresponds to the distinct-pulse regime, while the dashed lines correspond to the onset of continuous-offset.

[†] It also appears possible to also correlate the change in α to a change in shape factor.

regime, it is observed qualitatively that the pulse shape is only weakly dependant on P_{av} and N for N<15. This is demonstrated in Figure 5.3-10. Over the range of experiments considered here, S varies by about 20% in the distinct-pulse regime. For $f_b > 200$ Hz, a dramatic change in shape factor is evident. The inequality on N<15 can also be rephrased as a condition of similar shape factor. Consider for example Figure 5.3-1(b), where the onset of a flat-topped optical pulses is seen to occur at approximately N=15.

It is instructive to consider a final illustration of (5.3-6), namely, the dependence of P_p on f_b for constant N. In Figure 5.3-11, the experimental data for N=7 at all power levels is compared with empirical equation (5.3-6). It is significant that although (5.3-6) was derived for only f_b<200, the agreement between the experimental data and the empirical relation is quite good even in the continuous-offset regime.

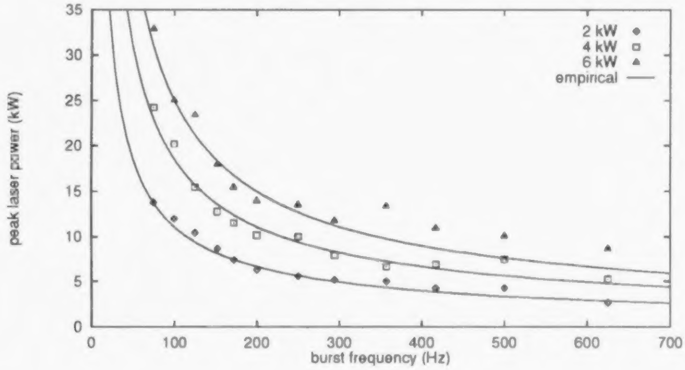

Figure 5.3-11 Peak laser power with respect to burst frequency, for N=7 pulses. Points are experimental data and the solid line represents empirical equation (5.3-6), which are here extrapolated into the continuous-offset regime.

5.3.3 Summary

Investigation of the distinct-pulse regime indicates that laser output characteristics may be predicted through the use of two simple empirical relationships. The validity of the empirical relationships is confirmed through a number of test cases where they accurately reproduce data obtained experimentally. Functional dependence of D_o on N and f_b is represented by empirical relationship (5.3-5) with 5% error. Empirical relationship (5.3-6) is not as accurate, representing the relationship between P_p, E_p and N with a 25% error. Improvement of the latter empirical relationship is anticipated through investigation of how pulse shape depends on N.

The importance of these empirical relationships have resulted in an improved understanding and control of the burst parameters which govern deep penetration welding performance. [3]

5.4 Summary

A unique advancement in the flexibility of high-power CO_2 lasers has been presented. Convenient control of laser output waveform has been achieved through burst-mode operation of a PIE CO_2 laser. When operated in burst-mode, PIE lasers are able to produce a broad range of optical output characteristics. Laser output can be varied from distinct, independent pulses through to a continuous wave. In this chapter, we have demonstrated simultaneous control of optical pulse duration and peak power, through choice of the excitation burst frequency and the number of impulses per burst. Since burst-mode operation encompasses both high peak and high average power pulsed operation, it promises to lend itself to a wide variety of applications. Empirical relationships summarizing the dependence of optical duty cycle and peak laser power on the burst-mode control parameters have been developed to impart control and insight into deep penetration welding.

The current and optical waveform monitors developed for the analysis of this chapter are expected to have further application in the analysis of PIE system behavior. In particular, information about the instantaneous discharge state will aid subsequent simulations of both discharge instability and laser kinetics.

Bibliography

[1] Scott, S. W. C., Rogozinski, K. and Seguin, H. J. J. (1994): High peak power, burst mode operation of a multikilowatt CO_2 laser for deep penetration welding. Appl. Phys. Lett. **65**, 286-288.

[2] Thompson, A. (1989): Advances in laser-pulse performance. Ind. Laser Rev. **2**, 10-15.

[3] Scott, S. W. C. (1996): *A CO_2 Laser Burst Excitation Technique for Deep Penetration Welding* (Ph.D. Dissertation, University of Alberta).

[4] Schock, W., Hall, Th., Wildermuth, E., Wessel, K., Gehringer, E., Schnee, P., and Hadinger, F. (1988): Compact transverse flow CO_2 laser with RF excitation. Proc. SPIE **1031**, 76-81.

[5] Schwarzenbach, A. P., and Hunziker, U. W. (1987): Industrial CO_2 laser with high overall efficiency. Proc. SPIE **801**, 43-48.

[6] Kimura, S., Sano, N., Sugiyama, S. and Mizutame, M. (1987): Welding properties with high power pulsed CO_2. lasers. Proc. LAMP '87, 169-174.

[7] McCay, M.H., McCay, T.D., Dahotre, N.B., Sharp, C.M., Sedghinasab, A. and Gopinathan, S. (1989): Pulsed laser welding of INCO 718. L.I.A. ICALEO '89, 229-238.

[8] Scott, S. W. C., Strohschein, J. D., and Seguin, H. J. J. (1995): Deep penetration welding performance of a high average power, multi-kilowatt peak power carbon dioxide laser. ICALEO '95.

[9] Scott, S. W. C., Strohschein, J. D., Seguin, H. J. J., Capjack, C. E., and Reshef, H.W. (1996): Optical performance of a burst mode multi-kilowatt CO_2 laser. Appl. Opt **24**., 4740.

[10] Merchant, V. E., Cervenan, M. R. and Seguin, H. J. J. (1985): An industrial quality 20 kW infrared laser. Proc. LASERS '85, 642-646.

[11] Akitt, D. R., Seguin, H. J. J., Cervenan, M. R. and Nikumb, S. K. (1990): Electronic mode and power control of a high-power CO_2 laser. IEEE J. Quant. Electron. **26**, 1413-1417.

[12] Sellathamby, C. V., Seguin, H. J. J. and Nikumb, S. K. (1990): Performance characteristics of a high power CO_2 laser with computer vision mode and power control. Appl. Opt. **29**, 4499-4503.

[13] Nikumb, S. K., Seguin, H. J. J., Seguin, V. A., Willis, R. J. and Reshef, H. W.(1989): High-average power-pulsed performance of a multikilowatt PIE laser. IEEE J. Quant. Electron. **25**, 1725-1735.

[14] Nikumb, S. K., Seguin, H. J. J.,Seguin, V. A., Willis, R. J., Cheng, Z. and Reshef, H. W. (1989): Burst-mode gain switched technique for high peak and average optical energy extraction. Appl. Opt. **28**, 1624-1627.

[15] Vigo Sensor, *Model PEM-L-2*, Boston Electronics.

[16] Seguin, V. A., personal communication.

[17] Scott, S. W. C., personal communication.

[18] Seguin, H. J. J., Seguin, V. A., Nath, A. K., and Radzion, J. (1986): Spinning water film power meter for high-power cw lasers. Rev. Sci. Inst. **57**, 185-190.

[19] Williams, T., and Kelley, C. (1993): *GNUPLOT: An Interactive Plotting Program.* (info-gnuplot@dartmouth.edu).

[20] Stremler, F. G. (1982): *Introduction to Communication Systems* (Addison-Wesley, Reading).

[21] Press, W. H., Teukolsky, S. A., Vetterling, W. T., and Flannery, B. P. (1992): *Numerical Recipes in C: The Art of Scientific Computing*, 2nd ed. (Cambridge University Press).

[22] Merchant, V. E., Seguin, H. J. J. and Dow, J. (1979): Novel transformer designs for high-power high-repetition-rate applications. Rev. Sci. Inst. **50**, 1151-1153.

[23] Seguin, H. J. J., Nam, A. K. and Tulip, J. (1978): An efficient multielement cathode for high-power electric discharge laser applications. J. Appl. Phys. **49**, 4566-4567.

Appendix 5.A:
Ultra-Fast High-Resolution Optical Isolator

Optical isolators are not readily available which provide both the required degree of voltage isolation (10's kV), and μsec resolution. Consequently, a fiber optic transmitter and receiver pair was constructed, based on a Motorola MFOE76 LED and a MFOD71 PIN diode. The pair was separated by 1 m of EH4001 plastic core fiber, which provides effectively ideal isolation, considering that 5 cm of fiber isolates 40 kV and has capacitance of 0.01 pF. With this isolator, it was possible to resolve a mV signal having an offset of many kV.

The performance of the optical isolator in terms of its transfer function is given Figure 5.B-1. That the isolator bandwidth considerably exceed the measured signal bandwidth is a necessary condition for measurement accuracy. The power spectrum [20] of a typical current waveform obtained with the isolator is presented in Figure 5.B-2. The isolator bandwidth is seen to be more than sufficient for the present application. Computations were performed with the routine SPCTRM from reference [21], using 128 point periodograms.

Construction Details

Circuit diagrams for the transmitter and receiver units are given in Figures 5.A-3 and 5.A-4, respectively.

Because the laser pulser circuit emits strong RFI, the isolator circuit must be well shielded. The transmitter circuit and its power supply are contained within a small copper box (3.5 x 7 x 5.5 cm^3) which floats at the potential of the laser discharge circuit (several kV). This box is in turn nested within a much larger aluminum box (3.5 x 7 x 5.5 cm^3), which is grounded with a broad copper strap. Separation between the boxes is maintained by perspex spacers. The role of the interior box is to collect the displacement current due to the 1 pF capacitance of the nested structure. In this way, the effect of displacement current on circuit performance is minimized.

Noise in the receiver circuit is minimized through shielding and single point grounding. The receiver circuit enclosure is not grounded, while the receiver circuit common is grounded only at the oscilloscope.

For both circuits, power is supplied by 9V battery sources. This voltage is then regulated to prevent battery aging from altering circuit bias conditions. Bias stability is especially important in the transmitter circuit, to ensure that the LED remains in the (small) linear region of its characteristic.

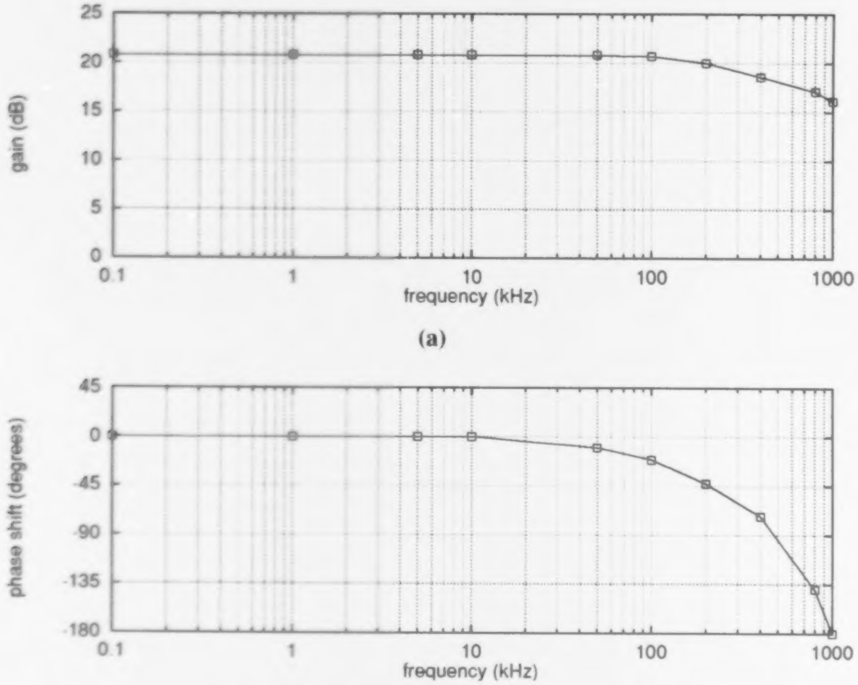

(a)

(b)

Figure 5.A-1 Optical isolator transfer function
(a) amplitude response (b) phase response

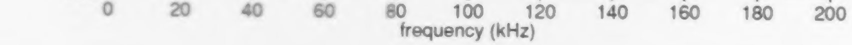

Figure 5.A-2 Normalized spectral power density of typical current waveform.

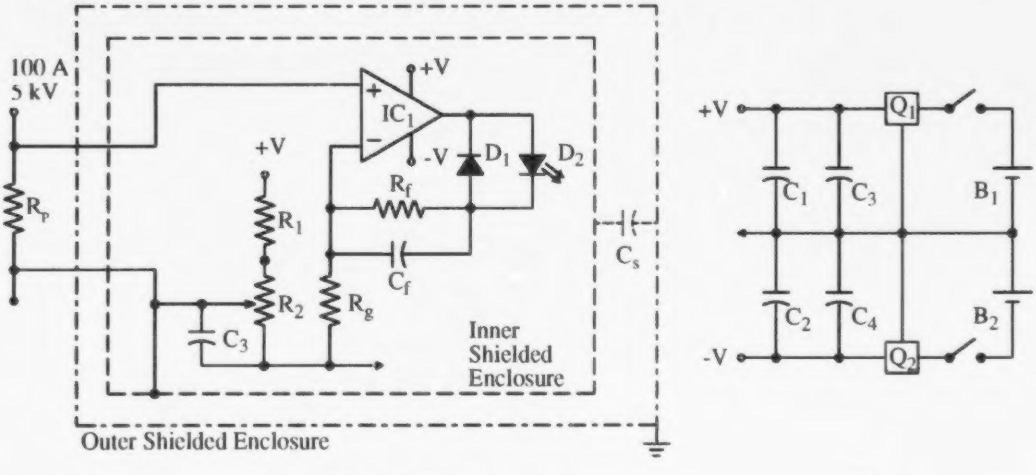
100 A
5 kV
R_p
+V
IC_1
-V
D_1
D_2
R_f
R_1
C_f
R_2
R_g
C_3
Inner Shielded Enclosure
C_s
Outer Shielded Enclosure
+V
-V
Q_1
Q_2
C_1
C_3
C_2
C_4
B_1
B_2

(a) **(b)**

Figure 5.A-3 Optical isolator: circuit diagrams for (a) the transmitter, and (b) the transmitter power supply.

Table 5.A-1 Optical isolator: transmitter circuit elements

element	description	value
B_1, B_2	battery supply	9 V
C_1, C_2, C_3	line filters	100 μF
C_4, C_5	regulator filters	0.1 nF
C_f	stabilization capacitor	1.5 nF
C_s	nested enclosure structure capacitance	≈1 pF
D_1	reverse spike protection diode high speed switching	1N4148
D_2	visible (red) LED emitter: connected to receiver diode D_1 with 1 m of EH4001 plastic core fiber	MFOE76
IC_1	high speed ultralow noise op-amp	OP 37
Q_1 Q_2	voltage regulators	78L05 (+5V) 79L05 (- 5V)
R_1 R_2	set point bias resistors: 5 mA offset is required to place D_2 in linear region of its characteristic for a 2mA signal	3.9 kΩ 0.5 kΩ potentiometer
R_f	feedback and protection resistor	91 Ω
R_g	trasconductance resistor	39 Ω
R_p	high current resistor	1.1 mΩ

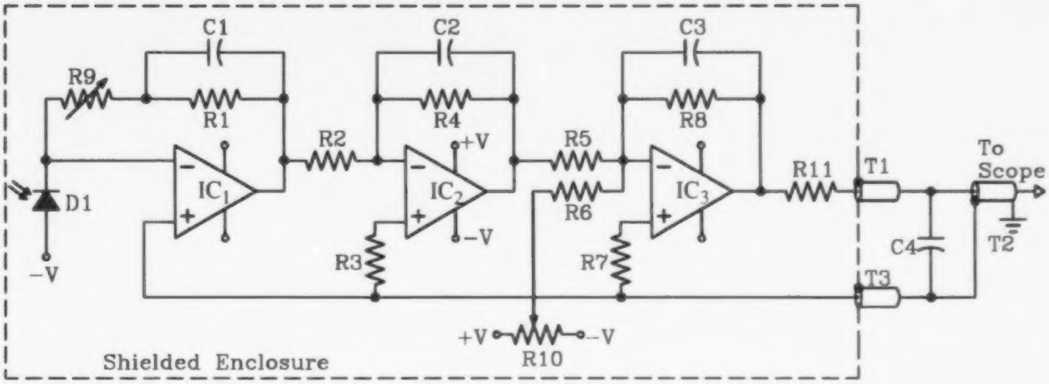
C1
C2
C3
R9
R1
R4
R8
R2
R5
+V
IC1
IC2
IC3
R11
T1
To Scope
D1
R6
-V
C4
T2
R3
R7
T3
-V
+V
-V
R10
Shielded Enclosure

Figure 5.A-4 Optical isolator: receiver circuit diagram. This circuit uses a power supply identical to that of the transmitter circuit (Figure 5.A-3 (b)).

Table 5.A-2 Optical isolator: receiver circuit elements

element	description	value
D_1	PIN diode: connected to transmitter D_2 with 1m of EH4001 plastic core fiber	MFOD71
C_1,C_2 C_3	stabilization capacitor	22 pF 3.3 pF
C_4	filter capacitor	8.0 pF
IC_1,IC_2,IC_3	ultralow noise high gain op-amp	OP 37
R_9	gain adjustment resistor	10 kΩ
R_1,R_4 R_8	feedback resistor	5.6 kΩ 51 kΩ
R_2 R_5	input resistor	820 Ω 8.2 kΩ
R_6 R_{10}	offset adjustment resistor	39 kΩ 10 kΩ pot
R_3 R_7	offset compensation resistor	680 Ω 6.8 kΩ
R_{11}	matching resistor	51 Ω
T_1,T_2,T_3	coaxial line	RG-58 (20 m)

Appendix 5.B:
Optical Detector

Many detectors are available for 10.6 μm IR radiation, however multi-kilowatt CO_2 laser beam detection is hampered by the high average power incident on sensor devices. Pulsed lasers with sufficiently small duty cycles pose less of a problem in terms of average power, but peak powers can also lead to detector saturation and damage. For detection of high peak power signals, pyroelectric detectors are commonly used.

For the burst application in this study, it is of interest to resolve both the low and high frequency content of the optical pulses. Consequently, a broad bandwidth detector is required. While pyroelectric detectors have excellent high frequency response, they saturate easily in low frequency applications. Photovoltaic detectors are more commonly used in such situations. The Mercury Cadmium Telluride (MCT) detector is the most common type of photovoltaic detector for such applications. MCT detectors are available in cryogenically cooled, thermoelectrically cooled and room temperature (RT) models. In general, the sensitivity increases with decreasing operating temperature.

For this application, a RT MCT detector [15] was chosen for its broad bandwidth (DC-800 MHz) and relative insensitivity. It was still necessary to attenuate the laser output by 6 orders of magnitude. This was done with ZnSe attenuators. [3]

The low-noise amplifier circuit used with the detector is given in Figure 5.B-3 and Table 5.B-1. Amplifier performance in terms of its transfer function is given in Figure 5.B-1. The power spectrum [20] of a typical optical waveform measured with this detector and amplifier is presented in Figure 5.B-2, demonstrating that the circuit bandwidth is sufficiently wide for the present application. Computations were performed with the routine SPCTRM from reference [21], breaking the 4096 sample-point waveforms into 128 point periodograms

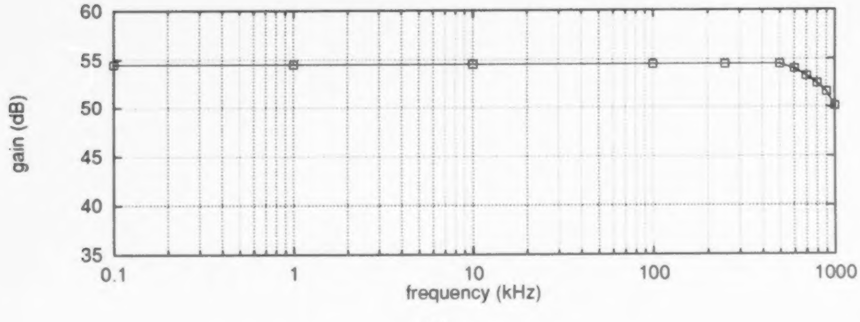

(a)

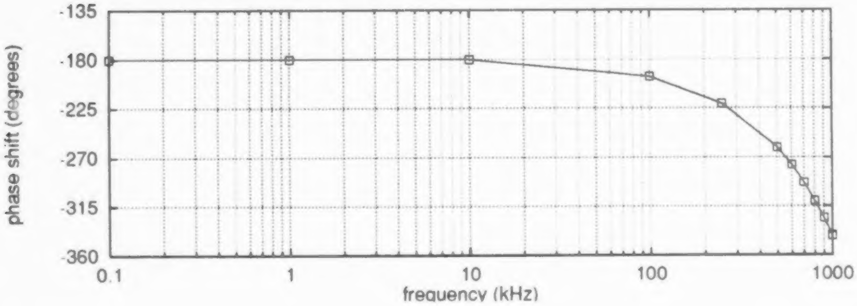

(b)

Figure 5.B-1 PEM amplifier gain characteristics
(a) amplitude response (b) phase response

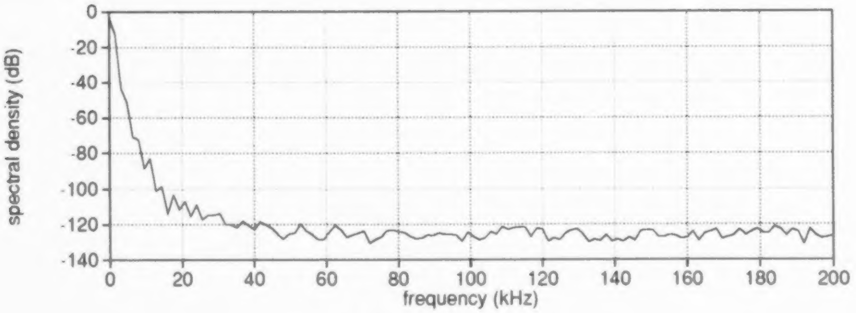

Figure 5.B-2 Normalized spectral power density of typical optical waveform.

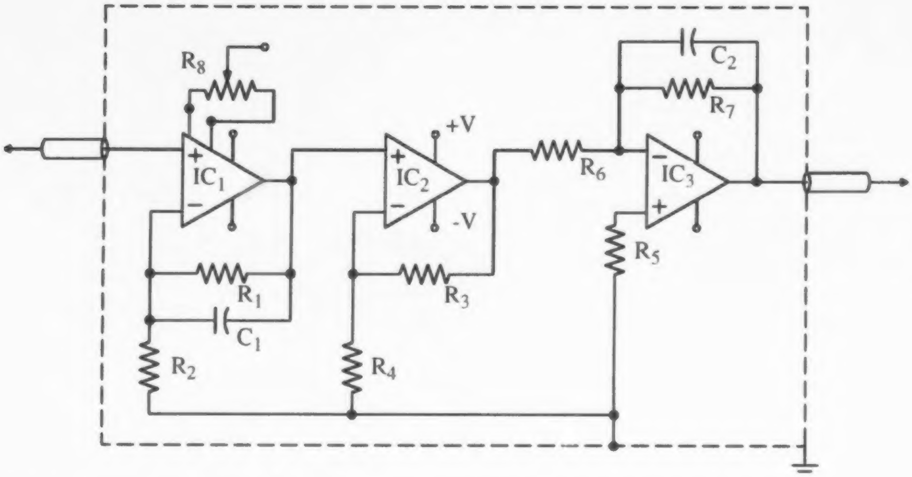

Figure 5.B-3 PEM amplifier circuit diagram.

Table 5.B-1 PEM amplifier circuit components

element	description	value
C_1 C_2	stabilization capacitor	100 pF 3.3 pF
IC_1, IC_2, IC_3	ultra-low noise high gain op-amp	OP 37
R_1, R_3 R_7	feedback resistors	2 kΩ 20 kΩ
R_2, R_4 R_6	input resistors	270 Ω 2.7 kΩ
R_5	offset compensation	2.4 kΩ
R_8	offset adjustment	10 kΩ pot
V	battery supply	9 V

6

PIE Burst-Mode: Electron Transport and Rate Coefficients

In the two previous chapters, we have studied the effects of burst-mode operation on discharge stability and on the laser output waveform. It was concluded that both studies could benefit considerably from further numerical analysis. However the available published electron transport and rate coefficients, required for such analysis, were found to be inadequate for treatment of PIE discharges. In this chapter, in order to facilitate further numerical analysis of PIE discharges and burst-mode effects, we solve the Boltzmann Equation to obtain the electron transport and rate coefficients for typical PIE discharge conditions.

6.1 Introduction

Electron transport and rate coefficients are fundamental to discharge and laser modelling. In particular cases, these may be obtained experimentally. However, in general they must be obtained computationally by either solving the Boltzmann Equation (BE) for the electron energy distribution function, or by direct simulation with a Monte Carlo method. [1] Since the latter method is prohibitively expensive computationally, direct solution of the BE is prevalent.

To compute electron transport and rate coefficients useful for simulations of a PIE discharge, the BE solver ELENDIF [2] was acquired, as were the appropriate electron-collision cross-sections. A program GAMUT was created which calls ELENDIF as a subroutine. GAMUT monitors ELENDIF solution convergence, while altering both the resolution and extent of the ELENDIF finite difference mesh, until a prescribed accuracy is satisfied. GAMUT's algorithm, described in Section 6.2, is based on the observation that numerical errors introduced by mesh extent and resolution are not strongly interdependent. In Section 6.3, the accuracy of GAMUT, ELENDIF, and the cross-sections are tested by comparing computed electron transport and rate coefficients against available experimental data. In Section 6.3, computations of electron transport and rate coefficients for the PIE laser mix (He:N_2:CO_2:CO = 16:10:1:1) are presented and discussed.

6.2 Boltzmann Equation Solver

Boltzmann's transport equation for electrons in an electric field $\boldsymbol{E}$ is [1,3,4]

$$\left(\frac{\partial}{\partial t} + \boldsymbol{v} \bullet \nabla_r + \frac{e\boldsymbol{E}}{m_e} \bullet \nabla_v\right) nf = n\left(\frac{\partial f}{\partial t}\right)_{\text{collisions}}, \tag{6.2-1}$$

where $n(\boldsymbol{r}, t)$ is the number of electrons at position $\boldsymbol{r}$ with time t, and $f(\boldsymbol{r}, \boldsymbol{v}, t)$ is the velocity distribution function for electrons at time t with position $\boldsymbol{r}$ and velocity $\boldsymbol{v}$. This equation expresses conservation of electrons in phase-space. Specifically, the left side of the equality describes advection in phase-space, and the right side amounts to source terms which account for collisional effects. Collisions cause electrons to jump between non-adjacent regions of phase-space. Note that the electron energy distribution function is simply related to the velocity distribution function by $\varepsilon^{1/2} f(\varepsilon)\, d\varepsilon \sim v^2 f(v)\, dv$.

ELENDIF

ELENDIF solves a spatially uniform version of (6.2-1), treating in detail the effects of elastic, inelastic, and superelastic collisions. [2] The solution is expanded in terms of spherical harmonics, which makes use of its symmetry with respect to a uniform electric field $\boldsymbol{E}$. It is assumed that the solution is only weakly anisotropic, such that the harmonic expansion may be limited to two terms: an isotropic term f_0 and a small directional term $f_1 \ll f_0$, *i.e.*,

$$f(\boldsymbol{v}) = f_0(v) + \frac{\boldsymbol{v} \bullet \boldsymbol{E}}{vE} f_1(v). \tag{6.2-2}$$

Further, it is assumed that inelastic collisions are effectively isotropic, so that collision anisotropy is fully accounted for in the elastic momentum transfer cross-sections. This approach, known as the two-term isotropic inelastic formulation, is the conventional method used to solve Boltzmann's equation for weak to moderate electric fields. [1]

For this formulation to be valid, the sum of inelastic cross-sections must be small compared to the sum of the elastic momentum transfer cross-sections. [6] This condition is known to be violated by molecular gases such as CO_2, CO, N_2, particularly at moderate E/n, where vibrational cross-sections are relatively large. [1] Pitchford *et al.* have estimated that for N_2, the errors introduced by the two-term spherical harmonic approach are roughly 1%, 5%, and 30% respectively for drift velocities, diffusion coefficients, and electronic excitation.[†] [6] Hayashi [7] suggests that in general, the error introduced by a two-term approximation is 10 to 20%.

Solvers using multi-term spherical harmonics expansions have been developed which produce results comparable in accuracy with those obtained by Monte Carlo simulations. [4] However, neither these nor the Monte Carlo codes are widely available. Moreover, the body of available cross-sections sets[‡] have been derived for use with two-term BE solvers. Hence, there is little option at this point but to use a two-term solver.

[†] Note that these errors are relative to Monte Carlo simulation results derived the *same* cross-section set (*i.e* the errors are not relative to experimental results)

In any case, errors of 20% are tolerable for the present purposes. However, the potential errors do motivate the confirmation of ELENDIF accuracy in Section 6.3.

GAMUT

GAMUT uses ELENDIF to automatically compute BE solutions for a specified list of discharge conditions. GAMUT ensures that for each case considered, the ELENDIF solution converges to a specified accuracy. Achievable accuracy is typically on the order of 1%. ELENDIF solution convergence is controlled by two numerical parameters: EEDF mesh extent (ε_{max}), and mesh resolution ($\Delta\varepsilon$). These two parameters are observed to have essentially independent effects on solution accuracy, and are hence adjusted independently. Mesh refinement by GAMUT proceeds as follows.

First, it is desirable to minimize mesh extent, so that allowable resolution is maximized for a fixed number of mesh points. Beginning with a case of moderate mesh resolution, the mesh extent is reduced while resolution is held constant. Meanwhile, variation of the important solution parameters (*e.g.*, vibrational excitation rates) are monitored. Mesh extent is reduced until the accumulated change in solution exceeds a specified tolerance (typically 0.1%). This approach assumes that the EEDF truncation error is negligible for the first ε_{max}. To ensure that this is the case, the list of discharge cases input to GAMUT is arranged in order of decreasing E/n, so that ε_{max} decreases monotonically as the list is processed.

Second, with the mesh extent now fixed, mesh resolution is increased until the solution accuracy meets a specified accuracy (typically 1%). Solution accuracy is not directly observable. However, it can be estimated from the solution convergence rate, if the convergence order is known. Convergence trials with ELENDIF suggest that the convergence order is between one and two. An upper bound on solution error (e) may therefore be obtained by assuming the convergence is first order. If the mesh is refined according to $\Delta\varepsilon_{i+1} = f\Delta\varepsilon_i$ (where i counts the steps in the resolution sequence), and the solution error $e \sim \Delta\varepsilon$, then

$$|e_{i+1}| \approx \frac{f|\delta_{i+1}|}{1-f}, \qquad (6.2\text{-}3)$$

where δ_{i+1} is the solution change as the mesh resolution is refined from $\Delta\varepsilon_i$ to $\Delta\varepsilon_{i+1}$. Eq. (6.2-3) follows from $\delta_{i+1} = e_{i+1} - e_i$.

The large volumes of ELENDIF output generated by GAMUT are processed automatically with a UNIX awk script, which extracts and tabulates the data of interest. This script is approximately 200 lines in length.

---

‡ At electron energies where vibrational and electronic excitation become important, cross-sections cannot be determined uniquely. Rather a *set* of cross-sections can be created which in a self-consistent way reproduce the experimental swarm data. Cross-section sets are generally determined by iteratively comparing the swarm parameters predicted by the cross-sections and the actual experimental data. Computer codes based on the two-term spherical approximation have been most frequently used because of their superior computational speed. See for example references [1] and [6].

Cross-Section Data

The cross-section sets required to determine the EEDF in a pure CO_2 laser gas mix are summarized in Table 6.2-1. A cross-section for rotational excitation is included within the N_2 set., but with neither CO_2 nor CO. For the latter cases the, collisional excitation of molecular rotational modes is accounted for in ELENDIF with the continuous approximation to rotation (CAR). [2]

Table 6.2-1 Electron collision cross-sections and CARS parameters used in ELENDIF computations.

gas	cross-section source	CAR parameter [2]
He	Hayashi [10,11]	
N_2	Phelps *et al.* [5,2]	
CO_2	Hayashi [9,11]	$4.10\ 10^{-4}$ (quadrupole)
CO	Hayashi [10,11]	$1.45\ 10^{-12}$ (dipole)

6.3 Tests of ELENDIF, GAMUT and Cross-Sections

ELENDIF, GAMUT, and the cross-sections were tested by comparing simulation predictions with available experimental data, prior to computing electron transport and rate coefficients for the PIE laser gas mixture.

For instability analysis and laser kinetics studies, vibrational excitation rate coefficients are of particular importance. These are not directly measurable, however. Lakshiminarasimha *et al.* [12] argue that comparison with more accessible swarm parameters can provide a good check of computed vibrational excitation rate coefficients. Two such measurable swarm parameters which closely reflect details of the EEDF are the ionization coefficient and the characteristic energy (the ratio of transverse diffusion coefficient to mobility; $\varepsilon_k = D_T/\mu_e$).

The following comparisons suggest that ELENDIF, GAMUT, and the cross-sections of Table 6.2-1 are sufficiently accurate for the present purposes.

Pure Gases

As a first test, computed electron drift velocities were compared with representative electron swarm data for pure mixtures of the primary CO_2 laser constituents. These comparisons are summarized in Figure 6.3-1. For He (Figure 6.3-1(a)), ELENDIF predictions agree well with experiment. For the molecular gases, the agreement is similarly good only for low reduced field strengths. Above 20Td, ELENDIF overestimates the drift velocity in N_2 (Figure 6.3-1(b)) and CO_2 (Figure 6.3-1(c)) by as much as 30%. For the case of CO (Figure 6.3-1(d)), ELENDIF predictions were compared with those produced by the BE solver BACKPR [13] using Land's cross-sections. [14] The two codes produce similar results when Land's cross-sections are used for both. This agreement confirms that ELENDIF has been implemented properly here. (Note that BACKPR also

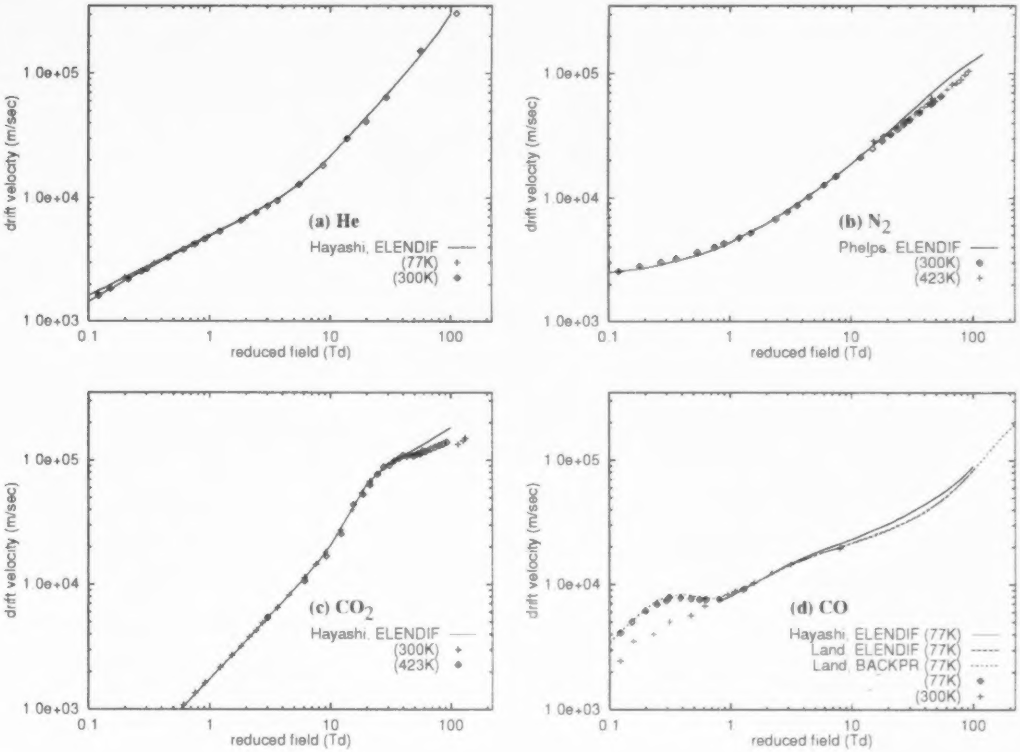

Figure 6.3-1 Electron drift velocity in pure mixes of the primary CO_2 laser gases. Points are experimental data, and lines are ELENDIF results. Data for 423K is from [16]. All other data is from [18], and originates in various work: (a) [19] and [21] with additional 300K points from [17] (b) [21] (c) [22] with additional 300K points from [20] (d) [22]

uses the two-term approximation.) Drift velocities produced with Hayashi's cross-sections exceed those predicted by Land's by as much 30%. Again this discrepancy is over the range 10-100eV.

These discrepancies for the molecular gases are presumably due to the onset of strong vibrational excitation above $E/\mathrm{n} \approx 20$ Td, which renders the two-term approximation inaccurate. Pitchford *et al.* observed that, for pure N_2, the errors introduced by the two-term approximation were largest at 70 Td, where the ratio of inelastic to elastic cross-sections is largest. [6] Notably though, in their tests errors in drift velocity did not exceed a few percent. This would suggest that the discrepancies observed here for molecular gases are not due to the two-term approximation, but rather are inherent to the cross-sections. That this is the case seems unlikely though, since cross-sections sets are specifically derived to accurately reproduce swarm data, in particular drift velocity.

In the following section, laser gas mixtures with low molecular fractions are considered. Good agreement between computation and experiment is observed, which suggests that the discrepancies observed here with the pure gases may in fact be due to the two-term approximation.[†] Pitchford *et al.* do note that the two-term approximation, although invalid for a pure molecular gas, may be valid if that molecular gas is sufficiently dilute in an atomic gas. [6] As the molecular gas fraction is decreased, the sum of the elastic momentum transfer cross-sections increases relative to the sum of inelastic cross-sections, until eventually the two-term approximation is applicable.

CO_2 Laser Gas Mixtures

As a second and more relevant test, transport coefficients and ionization rate coefficients were computed for two typical CO_2 laser gas mixtures and compared against available experimental data. Results are summarized in Figure 6.3-2. These comparisons are seen to more favorable than those for the pure molecular gases. In all cases, the discrepancy between computation and experiment is less than 20%. Notably, the agreement is good not only for drift velocities, but also for characteristic energy and for ionization rates, which are expected to be more sensitive to errors in the computed EEDF. [12] These results suggest that ELENDIF and the cross-sections of Table 6.2-1 may reasonably be applied to compute electron transport and rate coefficients for CO_2 laser gas mixtures.

In any case, applicability of the two-term approximation to CO_2 laser gas mixtures merits further investigation.[‡] Specifically, detailed consideration of the mixture-weighted cross-sections, and tests of mixtures with higher molecular gas fractions would be instructive.

6.4 Solutions for a PIE Gas Mixture

Transport and reaction rate coefficients computed with ELENDIF for a typical PIE gas mixture are summarized in Figure 6.4-2 and Figure 6.4-3. The concentrations of minority constituents are

---

[†] In which case, the observations of Pitchford *et al.* are particular to the cross-section set used in their tests.

[‡] Also important in this connection are the cross-section sets themselves. [6] Cross-section sets which, when used with a two-term method, accurately reproduce swarm data under conditions when the provisos of the two-term method are violated (e.g., pure CO), are not be expected to produce accurate results when used under conditions when the two-term provisos are satisfied (*e.g.*, a He-rich CO_2 laser gas mix). Conversely, cross-sections sets derived to produce accurate results with a Monte Carlo method are expected to produce accurate results when used with a two-term method under conditions which satisfy the two-term method provisos. These observations lead one to conjecture that the discrepancies between drift velocities in CO predicted by the different cross-section sets (Figure 6.3-1(d)) may result from such a distinction. Supporting this hypothesis is that in [15], Land's cross-sections are shown to reproduce experimental data within 1%, when used with a two term method under conditions where the method is presumably inaccurate.

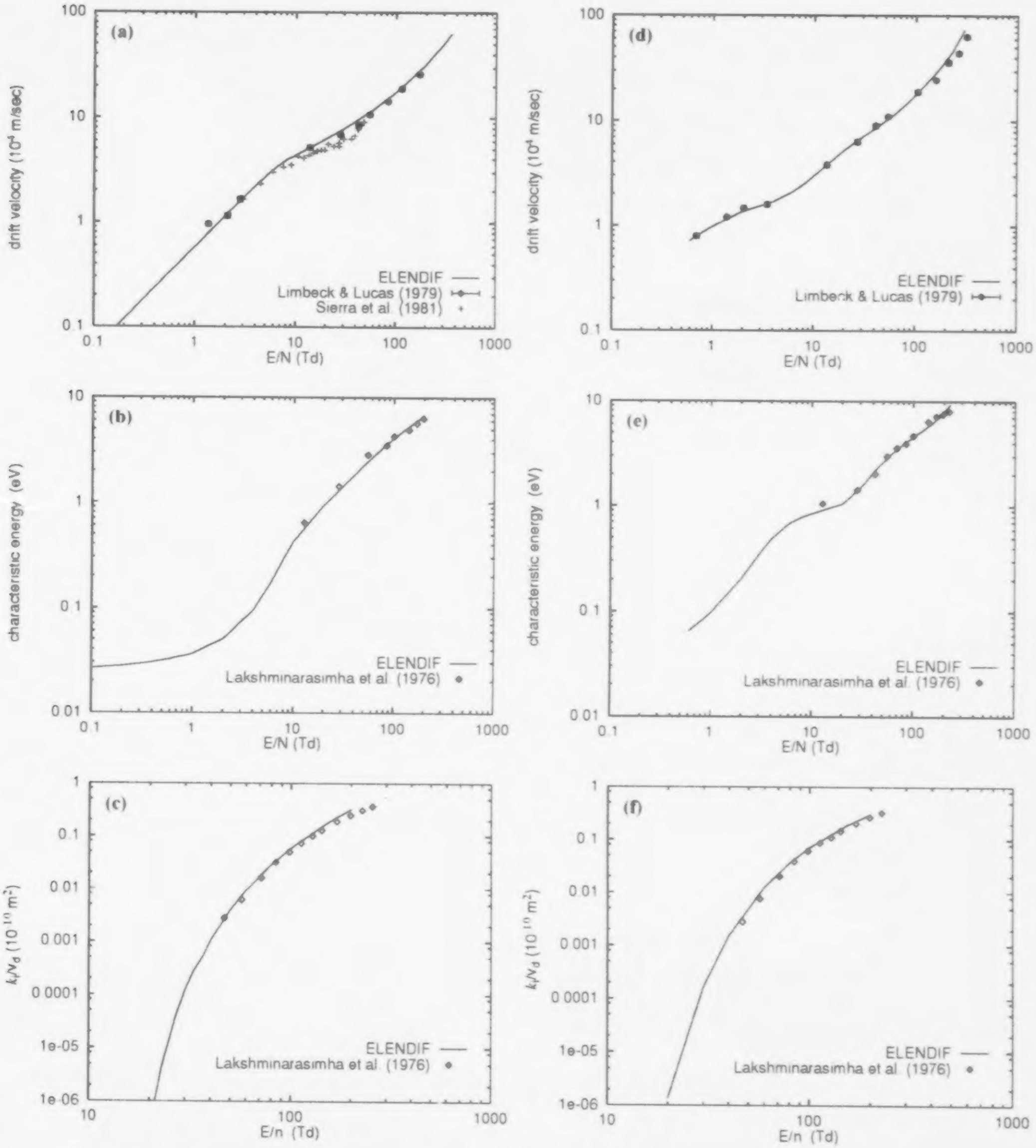

Figure 6.3-2 Comparison of ELENDIF calculations with experimental data for two CO_2 laser gas mixes at 300 K: (a) $He:N_2:CO_2$ = 12:1:4, and (b) $He:N_2:CO_2$ = 30:7:1. Experimental data from references [12,16,23].

assumed to be sufficiently low that they effect the EEDF negligibly.† Reaction rate coefficients (k) involving to these minority species may be computed with [2]

$$k = \left(\frac{2e}{m_e}\right)^{1/2}\int_0^\infty \sigma(\varepsilon)f(\varepsilon)\,\varepsilon\, d\varepsilon, \tag{6.4-1}$$

where $\sigma(\varepsilon)$ is the processes cross-section [27,28], and $f(\varepsilon)$ is the EEDF, normalized such that

$$\int_0^\infty \varepsilon^{1/2} f(\varepsilon)\, d\varepsilon = 1. \tag{6.4-2}$$

Power transfer fractions are summarized in Figure 6.4-1. From the standpoint of excitation efficiency, reduced field strengths around 30 Td appear best suited to efficient laser operation. At 30 Td, approximately 80% of discharge power is deposited into the upper laser level. At this *E/n*, only 1% of power goes directly to translational-rotational heating. An additional 14% goes to CO vibrational excitation. Deviation from 30 Td results in a considerable decline in direct excitation of the upper laser level. At lower *E/n*, the power is redirected to CO excitation, and at higher *E/n* it goes to electronic excitation.

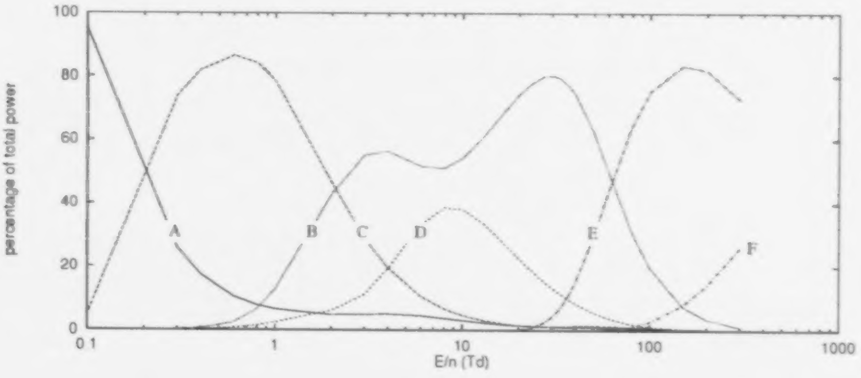

Figure 6.4-1 Electron-collision power transfer fractions in He:N$_2$:CO$_2$:CO = 16:10:1:1. at 300 K to (A) elastic collisions and rotational excitation; (B) excitation of upper laser ASM of CO$_2$ and the first eight vibrational modes of N$_2$ (together these effectively constitute the upper laser level); (C) excitation of BM and SSM of CO$_2$; (D) excitation of CO vibrational modes; (E) electronic excitation; and (F) ionization.

---

† Note that is has been assumed here that CO and CO$_2$ concentrations are constant. In fact, their concentrations are expected to change significantly in the presence of a discharge, due to CO$_2$ dissociation $e + CO_2 \rightarrow CO + O + e$ and reformation. [25,26]

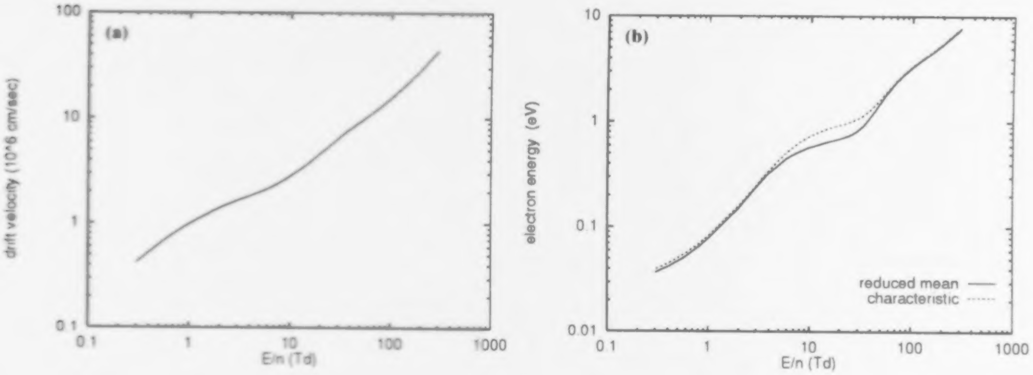

Figure 6.4-2 Transport coefficients for electrons in He:N_2:CO_2:CO = 16:10:1:1 at 300 K: (a) drift velocity; and (b) reduced mean energy and characteristic energy.

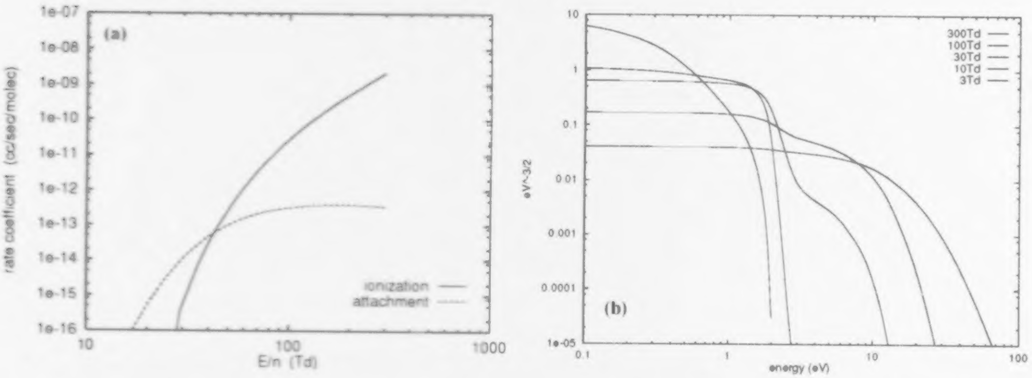

Figure 6.4-3 Reaction rate coefficients for electrons in He:N_2:CO_2:CO = 16:10:1:1 at 300 K: (a) mixture weighted ionization and attachment rates for the primary gas constituents; and (b) the EEDF, from which other reaction rates for minority species can be derived using (6.4-1).

All computations summarized here assume that the gas mixture is at thermal equilibrium. Under discharge conditions of interest for laser operation, the vibrational modes in particular are at considerable non-equilibrium with the ambient gas temperature. The EEDF is known to be strongly affected by vibrational temperatures via superelastic collisions. [29,30] Since the high-energy tail of the EEDF is sensitive to effects of superelastic collision, processes such as ionization are also expected to be strongly affected. It remains to investigate this sensitivity, and to make appropriate allowance in subsequent instability and laser kinetics studies.

It should also be noted in Figure 6.4-1 that at 10 Td, the excitation rate of CO vibrational modes is comparable to that of the upper laser level. Clearly then, any proper consideration of laser kinetics and optimal excitation conditions must account for effects of resonant energy transfer between CO, CO_2, and N_2.

6.5 Summary

To assuage concerns that assumptions in the ELENDIF algorithm were violated by the molecular gas mixtures typical of CO_2 lasers, transport and rate coefficients predicted by ELENDIF for a variety of pure gases and laser gas mixtures were compared against published experimental results. Acceptable agreement was found over the E/n range of interest in PIE calculations, so calculations were performed for a typical PIE laser mixture. These results, summarized in Section 6.4, will be useful for the laser kinetics simulations proposed in Chapter 5, and for the further instability studies required by Chapter 4. They will allow gas-mixture dependent effects to be better modelled. Also, because of their much wider range of parameterization, the problems experienced with CODE1 due to limited parameterization ranges may be avoided.

The results of this chapter are also required for operation of the public domain codes PLASKEM [31-33] and TLASER, [34] which were acquired along with ELENDIF from the Computer Physics Communications library, and debugged. PLASKEM, a plasma chemistry simulator, can be used to determine dominant discharge chemical species and reactions. Additional knowledge of plasma chemistry is required for extensions to the instability modelling effort. TLASER, a five temperature laser kinetics simulation, is useful for several investigations. First, in connection with the instability simulations, it can be used to investigate the strength of coupling between vibrational levels in a PIE discharge. Second, in connection with optical waveform control studies, a kinetics simulation can be used to investigate the wave-shaping possibilities of burst-mode operation.

The ELENDIF & GAMUT package will also be useful for generating BE solutions for ZODIAC gas mixtures and discharge conditions, required for future ZODIAC simulations. This, and other possibilities for further work will be discussed at greater length in Chapter 7.

Bibliography

[1] Hunter, S. R., and Christophorou, L. G. (1984): Electron motion in low- and high-pressure gases *in Electron-Molecule Interactions and their Applications II* (L. G. Christophorou, ed.), pp. 90-221. (Academic Press, Orlando).

[2] Morgan, W. L., and Penetrate, B. M. (1990): ELENDIF: A time-dependent Boltzmann solver for partially ionized plasmas. Computer Phys. Commun. **58**, 127-152.

[3] Mitchner, M., and Kruger, C. H. (1973): *Partially Ionized Gases* (John Wiley & Sons).

[4] Phelps, A. V., and Pitchford, L. C. (1985): Anisotropic scattering of electrons by N_2 and its effects on electron transport. *Phys. Rev. A* **31**, 2932-2949.

[5] Phelps, A. V., and Pitchford, L. C. (1985): JILA Information Center Report No. 26. (Joint Institute for Laboratory Astrophysics).

[6] Pitchford, L. C., and A. V. Phelps (1982): Comparative calculation of electron-swarm properties in N_2 at moderate E/n values. Phys. Rev. A **25**, 540-554.

[7] Hayashi, M. (1987): Electron collision cress-section determined from beam and swarm data *in Swarm Studies and Electron-Molecule Collisions*, p. 167. (Springer-Verlag)

[8] Hayashi, M. (1989): Electron collision cross-sections for atoms and molecules determined from beam and swarm data *in Proceedings of IAEA Advisory Group Meeting on Atomic and Molecular Data for Radiotherapy*, pp. 193 - 199. (Vienna, 13-16 June 1988)

[9] Hayashi, M. (1990): Electron collision cross-section determined from beam and swarm data by boltzmann analysis *in Nonequilibrium Processes in Partially Ionized Gases*. (M. Capitelli and J. N. Bardsley eds.), pp. 333-340. (Plenum Press, New York).

[10] Hayashi, M. (1992): Electrons collision cross-sections *in Handbook of Plasma Material Science*, pp. 748-766. (printed in Japan, ISBN 4-27-02232-3).

[11] Hayashi, M. (1994): personal communication

[12] Lakshminarasimha, C. S., J. Lucas, J. L. Moruzzi, and I. L. Spalding (1976): Electron swarm parameters in CO2 laser gas mixtures. J. Phys. D: Appl. Phys. **9**, 1727-1735.

[13] Luft, P. E. (1975): JILA Information Center Report No. 14: *Description of a backward prolongation program for computing transport coefficients*. (Joint Institute for Laboratory Astrophysics).

[14] Land, J. E. (1977): Atomic Collision Cross Section Data Center Data Memo No. 2: *Cross section and transport coefficients for electrons in carbon monoxide*. (Joint Institute for Laboratory Astrophysics).

[15] Land, J. E. (1978): Electron scattering cross section for momentum transfer and inelastic excitation in carbon monoxide. J. Appl. Phys. **49**, 5716-5721.

[16] Sierra, R. A., Brooks, H. L., Sommerer, A. J., Foltyn, S. R., and Nygaard, K. J. (1981): Effective swarm parameters and transport coefficients in CO2 laser mixtures. J. Phys. D: Appl. Phys. **14**, 1791-1801.

[17] Kucukarpaci, H. N., Saelee, H. T., and Lucas, J. (1981): Electron swarm parameters in helium and neon. J. Phys. D: Appl. Phys. **14**, 9-25.

[18] Dutton, J. (1975): A survey of electron swarm data. J. Phys. Chem. Ref. Data **4**, 577-856.

[19] Compton, R. W., Elford, M. T., and Jory, R. L. (1967), Aust. J. Phys. **20** 369-400

[20] Elford, M. T. (1966), Austr J. Phys. **19**, 629.

[21] Pack, J. L., Voshall, R. E., and Phelps, A. V. (1961), Phys. Rev. **121**, 798

[22] Pack, J. L., Voshall, R. E., and Phelps, A. V. (1962), Phys. Rev. **127**, 2084.

[23] Limbeek, J. W., and J. Lucas (1978): Time-of-flight measurements of electron transport parameters in CO_2-N_2-He gas mixtures. IEE Solid-State Electron Dev. **2**, 161-163.

[24] Limbeek, J. W., and J. Lucas (1978): Computations and measurement of the fluorescent infrared radiation from glow discharges in CO_2-N_2-He gas mixtures. IEE Solid-State Electron Dev **2**, 155-160.

[25] Byron, S. R., and Apter, H. (1992): Model of gas composition and plasma properties in sealed cw CO_2 lasers. J. Appl. Phys. **71**, 1976-1991.

[26] Hokazono, H., Obara, M., and Midokoriwa, K. (1991): Theoretical operational life study of the closed-cycle transversely excited atmospheric CO_2 laser. J. Appl. Phys. **69**, 6850-6868.

[27] Rapp, D., and Englander-Golden, P. (1965): Total cross sections for ionization and attachment in gases be electron impact. I. Positive Ionization. J. Chem. Phys. **43**, 1464-1476.

[28] Rapp, D., and Englander-Golden, P. (1965): Total cross sections for ionization and attachment in gases be electron impact. I. Negative-Ion Formation. J. Chem. Phys. **43**, 1480-1489.

[29] Sazhin, S., M. Makhlouf, and D. Toebaert (1994): The Boltzmann equation for the electron energy distribution function in CO_2 laser discharges. Phys. Lett. A **185**, 99.

[30] Smith, K., and Thompson, R. M. (1978): *Computer Modelling of Gas Lasers* (Plenum Press, New York).

[31] Roberts, S. A. (1979): Numerical modelling of a chemical plasma I. REACS: A program to generate all reactions which take place in a plasma of a given chemical content. Computer Phys. Commun. **18**, 353-362.

[32] Roberts, S. A. (1979): Numerical modelling of a chemical plasma II. PLASKEM: A program to predict the variation with time of the number densities of chemical species within a plasma. Computer Phys. Commun. **18**, 363-376.

[33] Roberts, S. A. (1979): Numerical modelling of a chemical plasma III. DATSTOR: A program to create a data base containing information on rate coefficients of chemical reactions. Computer Phys. Commun. **18**, 377-384.

[34] Davis, A. R., Smith, K., and Thompson, R. M. (1975): TLASER – A CO_2 laser kinetics code. Computer Phys. Commun. **10**, 117-132.

7

Conclusions and Recommendations

7.1 Conclusions

For high-power CO_2 lasers to be a viable alternative for many potential applications, new laser devices are required which are more versatile, more compact, and more cost effective than those presently available. This thesis has presented several studies which will contribute to making existing convectively cooled devices considerably more flexible and amenable to custom processing applications, and also more compact through a better understanding of discharge thermal instability. Also, several studies have been presented which have aided the advancement of multi-kW slab arrays. ZODIAC radial arrays are remarkable for their compactness and simplicity, and they may possibly represent the next phase of high-power laser evolution. A brief summary is given below of the results presented in this thesis, and of their original contributions.

7.1.1 ZODIAC Multi-kW Slab Array

In this thesis, two numerical models, SLIM and M2, have been developed to address the two problems presently facing the advance of multi-kW slab arrays: how to attain a uniform discharge over large-area electrodes; and how to combine the emissions of many array elements to produce one "high quality" beam.

Discharge Uniformity

SLIM, the loaded electrode model developed in Chapter 2, can be used to predict the uniformity of discharge excitation on waveguide electrodes, including large-area slabs. It is the first published electrode model which accounts for the effects of discharge loading, and for the dependence of discharge properties on gas pressure, excitation frequency, and local power loading. Additional advantages related to its generality are that it readily accommodates an arbitrary configuration of distribution-smoothing elements connected along the electrode length. Indeed, the model appears sufficiently general to facilitate development of electrode optimization protocols for gas slab lasers.

Another original contribution of Chapter 2 is the non-invasive fiber-optic detector developed to verify the accuracy of SLIM. This luminosity sampler is superior to previous TL probes in that it does not perturb the local discharge state, and its calibration is independent of discharge and excitation conditions.

Together, the model and detector have made possible the development of a new approach to attaining homogeneous excitation between waveguide electrodes. In this method, a uniform standing wave is established by matching shunt resonating inductors directly to the discharge load, instead of to an augmented structure capacitance. This approach is particularly well suited to large-area slab electrodes, especially when it is desirable to have open-channel electrodes, or to minimize the number of resonating inductors.

Finally, the model, detector, and method have been successfully applied to developing doubly end-driven electrodes for a high-power slab array. These electrodes make possible the uniform distribution of laser gain amongst many parallel channels, while also allowing for free gas flow and for optical modes to exit transversely from the electrodes, as are required for a multi-kW ZODIAC array. [1]

Beam Propagation Characteristics

The code M2, described in Chapter 3, computes the M^2 of an arbitrary paraxial beam, given its electric field distribution at the beam waist. Together with confocal resonator and gaussian beamlet approximations, M2 can be used to estimate a lower bound on M^2 attainable with radial arrays, and also to predict the effects of array configuration on far-field properties. These approximations, which do not require knowledge of the actual beamlet modes, have facilitated the first analysis of radial array beam propagation and focusing.

In estimates of best-possible performance, radial arrays were demonstrated to produce a circular focal spot which is inherently well suited to multi-directional materials processing. However, with non-phase locked beamlets, attaining $M_r^2 < 5$ is not possible without corrective optics which enhance the array fill-factor. M2 predicts that even with complete phase-locking, aperture-filling corrections are required if M_r^2 is to be reduced by more than 20% relative to that of the corresponding non-PL case. M2 demonstrates, however, that complete phase-locking can reduce the far-field central lobe to nearly diffraction limited sizes. The power fraction contained by this central lobe then varies inversely with the array fill-factor.

Achieving $M^2 < 4$ appears to require either low-pass spatial filtering, which is relatively simple to implement but has a potentially large cost in lost beam power (*e.g.*, >50% to attain $M^2 \approx 1.3$), or aperture-filling techniques, which are more complex to implement but which potentially have low losses and which can also be used to phase-lock the array. One possible aperture-filling configuration for a ZODIAC geometry would employ reflective compactors to increase the radial fill-factor, and diffractive elements to increase the angular fill-factor. Details of optimization and implementation must be the subject of future studies.

In any case, given ZODIAC's advantages in terms of axial-symmetry, compactness, and simplicity, improved beam quality should not be required for it to be an attractive choice for a variety of materials processing applications, particularly those which do not require a small M^2. Indeed, with a truly portable laser in the 10's of kilowatts range, many new applications will undoubtedly be created.

7.1.2 PIE Burst-Mode Operation

This thesis has also investigated two promising implications of burst-mode operation on PIE laser performance. Enhanced discharge stability, which allows higher operational powers, was investigated with the numerical model CODE1, developed specifically for the purpose. Optical waveform control, which imparts an additional degree of control to materials processing, was demonstrated experimentally, and empirically characterized. To facilitate future investigative simulations of both phenomenon, the GAMUT/ELENDIF/cross-section suite was assembled to compute electron transport and rate coefficients.

Enhanced Discharge Stability

CODE1, the 1D positive column simulation developed in Chapter 4, can be used to simulate current filamentation in the positive column region of a PIE discharge. CODE1 has facilitated the first modelling of PIE discharge phenomena, and the first simulation of instability in a non-steady discharge. In particular, with CODE1 the burst-mode stabilization effect observed by Nikumb *et al.* [2] was studied. Mechanisms which stabilize intermediate burst rates relative to CW operation were sought, as were mechanisms which destabilize low burst rates relative to intermediate burst rates.

One primary factor was identified with the CODE1 simulations which would cause PIE discharges to be least stable at low burst rates, as was observed by Nikumb *et al.* Thermal instability growth was observed to be most rapid during the inter-burst interval, which is self-sustained and therefore inherently less stable than the impulse-sustained burst interval. The problem of instability growth during the inter-burst interval was also found to be compounded by negative ions accumulating during that interval due to its higher E/n.

Several factors were identified which may lead to enhanced discharge stability at intermediate burst rates, as was observed by Nikumb *et al.* First, strong photoionization was found to stabilize the discharge by selectively creating fewer electrons within regions of depressed gas density. This stabilization mechanisms was overwhelmed at lower burst rates by rapid instability growth during the inter-burst interval, once it was sufficiently long to allow the self-sustained conditions to be established. A second stabilizing factor was observed experimentally. Both the impulse amplitude and average energy per impulse were found to increase with decreasing burst rate, under experimental conditions similar to those of Nikumb *et al.* Higher impulse amplitudes are expected to more strongly stabilize the discharge during the burst interval, regardless of whether avalanche ionization or photo-ionization dominates. Finally, another possible mechanism was identified, although observed neither in the simulation nor in experiments. When instability growth during the inter-burst interval may be neglected (which would be possible, for example, if the power density during the inter-burst interval was sufficiently small), then discharge stability is expected to increase at lower burst rates, because the instantaneous growth rate during the burst interval varies more weakly than JE^{-1}. Because there are uncertainties in the experimental discharge waveforms, this mechanism bears further investigation.

The CODE1 effort, though indeed a major one, must be considered as the first increment in the solution of a very complex problem. It will provide the basis for future analysis of the burst-mode stabilization effect.

Optical Waveform Control

Optical envelope control at multi-kW average powers, demonstrated experimentally with a PIE laser and described in Chapter 5, will impart an additional degree of control to materials processing. When operated in burst-mode, PIE lasers are able to produce a broad range of optical output waveforms. Laser output may be readily varied from distinct, independent pulses through to a continuous wave. Considerable variation in optical pulse shape is also possible. Since burst-mode operation encompasses both high peak and high average power pulsed operation, it promises to lend itself to a wide variety of applications. The high-power pulsed radiation produced under burst-mode operation has proven to be particularly useful for deep-penetration welding of heavy metal sections. [3]

In this first study of burst-mode optical waveform shaping, simultaneous control of optical pulse duration and peak power has been demonstrated, through choice of the excitation burst frequency and the number of impulses per burst. Empirical relationships characterizing the dependence of optical duty cycle and peak laser power on these burst-mode control parameters have been developed. These will aid further improvements of the deep penetration welding process.

The current and optical waveform monitors developed for the analysis of this chapter are expected to have further application in the analysis of PIE system behavior. In particular, information about the instantaneous discharge state will aid subsequent simulation of both discharge instability and waveform control.

Electron Transport and Rate Coefficients

The GAMUT/ELENDIF/cross-section suite, assembled and tested in Chapter 6, can be used to compute electron transport and rate coefficients, which are fundamental to laser and discharge modelling. In particular, these coefficients will be useful for the laser kinetics simulations that were proposed in Chapter 5 for further investigation of optical waveform control, and for the further instability studies required by Chapter 4. This package will also be useful for generating the coefficients required for future ZODIAC discharge and laser kinetics simulations.

The suite is based on the public domain Boltzmann equation solver ELENDIF. [4] This code was incorporated as a subroutine within GAMUT, created to control solution convergence and accuracy, and to generate BE solutions for a specified list of discharge conditions The accuracy of

GAMUT, ELENDIF, and the cross-sections were tested by comparing computed coefficients with available experimental data. This test was necessary to confirm that ELENDIF, which assumes a two-term isotropic inelastic solution, is sufficiently accurate for the molecular gas mixtures of CO_2 lasers. Given satisfactory agreement in these comparisons, coefficients were computed for a typical PIE laser mixture. It was observed that for future simulations, the presence of CO in the discharge must be accounted for.

7.2 Recommendations for Further Work

7.2.1 ZODIAC

Discharge Uniformity

Possibilities for further work with SLIM may be separated into further model applications, and extensions of the existing model. Related to further applications, given the model's generality it will be of interest to perform a broader study of how variations in frequency, pressure, and inductor position and magnitude affect discharge uniformity. The resulting insights could be distilled into a design optimization protocol. In this connection, to test various protocols it will be helpful to define these as minimization problems, and use a computational algorithm such as simulated annealing [5] to find optimal solutions.

There are many possibilities for model extension. First, it will be of interest to extend the model to treat pulsed discharge operation, which is known to alter the effective discharge impedance, [6] and to determine model coefficients for gas mixtures other than $He:N_2:CO_2 = 3:1:1 + 5\%$ Xe. The required experiments could be performed with a small test cell similar to that of Vitruk *et al.* [7] Further development of the uniformity detector will also be of interest. In particular, characterizing discharge luminosity for a range of excitation frequencies, gas mixtures and pressures, and pulse configurations will be required for SLIM to be tested under a wider variety of conditions.

Regarding theoretical aspects, scaling laws for sheath power dissipation require further investigation, as was noted in Chapter 2. It may also be of interest to extend SLIM to 2D for proper treatment of transverse variations on very wide electrodes.

Beam Propagation Characteristics

The M^2 estimates computed in Chapter 3 suggest that without spatial filtering or aperture filling, a low M^2 (<3) cannot be attained with a radial array. This result motivates more specific considerations of how ZODIAC M^2 might be improved. Computer modelling will be a key part of such considerations, allowing the exploration of many combinations of aperture filling and spatial filtering which are not conveniently accessible experimentally.

The code M2 is readily extended to treat paraxial beam propagation, spatial filtering, and effects of both diffractive and refractive optics. Simplest is the consideration of spatial filtering, which requires only an aperturing of the far-field distribution and then a second Fourier transform to obtain the new near-field distribution. Effects of paraxial propagation are also readily incorporated into M2. This would require only an additional multiplication by a phase factor dependent on the propagation distance [*cf.* (3.2-8)], and a subsequent reverse Fourier transform. Accommodating beam propagation will generalize M2 to allow M^2 computation given a beam's electric field profile on *any* plane, not just at the beam waist. This generalization will also allow treatment of variously positioned transmissive or reflective optical elements, each of which would be accounted for by a transformation amounting to an array multiplication.

Ultimately it will be of interest to compute actual ZODIAC resonator modes with the Fox and Li method, [8] and to perform a comprehensive analysis of how resonator configurations and variations such as misalignments affect mode production (for an excellent example of such an analysis, see reference [9]). A comprehensive resonator model will also be useful for selecting optimal corrective optics schemes and for phase-locking studies.

7.2.2 PIE Burst-Mode

Discharge Stability

Further experimental studies of PIE discharge operation are required. Specifically, prior to further theoretical analysis, the actual discharge current and voltage waveforms must be known, as must be pulser conditions. Also, the effect of pulser conditions on discharge state should be better understood. A model of the PIE discharge and circuit would be useful in this connection, to determine the relative importance of photoionization and electron-impact ionization during the impulse events.

Regarding future modelling efforts of discharge stability, ultimately it will be desirable to create a two-dimensional simulation which treats in detail instability growth in both the sheath and positive column regions of the discharge. However such a simulation must certainly be a long-term goal, considering the extreme complexity of the problem. Until then, a sequence of increasingly sophisticated models, each benchmarked against experiment and previous simpler theoretical models, is required to clarify separate aspects of the problem. [10]

The next phase of theoretical instability analysis should be a linear-perturbation analysis of a spatially uniform discharge state, which accounts more completely for effects of discharge chemistry and vibrational kinetics in the discharge positive column. Solution in the case of a PIE discharge is not tractable in closed-form, but solution with high-accuracy numerical methods is a viable alternative. In a numerical implementation, the reduced computational burden relative to a simulation would allow many more physical processes to be included in detail. To this end, an ODE-solving package has been written in C, based on the adaptive extrapolation algorithm of Deuflhard. [11-14] In this code, high precision and flexibility were emphasized above other concerns. In the final object-oriented implementation, equations and Jacobians are conveniently entered in operator format.

Optical Waveform Control

Because the PIE excitation method is so flexible, the burst-mode principle may be readily generalized beyond its present simple realization. Specifically, both pulse-position modulation (PPM) and pulse-amplitude modulation (PAM) of the impulse stream are possible. PPM may be achieved through simple modification of the pulse generator which triggers the thyratron grid driver. Microprocessor control would allow rapid reconfiguration of arbitrarily complicated impulse sequences. The only configuration constraint would be the pulser circuit recharging time, which would limit the minimum impulse spacing. PAM, more difficult to achieve, could be produced by modulating the pulser charging voltage. PPM or PAM would provide additional discharge control parameters allowing further PIE-process optimization. They could perhaps also facilitate custom tailoring of optical pulse envelopes to suit particular material processing requirements. For example, it has been suggested that under certain pulse conditions, weld solidification may ensue prior to completion of a laser pulse. It may therefore be possible to control the weld microstructure through manipulating the temporal profile of the laser pulse. [15]

To aid implementation and application of generalized burst-mode, a laser kinetics simulation will be useful. For example, the simulation could be used to work backwards from a desired optical waveform to determine the discharge conditions required to produce it. More generally, a wider range of experiments are conveniently accessible to simulation than are to direct experimentation. Simulation will therefore be useful in the exploration of other wave-shaping possibilities and in the refinement of wave-shaping techniques. Anticipating this application, the laser kinetics simulation TLASER [16] has been acquired and modified to accept input of experimental current waveform data. It remains to accommodate time-dependent excitation rates into the model. The required excitation rates may be obtained from the GAMUT/ELENDIF solutions of Chapter 6. A more direct and more accurate alterative is to incorporate ELENDIF into the kinetics simulation as a subroutine.

Electron Transport and Rate Coefficients

While the cross-sections and BE solver ELENDIF assembled in Chapter 7 are the best which are readily available at the present time, continued attention should be paid to developments in gaseous electronics. With the increasing availability of cheap computing power, and a renewed interest in gas discharge physics by western science,[†] multi-term BE solvers and companion cross-section sets should soon be more readily available.

[†] These trends are related, since it is primarily the microelectronics industry which is driving present advances in gas discharges technology. [17]

Bibliography

[1] Bilida, W. D. (1996): Radial Array Slab Laser Excitation with a Resonant Cavity (Ph.D. Dissertation, University of Alberta).

[2] Nikumb, S. K., H. J. J. Seguin, V. A. Seguin, R. J. Willis and H. W. Reshef (1989): High-Average Power-Pulsed Performance of a Multikilowatt PIE Laser. *IEEE J. Quantum Electron.* **25**, 1725-1735.

[3] Scott, S. W. C. (1996): *A CO_2 Laser Burst Excitation Technique for Deep Penetration Welding.* (Ph.D. Dissertation, University of Alberta).

[4] Morgan, W. L., and Penetrate, B. M. (1990): ELENDIF: A time-dependent Boltzmann solver for partially ionized plasmas. Computer Phys. Commun. **58**, 127-152.

[5] Press, W. H., Teukolsky, S. A., Vetterling, W. T., and Flannery, B. P. (1992): *Numerical Recipes in C: The Art of Scientific Computing*, 2nd ed (Cambridge University Press).

[6] Baker, H. J., and Laidler, I. (1990): Electrical characterization of pulsed and CW fast axial flow RF excited CO_2 lasers in High-Power Gas Lasers (, ed.). Proc. SPIE **1225**, 349-356.

[7] Vitruk, P. P., Baker, H. J., and Hall, D. R. (1992): The characteristics and stability of high power transverse radio frequency discharges for waveguide CO_2 slab laser excitation. J. Phys. D: Appl Phys. **25**, 1767-1776.

[8] Fox, A. G., and Li, T. (1961): Resonant modes in a laser interferometer. Bell Syst. Tech. J. **40**, 453-488.

[9] Ehrlichmann, D., U. Habich, and H. Plum (1993): High-power CO_2 laser with coaxial waveguide and diffusion cooling. IEEE J. Quantum Electron. **29**, 2211-2219.

[10] Winkler, K.-H. A., Norman M. L., Mihalas, D. (1985): Implicit Adaptive-Grid Radiation Hydrodynamics *in Multiple Time Scales*, (J. U. Brackbill, and B. I. Cohen, eds.), pp. 146-183. (Academic Press)

[11] Hairer, E., Bader, G., Libich, Ch. (1982): On the stability of semi-implicit methods for ordinary differential equations. BIT **22**, 211-232.

[12] Deuflhard, P. (1983): Order and stepsize control in extrapolation methods. Numer. Math. **41**, 399-422.

[13] Bader, G., Deuflhard, P. (1983): A semi-implicit mid-point rule for stiff systems of ordinary differential equations. Numer. Math. **41**, 373-398.

[14] Deuflhard, P. (1985): Recent progress in extrapolation methods for ODEs. SIAM Review **27**, 505-535.

[15] Basu, B. (1991): Critical heat transfer analysis of pulsed laser melting of pure metals. Appl. Phys. Lett. **58**, 656-658.

[16] Davis, A. R., Smith, K., and Thompson, R. M. (1975): TLASER – A CO_2 laser kinetics code. Computer Phys. Commun. **10**, 117-132.

[17] Graves, D. B. (1989): Plasma processing in microelectronics manufacturing. AIChE J. **35**, 1-29.